Growth and Characterization of Nanocomposite YBa2Cu3O7-δ – BaMO3 (M = Zr, Hf) Thin Films from Colloidal Solutions

Ziliang Li

Universitat Autònoma de Barcelona

Growth and Characterization of Nanocomposite $YBa_2Cu_3O_{7-\delta}$ – $BaMO_3$ (M = Zr, Hf) Thin Films from Colloidal Solutions

Ziliang Li

Doctoral Thesis

Supervisors

Prof. Xavier Obradors Berenguer

Dr. Mariona Coll Bau

PhD program in Materials Science
Physics Department, Sciences Faculty
Universitat Autònoma de Barcelona (UAB)

Superconducting Materials and Large Scale Nanostructures
Materials Science Institute of Barcelona (ICMAB-CSIC)

Tutor
Prof. Javier Rodríguez Viejo

Universitat Autònoma de Barcelona
Department of Physics, Faculty of Science

ICMAB INSTITUT DE CIÈNCIA DE MATERIALS DE BARCELONA

EXCELENCIA SEVERO OCHOA

CSIC CONSEJO SUPERIOR DE INVESTIGACIONES CIENTÍFICAS

June 2018

Universitat Autònoma de Barcelona

Prof. Xavier Obradors Berenguer, full professor of the Superconducting Materials and Large Scale Nanostructures of the Materials Sciences Institute of Barcelona (ICMAB-CSIC); **Dr. Mariona Coll Bau**, Ramon y Cajal Scientist of the Superconducting Materials and Large Scale Nanostructures of the Materials Sciences Institute of Barcelona (ICMAB-CSIC) and **Prof. Javier Rodríguez Viejo**, applied physics professor at Universitat Autònoma de Barcelona

CERTIFY

that the dissertation "Growth and Characterization of nanocomposite $YBa_2Cu_3O_{7-\delta}$ – $BaMO_3$ (M = Zr, Hf) Thin Films from Colloidal Solutions" submitted by Mr. **Ziliang Li** to the Science Faculty in fulfillment of the requirements for the degree of Doctor of Philosophy in the Materials Science program has been performed under their supervision.

For that record they sign the certificate.

Bellaterra, Barcelona, June 2018

Supervisor:	Supervisor:	Tutor:
Prof. Xavier Obradors Berenguer	Dr. Mariona Coll Bau	Prof. Javier Rodríguez Viejo

List of abbreviation

YBCO	$YBa_2Cu_3O_{7-\delta}$
Y248	$Y_2Ba_4Cu_8O_{16}$
Y225	$Y_2Cu_2O_5$
YO	Y_2O_3
BYF	$Ba_{1-x}Y_xF_{2+x}$
OF	Ba Oxyfluoride
BZO	$BaZrO_3$
BHO	$BaHfO_3$
BYTO	Ba_2YTaO_6
APC(s)	Artificial Pinning Centre(s)
NP(s)	Nanoparticle(s)
NC(s)	Nanocomposite(s)
CC(s)	Coated Conductor(s)
TFA	Trifluoroacetates Route
MeOH	Methanol
LAO	$LaAlO_3$
STO	$SrTiO_3$
PLD	Pulsed Laser Deposition
CSD	Chemical Solution Deposition
MOD	Metalorganic Decomposition Route
MOCVD	Metal-Organic Chemical Vapor Deposition
HTS	High Temperature Superconductors
LTS	Low Temperature Superconductor
FWHM	Full Width at Half Maximum
F_L	Lorentz Force
F_P	Pinning Force

λ	Penetration Depth
ξ	Coherence Length
ϕ_0	Flux Quantum
ε	Nanostrain
H_{c1}	Lower Critical Field
H_{c2}	Upper Critical Field
IL	Irreversibility Line
G	Growth Rate
SEM	Scanning Electron Microscopy
TEM	Transmission Electron Microscopy
LAADF	Low Angle Annular Dark Field
SQUID	Superconducting Quantum Interference Device
ZFC	Zero Field Cooled
GADDS	General Area Detector Diffraction System
T_c	Critical Temperature
J_c	Critical Current Density
J_c^{sf}	Critical Current Density at self-field
XRD	X-Ray Diffraction
HRXRD	High resolution XRD
EDX	Energy Dispersive X-ray Detector
AFM	Atomic Force Microscopy
OM	Optical Microscope
M	Magnetization
FH	Flash Heating
CTA	Conventional Thermal Annealing
2D	Two-dimension
ss-nanocomposite	Spontaneously Segregated nanocomposites
pn-nanocomposite	Preformed Nanoparticle nanocomposite

Contents

Acknowledgments

I would like to express my appreciation to the people and institutions that have made this thesis possible.

First of all, I would like to give my special acknowledgements to China Scholarship Council (CSC) for giving me the opportunity to study abroad. Also, to Prof. Xavier Obradors and Prof. Teresa Puig for letting me being a member of the Superconducting Materials and Large Scale Nanostructures (SUMAN) group.

I give my very special gratitude to my supervisors Prof. Xavier Obradors and Dr. Mariona Coll for their patient guidance, enthusiastic help and constant encouragement during this time. Also, I would like to extend this gratitude to Prof. Teresa Puig for all the discussions and knowledge we have shared.

I would like to acknowledge the European Union, the Spanish Government and the Generalitat de Catalunya for the financial support with the research projects: the European development of Superconducting Tapes (EUROTAPES, FP7-NMP-Large-2011-280432), the EU (EU-FP7 NMP-LA-2012-280432 EUROTAPES project), MINECO (COACHSUPENERGY, MAT2014-51778-C2-1-R), Generalitat de Catalunya (2014SGR 753 and Xarmae) and the Center of Excellence award Severo Ochoa SEV-2015-0496. With their funding, it is possible for my attendance to a number of european and international conferences and courses.

The completion of this work would not be possible without the collaboration and discussion with scientific experts in various fields. Therefore, I will like to express my great gratitude:

To Dr. Pablo Cayado and Mrs Mariona de Palau, for their professional, courteous and patient support in techniques at the beginning of my work;

To the members of “Inorganic nanoparticles and functional ligands” group at Autonomous University of Barcelona (UAB), particularly to Miss Natalia Chamorro and Dr. Susagna Ricart, for the nanoparticle colloidal solutions supply and for everything that I have learned from them about chemistry and nanoparticle synthesis;

To Dr. Jaume Gázquez and, particularly, Mr. Bernat Mundet for all the TEM work they have provided, which are essential for the investigation and interpretation of the microstructural characteristics of our samples;

To Dr. Anna Palau and Mr. Ferran Vallès from the transport measurements team of SUMAN group, for the transport measurements and all the information have provided, which are vital for reaching valuable conclusions of this work;

To all the scientific and technique services from ICMAB: Anna Crespi, Joan Esquius and Francesc Javier Campos Campos for the XRD measurements and their patient and enthusiastic knowledge sharing, Bernat Bozzo for the magnetometry measurement, Ana Esther for the SEM measurements, Maite Simón and Andrés Gómez for the AFM measurements, Luigi Morrone and Neus Roma for profilometry measurements.

To the administrative staff of ICMAB for their help with the public affairs;

To all the previous and present members of our group: Dr. Pablo Cayado, Dr. Xavier Granados, Dr. Albert Calleja, Dr. Marta Vilardell, Dr. Valentina Roxana, Dr. Albert Queraltó, Dr. Rafael Ortega, Dr. Juan Carlos Gonzalez, Mr. Jukka Malinen, Dr. Cornelia Pop, Dr. Mar Tristany, Dr. Roger Guzmán, Dr. Flavio Pino, Mr. Joshua Bailo, Dr. Mateusz Scigaj, Mr. Bohores Villarejo, Mr. Alexander Stangl, Mr. Juri Banchewski, Dr. Max Sieger, Mrs. Can Fu, Mr. Hailin Wang and Mrs. Pengmei Yu for their valuable help but also for their friendship during this time. Special thanks to to all my officemates Dr. Pablo Cayado, Dr. Albert Queraltó, Mr. Artur Romanov, Mrs. Pamela Machado and Mrs. Julia Jareño for their encouragement, kind help and good climate of work.

I am very grateful for all my friends from ICMAB who have comforted and encouraged me during my most difficult time.

Finally, I would like to express my special gratitude to my parents, for their love, care and continuous support in all my life.

Abstract

$YBa_2Cu_3O_{7-\delta}$ is the best material choice to address the performances required in superconducting power applications and magnets working under high magnetic fields. However, it is still challenging to achieve low manufacturing costs and high superconducting performances of coated conductors for large scale power applications. Chemical Solution Deposition has emerged as a very competitive technique to obtain epitaxial films and multi-layers of high quality with controlled nanostructures.

We have developed a novel Flash Heating growth process that shows high potential to be compatible with the industrial reel-to-reel production of $YBa_2Cu_3O_{7-\delta}$ coated conductors. Here we have set up, for the first time, a full image describing the intermediate phase and microstructure evolution during this heating process. We have extended the growth temperature window to lower temperature without any degradation of superconducting properties, making it compatible with the deposition of $YBa_2Cu_3O_{7-\delta}$ coated conductors on CeO_2-caped metallic tape substrates. In addition, we have also found that this growth process promotes the formation of a high concentration of stacking faults and so of nanostrain.

$YBa_2Cu_3O_{7-\delta}$ and nanocomposite ultrathin films, in the range of 5-50 nm, have been prepared after a series optimization of growth parameters. The relief of the interfacial energy induces a high density of stacking faults, leading to a highly distorted $YBa_2Cu_3O_{7-\delta}$ matrix. Such microstructural disorder becomes extremely serious when the film thicknesses decrease below 25 nm, significantly degrading the superconductivity. We have also studied the evolution of the characteristics of spontaneously segregated nanoparticles with nanocomposite film thicknesses and their influence on the vortex pinning efficiency.

The preparation of $YBa_2Cu_3O_{7-\delta}$ nanocomposites from non-reactive preformed oxide nanoparticles from colloidal solutions has demonstrated to be a very successful strategy to achieve a tight control of the nanoparticle characteristics and the optimized nanostructural landscape on the superconducting films for enhanced pinning efficiency. $BaMO_3$ (M = Zr, Hf) perovskites are shown to be the most promising compositions of preformed nanoparticles up to now that led to high quality nanocomposite films at high nanoparticle concentrations (20-25 mol%). The composition and size of nanoparticles have demonstrated to be crucial factors for tailoring vortex pinning performance in applied magnetic field. The application of the Flash Heating growth process in the growth of nanocomposite films allows both the preservation of nanoparticle size and the generation of a high density of short stacking faults, which play a synergistic effect to increase the artificial pinning centers and enhance the strong pinning contribution. Multi-deposition technique is proved effective to further enhance the film thickness while vortex pinning efficiency is preserved and current-carrying capacity of the nanocomposite films is increased.

Resumen

El $YBa_2Cu_3O_{7-\delta}$ es el superconductor de alta temperatura con mayor potencial tecnológico para aplicaciones de potencia e imanes que trabajan bajo campos magnéticos elevados. Sin embargo, todavía es un reto mejorar sus prestaciones en forma de película delgada epitaxial con un coste bajo de fabricación. La deposición de soluciones químicas ha surgido como una técnica muy competitiva para obtener láminas delgadas epitaxiales y multicapas de alta calidad con nanoestructuras controladas.

Hemos desarrollado un proceso novedoso de crecimiento mediante Calentamiento Flash que muestra un excelente potencial para la producción industrial en continuo de conductores epitaxiales de $YBa_2Cu_3O_{7-\delta}$. En esta tesis hemos establecido, por primera vez, una imagen completa que describe las fases intermedias y la evolución de la microestructura durante el calentamiento. Hemos extendido la ventana de la temperatura de crecimiento sin ninguna degradación de las propiedades superconductoras, por lo que la deposición de conductores epitaxiales de $YBa_2Cu_3O_{7-\delta}$ es compatible con el uso de sustratos de cinta metálica con capas tampón de CeO_2. Además, también hemos encontrado que este proceso de crecimiento promueve la formación de una alta concentración de defectos de apilamiento y, por lo tanto, de tensiones a escala nanométrica.

Las láminas ultrafinas de $YBa_2Cu_3O_{7-\delta}$ y nanocompuestos, en el rango de 5-50 nm, se prepararon después de una optimización de los parámetros de crecimiento. La reducción de la energía interfacial induce una alta densidad de defectos de apilamiento, lo que conduce a una matriz de $YBa_2Cu_3O_{7-\delta}$ altamente distorsionada. Esta modificación microestructural se vuelve extremadamente grave cuando el grosor de la lámina delgada disminuye por debajo de 25 nm, degradando significativamente las propiedades superconductoras. También hemos estudiado la evolución de las características de las nanopartículas segregadas espontáneamente con el espesor de las láminas delgadas y su influencia en la eficiencia del anclaje de vórtices.

La preparación de nanocompuestos de $YBa_2Cu_3O_{7-\delta}$ a partir de nanopartículas de óxido preformadas y no reactivas que forman soluciones coloidales ha demostrado ser una estrategia muy exitosa para lograr un estricto control de las características de las nanopartículas y la optimización de la nanoestructura de las láminas delgadas superconductoras. Las perovskitas $BaMO_3$ (M = Zr, Hf) son las composiciones más prometedoras de nanopartículas preformadas que hasta ahora han conducido a láminas delgadas de nanocompuestos de alta calidad con altas concentraciones de nanopartículas (20-25% molar). La composición y el tamaño de las nanopartículas han demostrado ser factores cruciales para adaptar el rendimiento del anclaje de vórtices bajo campos magnéticos aplicados. La aplicación del proceso de crecimiento de calentamiento flash al

crecimiento de láminas delgadas nanocompuestas permite la preservación del tamaño de las nanopartículas y la generación de una alta densidad de defectos de apilamiento de pequeña longitud, que desempeñan un efecto sinérgico para aumentar la eficiencia de los centros de anclaje de vórtices artificiales y mejorar así las propiedades de los conductores. La técnica de multideposición es efectiva para aumentar aún más el espesor de la lámina delgada, mientras que la eficacia del anclaje de vórtices se conserva y la capacidad de transporte de corriente eléctrica de las láminas delgadas nanocompuestas aumenta.

Motivation

The discovery of high temperature superconducting (HTS) materials in 1986 has stimulated worldwide research in superconductivity due to their wide range of power application prospects. To achieve reliable and large scale applications in power grid, superconductors should fulfill two main requirements: high superconducting performances and low manufacturing cost.

$YBa_2Cu_3O_{7-\delta}$ (YBCO) has high potential to carry high currents at high magnetic fields and high temperatures, making it the most promising material for HTS wires (second-generation coated conductors (CCs)). Nowadays, YBCO CCs can properly satisfy the requirements for power applications at low external magnetic field. However, the applications requiring high magnetic fields are limited by the significant degradation of critical current at high external magnetic field. To meet this requirement, the trick is to introduce well-controlled nanometric secondary phases or structural imperfections inside epitaxial YBCO matrix acting as artificial pinning centers (APCs) and thus immobilizing quantized vortices. Thus, the key is to minimize the current blocking defects (e.g. pores, residual intermediate phases, large angle grain boundaries, etc.) and generate controllable nanometric defects acting as effective APCs (nanostrain, nanoparticles, nanorods, etc.).

Chemical solution deposition (CSD) is becoming one of the most promising routes toward cost-effective production of YBCO thin films and long-length CCs. However, a full understanding of the influence of processing parameters, in particularly the ones involved in the CSD which may become important in industrial production of CCs, on the microstructure and superconducting performances, is still far from being achieved. Therefore, a comprehensive investigation of the influence of the processing parameters related to the production of CCs with high performance and low cost is essential for achieving a high throughput production of CCs and a wide penetration into industrial power systems.

In addition, an in-depth comprehension of the microstructure of YBCO and nanocomposite films down to several unit cells is crucial if one wants to unveil the structure-texture-stress-properties interrelationships of YBCO superconducting films from a fundamental point of view. Despite abundant research works have been devoted to describe the complex relationship among several microstructural scenarios and the corresponding superconducting properties, many aspects involved in the development of CSD-based YBCO films, still remain poorly known, as well as their influence on the superconducting performance.

The incorporation of nano-sized secondary phases within YBCO matrix as APCs is an effective approach to improve the superconducting performances of YBCO conductors. Challenges in engineering the desired nanostructures for the best superconducting performance up to now are to obtain controllable nanoparticle characteristics, such as the size, the distribution and their influence on the secondary defect (stacking fault) characteristics. To achieve these objectives, an elaborate development of the YBCO nanocomposite route (i.e. YBCO + nanoparticles of a secondary phase) is required.

This work is mainly performed in project framework of the "European Development of Superconducting Tapes (EUROTAPES)" for the purpose of developing a cost-effective and performance-attractive route for promoting the applications of YBCO CCs in industrial power systems. This thesis mainly consists of six chapters. The main background knowledges and the basic experimental techniques are detailed in Chapter 1 and Chapter 2, respectively. Chapter 3 is dedicated to the development of a novel Flash Heating (FH) growth process. The intermediate transition phenomena (intermediate phase evolution, growth kinetics and microstructure evolution) that occur during the FH growth process has been investigated. We have also investigated the influence of processing parameters, such as water vapor introduction time and growth temperature and we have determined their influence on the microstructure and superconducting performance of YBCO thin films and CCs. In Chapter 4, I describe the detailed characterization of YBCO and nanocomposite ultrathin films from the microstructure, surface morphology and superconducting performances point of view. Chapter 5 is focused on our progressively improved nanostructuring strategy for engineering an optimized YBCO microstructure landscape for enhancing superconducting properties. We have successfully used non-reactive preformed $BaMO_3$ (M = Zr, Hf) perovskites to prepare nanocomposite films. Finely tuned YBCO microstructural and superconducting properties have been achieved by a tight control of several parameters, such as nanoparticle composition and size, growth kinetics and multi-deposition technique. Finally, I present the general conclusions of this study in Chapter 6.

1. Introduction

1.1 Superconductivity

1.1.1 Superconducting materials and properties

The phenomenon of superconductivity was firstly observed in mercury when temperature goes below 4.2 K (-269 °C) in 1911 by the Dutch physicist Heike Kamerlingh Onnes and his team. This phenomenon occurs below a critical temperature (T_c), mainly characterized by Zero resistance effect which enables electrical current circulate inside the material without any dissipation of energy. To date, the probe of new superconducting material has been extensively carried out, and abundant materials such as alloys, cuprate ceramics, organic materials, or iron pnictides, etc. have been discovered to be superconductors at sufficiently low temperature. Figure 1-1 summarizes the timeline of superconducting materials during the past century, where a progressive development of material category and T_c can be well followed. Importantly, the discovery of superconductive cuprates and perovskites (T_c > 30 K) in 1986 opens a new era for high temperature superconductor (HTS), which is a radical breakthrough compared with the conventional low temperature superconductor (LTS, T_c < 30 K). Especially, the further development achieved in 1987 in this field (i.e. the discovery of $YBa_2Cu_3O_{7-\delta}$ (YBCO)) [1] is of epoch-making significance because they present superconductivity above the boiling point of liquid nitrogen (~77 K), making them the most promising candidate for cost-efficient large scale power applications.

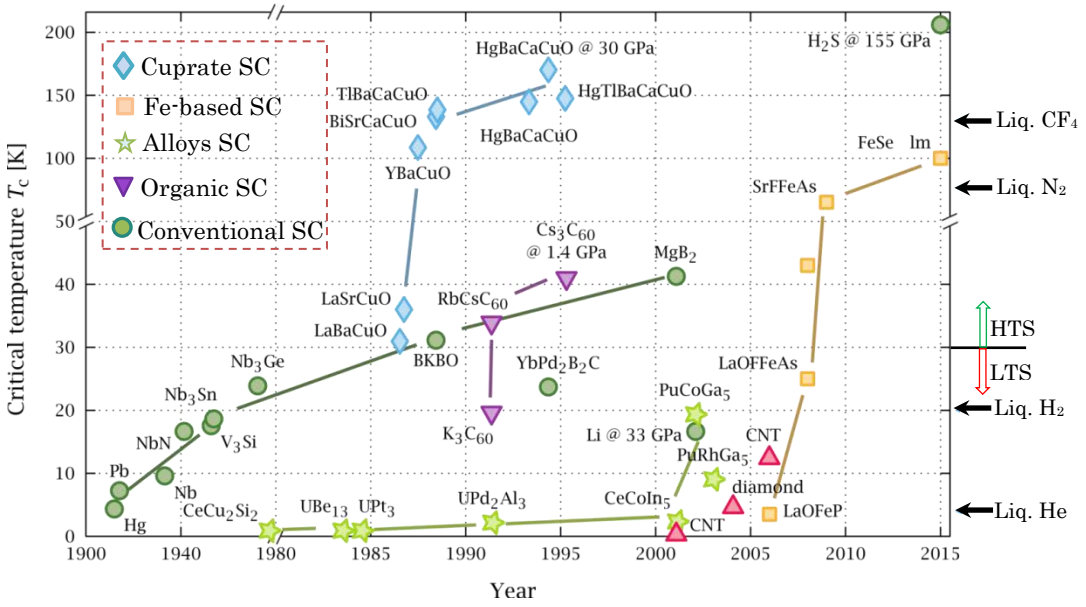

Figure 1-1: Timeline of superconductivity from 1900 to 2015 [2].

Besides, superconductors can also be classified into Type I and Type II materials according to their magnetic properties. It is generally known, on the other hand, that superconductivity is also characterized by Meissner effect (i.e. fully expulsion of the applied magnetic field). With a rise in temperature or in the applied magnetic field, the superconducting state can be destroyed by the penetration of external magnetic field into the superconductor, and then the superconducting material goes to the normal state. In type I, the superconductors undergo a sharp transition, as shown in Figure 1-2 (a). In comparison, type II superconductors present gradual transition in the form of a mixed state (see Figure 1-2 (b)) which is delimited by two critical fields, i.e. lower critical field (H_{c1}) and higher critical field (H_{c2}).

In the mixed state region of type II superconductors, the penetration of external magnetic field starts at $H_{c1}(T)$ with the formation of quantized cylindrical flux line (vortices) parallel-aligned within the material. The vortices are characterized by a normal core of radius ξ, which is surrounded by a region of larger radius λ, where superconducting currents are flowing inside. The values of ξ and λ depend on the material. The circulating currents confine the flux lines of the penetrated magnetic field to the vortex region in such a way that each vortex carrying an identical quantum of flux, i.e. $\phi_0 = 2.07 \times 10^{-15}$ Tm^2 [3]. These vortices are regions in a normal state, and thus present higher energy contrasting with their adjacent superconducting area. They minimize their free energy by forming a triangle lattice, repel each other and uniformly distributed, leading to each of them in a force balance state [4]. When the external magnetic field increase from $H_{c1}(T)$ to $H_{c2}(T)$, more and more vortices generated and gradually filled up the material. Finally, the superconductivity is completely destroyed by the uniformly penetrated external magnetic field and the material goes into the normal state.

In addition to the two intrinsic parameters (i.e. T_c and $H_{c2}(T)$) of superconducting materials, another important parameter to characterize the superconducting properties of one type II superconducting material is the critical current density (J_c). With increasing the current density (J) larger than J_c, the Zero resistance effect of a type II superconducting material is also lost leading to energy dissipation due to the vortices motion. To understand the origin of J_c, a detailed depiction is shown schematically in Figure 1-2 (c). When current flows though the superconductor in the mixed state, a force which is equivalent to the Lorentz force ($F_L = J \times \mu_0 H$) [5] will act on the vortices and thus lead to the vortex motion. The motion of vortices produces an electric field ($E = v \times \mu_0 H$, v resent the local velocity of vortices) parallel to J, thus causes a resistance and eventually leads to energy dissipation.

To solve this problem, the idea of immobilize vortices at structural imperfect sites (i.e. vortex pinning) was generated and was confirmed to be effective for preventing the vortex motion. Efficient pinning centers should be non-superconducting (to decrease the vortex free energy) [4], and with dimensions similar to the vortex core (2-4 nm) [3]. More detailed

illustration of pinning centers will be presented in section 1.3. Here, we just mention that the maximum macroscopic pinning force (i.e. F_p) for the whole system of vortices in a superconductor consists of a variety of pinning forces between individual vortex and pinning centers as well as the interaction between vortices themselves. Macroscopically, the vortex motion can be effectively prevented until the F_L exceeds the F_p. In this case, J_c was defined as the maximum current that circulates though the superconductor without energy dissipation. This phenomenon occurs on the basis of an effective vortex pinning (i.e. $F_p = F_L$) and thus, the formula used to define the J_c ($J_c = F_p/\mu_0 H$) can be obtained as well.

In this case, a border line should exist in the mixed state of type II superconducting materials for separating this two regions ($J_c \neq 0$ and $J_c = 0$) with the name of irreversibility line (IL), as shown by the red line in Figure 1-2 (b). It is worth mentioning that vortices move at any small J when the superconducting material in the H-T region situated between IL and H_{c2} although the material is still in a superconducting state (kept until H_{c2}), in a sense that the order parameter is not zero and the flux lines move reversibly with ease. Hence, the IL for a type II superconducting material is more important than its H_{c2} regarding the H-T region for technological applications.

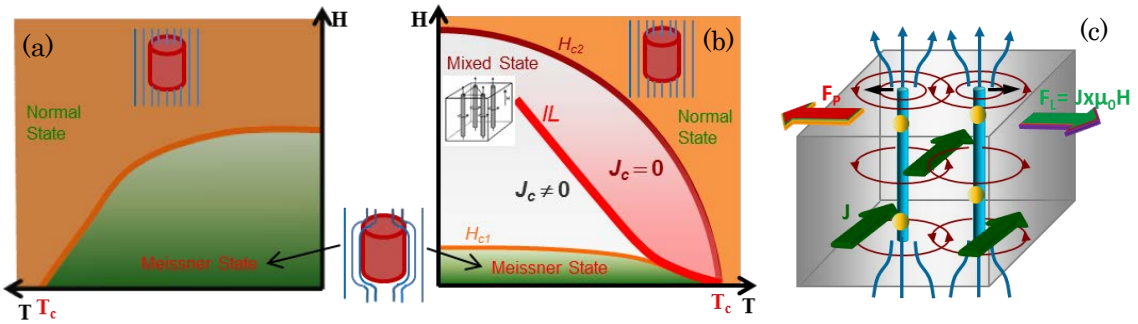

Figure 1-2 (a)-(b): Magnetic phase diagram for (a) type I and (b) type II superconductors; (c): a sketch depicting the stress states of vortices in the mixed state of a type II superconducting materials.

In Figure 1-3 [6] it is presented the IL and the H_{c2} for several type II superconducting materials. Among them, YBCO displays the highest IL, which can reach as high as ~7 T at 77 K, making it the most attractive candidate for developing a high temperature and high magnetic field applications such as generators, transformers, fault current limiters, etc.

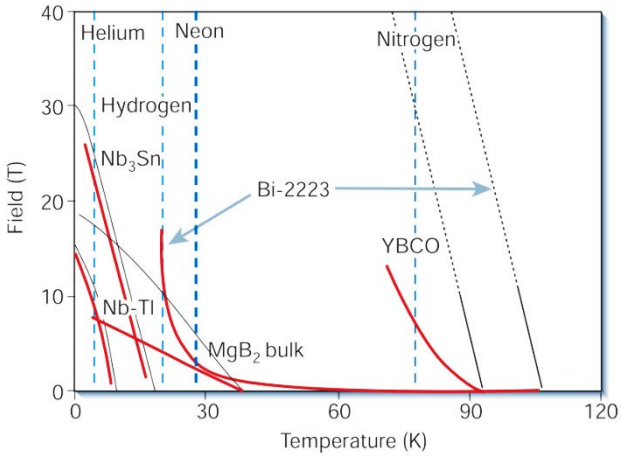

Figure 1-3: Magnetic field-temperature diagram for several type II superconductors [6]. The irreversibility lines are indicated in red solid line, while the upper critical fields are indicated in black.

1.1.2 Structure of YBCO

YBCO is a cuprate superconducting material with high critical temperature, $T_c \sim 92$ K. Its crystalline structure is based on a triple perovskite structure ABO_3 (Figure 1-4). To be more precise, the YBCO unit cell consists of a central $YCuO_3$ perovskite with two adjacent $BaCuO_3$ stacked vertically along the c-axis; see Figure 1-5. However, the phase is in the stoichiometry of $YBa_2Cu_3O_{7-\delta}$ instead of $YBa_2Cu_3O_9$, due to the appearance of permanent oxygen vacancies where the oxygen sites are never occupied. These vacancies are located at both the basal planes (z = 0) and the Y-plane (z = 1/2), leading a reduction of two O atoms in the stoichiometric unit formula $YBa_2Cu_3O_9$. Such oxygen deficiency implies that Cu ions are present in mixed oxidation states: Cu^{2+} and Cu^{3+}.

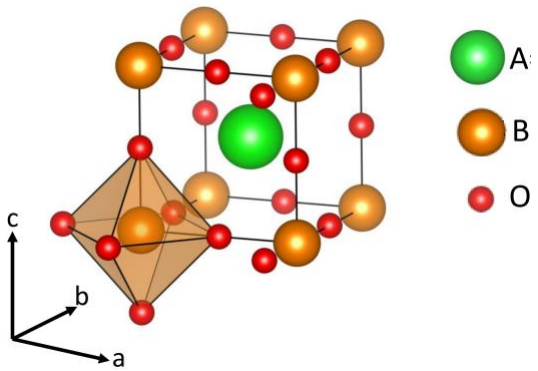

Figure 1-4: Representation of the perovskite structure.

On the other hand, in the stoichiometric unit formula $YBa_2Cu_3O_{7-\delta}$, where the value of δ ranges from 0 to 1, the stoichiometric deviation of O atom is also attributed to the partial O vacancies which are only distributed in the CuO chains located in the basal plane (z = 0). Depending on the atom occupation in these partially occupied oxygen sites, the YBCO phase can display tetragonal ($0.5 < \delta \leq 1$) or orthorhombic ($0 < \delta \leq 0.5$) crystalline structure.

Especially, in the orthorhombic YBCO lattice, the oxygen ions are fully ordered onto the (0, 1/2, 0) positions, resulting in a one-dimensional Cu-O chain parallel to the b-axis [7].

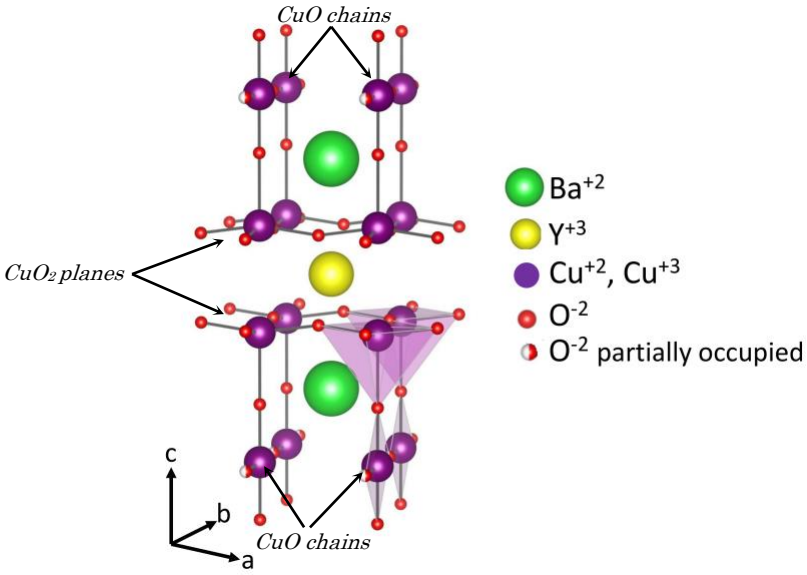

Figure 1-5: Crystalline structures of the $YBa_2Cu_3O_{7-\delta}$ compound: the tetragonal P4/mmm phase for $\delta > 0.65$ and the orthorhombic Pmmm phase for $\delta < 0.65$ [8].

YBCO lattice parameters of both tetragonal and orthorhombic phases are listed in Table 1-1.

Table 1-1: List of lattice parameters in the tetragonal and orthorhombic YBCO phases

	Tetragonal (x=1)	Orthorhombic (x~0,1)
a (Å)	3,865	3,823
b (Å)	3,865	3,886
c (Å)	11,852	11,684

The superconducting properties of YBCO rely strongly on the oxygen stoichiometry. The CuO_2 planes contain mobile charge carriers and there is where supercurrents flow. These planes are separated by charge-reservoir interleaved layers which contain free carriers and contribute to the normal conductivity. More precisely, these charge reservoir layers take the main responsibility for a proper carrier density in the superconducting CuO_2 planes. Consequently, the current that flows though YBCO displays anisotropic behavior, i.e. $J_c^{ab} >> J_c^c$. As a result, in YBCO thin films, the material should be grown highly epitaxial with the c-axis normal to the substrate in order to get the current to its maximum.

Considering $YBa_2Cu_3O_x$ notation, for the composition with oxygen content of $6 \leq x < 6.5$ the phase is tetragonal structure and it is an insulator. Increasing the oxygen content up to $x = 6.5$, the compound undergoes a phase transition from tetragonal to orthorhombic

being only superconducting in the latter. T_c increases with the increase of oxygen content until x reach the value of 6.94 where T_c approaches its maximum value (~92 K). Above x = 6.94 the compound is overdoped and T_c drops; see Figure 1-6 [9]. Optimum oxygen stoichiometry for achieving optimized T_c (x = ~6.94) [9] or J_c (slightly overdoped) [10] is achieved by processing conditions (i.e. temperature, annealing time and oxygen pressure) [11, 12].

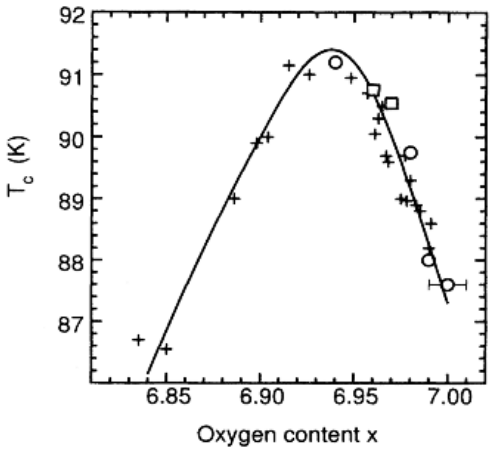

Figure 1-6 Variation of T_c with oxygen content for $YBa_2Cu_3O_x$ [9].

1.1.3 YBCO coated conductors

Conductors for power applications are wires or tapes of high temperature superconductor and metal. Such HTS conductors must be reliable, robust and cost-effective with low AC-losses [6, 13]. Extensive efforts have been devoted to the development of practical HTS conductors with high current-carrying capability. These works are, firstly focused on the first generation (1G) $Bi_2Sr_2Ca_2Cu_3O_x$ (Bi-2223) multifilamentary conductor and then on the second-generation (2G) YBCO coated conductor (CC) [6, 14], as shown in Figure 1-7. However, large scale power application of 1G Bi-2223 HTS wires is limited by their low irreversibility field at 77 K (see Figure 1-3), higher manufacturing cost and high AC-loses [13]. Worldwide activities are therefore, focused on developing the 2G HTS CCs technology based on YBCO, which displays high irreversibility field at 77 K (i.e. ~7 T).

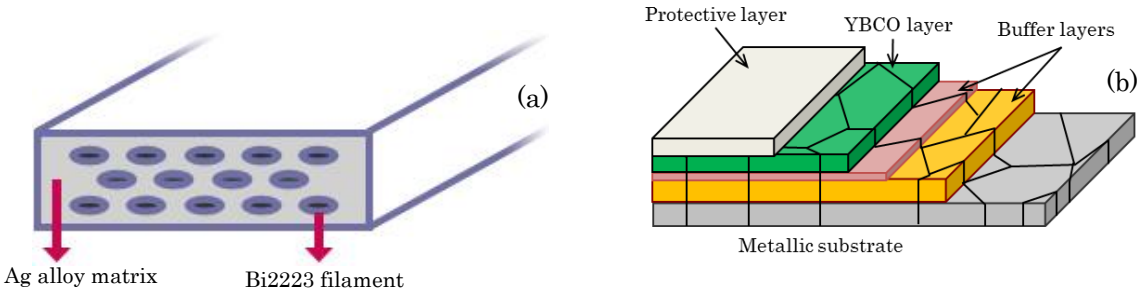

Figure 1-7: Cross-sectional sketches of (a) First-generation superconductive wire based on Bi-2223 superconductive filaments in a silver matrix and (b) second generation YBCO coated conductor.

Unfortunately, the applicability of YBCO in large scale power application (e.g. magnets, motors and power-transmission lines) is limited by two difficulties, i.e. the brittleness of YBCO and weak links between grains. The first difficulty has been successfully overcome owing to the development of 2G CC architecture (see Figure 1-7 (b)) where the application of metallic substrates fabricated by either the Rolling Assisted Biaxial Textured Substrates (RABiTS) technology [15, 16] or the Ion Beam Assisted Deposition (IBAD) technology [17] plays a vital role. However, a straightforward deposition of YBCO films on the metallic substrate is not possible, due to some intrinsic issues such as high mismatch, different thermal expansion induced stress and destructive reaction between YBCO and metallic substrate. To achieve competitive superconducting performances it is required that YBCO provides in-plane and out-of-plane crystallographic texture, i.e. biaxially textured; see Figure 1-8. These requirements were fulfilled by applying epitaxial oxide buffer layers in between metallic substrate and YBCO layer. The applied oxide buffer layers are required to be effective for: (a) preventing the destructive reaction between the metal alloy substrate and the YBCO film, (b) minimizing the oxidation of the metallic substrate and (c) transferring the substrate texture to the YBCO film which allows for high critical current density [18]. The most commonly used buffer layer are yttrium-stabilized zirconia (YSZ), $Gd_2Zr_2O_7$, MgO, CeO_2, Y_2O_3, $SrTiO_3$, $BaZrO_3$, however, the optimum combination of oxide buffers and their arrangement also depend on the nature of the metallic substrate [3, 19, 20]. Finally, a deposition of a protective layer on the top of the CCs is also necessary to protect the superconducting layer from the environment.

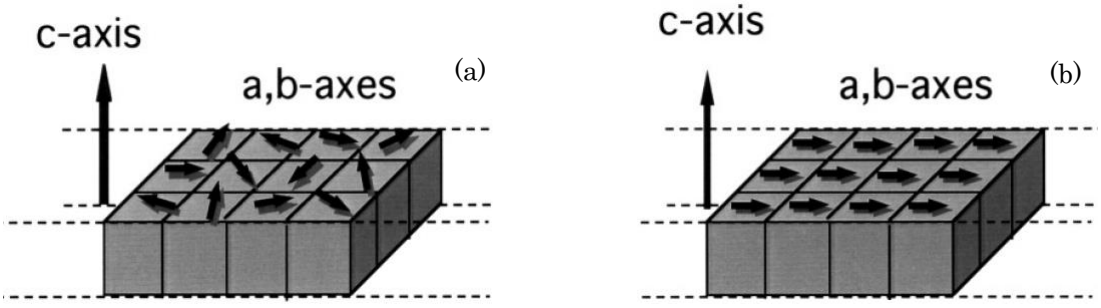

Figure 1-8: Schematic diagrams for crystalline alignment structures (a) uniaxially aligned and (b) biaxially aligned [21].

There are many deposition techniques available for the fabrication of high performance YBCO films. All the techniques can be classified as in-situ growth technique (Pulsed Laser Deposition (PLD), Metal-Organic Chemical Vapor Deposition (MOCVD), sputtering, etc.) and ex-situ growth technique (Chemical Solution Deposition (CSD)) depending if the objective material is formed as the material is being deposited (in-situ) or in a subsequent thermal process (ex-situ). Among them, the vacuum-based deposition methodologies, in particular PLD, are predominant for manufacturing YBCO CCs with relatively long-length and high current-carrying capacity, however, such techniques have intrinsic problems e.g.

high cost of the vacuum system and the targets or precursors. Based on the strong attractiveness from the cost-effective, high performance and large-scale manufacturing point of view, the manufacture of long length YBCO CCs based on the non-vacuum CSD process is being extensively developed. After a series of growth parameter optimization, the superconducting performances of CSD-based YBCO films have been dramatically enhanced resulting in J_c values as high as 3-5 MA/cm^2 at 77K, which are comparable with the vacuum-based deposition techniques. Therefore, our efforts in this thesis are concentrated on a simple deposition of YBCO by the so-called Metal-Organic Decomposition of Trifluoroacetate (MOD-TFA) precursors on top of (00l)-oriented single-crystals (LAO and STO) in a lab scale. These systems serve as a model system to conduct fundamental investigation, being then transferred to CCs which have already been deployed worldwide.

1.2 YBCO thin films formation based on the CSD route

CSD is becoming one of the most competitive techniques to obtain epitaxial YBCO films and CCs. The MOD-TFA route has been up to now the most successful CSD approach to achieve high quality YBCO layers. However, achieving a cost-effective manufacturing technique for long-length CCs with high performance based on the CSD route it is required a deep understanding of all the individual consecutive processing steps (solution chemistry, intermediate phase evolution, fundamentals of nucleation and growth, etc.), as well as their mutual influences and relationships. The whole process of growing high quality YBCO films based on the MOD-TFA route is shown in Figure 1-9 [22]. In this section, we review advances in the knowledge of processing of YBCO thin films based on TFA precursors and give an overview of the general knowledge for YBCO nucleation and growth.

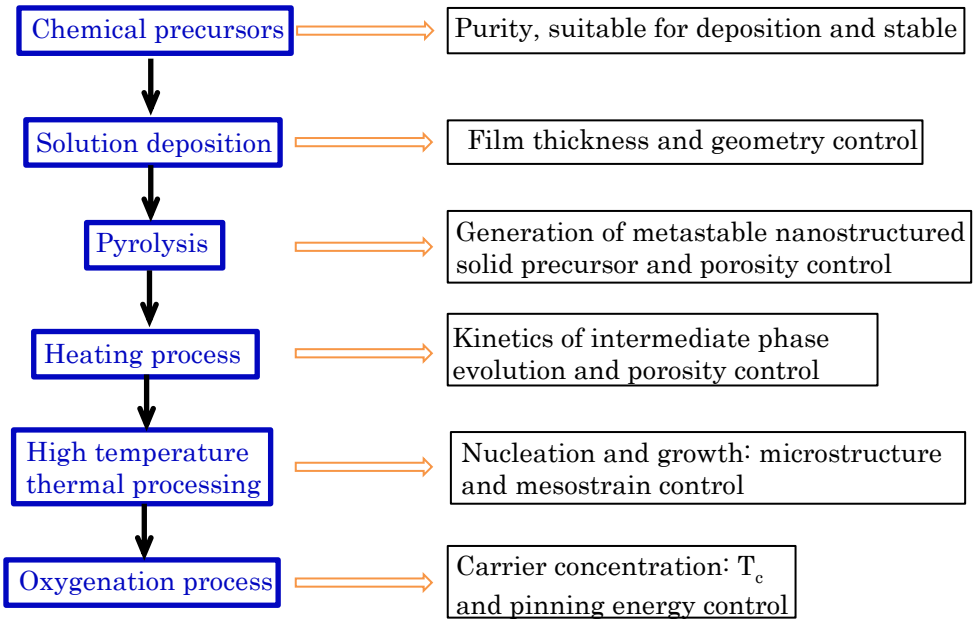

Figure 1-9: General schema of the different processing steps and parameters required to prepare YBCO thin films based on the CSD techniques [22].

1.2.1 Precursor solution and intermediate phase evolution

Firstly, it is important to prepare the TFA precursor solutions of adequate purity, desired rheological parameters adapted to the selected deposition technique and stable. These requirements were fulfilled by the development of a novel solution preparation approach based on the use of trifluoroacetic anhydride (TFAA) to dissolve dehydrated acetates or YBCO powder [23]. Several solution deposition methods (spin coating [24], dip coating [25] and ink-jet printing [26, 27]) can be used nowadays in MOD, allowing one to achieve a tight control of the film thickness where the rheological properties of the solutions are properly tuned through the use of suitable additives [22]. Subsequently, a pyrolysis process is necessary for as-deposited films in order to obtain dense, homogeneous and nanostructured solid precursor film which consists of amorphous $Ba_{1-x}Y_xF_{2+x}$ (BYF) phase with homogeneously dispersed CuO nanoparticles [28]. Several investigations of the pyrolysis process for MOD-TFA route have been reported [29-31] and some achievements such as smooth stress relief, significantly shortened annealing time and minimized porosity or nanoparticle coarsening (mainly CuO) were obtained. The so-called conventional pyrolysis process that has been used in this Thesis is described in detail in Chapter 2 (subsection 2.1.2.3)

Afterwards, a higher temperature thermal processing is needed to convert the solid precursors into the biaxially-textured crystalline YBCO films. The microstructural and compositional evolution paths of different intermediate phases before the formation of YBCO phase were earlier investigated [28, 32-34] via TEM and XRD techniques. Results indicate that the intermediate conversion process towards YBCO phase is a chemical reaction and long-range diffusion involving complex thermodynamics and kinetics. Upon heating (25 ºC/min), the microstructural evolution of the precursor is driven by the reduction of the solid solubility of Y in the BYF solid solution. Thus the BYF phase evolves towards Ba oxyfluoride (OF) phase where the yttrium is completely absent, and this phase keeps stable until YBCO forms. In the meantime, Y is released in the form of Y_2O_3 phase, which is initially in amorphous state and then crystallize at higher temperature. It is reported [32, 35] that reaction $Y_2O_3 + CuO \rightarrow Y_2Cu_2O_5$ occurs at ~700 °C, which is very close to the epitaxial nucleation of YBCO phase, and thus both processes may compete each other thereof affecting the kinetics of the conversion process [28]. Besides, CuO nanoparticles coarsen during heating at a rate depend on the $P(H_2O)$ [36]. In ex-situ grown TFA-YBCO films, the primary chemical process of YBCO formation has been written as follows (Scheme 1) [29, 37]:

$$4Ba(O_xF_y)_2 + 6CuO + Y_2O_3 + yH_2O \rightarrow 2YBa_2Cu_3O_{6.5} + 8yHF \qquad \text{Scheme 1}$$

where $0 < y \leq 1$ and H_2O and HF are gaseous species [37]. On the other hand, the intermediate phase $Y_2Cu_2O_5$ (Y225) was also identified as reactant for the formation of YBCO following a competing reaction path (Scheme 2) towards YBCO [22]:

$$Y_2Cu_2O_5 + 4BaO + 4CuO \rightarrow 2YBa_2Cu_3O_{7-x} \qquad \text{Scheme 2}$$

Detailed TEM observation [28] pointed out that the reactions are assisted by long-range diffusion (hundreds of nanometers) within the OF matrix rather than interphase reaction among the different phases. In this case, eventually, the full reactions are limited by kinetic hindrances and thus some secondary precipitates (e.g. CuO, Y_2O_3, Y225) might remain. Moreover, the as-pyrolyzed precursor film undergoes a progressive densification process during the heating process [32, 34], but the rate is also influenced by several factors such as the addition of silver [38] and $P(H_2O)$ in the gaseous atmosphere [39].

1.2.2 Fundamentals of YBCO Film Crystallization and Growth

1.2.2.1 YBCO Nucleation

Nucleation is the initial stage that occurs during the formation process of crystals from a precursor, in which a small number of particles (ions, atoms, or molecules) become ordered in a pattern of crystalline solid, forming crystal nuclei upon which particles continues deposited as the crystal growth process. The nucleation processes can be classed as homogenous or heterogeneous, depending on where the nucleation centers are formed. In both cases, the nucleation undergoes a complex thermodynamic process, in which structural fluctuation, thermal fluctuation and the degree of supercooling or supersaturation are required. For a heteroepitaxial growth, it is generally accepted that there are three possible modes, i.e. Volmer-Weber mode [40], Frank-van der Merwe mode [41] and Stranski-Krastanov mode [42], can be followed for the nucleation on single crystal substrates, depending on the interaction strength between adatoms and surfaces.

The formation of YBCO films based on the MOD-TFA route has been demonstrated to follow the Volmer-Weber heterogeneous growth mode, i.e. single YBCO nuclei form at stochastic sites of the precursor/substrate interface and subsequently grow along different directions at different growth rates, and finally coalesce leading to a continuous film [28, 38, 43]. Classical Nucleation Theory (CNT) states that the first stable nucleus appears when a Gibbs free energy barrier (ΔG^*) is overcome, more precisely, this occurs after they grow beyond a critical size r*. From a thermodynamic perspective, the driving forces governing this transformation are the energy differences (ΔG_V) between the precursor and the crystalline states (Figure 1-10) [44]. This change can be generally written as [45] (Equation 1-1):

$$\Delta G = \underbrace{V\Delta G_V}_{\text{Volume term}} + \underbrace{\Phi}_{\text{Surface term}} \qquad \text{Equation 1-1}$$

The first term is the total Gibbs free energy difference which provides the driving forces for the transformation, where V is the volume of the neclei, $\Delta G_V = \Delta\mu/v$ is the Gibbs free energy difference per unit volume which depends on the change in chemical potential change ($\Delta\mu$) and the volume of the smallest unit v (e. g. unit cell volume); and the second term Φ is the change in surface energy which consists of the change in surface free energy and elastic strain energy, due to the formation of new surfaces and interfaces.

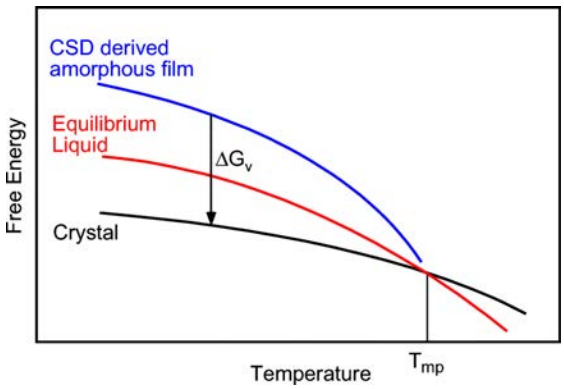

Figure 1-10: Schematic diagram of free energies in a CSD derived amorphous film (blue curve), equilibrium liquid (red curve) and crystal (black curve) as a function of temperature [44]. ΔG_v provides the thermodynamic driving force for crystallization.

Nucleation of YBCO

Detailed thermodynamic analyses have been established in the earlier works of our group [38, 46] based on a cylindrical-shaped nucleation mode (see Figure 1-11(a)). The total Gibbs free energy difference ($\Delta G(r)$) was written as Equation 1-2, where the elastic energy contribution was neglected due to the small size of the first stable YBCO nuclei [47, 48].

$$\Delta G(r) = \frac{\pi h r^2}{v}\Delta\mu + 2\pi h r\gamma_{lat} + \pi r^2(\gamma_{up} + \gamma_{int} - \gamma_{sub}) \qquad \text{Equation 1-2}$$

where v and γ represent the unit cell volume and surface free energy per unit area (lat = lateral surface, up = upper surface, int = interface, sub = substrate) (see Figure 1-11 (b)), $\Delta\mu$ (< 0) is the chemical potential change per molecule between the epitaxial YBCO phase and the precursor random nanocrystalline state. In this case, the critical radius r* and the corresponding ΔG^* for the heterogeneous nucleation of MOD-TFA based YBCO films can be deduced by maximizing the $\Delta G(r)$ value (i.e. $\frac{\partial \Delta G}{\partial r} = 0$), as follows:

$$r^* = \frac{-h\gamma_{lat}}{\left(\frac{h}{v}\right)\Delta\mu + (\gamma_{up} + \gamma_{int} - \gamma_{sub})} \qquad \text{Equation 1-3}$$

$$\Delta G^* = \frac{\pi(h\gamma_{lat})^2}{-\left(\frac{h}{v}\right)\Delta\mu - (\gamma_{up} + \gamma_{int} - \gamma_{sub})} \qquad \text{Equation 1-4}$$

A thermodynamical model [49, 50] has been set up to describe the competition between a-axis and c-axis nuclei formation in YBCO films. A computation of the surfaces appearing during the growth of YBCO crystals disclosed that the YBCO surface Gibbs energies follow

the inequality: $\gamma_{(001)} < \gamma_{(100)} < \gamma_{(010)}$, leading to a variation in the critical nucleus dimension (N*) in different orientations. In a CSD-based YBCO system, the N* depends on the supersaturation and their relation can be written as:

$$\Delta\mu \approx \frac{E(N^*)}{N^*} \qquad \text{Equation 1-5}$$

Accordingly, it is evident that at high supersaturation the supercritical nuclei dimension is small, which can fulfill the thermodynamical requirements for the formation of nuclei with small N* (i.e. (100) or (010)) orientation). Decreasing supersaturation, the supercritical nuclei dimension increases according to Equation 1-5. For a certain nucleus dimension, a nucleation crossover appears and the (001) oriented nuclei start to appear. A further decrease of supersaturation leads to a decrease of the volume ratio of a-axis and c-axis oriented nuclei (V_a/V_c). At a certain supersaturation condition, a $V_a/V_c = 0$ takes place and a solely (001) oriented nuclei can be achieved [49]. In this scenario, a clear diagram showing ΔG^* vs $|\Delta\mu|$ dependence was plotted taking into account the corresponding combination of surface energies , as shown in Figure 1-11 (c) [38, 49, 51].

In CSD-based YBCO thin films, the chemical conversion process has been described in the form of Scheme 1-1. Therefore, the chemical potential change ($\Delta\mu$) of this reaction process was written as follows [43, 46, 52]:

$$\Delta\mu = \Delta\mu_0 + yK_BT\ln(P_{HF}^2/P_{H_2O}) \qquad \text{Equation 1-6}$$

where $\Delta\mu_0 = \Delta h_0 - T\Delta S_0$ represents the chemical potential change at equilibrium state, while Δh_0 and ΔS_0 being the enthalpy (heat of sublimation) and entropy change between the precursor film and the crystalline YBCO; K_B is the Boltzmann′ constant; T is temperature; y is the same value taken from Scheme 1-1; P_{HF} and P_{H_2O} are HF and H_2O partial pressure near YBCO nuclei front. It is important to note that both terms in this formula show a negative sign and that when in situ growth techniques are used only the first term of this formula needs to be considered due to the absence of gaseous composition in these processes. In order to achieve optimal processing conditions for c-axis nucleation (low $|\Delta\mu|$), the influence of several crucial parameters such as water vapor partial pressure ($P(H_2O)$), O_2 partial pressure ($P(O_2)$), total pressure (P_t), gas flow (F) and growth temperature (T) on YBCO nucleation was investigated in previous works [46, 53].

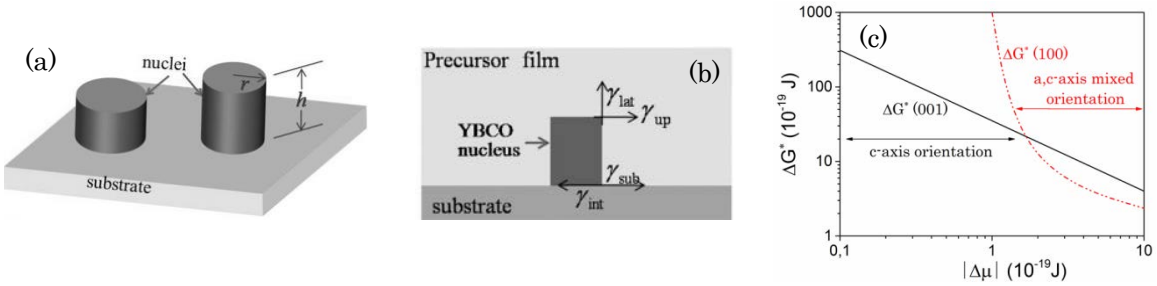

Figure 1-11 (a) Typical cylindrical geometry of YBCO nucleation[46]; (b) Schema of the different surface and interfacial energies involved in the nucleation process of an island on a substrate surface[46]; (c) Typical dependence of the nucleation energy barriers (ΔG*) on the supersaturation (|Δμ|) in YBCO growth [38, 51].

Nucleation of nanoparticles in YBCO matrix

In the case of spontaneously segregated YBCO nanocomposites, it is generally accepted that the first nuclei of secondary nanodots within YBCO matrix show spherical shape with a radius of r [54, 55], thus, the total Gibbs free energy change for homogeneous nucleation (ΔG_{hom}) can be written as follows (Equation 1-7),

$$\Delta G_{hom} = \frac{4}{3}\pi r^3 \Delta G_V + 4\pi r^2 \gamma_f \qquad \text{Equation 1-7}$$

where γ_f is the surface energy. And thus, the critical radius (r*) and Gibbs free energy barrier (ΔG*) can be written as Equation 1-8 and Equation 1-9, respectively,

$$r^* = \frac{-2\gamma_f}{\Delta G_V} \qquad \text{Equation 1-8}$$

$$\Delta G^*_{hom} = \frac{16\pi}{3}\frac{\gamma_f{}^3}{(\Delta G_V)^2} \qquad \text{Equation 1-9}$$

and

$$\Delta G^*_{het} = \Delta G^*_{hom} f(\theta) = \frac{16\pi}{3}\frac{\gamma_f{}^3}{(\Delta G_V)^2} f(\theta) \qquad \text{Equation 1-10}$$

where θ is the contact angle and $f(\theta) = \frac{(2+\cos\theta)(1-\cos\theta)^2}{4}$ is a function associated to the heterogeneous nucleus′ shape [45].

In addition, it seems that the Gibbs free energy barrier must be modified accordingly to consider the influence of strain energy (ΔG_{str}), which is another energy barrier for nucleation [45]. In this case, the energy barrier will be larger for a strained system at a given supersaturation, and thus, more energy will be needed to achieve nucleation.

Nucleation rate

The previous thermodynamic analysis of nucleation provides a clear guidance for controlling the grain orientation and their distribution. Now we turn our interest into the nucleation rate, $\dot{N} = \frac{dN}{dt}$, which enables us to estimate the density of nuclei that are possible formed under the suitable thermodynamic conditions for nucleation. Generally, the

nucleation rate is a thermally activated process also depending on the atomic mobility. However, the limitation from atomic diffusion can be neglected at high enough temperature in most systems [45], and thus, the nucleation rate can be written as (Equation 1-11) [22]:

$$\dot{N} = \frac{dN_0}{dt} \exp\left(-\frac{\Delta G^*}{k_B T}\right) \qquad \text{Equation 1-11}$$

where N is the density of stable nuclei, t is time and $\frac{dN_0}{dt}$ is the nucleation rate at a negligible nucleation barrier, $\Delta G^* \approx 0$. Therefore, the kinetics of nuclei formation in any process (heating or annealing process) will be determined by a particular time integration of Equation 1-12. The so-called incubation time which express the formation of a first continuous YBCO layer through heterogeneous island nucleation and coalescence has been measured by in-situ resistance measurement [56] and X-ray diffraction technique [32]. According to Equation 1-12 and taking into account Equation 1-5 as well, the nucleation rate strongly depends on several processing parameters that influence the supersaturation for nucleation.

Moreover, in the Thesis of Albert Queraltó [45], it is also calculated the ratio between heterogeneous nucleation rate ($\dot{N}_{het}$) and homogeneous nucleation rate ($\dot{N}_{hom}$) assuming that the related atomic diffusion terms are constant (C_{het} and C_{hom}):

$$\frac{\dot{N}_{het}}{\dot{N}_{hom}} = \frac{C_{het}}{C_{hom}} \exp\left(\frac{\Delta G^*_{hom}\,(1-f(\theta))}{k_B T}\right) \qquad \text{Equation 1-12}$$

Therefore, careful control of supersaturation conditions is vital to finely tune the ratio between heterogeneous and homogeneous nucleation rate, in order to meet the requirements for the nucleation of YBCO grains and nanoparticles within YBCO matrix.

1.2.2.2 Growth in heteroepitaxial systems: epitaxial crystallization and grain coarsening

After the achievement of properly controlled nucleation process, the next important step towards the fabrication of high-quality YBCO heteroepitaxial systems is to achieve a controlled growth rate of YBCO grains and inserted nanoparticles. This step is particularly crucial if one wants to obtain high production throughput for producing CCs with higher thickness as well as achieving a controllable nanoparticle size for vortex pinning. It is therefore important to achieve a clear understanding of the fundamental mechanisms and influences from processing parameters.

In essence, growth is a thermodynamically and kinetically governed process which starts after the appearance of stable nuclei with the expense of other phases. The thermodynamic process called Ostwald ripening [57] is a thermodynamically-driven spontaneous process occurring because larger particles are more energetically favored (i.e. lower energy) than smaller particles, what has also been called coarsening. This process is promoted by atomic diffusion which is principally ruled by kinetic processes. In addition, another important

path for growth is the grain coalescence, which can be either a static process [58] arising from merging of several grains until matching and merging each other or a dynamic process [59] associated with diffusion, eventually driven by attraction forces between different nuclei.

During the epitaxial growth of YBCO grains from polycrystalline phases, the grain size of the random grains is of a great significance from a thermodynamic perspective. Therefore, the random grains should be kept with small size in order to provide higher driving forces towards the formation of epitaxial YBCO films [45]. On the other hand, the atomic diffusion process is usually described by the Fick′ laws [60]:

$$J_C = - D_C \nabla C \text{ (First law)} \qquad \text{Equation 1-13}$$

and

$$\frac{\partial C}{\partial t} = -\nabla \cdot J_C = D_C \nabla^2 C \text{ (Second law)} \qquad \text{Equation 1-14}$$

where J_C is the diffusion flux, representing the amount of substance that diffuse through a unit cross-sectional area during a unit time interval; C is the concentration of diffusing species; D_C is the diffusion coefficient. The diffusion coefficient (D_C) is a very important parameter for representing the substance diffusion. Taking into account that the diffusion is a thermally activated process, the dependence of diffusivity with temperature is generally found to be well predicted by the Arrhenius equation [61-63]:

$$D_C = D_0 \exp\left(-\frac{Q_d}{k_B T}\right) \qquad \text{Equation 1-15}$$

where D_0 is a pre-exponential factor which depends on parameters such as geometrical constants and the lattice constant; Q_d is the activation energy for diffusion in dimensions. Therefore, the D_C is influenced by several factors, such as temperature, pressure, the microstructure of the substance, the characteristics of the component and composition.

In the earlier work of our group, an empirical multi-exponential model has been achieved based on the previous experimental studies performed at 740 ºC and different growth conditions such as water partial pressure (P_{H_2O}), total pressure (P_t) and gas flow rate (F) in our group [37, 46] using the theoretical solid-gas reaction-diffusion model, the corresponding equation is:

$$G = C\frac{P_{H_2O}^{1/2}}{\alpha + \beta P_t + \gamma P_t/F} \qquad \text{Equation 1-16}$$

where C, α, β and γ are constants previously defined and experimentally determined for YBCO/LAO thin films grown at 740 ºC with a heating rate of 25 ºC/min. After combining several growth parameters in these experiments, it was found that the maximum growth rate allowing achievement of only c-axis nucleation and $J_c > 1$ MA cm^{-2} was limited to G ~ 0.6 nm/s. Taking into account of the temperature dependence of the chemical reaction

equilibrium constant K_e, Sánchez-Valdés C F et al [56] extended the growth rate Equation 1-17 to include the temperature dependence via the incorporation of the Van' Hoof equation, as follows:

$$G(T) \approx C' \left[\frac{P_{H_2O}^{1/2}}{\alpha + \beta P_t + \gamma P_t/F}\right] K_{eo} \exp -\left(\frac{\Delta H^\theta}{RT}\right) \qquad \text{Equation 1-17}$$

where ΔH^θ is the enthalpy change of the reaction, R is the gas constant and K_{eo} is the standard equilibrium constant. In the case of the conventional heating process, the growth rates at 750 and 810 ºC were measured via in-situ electrical conducting relaxation method to be ~0.2 and ~0.6 nm/s, respectively, while the formation enthalpy of the YBCO formation was estimated to be ΔH^θ = ~190 KJ/mol F.

For MOD-based REBCO nanocomposite superconductors, a tight control of nanoparticle size is an extremely difficult work [64], although prominent superconducting properties have been achieved in the previous works [54, 65]. In contrast to the nanocomposite route based on the spontaneous deposition and growth methods, the formation of nanoparticles based on the MOD method occurs prior to the YBCO matrix formation [55, 64]. Therefore, the key factors determining the size of nanoparticles in the MOD process are the interfacial energy between the precursor and the secondary phase and/or the secondary phase diffusion coefficient during formation and growth of the (Y,Gd)BCO layer [64]. Valid routes for a tight control of nanoparticle size were achieved by controlling diffusion during the nanoparticle formation stage by selecting the second-phase material and modulating the precursor composition spatially, as reported by Miura et al [66]. However, a further decrease of nanoparticle size, in particular down to similar dimensions as YBCO coherent length ξ (i.e. ~2-4 nm) is still unattained.

At this stage, it is particularly crucial to control any source of macro- or microstructural inhomogeneities which could be detrimental to the current percolation [67, 68]. Several types of macro- or microscopic imperfections in TFA-MOD thin films such as residual pores [29, 69], secondary precipitates [53, 70], film dewetting [71] and large angle grain boundaries [68], have been identified and described as current blocking defects. Strictly speaking, any film inhomogeneity which perturbs the superconducting order parameter in lengths exceeding the coherence length ξ will reduce supercurrent percolation and should be avoided during all the stages [22].

As we have introduced in Section 1.1.2, a proper oxygenation process is vital for achieving high performance YBCO phases. The oxygenation kinetics of CSD-based YBCO films was earlier studied in our group [12, 72] though electrical conductance relaxation measurements. Results indicate that oxygenation kinetics of YBCO films strongly relies on the surface exchange process of oxygen molecules prior to bulk diffusion into the films. In addition, the required oxygenation time is also determined by several microstructural

origins such as grain size, the porosity or the mosaic structure and thickness of the films, taking into account the anisotropic behavior of oxygen diffusion along the ab plane and the c-axis (i.e. $D_{ab} = \sim 10^6 D_c$) [22].

1.2.3 Introduction of strain

Lattice deformation of crystalline materials, generally known as strain, has been shown to significantly influence their functionalities: mechanical, chemical and physical properties [54, 73-75]. For example, strain engineering via nanocomposite route provides an easy and effective way to enhance flux pinning properties of high-temperature superconductors and thus promote their potential for power applications at high temperature and high magnetic field [76, 77]. However, taking into account the coherence length ξ of this type of superconducting materials, a careful control of strain dimensions is required. Therefore, microstructural analyses of strain and their formation within heteroepitaxial superconducting films become indispensable in order to achieve effective flux pinning and further improve the superconducting properties.

In thin film epitaxy, strains are induced by residual stresses which can arise from mechanical processing, thermal expansion between film and substrate, lattice misfit between phases and crystallographic defects, etc. The residual stresses acting in the solid body of films are in an equilibrium state, leading to local atomic deviation of the lattice parameter from its free state. In general, considering the range of actions, residual stresses can be defined as macroscopic stress σ′ (acting on ~mm), microscopic stress σ″ (acting on ~μm) and nanoscopic stress σ‴ (acting on ~1-100 nm), as shown in Figure 1-12. Correspondingly, the strains existing within YBCO films can be categorized into 3 types (i.e. macrostrain, mesostrain and nanostrain), taking into account the coherent length (ξ) and penetration depth (λ) as well.

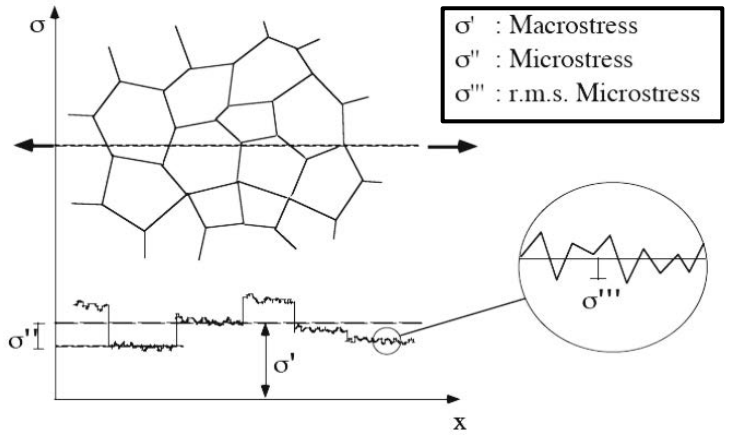

Figure 1-12 A sketch showing the definition of stresses in different dimensions in a polycrystalline material [3].

Macroscale strain: in which the $\ell >> \xi, \lambda$ and acting on the macroscopic scale (i.e. ~mm), it is uniform and can modify the T_c homogeneously but no direct influence on critical current. This type of strain is formed due to deficiency or substitution of elements [78] or large lattice mismatch between YBCO and substrates.

Mesoscale strain: in which the $\ell >> \xi$, $\ell \sim \lambda$ and acting on the mesoscopic scale (i.e. ~μm), it can modify T_c inhomogeneously and act as a limiting factor of percolating critical currents. In heteroepitaxial YBCO films, the formation of this type of strain occurs mostly during the grain zipping process [38] and adequate annealing time is needed for grain boundaries healing in order to minimize it.

Nanoscale strain: in which the $\ell \sim \xi$, $\ell << \lambda$ and acting on the nanoscopic scale (i.e. ~nm). In nano-sized strained regions, the Cooper pair formation is suppressed, and thus leads to non-superconducting regions in nanoscale within YBCO matrix [54]. These regions can reduce the vortex free energy [4] and then generally act as vortex pinning centers. No influence on T_c can be observed through macroscopic physical measurements (magnetic or transport) due to the nanoscale size of the region which are shielded by supercurrents.

On the other hand, the strains within YBCO matrix can also be categorized as homogeneous strain and inhomogeneous strain, depending if the interplanar distances deviation is homogeneously distributed or not. Any kind of interplanar spacing fluctuation will affect X-ray reflection and can be detected by analyzing the Bragg peak characteristics such as position (2θ) or shape (FWHM). We are able to quantify the distortion of YBCO lattice though the well-established methodologies [3, 54] based on the analysis of diffraction lines thanks to the application of XRD techniques.

Homogeneous strains are mainly induced by homogeneous stress such as epitaxial stress, which associates with lattice misfit between film and substrate. This type of strain causes a shift of Bragg peak positions, as shown in Figure 1-13 (b). In heteroepitaxial thin films, homogeneous strain usually appears at the initial growth stage and relaxes gradually with the increase of film thickness, inducing a large strain gradient region of tens of nanometres near the film-substrate interface, as shown in Figure 1-14 (a). For epitaxially grown YBCO thin films, in particular in ultrathin films, this type of strain usually causes a deviation of c-axis parameter, leading to homogeneous degradation of T_c [79].

On the other hand, oxygen depletion in the form of oxygen vacancies was often observed in the strained regions [80-82] (Figure 1-14 (b)). The strain gradient can be modulated by the variable oxygen stoichiometry in the strained layer combined with the high oxygen mobility [83, 84] results in oxygen loss or disorder which can act as a strain relieving mechanism. Apparently, the epitaxial strain induced oxygen-deficiency is also a resource of degradation of superconductivity.

However, the degradation of superconductivity in YBCO ultrathin films is still a controversial topic, which requires a carful distinction of each resource and interplay to improve the performance of YBCO films in particular at the initial growth stage.

Inhomogeneous strains (r.m.s. microstrain or nanostrain) are experimentally characterized by broadens of Bragg peaks due to the inhomogeneous fluctuation of the interplanar distances, as shown in Figure 1-13 (c). This type of structural distortion is generally quantified by applying the strain parameter $\varepsilon = \Delta d/d_0$, on the basis of the assumption that the contractions ($d < d_0$) and expansions ($d > d_0$) with equal probability in all directions. In YBCO thin films, the generation of these strained regions generally associates with crystalline defects (e.g. dislocations, grain and twin boundaries, stacking faults, vacancies, inclusions, etc.) as well as other resources (e.g. mechanical deformation or compositional gradients).

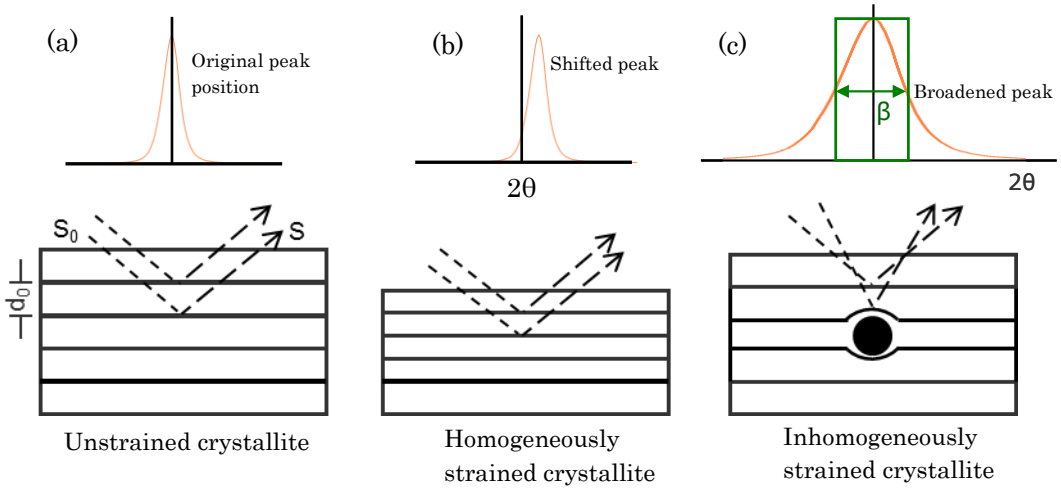

Figure 1-13: A sketch showing the influence of strain on the Bragg peak of YBCO phase.

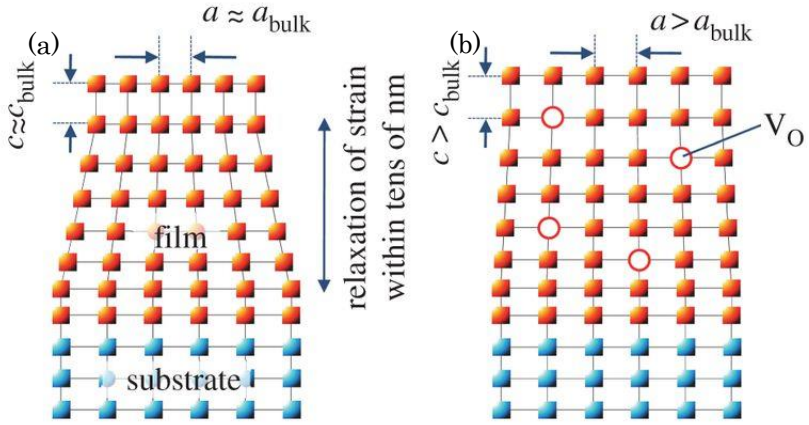

Figure 1-14: Schematic diagrams show strain relaxation (a) a large strain gradient layer formed near the film/substrate interface and (b) for a film with more oxygen vacancies as a mechanism for strain relaxation, which induced crystal-volume expansion [81, 82].

1.3 Progress in nano-engineered microstructures: YBCO nanocomposite

One of the most attractive properties that makes YBCO coated conductors (CCs) with high potential for power applications is the ability to carry high current in magnetic field without dissipation. To data, the achievements for YBCO CCs can meet the requirement in low magnetic field applications (< 1T) such as transmission power cable and fault current limiter systems. Nevertheless, higher magnetic field applications (e.g. transformers, motors, etc.) are limited due to the highly degraded performance in high magnetic fields, as shown in Figure 1-15. In addition, it is worth mentioning that the J_c values we achieved at present is still far from theoretical limit ones (based on fundamental physics) which is well above the requirements of devices, indicating that there is still room for further optimization.

Improvement of superconducting performance in magnetic field requires nanostructured conductors with high pinning forces, and thus an effective immobilization of vortices by effective pinning centers is required as well. A parameter, μ_0H^* [85] is widely used in this thesis to quantify the enhancement of the pinning efficiency. The μ_0H^* is the crossover magnetic field where the low field single vortex pinning regime switches to a higher slope usually towards a power law dependence characteristic of a collective pinning behavior, as shown in Figure 1-15. At the region where $\mu_0H < \mu_0H^*$, the vortex-defect interaction dominates over the vortex-vortex interaction and it is characterized by a J_c nearly independent of the applied magnetic field. In contrast, at the $\mu_0H > \mu_0H^*$ regime, the vortex-vortex interaction becomes important and J_c degradation can be described by a power law dependence $J_c(\mu_0H) \propto (\mu_0H)^{-\alpha}$. All the μ_0H^* appears in this work was defined as the magnetic field that fulfils the relation $J_c(\mu_0H^*)/J_c^{sf} = 0.9$ [85-87], although various criteria have been used in the previous works [86, 88, 89].

In fact, it is earlier realized that the superconducting properties of TFA-YBCO thin films are completely governed by vortex-pinning if current-blocking effects from large-scale strain (i.e. macrostrain and mesostrain) are properly controlled and the optimal growth condition is achieved to avoid current blocking effects from large angle boundaries, strong porosity and secondary precipitate within the body of films [22]. Our strategy is to achieve high quality epitaxial YBCO films with controlled nanosized defects with homogeneous distribution and high density. Our objective is to push μ_0H^* towards higher magnetic field (i.e. maintaining high vortex pinning efficiency at high magnetic field) while the film maintain high percolating critical currents.

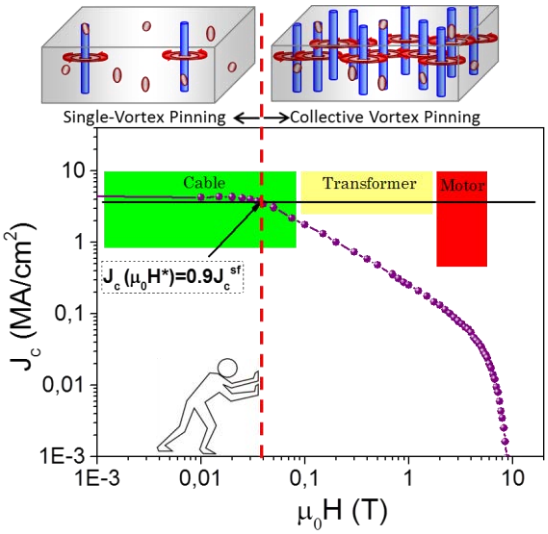

Figure 1-15: Log-log $J_c(H)$ plot showing the degradation of J_c in external magnetic field and the definition of μ_0H^* using the criterion $J_c(\mu_0H^*) = 0.9 \cdot J_c^{sf}$.

1.3.1 Vortex pinning centers

YBCO thin films exhibit a great diversity of nanoscale structural defects [75, 87, 90], e.g. oxygen vacancies, cation disorder, threading, screw or edge dislocations, in-plane dislocations, twin boundaries, antiphase boundaries, stacking faults, intergrowths, etc, which are sketched in Figure 1-16. However, an effective vortex-pinning is fully dependent on the defect structure at the nanoscale and is important to have a full control of it.

The pinning centers of YBCO thin films can be classified according to different criteria [22]. One is to use their dimensionality: 0D (oxygen or copper vacancies), 1D (dislocations), 2D (twin boundaries or stacking faults) and 3D (nanoparticles or local strained regions). Another criterion is according to their pinning length relative to the magnetic field orientation, where pinning centers can be clarified as isotropic (0D, 3D) or anisotropic (1D, 2D). In addition, depending on the pinning strength against temperature activation vortex depinning, the pinning centers can be clarified as weak or strong. The contributions of both can be distinguished though the analysis of $J_c(T)$ plots by using two different models [22, 87, 91-93]. Specially, strong defects have a smoother temperature dependence of J_c while weak defects lead to a fast decay of $J_c(T)$. The method for extracting the weak pinning (J_c^{wk}) and strong pinning (J_c^{str}) from $J_c(T)$ plot will be described in details in subsection 2.2.3.1. Correspondingly, H-T pinning phase diagrams expressing the relative weight of J_c from different types of pinning centers (i.e. J_c^{iso-wk}, $J_c^{iso-str}$ and J_c^{an-str}) were built [94, 95].

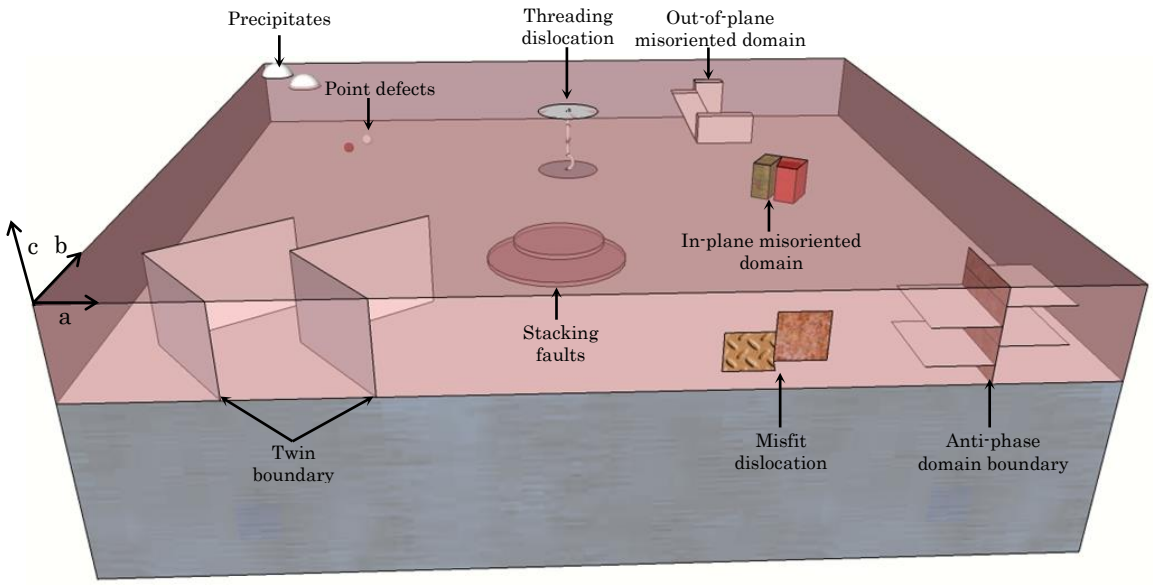

Figure 1-16: A sketch showing natural structural imperfections of epitaxial YBCO films.

1.3.2 Pinning mechanism in YBCO Nanocomposite

Unfortunately, enhancement of vortex pinning properties via these natural structural defects is significantly limited by the difficulty in obtaining desired defect landscape. Therefore, an effective approach for optimizing structural defects landscape of YBCO films was extensively developed via the introduction of secondary non-superconducting nano-sized inclusions as artificial pinning centers (APCs).

After the first identification of the effectiveness of YBCO nanocomposites (YBCO-$BaZrO_3$ via in situ) to enhance vortex pinning properties by MacManus-Driscoll [96], a large number of YBCO nanocomposites with various secondary nanoinclusions have been developed via in-situ [90, 97-99] or ex-situ [54, 65, 77, 100] techniques. In the case of in-situ techniques, such as PLD and MOCVD, simultaneous nucleation and growth of the YBCO and epitaxial nanoscale secondary phases occur. TEM investigations in the previous reports revealed that the in-situ growth mode promote the generation of nanoindclusions mostly in the form of columnar structure [96, 101-103] (Figure 1-17 (a)), as well as creating highly effective nano-sized particles [97, 98]. By carefully tuning the temperature or growth rate during PLD of YBCO nanocomposite films, a finely controlled ratio of splayed columnar defects and random nanoparticles can be achieved and thus, a highly effective vortex pinning landscape for optimizing current-carrying capability were obtained in the previous work [98]. By contrast, in YBCO films grown by ex-situ techniques (e.g. CSD), artificial secondary nanoinclusions are generated in a precursor film with a deferred sequential nucleation and growth of the YBCO matrix. In this scenario, the nanoinclusions remain trapped in the YBCO matrix during YBCO growth and they appear mainly in the form of randomly distributed nanoparticles (Figure 1-17 (b)). This methodology enables significant

enhancement of the pinning properties in a wider region of orientations [54, 77], making it very competitive with high-vacuum methodologies.

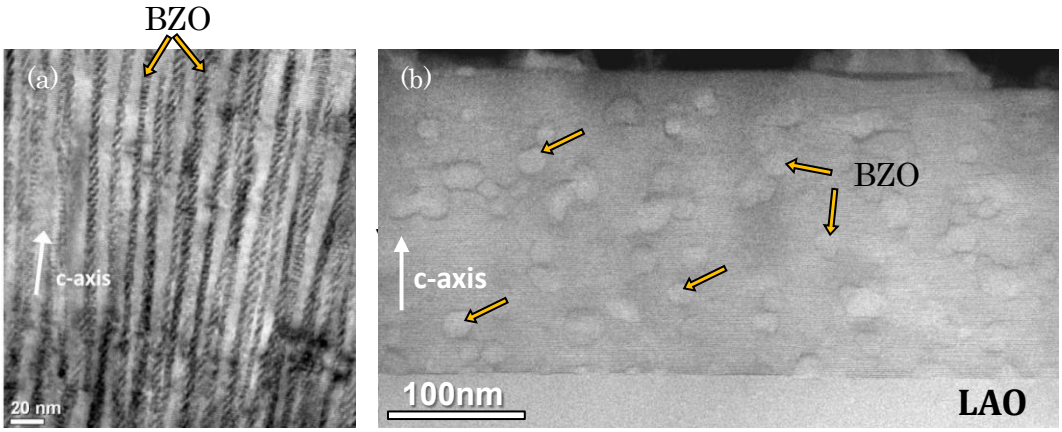

Figure 1-17: TEM images of YBCO-BZO nanocomposite grown from (a) in-situ [102] and (b) ex-situ techniques where the former present epitaxial BZO nanorods and the later displays homogeneously distributed BZO nanoparticles.

CSD-based YBCO nanocomposite films were firstly developed on the basis of using complex precursor solutions, i.e. extra metal salts with correct stoichiometry dissolved in the YBCO precursor solution. A subsequent spontaneous segregation of secondary phases occurs during the growth process. The nanoparticles are usually formed prior to the nucleation of YBCO grain during the heating step and thus, lead to randomly distributed nanoparticles [54, 55, 77]. On the basis of this route, several types of secondary phases, e.g. $BaZrO_3$ [54, 64, 77, 94, 104-109], $BaHfO_3$ [110-112], $BaNbO_3$ [64], $BaCeO_3$ [54], $BaSnO_3$ [100], $BaTiO_3$ [106], Ba_2YTaO_6 [54, 55, 65, 113, 114], Y_2O_3 [54, 107], with elaborate amount have been successfully segregated within epitaxial YBCO matrix and, significant enhancements of the pinning efficiency were achieved.

Unfortunately, for the YBCO ss-nanocomposites, nanoparticles could not act as pinning centers themselves up to now because the nanoparticle sizes are much larger than the order of YBCO coherence length (ξ) [54]. Instead, a detailed analysis of the nanostructure-properties relationship in a wide range of compositions revealed that the vortex pinning mechanism is mostly dominated by the presence of highly strained areas in the YBCO matrix, i.e. nanostrain [54]. When the oxide nanoparticles are randomly orientated, they trigger the formation of nanoscale defects in the YBCO matrix (see Figure 1-18 (a)), being the most relevant ones the $YBa_2Cu_4O_8$ (Y248) intergrowths (extra Cu-O chain) (see Figure 1-18 (b)) which is surrounded by a concatenation of partial dislocations and ultimately generate highly strained localized areas in the YBCO lattice, i.e. nanostrain (ε) (see Figure 1-18 (c)). In these strained nanoareas, the Cooper pair formation is quenched under tensile strain according to the so-called bond-contraction pairing model [115], forming new and effective core-pinning regions, as shown in Figure 1-18 (c).

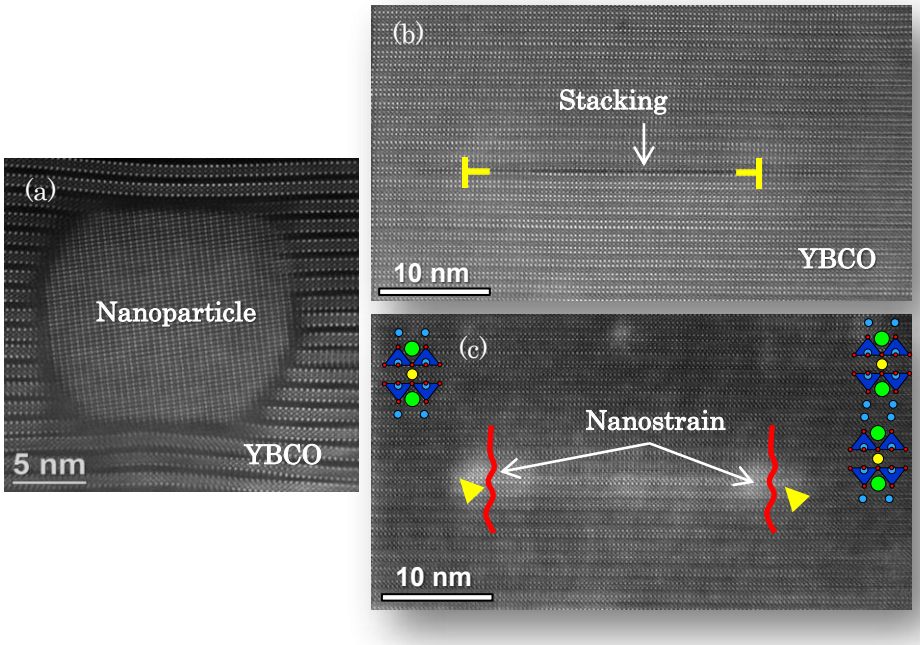

Figure 1-18: High-resolution TEM (HRTEM) Z-contrast images of spontaneously segregated YBCO-$BaZrO_3$ nanocomposite film. (a) An individual BZO nanoparticles surrounded by highly bended YBCO planes; (b) Normal YBCO lattice with intercalation of extra CuO layer forming stacking faults or Y248 intergrowths and the associated partial dislocations are indicated by yellow arrows; (c) Nanostrained regions (bright contrast regions indicated with yellow arrows) which act as normal regions that act as vortex-pinning centers.

It has been previously shown that the non-coherent interface between the nanodots and the YBCO matrix is the controlling parameter for generating nanostrain, instead of nanoparticle concentration itself, as shown in Figure 1-19 (a) [54]. The increased nanostrain can be effectively transformed into the improvement of vortex-pinning efficiency (Figure 1-19 (b)). Therefore, in this scenario, a tight control of nanoparticle properties (size, shape and distribution) and Y248 intergrowth characteristics (density, extension and distribution) is of fundamental importance for optimizing vortex-pinning landscape [55, 65]. In addition, the formation of intergrowths is also related to the release of strain energy accumulated at the contact between grains during the growth process, as well as to the Cu atom diffusion whose occurrence relies on the concentration gradient and the thermodynamic stability during the whole YBCO superconducting phase formation process [116]. Moreover, J. Gazquez et al. [117] described the Y248 intergrowths as double chains with quasi-1D arrays of defect clusters including two Cu vacancies decorated by three O vacancies embedded in particular chains, but the detrimental effect of Cu off-stoichiometry on T_c of the system have never been observed. Recently, an ingenious strategy based on the spontaneous segregation approach and multiple coating/calcination steps has been reported to achieve high nanoparticle loads (> 25 vol.%) with tuned size with remarkable superconducting performances [66].

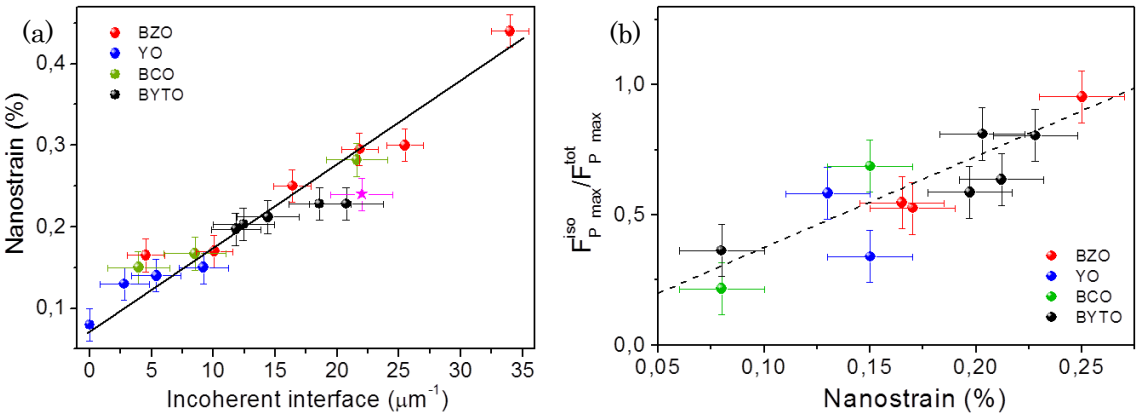

Figure 1-19: (a) Dependence of c-axis nanostrain values on the incoherent specific interface of nanodots in a large range of nanocomposites; (b) Pinning force dependence with the c-axis nanostrain values [54].

Although the CSD-YBCO nanocomposites prepared from spontaneous segregation has been proved effective for enhanced vortex-pinning properties for a wide variety of compositions, the control of nanoparticle size and distribution at high loads remains very challenging [55, 65].

1.3.3 Preformed YBCO Nanocomposite

1.3.3.1 YBCO nanocomposites from preformed nanoparticle colloidal solutions

In order to solve the intrinsic limitations in spontaneously segregated YBCO nanocomposite films, a novel approach to CSD-based YBCO nanocomposites has been developed, on the basis of using colloidal precursor solution which consists of YBCO precursor solution and preformed nanoparticles. This approach requires a valid synthesis of mono-dispersed nanoparticles and a high stability of the preformed nanoparticles in both precursor solution and YBCO matrix. Therefore, we could name this YBCO nanocomposite preparation route as "preformed nanoparticle nanocomposites" (pn-nanocomposite). A detailed illustration of this process will be presented in Section 2.1.1. The use of this nanocomposites route have been supposed, therefore, to be a very promising choice for achieving efficient YBCO nanocomposite films with controllable composition, size and concentration of inserted nanoparticles [118].

A successful synthesis of preformed nanoparticles is crucial to achieve high-quality epitaxial pn-nanocomposite films. Previously in our group, metal oxide nanoparticles which are magnetic ($MnFe_2O_4$ and $MnFe_2O_4$) [72, 119-121] and non-magnetic (CeO_2 and ZrO_2) [72, 118, 122, 123] were successfully synthesized using thermal or microwave (MW) activation via a "solvothermal synthesis process" [124]. A one-pot MW-assisted solvothermal synthesis method was successfully applied in producing spherical, high quality $MnFe_2O_4$ and $CoFe_2O_4$ nanoparticles with 5 nm in size [119]. After a series of optimization of processing

parameters (ligand, reaction process or time and precursor), individual rod-like ZrO_2 nanoparticles with a long edge of about 7-8 nm [118, 125] and high quality CeO_2 nanoparticles with diameters ranging from 2 to 10 nm were successfully synthesized [118, 123]. To achieve competitive nanocomposites, it is crucial to achieve colloidal solutions with small nanoparticles size, controllable nanoparticles shape, high stability in precursor solutions (e.g. TFA) and no nanoparticle aggregation.

The pioneering work about the preparation of the YBCO pn-nanocomposite films was first reported by Martínez-Julián, F. et al. [126] of our group. In this work, only a small amount of preformed Au nanoparticles (~2 mol%) could be homogeneously mixed with TFA-YBCO solutions. There was a strong tendency of nanoparticles to migrate to the film surface during the thermal processing, without any enhancement of vortex pinning. I. Bretos et al. [127] made a further step because they successfully incorporated preformed $BaZrO_3$ (BZO) nanoparticles to the YBCO matrix. Although attractive microstructural landscape and superconducting properties were identified in the YBCO films, large-scale applications of this approach were limited by the method they used to prepare the BZO nanoparticle solutions. In the recent reports of our group, we described the introduction of preformed nanoparticles with compositions of MFe_2O_4 spinels (M = Mn, Co) [119, 128, 129], CeO_2 fluorite [118, 130] and ZrO_2 fluorite [118, 125, 131] in YBCO films. Among them, the introduction of preformed CeO_2 and ZrO_2 nanoparticles to YBCO films were identified to be effective for enhancing vortex pinning [118, 125, 131]. Several difficulties, however, were still described in the initial investigations of this approach. A full description of these difficulties and the corresponding strategies has been achieved and considered to be essential for further optimizing microstructural characteristics and pinning performance of YBCO pn-nanocomposites [118, 125].

1.3.3.2 Open issues and strategies

In Figure 1-20, it has been summarized the previously encountered hurdles and the required readiness parameters involved in the CSD-based pn-nanocomposite route [118] and thus, helping to provide an outlook on the future of this approach.

The main challenges can be summarized in the following items: (1) highly ionic environment in YBCO precursor solution hampering the stabilization of the nanoparticles; (2) nanoparticles sedimentation onto the film/substrate interface during the deposition, pyrolysis or growth steps (see Figure 1-21 (a)); (3) the pushing phenomena during the growth process, e.g. preformed CeO_2 nanoparticles with size of 2 nm were prone to migrate to the film surface, as shown in Figure 1-21 (b); (4) chemical reactions between nanoparticles and YBCO during high temperature annealing step, e.g. MFe_2O_4 spinels (M = Mn, Co), CeO_2 fluorite and ZrO_2 fluorite reacted with YBCO precursors leading to final modified secondary phases after growth: $YBaCuFeO_5$, $Ba_3YFeMnO_9$ $BaCeO_3$ and $BaZrO_3$,

respectively (see Figure 1-21 (c)); (5) nanoparticle coarsening or coalescence during the growth process (see Figure 1-21 (d)), which are demonstrated to block the current percolation; (6) inefficient induction of secondary structural defects, leading to inefficient pinning of vortices (see Figure 1-21 (e)); (7) difficulties for reaching high nanoparticle concentration [118, 132]. All these nanoparticle behaviors are detrimental to the superconducting performance and should be avoided during the processing process.

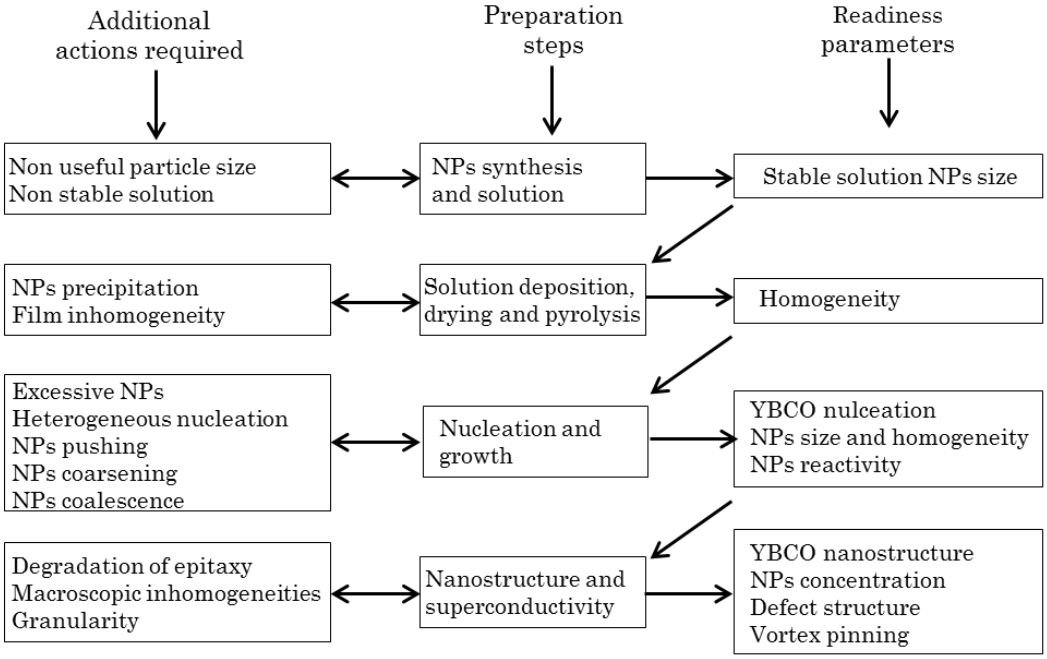

Figure 1-20: A summary of hurdles and readiness parameters involved in different steps of the CSD-based pn-nanocomposite approach [118].

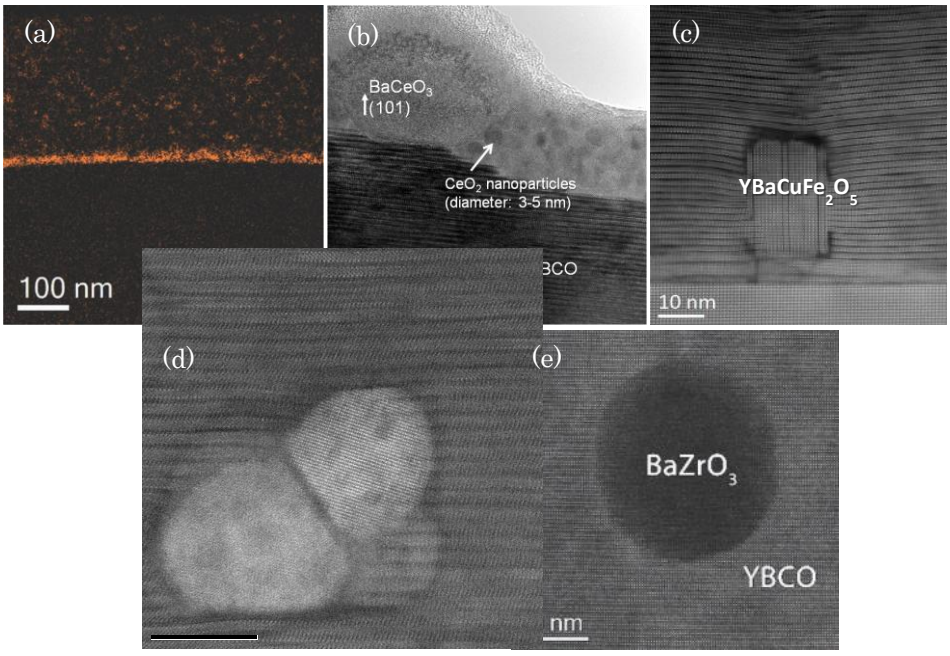

Figure 1-21: TEM images of YBCO pn-nanocomposite films showing different type of detrimental nanoparticle behaviors appear during the formation process nanocomposite films [118, 125, 128].

For this reason, it become clear then that a tight control of some parameters in the whole procedure, such as selection of nanoparticles (composition or lattice structure), valid synthesis of nanoparticles (mono-distributed, small size and desired shape), high stability of nanoparticles in YBCO precursor solution or during the growth process for avoiding several detrimental phenomena (particles aggregation, coarsening and inhomogeneous distribution), as well as an effective control of the induced secondary nanostructure within YBCO matrix, is very important for achieving our nanocomposite strategy successfully using the pn-nanocomposite approach.

The barium perovskite-type oxide, $BaZrO_3$ (BZO) and $BaHfO_3$ (BHO) have been well known as high melting temperature materials, displaying melting point values of ~2690 ºC [133] and ~2620 ºC [134], respectively. Both phases are chemically compatible with YBCO up to 1000 ºC [135]. We should mention, particularly, that BZO and BHO perovskites present highly mismatched interfaces with YBCO lattice which are beneficial to the nucleation of Y248 intergrowths. More importantly, recent investigations on APCs in CSD-based spontaneously segregated YBCO nanocomposite have shown that the vortex-pinning efficiency can be significantly enhanced by the introduction of BZO [54, 77, 104] and BHO [110, 112] perovskite nanodots into YBCO lattice. The introduction of preformed perovskite-type nanopartilces (BZO and BHO) based on the pn-nanocomposite route appears, therefore, as a very promising methodology to further improve superconducting performances of YBCO films and CCs.

2. Experimental Methodologies

In this chapter we will present a full detailed introduction of the experimental procedures and characterization methods used in our present work. We will first describe in section 2.1 all the experimental procedures based on the chemical solution deposition (CSD) methodology. In this section, the details of the synthesis of precursor solutions, the substrate treatment, the film deposition and the following thermal processes corresponding to the fabrication of epitaxially grown YBCO thin films will be depicted.

Subsequently, section 2.2 is devoted to the description of the characterization techniques used to describe the physicochemical characteristic of the precursor solutions as well as the surface morphology, microstructure and physical properties of both converting and fully converted YBCO thin films.

2.1 Layer formation procedures

CSD-based YBCO route consists of four basic stages, i.e. the preparation of metal-organic precursor solutions (TFA in our case), the deposition of the precursor solution on a substrate, the pyrolysis to remove the organic content and obtain an amorphous or nanocrystalline matrix and the growth process to obtain the final superconducting YBCO films, as depicted in Figure 2-1. The corresponding underlying mechanisms have been introduced in the section 1.2 and the operation details will be illustrated in the following text.

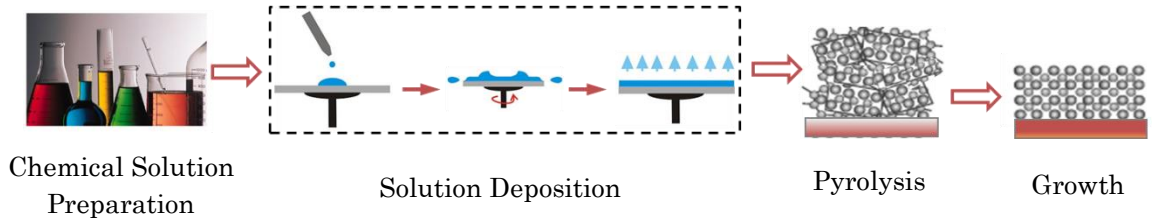

Figure 2-1: Flow chart of CSD route for preparing YBCO superconducting films.

2.1.1 Precursor solutions preparation

2.1.1.1 TFA-YBCO precursor solution

The preparation of stable TFA precursor solution with the adequate metal stoichiometry and free of impurities is the prerequisite for YBCO thin film preparation. In this thesis, all the work is based on the solution route that starts from YBCO ceramic powder reacted with trifluoroacetic anhydride (TFAA), which is firstly proposed by Roma et al [23] in our group. The whole process is summarized in Figure 2-2.

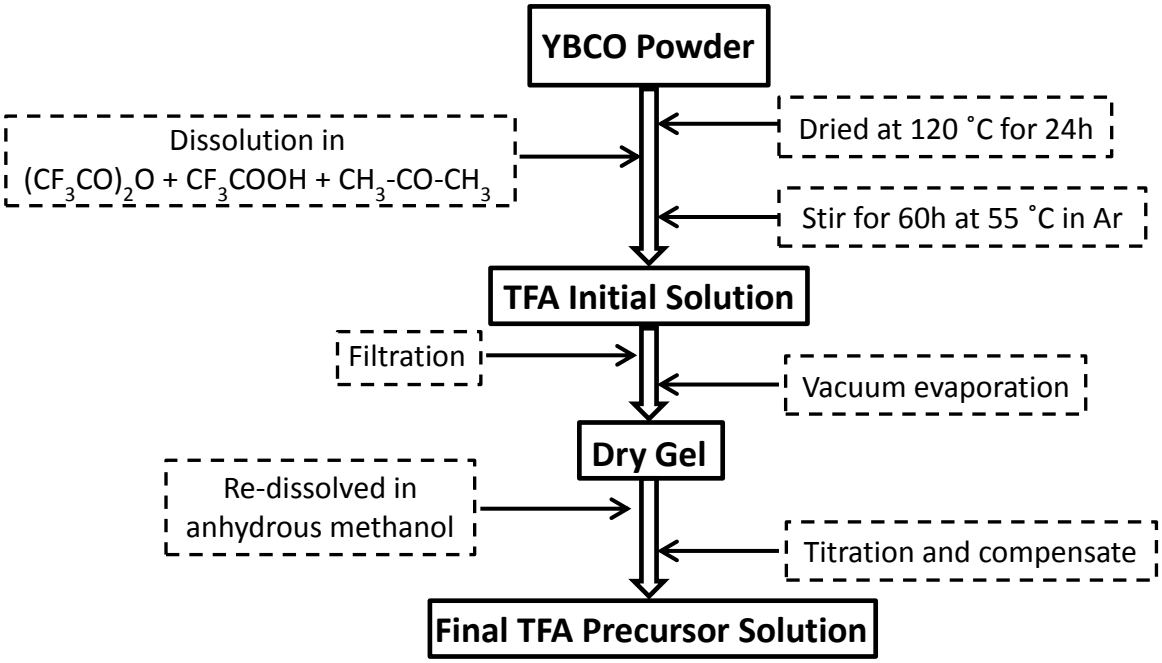

Figure 2-2: Flow chart of the methodology to prepare anhydrous TFA-YBCO solution.

The preparation of TFA-precursor solution starts from the chemical reaction between commercial YBCO powder ($YBa_2Cu_3O_x$, Ceraco) and an excess of TFAA (Sigma-Aldrich, ≥ 99%), in the meantime, a small amount of trifluoroacetic acid (TFAH, Sigma-Aldrich, 99%) is added as catalyst, as well as acetone (HPLC acetone, Scharlab, 99.98%) as solvent. Before dissolution, a drying treatment at 120 ºC for 24h for the as-received YBCO powder is needed, to remove the moisture. The mixture is stirred for 60h at 55 ºC in Ar shield. After the reaction, the initial TFA solution consisting of $Y(TFA)_3$, $Ba(TFA)_2$, $Cu(TFA)_2$ and some residues is obtained. Afterwards, the initial TFA solution is cooled down to room temperature and filtered by Teflon membrane filters (0.45 μm for pore size), in order to eliminate the remaining impurities. Next, a vacuum evaporation is conducted in a rotary evaporator at 55 ºC for 6h, after which residual reactants (i.e. trifluoroacetic acid) and solvent (i.e. acetone) are removed and ultimately a dry gel is obtained. After that, the dry gel is dissolved in a certain volume of anhydrous methanol (MeOH) (Sharlab 99.9%, max. 0.003% H_2O), and a following titration and compensation process is also needed to adjust metal concentration to the desired values. Finally, the TFA-YBCO precursor solution consisting of $Y(TFA)_3$, $Ba(TFA)_2$ and $Cu(TFA)_2$ in a stoichiometric ratio of 1:2:3 is obtained. The final precursor solution is proposed to be stable up to four months when properly preserved in sealed vials under inert gas (i.e. Ar or N_2) atmosphere.

Generally, the total metal concentration of the as-obtained precursor solution is 1.5 mol/L (M), from which film thickness can be controlled in the range of 250 nm with a standard deviation of ~50 nm. In this case, to achieve thicker films it is necessary to perform a multi-deposition process separated by intermediate pyrolysis steps. Furthermore,

the as-obtained precursor solution (1.5 M) can be highly diluted with metal concentrations down to 0.03, 0.06, 0.15 and 0.3 M using anhydrous methanol for the purpose of obtaining thin films with thicknesses of 5, 10, 25 and 50 nm, respectively, based on the single deposition process.

2.1.1.2 Nanoparticles synthesis

The synthesis of the $BaMO_3$ (M = Zr and Hf) colloids were carried out in the Inorganic Chemistry Department of Autonomous University of Barcelona (UAB). In order to meet the requirements for our YBCO nanocomposite strategy, the methodology called "solvothermal synthesis process" was applied in our present work. This nanoparticle synthesis route show significant advantages such as versatility, small nanoparticle size available (> 2 nm) and high concentration of nanoparticle colloidal solution obtainable (~100 mM) compared with other synthesis method (e.g. hydrolysis, oxidation process, etc.). The basic synthetic process of the solvothermal process for synthesizing $BaMO_3$ nanoparticles is displayed in Figure 2-3.

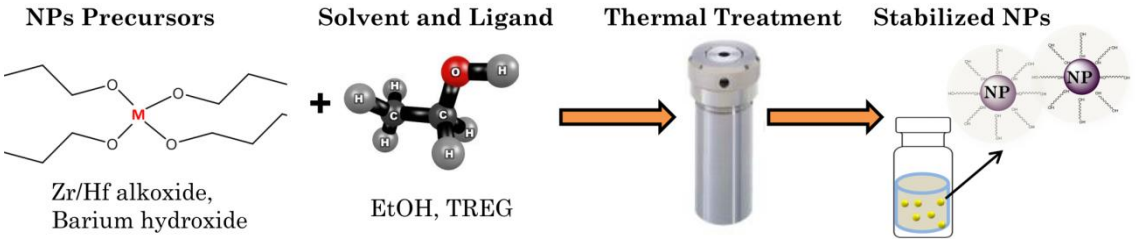

Figure 2-3: Scheme of the solvothermal synthesis process.

The $BaMO_3$ (M = Zr and Hf) nanoparticles were synthesized starting from Zr/Hf alkoxides and Barium hydroxide (Sigma Aldrich). The precursors with desired stoichiometric ratio were dissolved in a polar solvent (i.e. EtOH) and after that, the triethylene glycol (TEG) and the base were mixed until it dissolves completely. The chemical mixture was then placed in an autoclave and heated until 180 ℃. During the heating process, the nucleation event of nanoparticles occurs and grown to a certain supersaturation degree which is influenced by several parameters such as temperature, time and ligand. By controlling the reaction time and the ligand concentration one can achieve small steric stabilized nanoparticles. The stabilization of the preformed nanoparticles is on the basis of the ligand that forming a protective organic shell for avoiding the nanoparticles contact, as shown in Figure 2-3. At this point, cubic $BaMO_3$ (M = Zr, Hf) (BMO) nanoparticles with controllable crystallinity, size and shape are obtained.

A washing step is followed in order to separate the preformed nanoparticles from the excess ligand. After cleaning the preformed BMO nanoparticle solutions by using centrifugation for 3 times at 10000 rpm and 10 min each, nanoparticles are finally re-dispersed in EtOH and the preformed BMO nanoparticle colloidal solutions used in this thesis are prepared. The nanoparticle suspensions remain stable, at both EtOH and TFA

solution, for more than one year without any sign of agglomeration after stabilization of the colloidal solutions. The whole process of the solvothermal synthesis of BMO nanoparticles is shown in Figure 2-4. More detailed illustration of the synthesis of BMO nanoparticles can be found in reference [136].

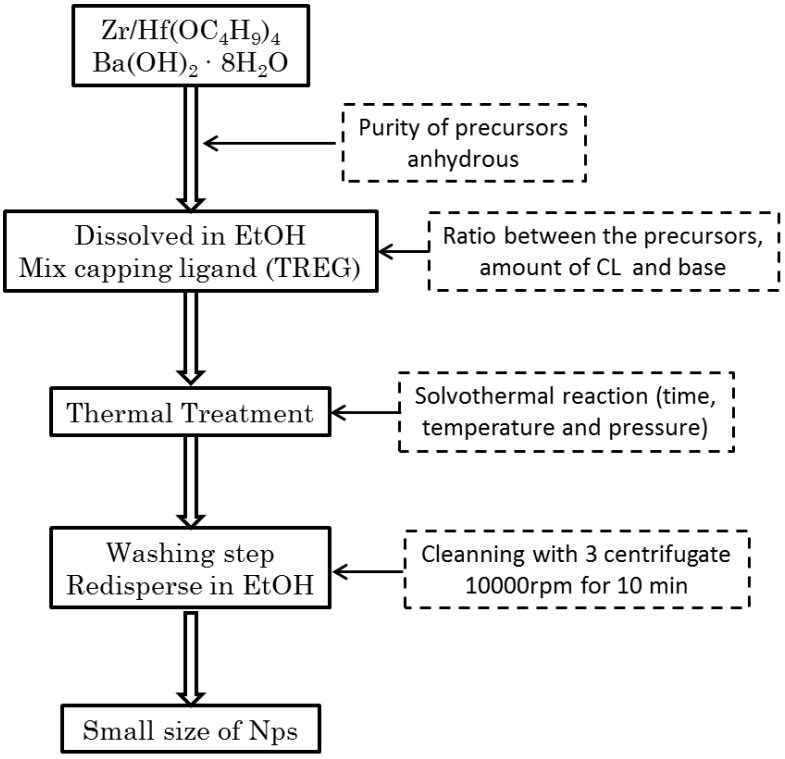

Figure 2-4: Flow chart and factors influencing the method for the synthesis of $BaMO_3$ (M = Zr, Hf) nanoparticles.

2.1.1.3 Preformed nanocomposite precursor solutions

A scheme presenting the preparation of the nanocomposite precursor solutions of this work is depicted in Figure 2-5. A certain amount of TFA-YBCO precursor solution and nanoparticle colloidal solution are taken by appropriate pipettes (RAININ, PR-20 or PR-200 or PR-1000), as well as anhydrous methanol (Scharlau, max. 0.003% H_2O) as solvent for tuning the metal concentration, and then mixed in a sealed vial. The mixing operation is carried out in shielding gas (N_2 or Ar) atmosphere. The mixed solutions are then stirred in ultrasonic bath in order to facilitate the nanoparticles in a monodispersed state. Afterwards, the solution is filtered by using a 0.2 μm membrane filter (Teflon) to remove impurities entrained during the mixing process. The YBCO-BMO nanocomposite precursor solutions are kept in sealed vials and inert gas atmosphere, ensuring it to be stable for more than 1 year. More detailed characterization of the preformed BMO nanoparticles behavior in both EtOH and TFA solution will be presented in Chapter 4 from phase-structural and morphological point of view.

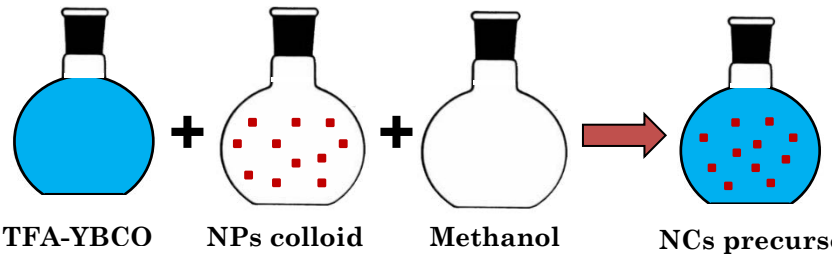

Figure 2-5: Scheme of the procedure to prepare YBCO nanocomposite precursor solutions from preformed $BaMO_3$ (M = Zr or Hf) nanoparticle colloidal solutions.

A precise calculation of the volume of different solutions desired for a nanocomposite precursor solution with certain molar percentage of nanoparticles is the prerequisite for conducting the solution route mentioned above. We should mention, firstly that the as-obtained TFA precursor solution with metal concentration of 1.5 M leads to a final YBCO of 0.25 M taking into account the stoichiometry of YBCO (i.e. $YBa_2Cu_3O_{7-x}$). For the sake of brevity, we can take the preparation of 2 ml of YBCO (0.75 M) + x mol% BMO nanocomposite precursor solution starting from 1 ml standard TFA precursor solution (1.5 M) and nanoparticle colloidal solution (y mM) as an example, then the volume of the colloidal solution can be written as follows:

$$V\ (ml) = 2.5 \cdot \frac{x}{y} \qquad \text{Equation 2-1}$$

In addition, methanol with the volume of (1-V) ml is taken to supplement the volume of the final precursor solution.

Finally, the YBCO-BMO precursor solutions lead to a final YBCO pn-nanocomposite with nanoparticle volume percentage (vol.%) of: $vol.\% = \frac{V_n \cdot x}{100 \cdot V_Y + V_n \cdot x} \cdot 100\%$, where V_Y = 173.6 $Å^3$ is the unit cell volume of YBCO; V_n is the unit cell volume of nanoparticles with the value of 73.7 $Å^3$ and 72.6 $Å^3$ for BZO and BHO, respectively.

2.1.2 YBCO films processing

2.1.2.1 Substrate treatments

All $LaAlO_3$ (one side polished, 30 pcs) or $SrTiO_3$ (one side polished, 20 pcs) (100)-oriented single-crystal substrates used in our present work are commercially obtained (CrysTec) with a uniform size of 5 mm × 5 mm × 0.5 mm. A series of cleaning and thermal treatment processes are carried out before solution deposition process, in order to ensure a clean and atomically flat substrate surface [3, 137] for the following fabrication of high quality epitaxial YBCO thin films.

The as-received substrates are cleaned by tissues, firstly, ensuring an absence of large scale impurities on the substrate surface, and then the substrates are deep cleaned by

using successive ultrasonic baths of acetone and methanol lasting 5 minutes each, an eventual drying process by pressed N_2 is followed. These cleaning processes are essential for avoiding carbon-containing impurities before the following high temperature treatment.

Next, the substrates are thermal-treated in a tube furnace; the thermal process is schematically shown in Figure 2-6 (a). The surface morphology evolution of the substrates during the thermal treating process has been detailed illustrated in the previous work of our group [3], which points that the surface structure ultimately reach a energetically favorable state via surface rearrangement either by diffusion or desorption of atoms. It is important to note that the thermal treated surface exhibit atomically flat terraces separated by unit-cell high steps, providing a valid growth template for obtaining high-quality YBCO thin films with high reproducibility. This points that the surface structure ultimately reach a energetically favorable state via surface rearrangement either by diffusion or desorption of atoms. It is important to note that the thermal treated surface exhibit atomically flat terraces separated by unit-cell high steps (Figure 2-6 (b)), providing a valid growth template for obtaining high-quality YBCO thin films with high reproducibility.

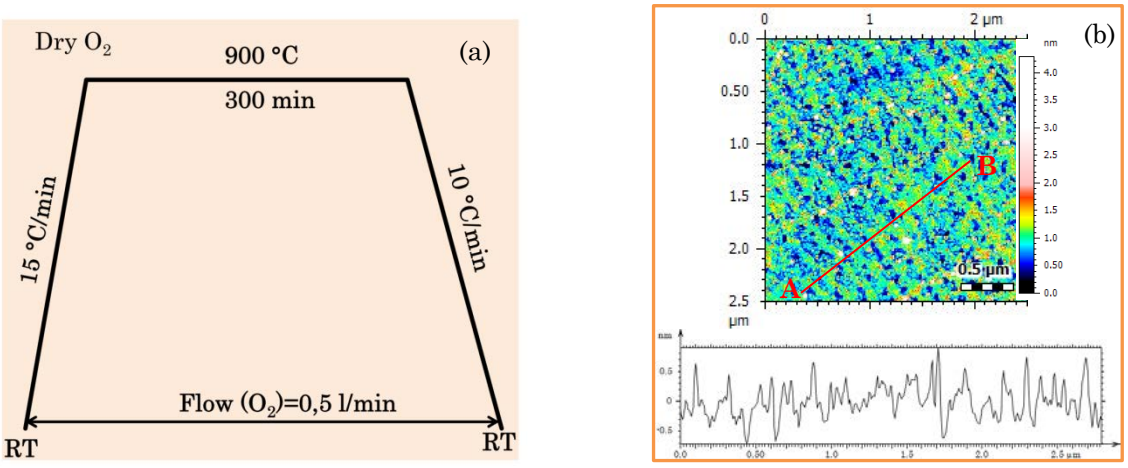

Figure 2-6: (a) Schematic of the thermal profile used in this study to treat the single crystal substrates (LAO or STO) in order to obtain impurities free surface with atomically flat terraces; (b) AFM analysis of an as-treated LAO substrate.

In addition, the deposition of YBCO thin layer has also been carried out on $^{CSD}Ce_{0.9}Zr_{0.1}O_2$(CZO)/^{ABAD}YSZ//SS metallic substrates. The ^{ABAD}YSZ/SS metallic tapes are provided by Bruker HTS (Germany) with a width of 4 mm and thickness of 0.1 mm [138]. On top of these metallic tapes, ^{CSD}CZO cap layers are deposited by spin coating. These ^{CSD}CZO cap layers were grown at 900 ºC during one hour in air, leading to a final thickness of ~25 nm. Several crucial parameters of the ^{CSD}CZO cap layer, such as film epitaxy, roughness and flatness, have been optimized and analyzed in the previous works of our group [139, 140].

2.1.2.2 Precursor solution deposition

At present, several film coating techniques such as spin coating, dip coating or Ink Jet printing are optional, in the case of preparation of YBCO thin films via CSD route. A precise control of the film thickness can be achieved via a tight control of properties of precursor solutions such as viscosity and metal concentration. In addition, a pre-cleaning process for the substrates should be conducted in an ultrasonic bath using acetone and methanol as cleaning agent for 5 minutes each.

In this study, TFA-YBCO precursor solutions with different metal concentration (15 mM-1.5 M) were spin coated onto the treated substrates. The spin coating process was carried out in a glove box with N_2 flowing, where a clean, temperature-controlled (18-23 ºC) and low humidity ($\leq$ 3 g/m^3) depositing atmosphere can be ensured. The substrate was placed on the spinner with ~15 μL precursor solution deposited on it. And then the spinner was accelerated to 6000 rpm in one second. This angular velocity was held for 2 min to ensure the homogeneous coverage of the substrate and the final film thickness. Subsequently, the as-deposited precursor film was placed in a heating plate at 70 ºC annealed for 5 min for drying treatment. Finally, the as-deposited precursor film was transferred to a tube furnace with protection of silicon in a culture dish.

However, one thing to be remarked is that any kind of film imperfection (e.g. inhomogeneity, large scale impurities and blistering) is unacceptable and the process should be repeated until a highly homogeneous as-deposited YBCO precursor film is obtained.

2.1.2.3 Pyrolysis process

After obtaining a homogeneous deposition of a YBCO precursor film onto a substrate, a pyrolysis process is followed, in order to remove the excess of solvent (i.e. methanol) and decompose the organic component (i.e. trifluoroacetates). Nevertheless, macroscopic defects (residual porosity, film cracking, buckling or blustering, etc.) often appear during the pyrolysis process, attributed to intermediate phenomena, such as film shrinkage, tensile stress relaxation and gaseous phase liberation accompanied with the film densification process. Therefore, a tight control of the processing parameters during the pyrolysis process is of crucial importance for achieving homogeneous solid precursor films prepared for the following YBCO superconducting film growth.

In this study, all the samples are pyrolyzed via our “conventional pyrolysis process” (Figure 2-7), which is performed in a quartz tube with an oxygen flow of 0,07 l/min. The heating process consists of an initial fast heating ramp (5 ºC/min) up to 230 ºC and then followed by a slow heating ramp (3 ºC/min) up to 310 ºC. After annealing at 310 ºC for 30 min, the furnace is then cooled down to room temperature at a ramp of 5 ºC/min. During

this thermal process, water vapor is introduced into gas flow at ~110 ºC during the heating process and then closed at 150-200 ºC during cooling process. In addition, humid oxygen gas flow with water partial pressure of ~23 mbar is obtained though injecting dry oxygen into flasks containing deionized water (20 ºC) by using gas dispersion tubes.

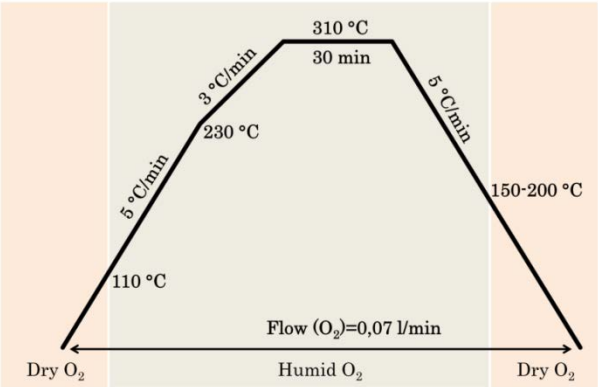

Figure 2-7 Schematic thermal profile used in our conventional pyrolysis process, after which YBCO solid precursor film consists of amorphous BYF matrix with embedded CuO nanoparticles is obtained.

Finally, it is important to remark, as well, that any type of large-scale defects such as cracking, buckling or blistering will be detrimental to the superconducting properties of YBCO thin films. However, solid precursor films with minor defects are still suitable for phase evolution study. Typical optical micrographs of homogeneous, cracked, buckled and blistered films after the conventional pyrolysis process are shown in Figure 2-8 (a)-(d), respectively.

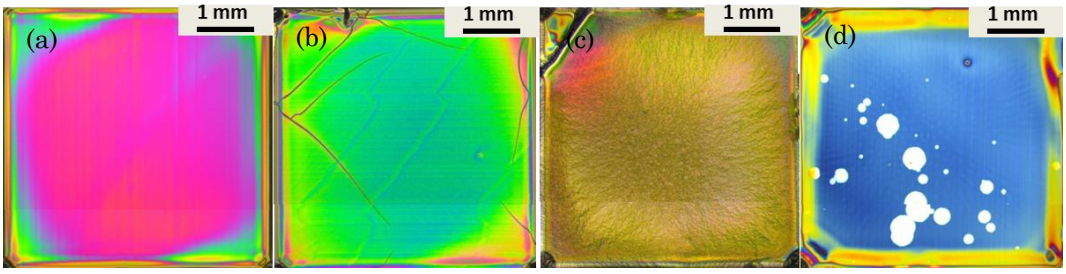

Figure 2-8 Optical micrographs of (a) homogeneous film, (b) cracked film, (c) buckled film and (d) blistered film after the conventional pyrolysis process.

2.1.2.4 Growth process

After the pyrolysis process, the so-called "growth process" includes nucleation and growth, followed by an oxygenation stage, to obtain YBCO thin films with an appealing microstructure and superconducting performance. This process is mainly conducted in two tubular furnaces located at ICMAB, named "Flautista" and "Leonidas", both of which have a quartz tube with an inner diameter of 0.022 m. The thermal annealing processes are schematically shown in Figure 2-9. In all cases parameters such as water partial

pressure, gas composition and gas flow rate follow the optimized growth conditions determined in previous works, [12, 37, 46, 53, 141] which are marked in Figure 2-9.

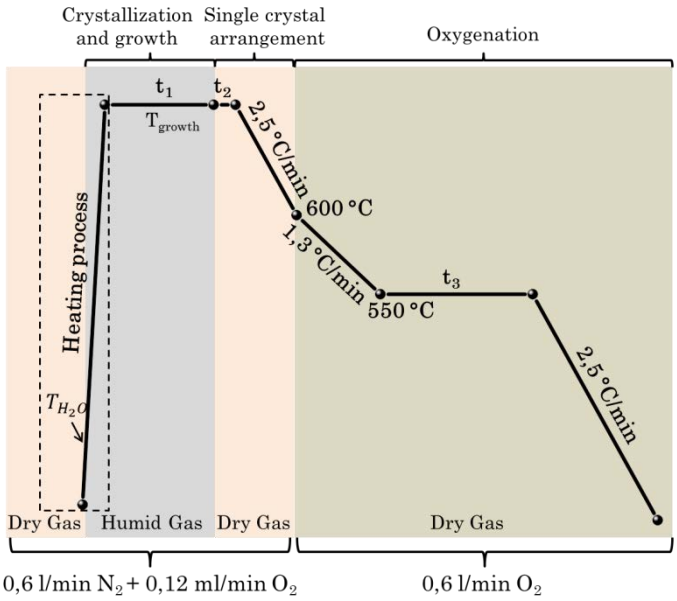

Figure 2-9 Schematic thermal profile used in the superconducting YBCO thin film formation process, during which the YBCO nucleation and growth and the oxygenation process are included.

In the whole process of the crystallization and growth stage, thin films are annealed in nitrogen and 200 ppm oxygen mixed gas atmosphere. The total gas flow rates of two different furnaces ("Flautista" and "Leonidas") are 0.6 l/min and 1.2 l/min, respectively, due to the internal structural difference of each. A precisely controlled gas composition is obtained using mass flow controllers in an atmosphere with a total pressure of 1 atm (1010 mbar). The humidified gas with $P(H_2O)$ = 23 mbar can be achieved via injecting the mixed gas into de-ionized water contained in two flasks in series prior to the gas flow into the tube.

Firstly, the as-pyrolyzed precursor films are heated up to the growth temperature (T_{growth}), during which two typical heating modes (i.e. conventional heating and flash heating) are applied in our present work. For the conventional heating mode, the samples are placed in the center of the furnace at room temperature and followed by the heating process with a constant heating ramp of 25 °C/min, during which the water vapour is introduced at 110 °C, as shown in Figure 2-10 (a). In the case of the flash heating mode, the furnace is required to be pre-heated to the T_{growth} and stabilized for 2h for the purpose of avoiding the influence of the overshooting. According to the water vapour opening temperature (T_{H_2O}) differences, the details of operation can be described in the following 4 cases: (1) T_{H_2O} = 20 °C, the as-pyrolyzed film is placed at the entrance of the tube (i.e. 20 °C) and water vapour is introduced in the meantime, and the film is then pushed into the center of the furnace without delay; (2) T_{H_2O} = 110 °C, the as-pyrolyzed film is placed at 110 °C point, annealed for 1 min in dry and humid gas atmosphere, respectively, and then

pushed into the center of the furnace, as schematically shown in Figure 2-10 (b); (3) T_{H_2O} = 740 ºC, the film is pushed directly into the center of the furnace and water vapour is introduced immediately, the real temperature at this point is measured to be 740 ºC even if the set point was higher, due to the cooling effect from the sample and crucible when they were introduced in the furnace; (4) T_{H_2O} = 810 ºC, the film is pushed into the center of the furnace and wait until the temperature increases up to T_{growth} and introduce the water vapour immediately. All the temperatures used during the operation process were detected by a thermocouple. The exact heating stage and the corresponding heating ramp which are measured by thermocouple are presented in Figure 2-11 (a)-(c), respectively. After the heating stages, an annealing stage for a certain time (t_1) is followed for the YBCO crystallization and growth. In our present works, all the growth related to the conventional and flash heating processes are conducted in the furnaces "Leonidas" and "Flautista", respectively.

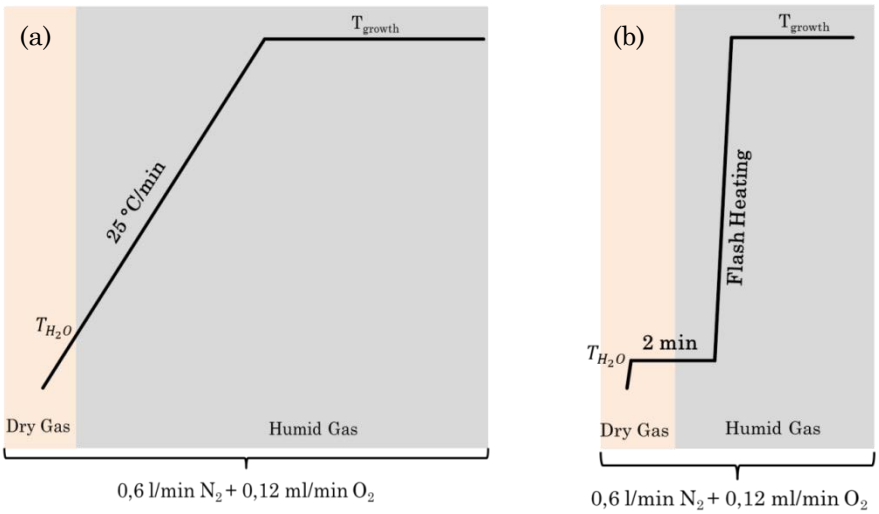

Figure 2-10 Schematic heating profile of (a) conventional mode and (b) flash heating mode.

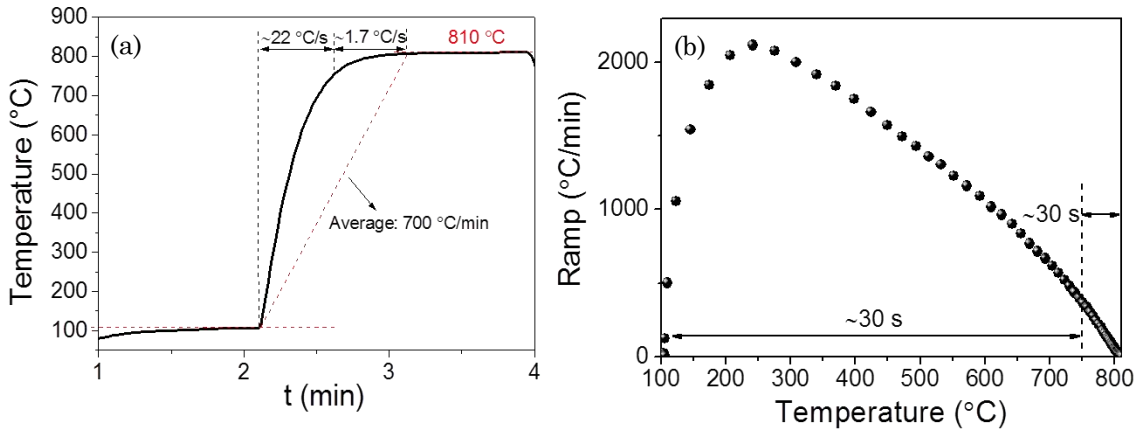

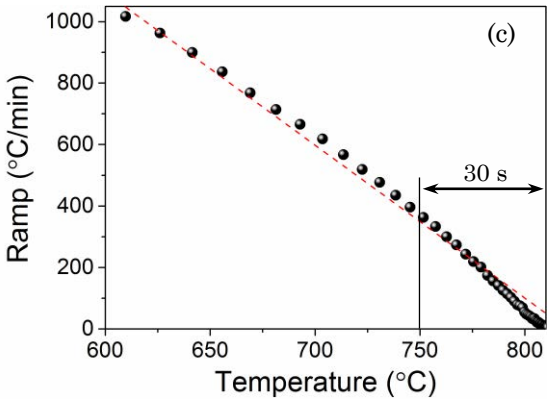

Figure 2-11: A realistic heating profile of flash heating stage of (a) temperature evolution with time, (b) heating ramp evolution with temperature and (c) heating ramp evolution in the temperature range of 600-810 ºC, where data is obtained via thermocouple following the exact sample route.

Subsequently, extra annealing for t_2 and then cooled down to 600 ºC with a ramp of 2.5 ºC/min is carried out in dry mixed gas atmosphere, for the purpose of further rearranging the formed single crystals such as zipping grain boundaries and healing mesostrain, etc. At 600 ºC the gas atmosphere is changed to dry oxygen (1 atm) with flow rate of 0.6 l/min in both furnaces, from where the oxygenation stage is initiated. The temperature decreases continuously down to 550 ºC with a ramp of 1.3 ºC/min followed by a annealing time of t_3, after which YBCO structural transformation from tetragonal to orthorhombic structure can be achieved. Finally, the films are cooled down to room temperature with a ramp of 2.5 ºC/min in the oxygen atmosphere.

In this study, diverse thermal treatment conditions, including different water opening temperature, growth temperature and annealing time are applied and will be illustrated in detail in the corresponding section.

2.2 Characterization techniques

2.2.1 Surface morphology characterization

2.2.1.1 Optical Microscopy (OM)

The surface quality of solid precursor films after pyrolysis is routinely examined using a Leica DM 1750 M optical microscope (5x and 10x objective) located at the ICMAB. An inhomogeneous as-pyrolyzed film (i.e. cracking, buckling or blistering, etc.) will not be subjected to further thermal processing for obtaining superconducting films, due to the fact that superconducting properties can be seriously affected.

2.2.1.2 Scanning Electron Microscopy (SEM)

The SEM is a type of electron microscope that uses a focused beam of high-energy electrons to generate a variety of signals at the surface of solid specimens. The signals that

derive from electron-specimen interactions disclose surface information about the sample, e.g., external morphology (texture), chemical composition, crystalline structure and orientation. Generally, a 2-dimentional image which displays spatial variations in these properties is generated though the data collection over a selected area of the surface of the specimen. Image magnification can be ranging from 10x to 100,000x in a scanning mode using conventional SEM techniques. Electrical conductibility is essential for the samples owing to the fact that they are studied with electrons.

Fundamental principle of SEM is briefly described below. The signals used by a SEM to produce an image result from the interaction between accelerated electron beam and atoms at various depths within the solid specimens which are placed in a vacuum chamber. Various types of signals are generated, including secondary electrons (SE), reflected or back-scattered electrons (BSE), characteristic X-rays and light (cathodoluminescence) (CL), absorbed current (specimen current) and transmitted electrons. Among them, SE and BSE are commonly used for imaging specimens. On one hand, SE, with lower energies (< 50 eV), which are most valuable for exhibiting surface morphology and topography information of samples. On the other hand, BSE consist of high-energy electrons (~50 KeV) originating in the incident electron beam which are reflected by elastic scattering interactions with specimen atoms, providing information about the distribution of different elements in the sample because its' signal intensity is strongly related to the atomic number (Z) of the specimen. The incident electron beam sweeps back and forth across the surface of the sample and these emitted signals (i.e. SE and BSE) are attracted by appropriate positively charged detectors for imaging. Image magnification can be up to 10 nm in diameter. Despite it is not as powerful as its TEM counterpart, the intense interactions that take place on the surface of the specimen provide a greater depth of view, higher-resolution and, ultimately, a more detailed surface picture. In addition, the number and energy of the characteristic X-rays emitted from a specimen can be measured by an energy dispersive spectrometer (EDS). Peaks at energy characteristic of the elements within that area can be identified and the concentration of the elements may be calculated. In the case of YBCO thin films, surface information (e.g. surface morphology, porosity, precipitate, grain size, grain orientation, particle distribution and composition) in this size range can be obtained.

In this work SEM images were made using a SEM Quanta 200 ESEM FEG located at ICMAB. An accelerating voltage around 10-15 kV was applied and we took the images at the following six magnifications: 500×, 2000×, 6000×, 10000×, 30000× and 60000×. No special sample preparation is required in our case since the YBCO films are electrically conducting once oxygenated. Investigation of bad conducting or insulating samples can be realized though either coating them with a thin conducting layer such as gold or conducting the operation at low vacuum.

2.2.1.3 Focused Ion Beam (FIB)

Focused Ion Beam (FIB) system is an imaging or milling instrument that uses a finely focused beam of gallium ions (Ga^+) which can be operated at either low beam current for imaging or high beam current for site specific sputtering or milling. Until recently, FIB cross-sectioning capacity has been widely used in material science field for site-specific analysis and selective ablation of materials. In the previous work of our group in ICMAB, FIB has been successfully applied in either SEM/TEM specimen preparation or direct nanopaterning of YBCO thin films.

In this study, the cross-sectional FIB images are taken using a dual-beam scanning electron microscopy/focused-ion-beam (SEM-FIB) system (Zeiss, Model 1560 XB) located at "Centre Nacional de Microelectrònica" (CNM). The operation is conducted in a CrossBeam operation mode, with which a real time monitoring of the ion beam milling at a defined area can be achieved by a simultaneous SEM observation (Figure 2-12). The cross-sectional images obtained via this mode provide various information of the inner part of specimen such as film porosity, phase segregation, film thickness, etc. which allows us to study the inner microstructure evolution of YBCO thin films. In our present work, the cross-sectional images are mainly used to study the densification process of CSD-based YBCO thin films during the thermal process.

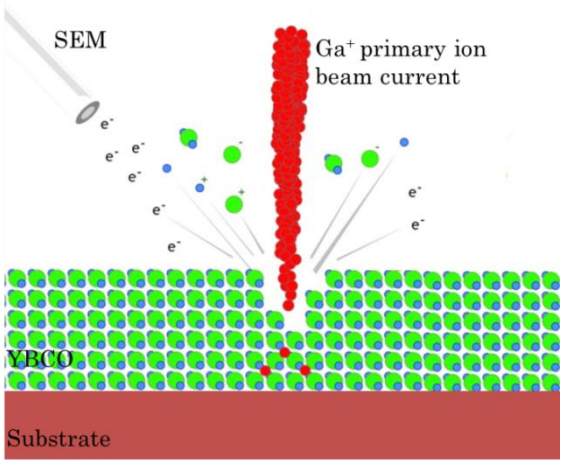

Figure 2-12: Schematic diagram of SEM-FIB operation mode, using which imaging (SEM) of the whole milling process (FIB) can be achieved.

2.2.1.4 Atomic Force Microscopy (AFM)

AFM is a versatile and powerful microscopy technology which provides high resolution and 3D information at atomic scale to the needs of scientists and engineers, with little sample preparation. Topography imaging is achievable on almost any type of surface, including polymers, ceramics, composites, glass, and biological samples. Besides, a wide array of material properties (e.g. friction, electrical forces, capacitance, magnetic forces,

conductivity, viscoelasticity, surface potential, and resistance) can be characterized quantitatively with advanced imaging modes.

The configuration of AFM will be simply illustrated below, as shown in Figure 2-13 (a). In AFM, a sharp tip (the probe) which is installed at the end of a cantilever is used to scan the specimen surface. When the tip approaches the surface, the surface-tip interactions can be detected indirectly though deflection of the cantilever according to Hooke's law. A laser beam is transmitted to and reflected from the back side of the cantilever for monitoring the cantilever deflections. Any cantilever deflection will cause slight changes in the direction of the reflected beam. The reflected laser beam is detected with a position sensitive detector (four quadrant photodiode), which allows to quantify the bending and torsion of the cantilever. The output of the photodiode provided to a computer for processing of the data, and then an accurate topographic map of the surface features is generated.

The operation of AFM can be ranked as one of the three basic modes, i.e. contact mode, tapping mode and noncontact mode, depending on the tip force and tip-specimen separation. Figure 2-13 (b) shows the tip-sample force-distance curve for AFM. At the rightmost side of the curve tip and sample are separated by large distance (>150 Å) with very weak atomic attraction beings, thus no tip deflection can be detected in this region. As the tip approach to the specimen surface to a distance ~50-150 Å, the attractive force strengthens to a maximum. This attractive regime of interatomic interaction is known as the “non-contact” regime. At this working region distance, the tip oscillates close or at its frequency of resonance, and forces are detected via measuring changes in amplitude, phase or frequency. Non-contact imaging generally provides low resolution and can also be hampered by the contaminant layer which can interfere with oscillation. When the tip-specimen distance decreases to a few angstroms (≤5Å), the interatomic repulsive force dominates and the atoms are in the “contact” regime. In contact AFM, electrostatic and/or surface tension forces from the adsorbed gas layer pull the scanning tip toward the surface. There are two approaches in the contact mode of imaging, i.e. maintain the tip in a constant force (to obtain height information) or height (to obtain force information) above the specimen surface. Because the tip is in hard contact with the surface, it can damage samples and distort image data. Therefore, contact mode imaging is heavily influenced by frictional and adhesive forces compared to non-contact or tapping mode. The tapping mode, also called intermittent contact, which is applied for images capturing in this thesis is developed as a method to achieve high resolution without inducing destructive frictional forces both in air and fluid. The cantilever oscillates at a constant frequency close to its resonance, and the tip is intermittently touching the surface of the sample. Consequently, lateral forces as well as issues associated with friction, adhesion, electrostatic forces and other difficulties are drastically overcome. With this technique, the imaging of very soft and fragile samples is realizable.

In this thesis, the AFM analysis was implemented with an Agilent 5100 AFM system equipped with silicone tips from Agilent Technologies located at ICMAB. Data acquisition was carried out in two different areas of each sample of 5 x 5 μm^2 in dimensions. The AFM data was processed with Mountains Map software from Digital Surf. Several topographic characteristics, such as the surface homogeneity, surface morphology and also the root-mean-square roughness of those samples were presented.

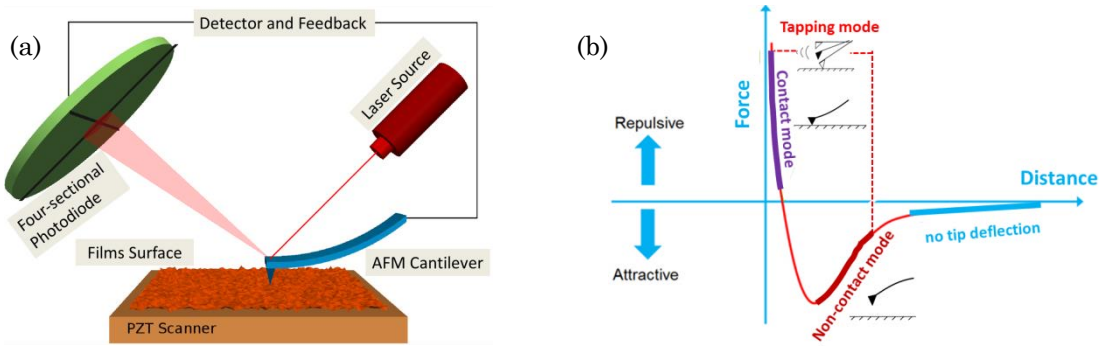

Figure 2-13: (a) the components in AFM system; (b) the operation mode of AFM tip and its corresponding interactions with the film surface.

2.2.1.5 Dynamic Light Scattering (DLS)

The DLS measurements of NP colloidal solutions were carried out by collaborators from the Inorganic Chemistry Department of Autonomous University of Barcelona (UAB).

The basic principle of DLS is schematically shown in Figure 2-14. The BMO nanoparticle colloidal solutions are illuminated by a laser beam and the fluctuations of the scattered light are detected at a certain scattering angle θ by a fast photon detector. Microscopically, the particles scatter the light and the information about their Brownian motion can be recorded. The nanoparticle size information can be obtained via analyzing the fluctuation of the scattered light. Therefore, the hydrodynamic diameter (d(H)) can be calculated by using the Stokes-Einstein Equation:

$$d(H) = \frac{k_B T}{6\pi\eta D} \qquad \text{Equation 2-2}$$

where k_B represents the Boltzmann-Konstant, T the temperature, η the viscosity and D is the translational diffusion coefficient. This method is valid for estimating nanoparticles with sphere shape without ligand surroundings.

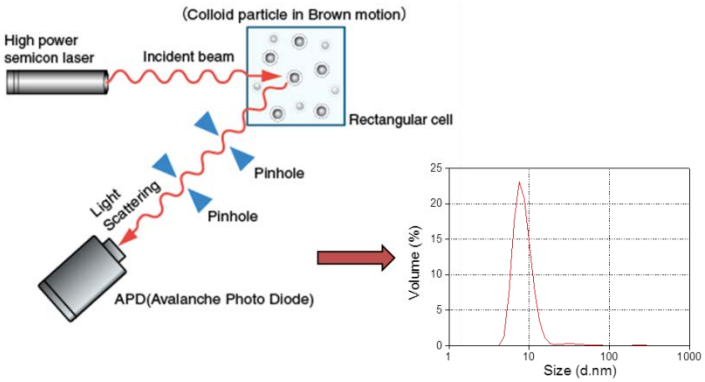

Figure 2-14: Schematic diagram of the DLS showing the basic principle.

In this work, the measurements were done with the Zetasizer Nanoseries Nano-ZS instrument (Malvern Instruments, UK) located at ICMAB, from which the particle size distribution of preformed BMO nanoparticles was estimated.

2.2.2 Microstructure characterization

2.2.2.1 X-ray diffraction

X-ray diffraction (XRD) is widely used to characterize the thickness, lattice parameters, strain, composition, texture and defect densities of YBCO thin films owing to its wavelength (e.g. 1.54 Å, Cu K_α radiation), non-destructive nature, high strain sensitivity, rapid analysis and representative results. X-rays are generated via bombardment of the accelerated electrons on a metal (typically Cu) within an evacuated tube and monochromatic x-rays are usually selected. When the monochromatic x-ray beam hits the specimen except for the absorption and other phenomena, the x-rays are mostly scattered by the electron cloud surrounding each atom of the crystal, generating a coherent X-ray scattering beam. The Bragg's law points out that constructive interference occurs between the scattered x-rays when the path difference AB ($n\lambda$) (Figure 2-15) is equivalent to $2d\sin\theta$, as follows:

$$2d_{hkl}\sin\theta = n\lambda \qquad \text{Equation 2-3}$$

where d_{hkl} is the interplanar spacing between the (hkl) family of planes, θ is the scattering angle, n is the order of reflection which is a positive integer and λ is the wavelength of incident wave. This is the basic of X-ray diffraction, on the basis of which the intensity and spatial distributions of the scattered X-rays form a specific diffraction pattern providing the "fingerprint" of certain crystals.

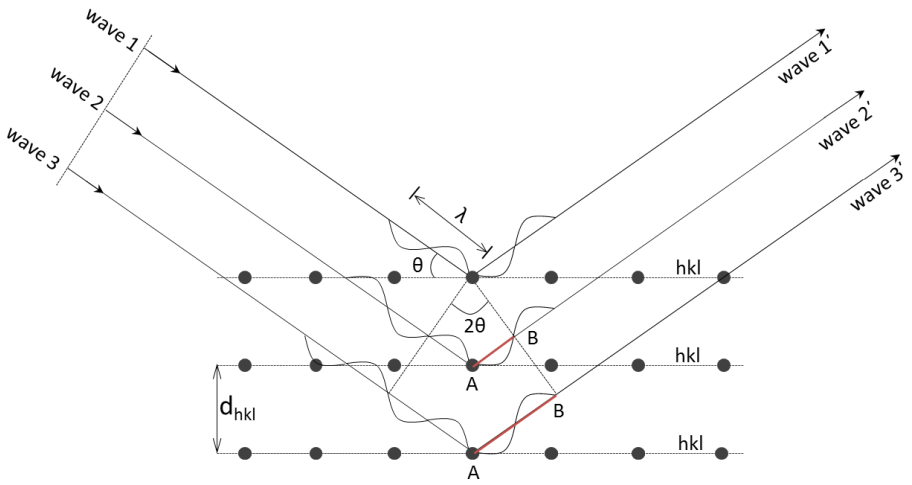

Figure 2-15: Schematic representation of X-ray diffraction from a set of atomic plane (hkl).

For real materials, atoms can be arranged orderly like a single crystal or disorderly in an amorphous state. Correspondingly, the scattered X-rays form specific diffraction patterns particular to the atomic arrangement of samples. Amorphous materials have short-range order only few atomic or molecular dimensions instead of long periodicity like crystalline materials, therefore, that the x-rays will be scattered randomly in a large 3D space leading to a large bump distributed in a wide angle or range (2θ). While, crystalline materials present different scattering and diffractive scenario. Figure 2-16 (a) and (b) display the diffraction from a single crystal and from a polycrystalline, respectively. In the case of single crystals, the diffracted x-rays distributed at discrete directions in a certain plane, while constructive interferences occur at certain positions each corresponding to a family of diffraction plane (Figure 2-16 (a)). In contrast, for polycrystalline materials on the condition that a large number of crystals oriented randomly in the space are fully covered by incident x-rays, the diffraction pattern appears as a series of diffraction cones, each of which corresponds to the diffraction from the same crystalline plane family in all the participating grains (see Figure 2-16 (b)). Generally, x-rays scattered from single crystal forming high intensity peaks with a narrow width. However, diffraction from polycrystal spreads in relative larger area, so the constructive interference of the scattered x-rays spreads among a wide range of 2θ in the form of XRD peaks with less intense and broad width. Therefore, materials with different atomic arrangement present various shapes of XRD pattern, as shown in Figure 2-16 (c).

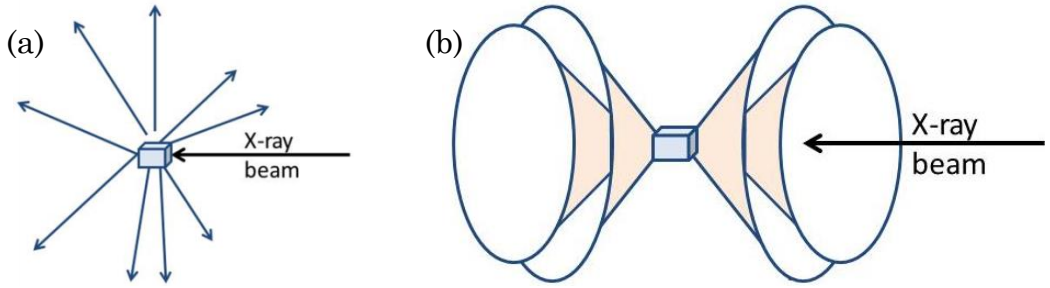

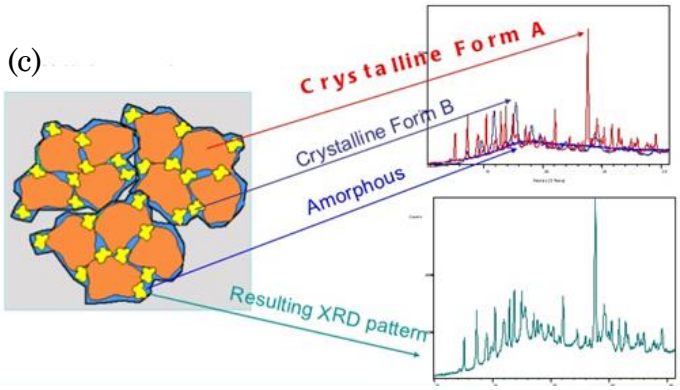

Figure 2-16: The patterns of diffracted X-rays from (a) a single crystal; (b) a polycrystalline specimen; (c) Contribution of crystalline and amorphous phases to an XRD pattern.

The XRD techniques have been widely applied in material science field, e.g. qualitative and quantitative analysis of phase composition, unit cell parameters calculation, Bravais lattice symmetry analysis, study of crystal texture, residual strain estimation, crystal structure determination, nano-scale crystallite calculation, etc. This technique is ideal for crystal characterization due to its non-destructive nature, high strain sensitivity, rapid analysis and representative results.

In this thesis, different types of structural analysis of YBCO thin films have been carried out by using three different diffractometers located at ICMAB, each of which can be operated in different mode, and detailed illustration will be presented in the following text.

Siemens D5000 diffractometer

The θ-2θ scan and the ω-scan of fully converted YBCO thin films have been mainly carried out using a Siemens D5000 diffractometer located at ICMAB, using a Cu K_α radiation with wavelength of $\lambda(K_{\alpha1})$ = 1.540560 Å and $\lambda(K_{\alpha2})$ = 1.544390 Å. Figure 2-17 presents the geometry of the conventional θ-2θ scan configuration, based on which this type of XRD diffractometer works. A point detector is confined within a diffractometer plane (principal plane) and the 2θ scan conducted along a detection circle. During the θ-2θ scanning process, the X-ray source remains motionless, while the scan ensured from a simultaneous rotation of sample (θ) and the detector (2θ). In the rocking curve (ω-scan) pattern, both X-ray tube and detector remain stationary and samples rotating along the diffractometer plane. This equipment has been mainly used for 3 types of measurements in this thesis, as follows,

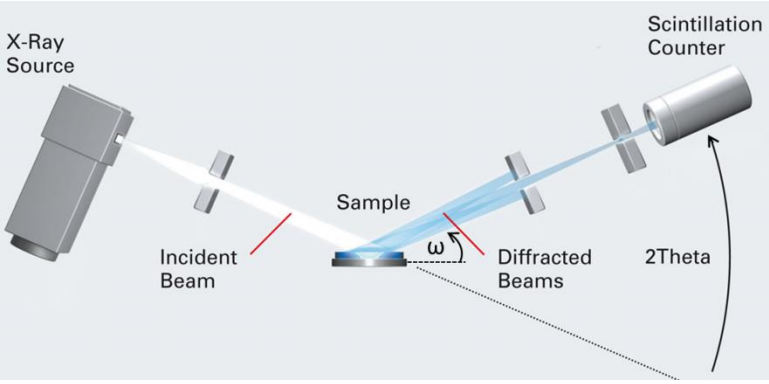

Figure 2-17: Geometry of the conventional θ-2θ scan configuration.

Rocking curve (ω-scan): A rocking curve is recorded by moving the diffractometer into a certain reflecting position (2θ angle) and then scans the shape of the reflection curve. This measurement is used to estimate the out-of-plane misorientation spread of fully converted YBCO thin films in our present work. The estimation is achieved by calculating the FWHM of the obtained rocking curve peak, which is proportional to the misorientation of the YBCO grains. Rocking curve measurements performed in this thesis are the (005) reflection of YBCO thin films located at 2θ = 38.5°, as typically shown in Figure 2-18 (a).

Nanostrain (ε) measurement: As illustrated in the "Introduction" chapter of this Thesis, the inhomogeneous strain (ε) can be determined by means of the Williamson-Hall (W-H) plots though the following equation,

$$\beta_w^2\cos^2\theta = \left(\frac{\lambda_{\alpha 1}}{L_\perp}\right) + 16\varepsilon^2\sin^2\theta \qquad \text{Equation 2-4}$$

, where β_W is the integrated breadth of the (00l) YBCO Bragg peaks after subtraction of the contribution from instrument, θ is the Bragg angle, $\lambda_{\alpha 1}$ = 1.54056 Å is the wavelength of the Cu K_α radiation, $L_\perp$ is the size of the coherent volume perpendicular to the scattering vector and ε is the inhomogeneous strain value.

Data acquisition for this measurement is based on XRD θ-2θ scan carried out in 4 separate 2θ ranges (5-15°, 24-45°, 50-70° and 80-100°), in order to avoid the peaks of substrates (LAO). The scan is performed with a step size of 0.02° and step time of 2s. The obtained (00l) YBCO peaks are fitted using "FullProf_Suite" software in "K_alpha Cu" mode, where the total β value (β_t) and the Bragg peak position (2θ) can be extracted. Afterwards, the β_W values can be obtained by subtracting the instrumental (β_i) values from the β_t, i.e. $\beta_W = \beta_t - \beta_i$. The β_i values were obtained by analyzing the spectrum of a LaB_6 as a reference sample. Finally, the ε can be extracted from the slope of the $\beta_w^2\cos^2\theta$-$\sin^2\theta$ plot, as shown in Figure 2-18 (b).

C-parameter calculation: This measurement is carried out using XRD θ-2θ scan within a 2θ range of 20°-120° using the step size of 0.01° and step time of 0.2s. The XRD data is then

fitted by using "FullProf Suite" software to obtain the precise 2θ positions of each (00l) reflection peaks of (00l) YBCO. Accordingly, the relation of lattice constant (a, b, c) and Miller indices (h, k, l) for each peaks in a orthorhombic structure can be written as follows (Equation 2-5),

$$\frac{1}{d^2} = \left(\frac{h}{a}\right)^2 + \left(\frac{k}{b}\right)^2 + \left(\frac{l}{c}\right)^2 \qquad \text{Equation 2-5}$$

Afterwards, we calculated the c-parameters of each diffraction planes for epitaxial YBCO films (h=k=0) though the following formula (Equation 2-6),

$$c = ld \qquad \text{Equation 2-6}$$

Subsequently, the Nelson-Riley function (Equation 2-7) [142, 143] was applied for each Bragg peaks, in order to eliminate some systematic errors [72] which can be effectively avoided at θ = 90°.

$$\frac{1}{2}\left(\frac{\cos^2\theta}{\sin\theta} + \frac{\cos^2\theta}{\theta}\right) \qquad \text{Equation 2-7}$$

Finally, a c-parameter vs Nelson-Riley function values scatter diagram for each (00l) YBCO Bragg peaks were plotted and linear fitted (Figure 2-18 (c)), where the desired c-parameter value was determined as the intercept of the fitting line (i.e. θ = 90°).

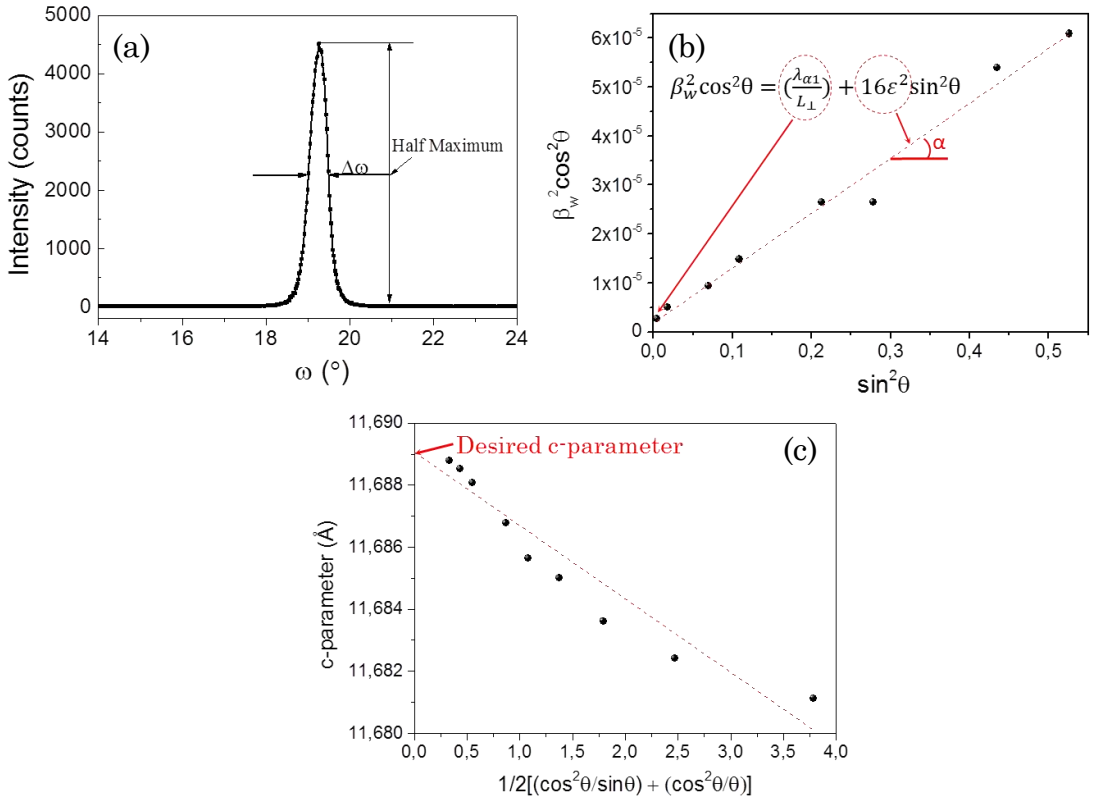

Figure 2-18: (a) Typical ω-scan of the (005) YBCO reflection at 2θ = 38.5°; (b) Typical W-H plot analysis for calculating the inhomogeneous strain in c-axis direction of epitaxially grown YBCO//LAO systems; (c) Typical c-parameter vs Nelson-Riley function for each (00l) YBCO reflection peak, where the desired c-parameter can be extracted from the intercept of the fitting line.

Two-dimensional x-ray diffraction: GADDS

GADDS (General Area Detector Diffraction System) operates on the same basic fundamental to the conventional X-ray measurement. It is a very advance X-ray diffraction technology, owing to installing a high performance two-dimensional (2D) detector and assisted by a series of 2D image processing and 2D diffraction pattern manipulation and interpretation, which ensures a 2D diffraction pattern contains abundant information about the atomic arrangement, microstructure and defects of a variety of materials. Therefore, widespread applications such as phase identification, texture measurement, stress measurement, percentage crystallinity, etc. have been developed based on this X-ray diffraction technique.

The sketched configuration of the full components of the GADDS system, including X-ray source, X-ray optics, goniometer and sample stage, sample alignment and monitor and a 2D area detector, is shown in Figure 2-19. The rotation and tilt angles in the GADDS is based on the same geometry of a conventional four-circle diffractometer, in which one circle (α) is used to tune the detector position and the other three circles (ω, ϕ and ψ) for adjusting sample orientations. The imaging process of GADDS is schematically shown in Figure 2-20 (a)-(c). The χ-2θ is fixed in a laboratory system $X_LY_LZ_L$, which is independence of the sample orientation in the goniometer. Importantly, the direction of the diffracted beam on the cone is represented by the χ angle, which is defined as the azimuthal angle from the $-Z_L$ direction with a right hand rotation axis to the $-Z_L$ direction; see Figure 2-20 (a). The x-ray diffraction cone can be intersected by the detector plane with the formation of the conic section, as shown in Figure 2-20 (b). The shape of the diffraction pattern is high dependent on the detector swing angle α and the detector distance D; see Figure 2-20 (c). The area detector frame is normally recorded as intensity values on a 1024 x 1024-pixel grid or a 512 x 512-pixel grid with a resolution in 2θ of ~0.03°. A GADDS software is used for the data analysis.

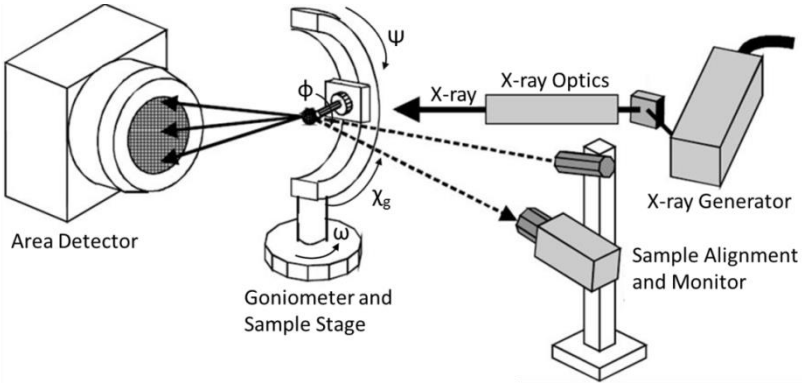

Figure 2-19: Configuration of the GADDS system, reproduced from [144].

In this thesis, the Bruker-AXS (model D8 Advance) GADDS diffractometer, the operation of which is based on a KFL Cu 2K (λ (CuK_α) = 1.541840 Å) X-ray tube and in a

power conditions of 40 KV and 40 mA, has been extensively applied for several measurement:

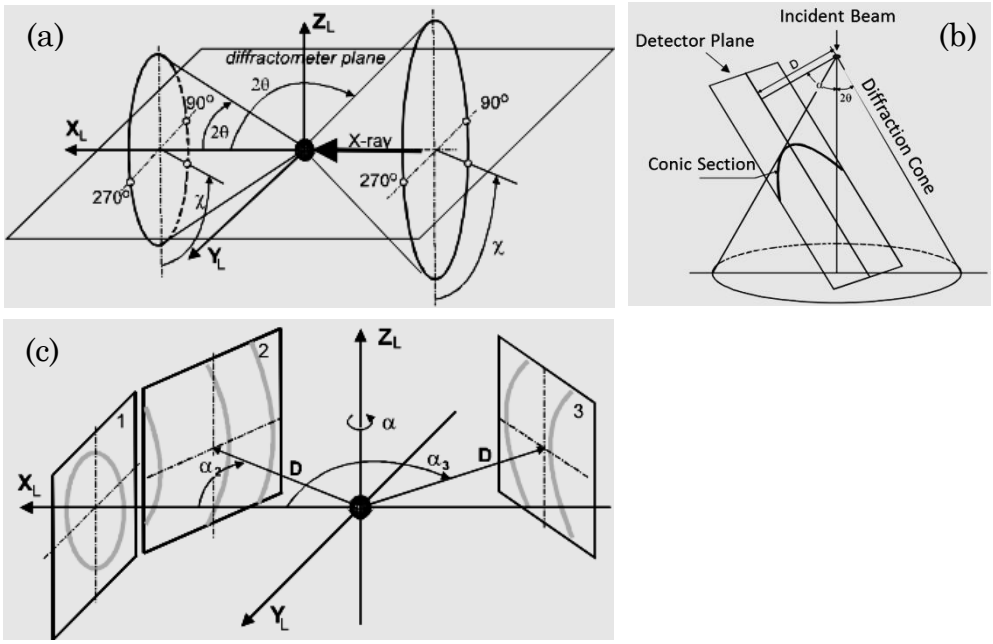

Figure 2-20: A geometric definition of diffraction rings in laboratory axes; (b) diffraction cone and the conic section with a 2D detector plane; (c) detector positions dependence with different imaging conditions.

Phase identification (Phase ID): Taking into consideration of the dimension of the detector, a 2θ window of 30° (i.e. 20°-50°) and Δχ window of 70° can be achieved simultaneously in a short data acquisition time without any kind of 2θ scan. For achieving this measurement in the case of YBCO thin films, the X-ray source and detector remain stationary, while the rotation of the sample along the ω direction will be the only motion. In the case of fully converted YBCO thin films, a short scanning time (~900 s) is routinely applied, while longer data collecting time and the avoidance of substrate reflections are needed in the case of as-pyrolyzed YBCO thin film. The 2D XRD frame can offer a quick overview of the crystallinity, composition and orientation information of a film. Phase composition and texture of films can by analyzed by the obtained χ-2θ frame, where finely grained polycrystalline, large grained polycrystalline and epitaxially grown films can be characterized by smooth and continuous ring, spotty and continuous ring and discrete spots, respectively.

Nanoparticle size assessment: The mean size of the ordered (crystalline) domains in the nano-scale range can be estimated by the Debye-Scherrer equation, as follows:

$$\tau = \frac{K\lambda}{\beta_s \cos\theta} \qquad \text{Equation 2-8}$$

where: τ is the mean size of the particles; K is a dimensionless shape factor, where a typical value of about 0.9 have been taken considering the spherical shape of CuO [28, 145]; λ is

the X-ray wavelength; β_s is the line broadening of FWHM of XRD peak (in radian), after subtracting the instrumental broadening contribution; θ is the Bragg angle (in degree).

However, there are several limitations for the application of this equation. First of all, the Debye-Scherrer equation is limited to nanoscale (1-100 nm) particles, giving the normal size of the corresponding crystal face. Secondly, various factors can contribute to the broadening of XRD diffraction peaks besides crystallite size, such as instrumental effects, inhomogeneous strain and some crystal imperfections (dislocations, stacking faults, chemical heterogeneities, etc.). Thirdly, the shape of XRD diffraction peak can be affected by the scanning speed. To obtain accurate size of nanodots, the total integral breath (β_t) values were subtracted by the corresponding instrumental (β_i) values which were obtained by analyzing the spectrum of a LaB_6 as a reference sample.

In-plane texture measurement: This measurement can be achieved by ϕ-scan, which are carried out at the appropriate tilt angle ($\chi = 45^o$) and diffraction angle (2θ) while the sample rotated along the azimuth (ϕ) angle, from where the in-plane texture quality can be estimated by the measurement of a given asymmetric reflection (e.g. YBCO (103)). Once the appropriate χ and 2θ are fixed, the sample rotated along ϕ direction, and GADDS images are the stored for step size (Δϕ) of 0.25° and scanning time of 25s. Typically, epitaxially grown YBCO films present of four peaks, 90° apart by crystal symmetry (Figure 2-21 (a)), denotes a unique in-plane orientation. Finally, the in-plane orientation distribution of YBCO crystallites can be evaluated by the mean value of FWHM of each peak, i.e. $\Delta\phi = (\Delta\phi_1 + \Delta\phi_2 + \Delta\phi_3 + \Delta\phi_4)/4$.

Pole figure measurement: This measurement enables the determination of the orientation relationship between different layers or phases in one crystallographic direction. In this thesis, this measurement was carried out at fixed $2\theta = 32^o$ and $\chi = 45^o$, which enabled the detection of both YBCO and substrate's crystal poles. In this selected 2θ-χ region, a series of ϕ-scans were carried out at every 1° with a step time of 20 s for each. Finally, 360 frames were obtained, which can be fast viewed by the "GADDSnew Vantec-500" software and analyzed using the Bruker "MULTEX AREA" software, as shown in Figure 2-21 (b).

Nanoparticle orientation: The GADDS system has been shown to be valid for the data analysis over the 2D frames to estimate the fraction of randomly oriented nanoparticles in the nanocomposites [3, 54]. This achievement enables the quantification of the random/epitaxial fraction of the nano-sized secondary phases (e.g. $BaZrO_3$ and $BaHfO_3$) within CSD-based YBCO matrix without further data refinement. With the calculation of the ratio of intensities of epitaxial and random contributions, it is possible to determine the random fraction of nanoparticles using the equation developed by A. Llordés [3]:

$$\frac{\nu_{random}}{\nu_{epitaxial}} = \frac{I_{random}}{I_{epitaxial}} = \frac{I_{ring}^{exp} \cdot \left(\frac{360}{\Delta\chi}\right) \cdot 4\pi}{8 \cdot I_{pole}^{exp}} \qquad \text{Equation 2-9}$$

, where I_{ring}^{exp} and I_{pole}^{exp} represent the experimental integrated intensity of the diffraction ring and diffraction pole after subtracting the corresponding background, respectively; $\Delta\chi$ is the integration range along the ring, which was typically taken as $\Delta\chi = 30^{o}$.

To do this, a θ-2θ scan is first performed to identify nanoparticle's orientation, i.e. the existence of randomly oriented or expitaxially oriented. In the case of the BHO nanoparticles, the X-ray source is placed at a fixed ω angle of ~15°, which corresponding to the BHO (110) diffraction ring with maximum intensity. The 2D detector is then centered at the $\chi = 45^{o}$ on this line, while ϕ angle is fixed and optimized in order to obtain the maximum intensity. Due to the low-volume, small size and finely dispersed feature of nanoparticles within YBCO matrix, an extended data collection, up to 1 h, is needed to ensure a reliable statistics in the intensity. Under these conditions, distinct diffracted intensities from random and epitaxial fractions can be better visualized for the following accurate quantification process, as shown in Figure 2-21 (c).

At this stage, it is important to calculate the total integral intensity of ring (I_{ring}^{total}), pole (I_{pole}^{total}) and the corresponding background (I_{ring}^{BC} and I_{pole}^{BC}), which was carried out using the "GADDS software". The integration of I_{pole}^{total} was performed in an area with $\Delta 2\theta = 1.5\text{-}2^{o}$ and $\Delta\chi = 10\text{-}20^{o}$ centered at $\chi = 45^{o}$ and $2\theta = 30.1^{o}$ (red square in Figure 2-21 (c)), while the background of this region was taken at the same Δ2θ, Δχ and 2θ position but at a different χ position beside taking into account that the I_{pole}^{total} is a sum of contribution from pole, ring and background. Subsequently, with the fixed 2θ and Δ2θ, we moved the integration area in χ direction with a range of $\Delta\chi = 30^{o}$ and integrated the I_{ring}^{total}, see pink ring area in Figure 2-21 (c), in the meantime, the I_{ring}^{BC} was integrated with the same integration area from different 2θ positions around the corresponding integration region. And then, the integral intensities of the random and epitaxial part were obtained by subtracting the corresponding intensity of background from the intensities of the ring and pole region, respectively. Finally, the obtained parameters were applied in the Equation 2-9.

Nanoparticle size estimation: The asymmetric 2D XRD frame for nanocomposite film (Figure 2-21 (c)) provides high diffraction intensity for both the epitaxial and random nanoparticles which enables us to get an estimation of nanoparticle size. To achieve this, the integration is carried out in a 2θ range of 27.5-31° and a χ range of 40-50°. Afterwards, the integrated peak is fitted and the calculation is carried out by using Debye-Scherrer equation (Equation 2-8).

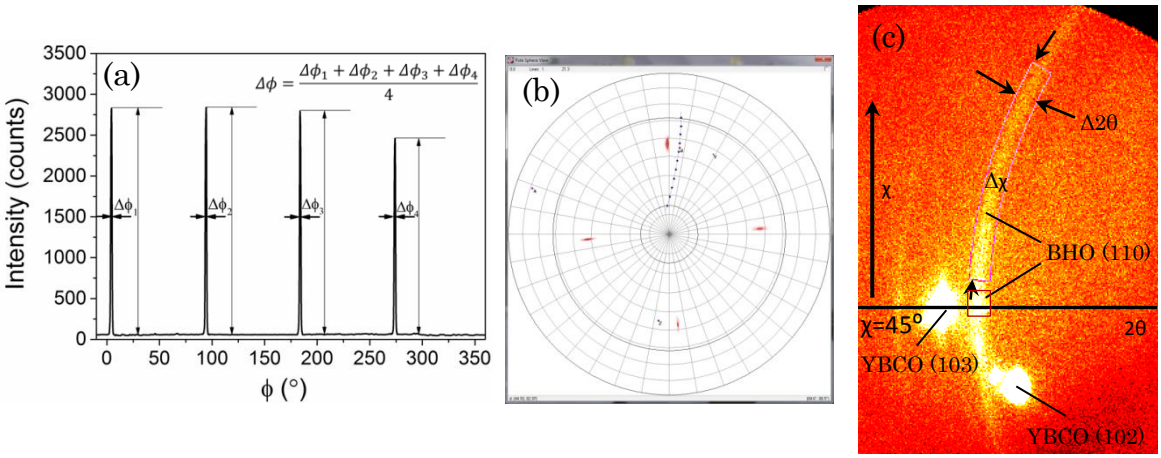

Figure 2-21 (a) Typical ϕ-scan of the YBCO (103) reflection performed in a YBCO//LAO system; (b) Typical pole figure of (104) reflection of YBCO; (c) XRD pattern of a YBCO-BHO pn-nanocomposite film measured at fixed ω and centered at the (110) Bragg reflection of BHO nanodots.

Bruker-AXS, model A25 D8 Discover

A recently acquired Bruker-AXS (model A25 D8 Discover) x-ray diffractometer equipped with KFL CU 2K ($\lambda(CuK_\alpha)$ = 1.5406 Å) X-ray tube and LinxEye XE-T detector (High-Resolution Position Sensitive Detector with Energy Resolution) was used to carry out high-resolution XRD (HRXRD) θ-2θ scans and direct in-plane measurements.

θ-2θ measurements: The experimental setup of the incoming beam contains a Göbel Mirror, a Ge(220) ACC2 monochromator and a divergence slit (0.6mm-1.2mm) allowing to realize measurements with a high resolution and a low degree of divergency. The x-ray source is being operated in line-focus to ensure the highest illumination area. For thin-films that exhibit a preferential growth direction, θ-2θ scans provide information along one specific family of lattice planes ((00l) direction for YBCO). Out-of-plane lattice parameters and local deviations of strain can be probed. In addition, random phases such as impurities and misoriented YBCO grains can be identified and estimated in their amount due to relative intensity comparison. Data acquisition for fully converted, epitaxial YBCO thin films is routinely performed in the range of 20-80° with a step size of 0.02° and a step time of 2 s. Conclusions on phase composition are based on the XRD-PDF database of YBCO (ICDD 04-002-2970), as well as secondary phases such as Y_2O_3 (ICDD #41-1105), $Y_2Cu_2O_5$ (ICDD #33-0511), BaF_2 (ICDD 00-004-0452), etc.

Direct in-plane measurement: The purpose of this measurement is to probe the information of planes perpendicular to the sample surface excluding any Qz contributions [146]. The diffractometer arms perform the same movement as in the θ-2θ configuration while the sample is rotated 90° in χ (Figure 2-22 (a)). The incident x-ray beam is set to enter the surface at very low grazing incidence angles [147, 148]. As the angle is chosen smaller than the critical angle for total external reflection (typically 0.05-1.5° [149], due to the x-ray refractive index being smaller than 1) a part of the beam forms an evanescent x-ray wave

penetrating the sample and scattering from crystal planes perpendicular to the surface. The crystallographic directions that can be accessed in that way are schematically illustrated in Figure 2-22 (b).

As the sample surface is rotated to $\chi = 90^{o}$, the source has to be operated in point-focus geometry allowing to maximize the intensity in this geometry. A two-axis goniometer, also referred to as "Tilt Stage", is mounted to ensure a precise adjustment of each individual in-plane [HK0] reflection (shown in Figure 2-22 (b)). Data is collected with a step size of 0.02^{o}. The time per step is individually adjusted to enhance the signal-to-noise ratio. Exemplary direct in-plane measurements of the (010)/(100), (020)/(200), (130)/(310) reflections of a twinned YBCO sample are presented in Figure 2-23. The data was fitted with Gaussian functions to extract the exact peak positions.

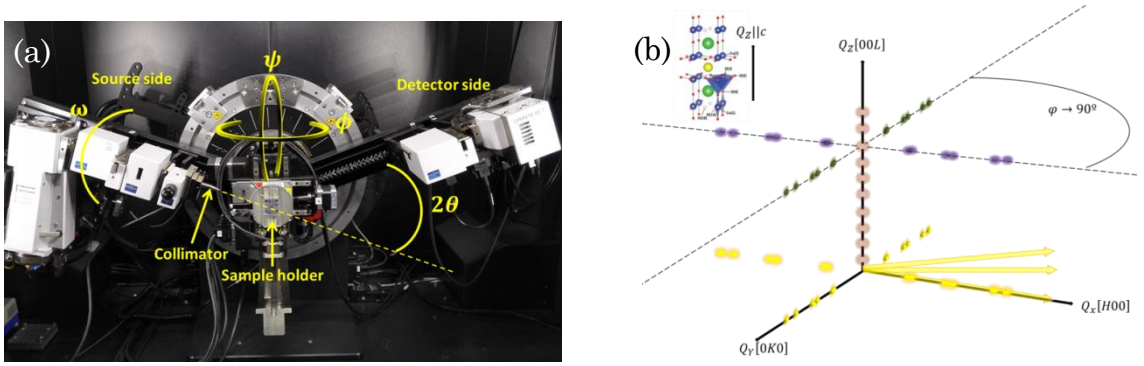

Figure 2-22: (a) Reciprocal space representation of epitaxial YBCO along specific directions. Reciprocal space points with in-plane component split due to different twin domains of YBCO. Direct in-plane direction represented by yellow points (lattice planes along [0K0], [H00] and [HK0]) (b) Experimental setup to access the direct-in-plane geometry: Sample tilt-stage rotated to $\chi = 90^{o}$

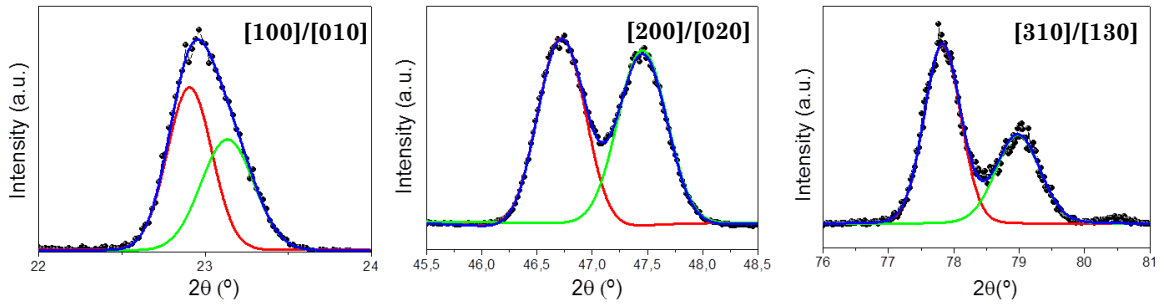

Figure 2-23: HRXRD direct in-plane measurements of different crystallographic directions of a twinned YBCO thin film.

All aforementioned peak positions are considered for a least-square fitting of the orthorhombic lattice spacing (Equation 2-10). In that way, the a and b lattice parameter can be obtained. Considering different [HK0] reflections and comparing only samples grown on LAO substrates allows to increase the accuracy of the lattice parameter determination.

$$\frac{1}{d^2} = \left(\frac{h}{a}\right)^2 + \left(\frac{k}{b}\right)^2 \qquad \text{Equation 2-10}$$

2.2.2.2 Scanning Transmission Electron Microscopy (STEM)

The imaging of TEM follows a similar fundamental to the optimal microscope except, rather than a beam of light, the TEM use a highly coherent beam of electrons that can transmit through an ultrathin specimen (< 100 nm) to form an image with high resolution owing to the smaller de Broglie wavelength of electrons. The operation scheme of a TEM is shown in Figure 2-24. The electron gun is the electron source that generates collimated and hairline electron beam with defined kinetic energy. The primary electron beam is focused or defocused into constant focal distance by a series of condenser lens as required and several apertures are also used to collimate the beam. The focused electron beam then travels though the specimen into an imaging or a diffraction pattern. The transmitted beam then traverses a series of lens and ultimately reaches a fluorescent screen and the final TEM image is obtained. All the operations of TEM are carried out in high vacuum environment in order to reduce as much as possible undesired electron scattering while travelling and avoid sample contamination.

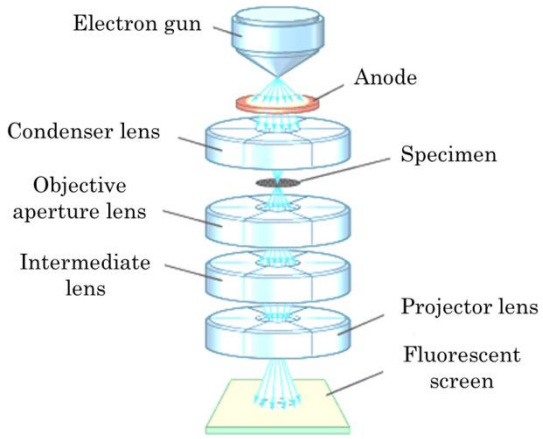

Figure 2-24: Operation scheme of Transmission Electron Microscope.

In fact, the previous work in our group [8] has proved that the most efficient way to visualize the internal structural information (defects, atomic arrangement, etc.) of the CSD-based YBCO is using an aberration corrected scanning TEM (STEM) in a high angle annular dark field image (HAADF) imaging mode. In HAADF STEM, the contrast ensures from a high angle scattering strength, giving rise to the so called Z-contrast imaging, which is ideal for describing and identifying structural defects in a highly distorted Y123 matrix. Moreover, in addition to the HAADF imaging, additional information can be gathered using the so called low angle annular dark field (LAADF) imaging.

In this thesis, the STEM images were taken by experts of our group. Two types of TEM equipment were used in our present work to meet the resolution required for

microstructural analysis. The cross-sectional TEM images and EELS analysis presented in this work were mainly obtained by a FEI Tecnai F20 S/TEM placed at "Catalan Institute of Nanoscience and Nanotechnology" (ICN2). Additionally, some High-Resolution STEM (HAADF and LAADF) micrographs were obtained in a Low-base FEI Titan (60–300 kV) operated at 200 KeV and equipped with a third order probe-aberration corrector, a monochromator and an X-field emission gun (FEG) located at Zaragoza in the "Advanced Microscopy Laboratory (LMA)". All the specimens in this work have been prepared by the traditional mechanical polishing method and followed by argon milling [8, 33]. Microstructural analyses were realized via a direct electron imaging on the cross section of the cut YBCO thin films. The cross-sectional images provide us information about film homogeneity, film thickness, nanoparticles (shape, size, distribution, orientation, etc.) and microstructural characteristics of YBCO matrix (nanoscale structural defects and their dimension, density, distribution, etc.).

Moreover, the morphological features of $BaMO_3$ (M = Zr, Hf) nanoparticles were characterized by a High-Resolution Transmission Electron Microscopy (HRTEM), which located at UAB and equipped a 200 kV JEOL 2011 TEM with a resolution point of 1.8 Å at 200 kV.

2.2.3 Superconducting properties characterization

2.2.3.1 Superconducting Quantum Interference Device (SQUID)

The SQUID is a very sensitive magnetometer can be used to measure the magnetic moment of YBCO thin films at different temperature and magnetic field in a non-destructive way. The magnetometer used in our present work allows DC measurement of magnetic moments, consists of a SQUID detection system and a precise temperature controller, as well as a superconducting coil which is able to provide a very uniform magnetic field up to 7 T. A group of pick-up coils constitute the pick-up detection system that located within the superconducting coils. In all our present cases, epitaxially grown YBCO films are placed with the c-axis parallel to the external magnetic field. The film is then moved along the pick-up coil, during which an electrical current proportional to the magnetic flux variation is induced on it. This will cause a variation in the enclosed magnetic flux, leading to a change in the measured output voltage which presents proportional relation with the magnetic moment of the film after a correct calibration of the system. This system provides a magnetic moment measurement with a resolution as high as 10^{-9} Am^2 (10^{-6} emu) within a temperature range between 1.8 K and room temperature ensured from a liquid helium refrigeration.

In this thesis, superconducting properties of YBCO films were mainly measured using a Quantum Design's Magnetic Property Measurement System MPMS XL-7T located at

ICMAB. Superconducting performances of YBCO films such as T_c, $J_c(T)$, and $J_c(H)$ were determined from the DC measurements of magnetic moment performed with the SQUID. Details about the determination of the superconducting properties from the measured magnetic moment are shown in Figure 2-25 and also in the following text. More extensive details in the magnetization measurement via SQUID and its derived applications can be found in refs [72, 150].

T_c and ΔT_c: The critical temperature (T_c) and superconducting transition width (ΔT_c) of YBCO thin films are determined from a magnetization vs temperature (m(T)) measurement conducted at H_a = 2 Oe. To achieve this measurement, the film is cooled down to 10 K under Zero Field Cooled (ZFC) condition. Subsequently, a weak magnetic field (~2 Oe) is applied to maintain the film in Meissner state. And then, the temperature increases continuously in this weak magnetic field until 95 K, where the film is in the normal state. Figure 2-25 (a) shows a typical m(T) curve obtained from SQUID measurement in a constant weak magnetic field of 2 Oe. The onset T_c is the transition point that from the superconducting state to the normal state (m = 0 emu), as indicated in the plot. In this work, all the T_c values correspond to the onset values. Moreover, ΔT_c is defined as $\Delta T_c = T_c^{onset} - T_c^{0.9}$, see the indication in the Figure 2-25 (a). Generally, we normalize the magnetic moment by the m_0, which makes the determination of the parameters (i.e. T_c and ΔT_c) conspicuous.

Self-field $J_c(T)$: In order to calculate the critical current ($J_c(T)$) at certain temperatures, a m(T) curve measured at ZFC condition is needed. To achieve this, the specimen is placed in the SQUID with H//c and cooled down to 5K at ZFC condition. After that, a magnetic field with intensity of 3T is applied and then decrease to 0 T in order to achieve a remanence state of the films, i.e. the film full of trapped vortex. Finally, the temperature increase from 5 K to 95 K and the magnetization data at different temperature is collected. Figure 2-25 (b) exhibits a typical measurement of the temperature dependence of the magnetic moment obtained in ZFC for a 250 nm YBCO thin film.

The J_c can be obtained by applying the Bean model [151]

$$J_c = \frac{3M}{R} = \frac{3m}{\pi t R^3} \qquad \text{Equation 2-11}$$

, where M is the magnetization value, R is the radius of the film, m is the obtained magnetic moment and t is the thickness of the film. In our case, the value R is treated as 2.57 mm due to the homogeneity of the CSD-based YBCO thin film grown on a 5 x 5 mm^2 substrate deposited by spin coating.

$J_c(H)$: The investigation of the J_c dependence of magnetic field is based on the measurement of m(T) plot at a certain temperature. To carry out this measurement, the film is cooled down to the temperature in the ZFC condition. And then, the magnetic field is increased up to certain intensity (H_M) and decreased to zero under isothermal conditions,

during which the magnetic moment with negative and positive values are collected, respectively. Figure 2-25 (c) displays a typical magnetic field (H//c) dependence of magnetic moment measured at 5K for a 250 nm pristine YBCO film. The J_c values at different magnetic field are calculated by the equation:

$$J_c = \frac{3(m_p - m_n)}{2\pi t R^3} \qquad \text{Equation 2-12}$$

, where m_p and m_n represent positive and negative values of magnetic moment, respectively.

J_c(T) under applied magnetic field: To determine the J_c(T) under applied magnetic field, m(T) curves are measured under the magnetic field in H//c configuration. The films are cooled to 5K under the ZFC condition, and then magnetic field is increased up to the required values, subsequently, the temperature is increased until 95 K measuring m(T) values. Finally, the J_c(T) values are calculated by using Equation 2-11.

Based on the J_c(T) plot, the discrimination of weak and strong APCs contribution can be achieved according, on the one hand, to the weak collective pinning model [87, 91, 92] which describes the behavior of defects leading to a fast decay of J_c(T):

$$J_c^{wk}(T) = J_c^{wk}(0)\exp(-T/T_0) \qquad \text{Equation 2-13}$$

where $J_c^{wk}(0)$ is the weak pinning controbution at 0 K and T_0 is associated with the characteristic vortex pinning energy of weak defects.

One the other hand, the strong pinning contribution can be extracted by the following expression [87, 91, 93]:

$$J_c^{str}(T) = J_c^{str}(0)\exp[-3(T/T^*)^2] \qquad \text{Equation 2-14}$$

where $J_c^{str}(0)$ is the strong pinning contribution at 0 K and T* is the corresponding characteristic vortex pinning energy of strong pinning defects. Figure 2-25 (d) displays typical $J_c^{wk}(T)$ and $J_c^{str}(T)$ plots fitted from a J_c(T) plot using the Equation 2-13 and the Equation 2-14 for a TFA-YBCO film.

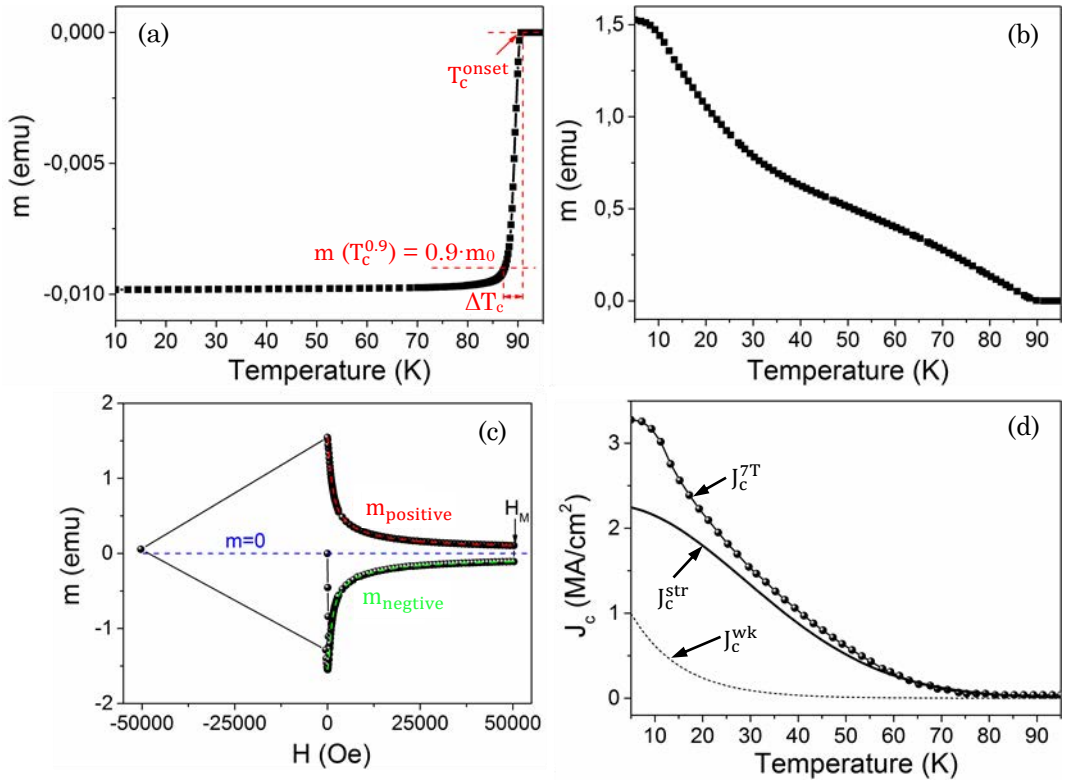

Figure 2-25: Initial data obtained from the SQUID measurement for a 250 nm pristine YBCO film of (a) temperature dependence of magnetic moment measured at low field; (b) remanent magnetization as a function of the temperature measured at Zero Field Cooled (ZFC) condition; (c) magnetic moment as a function of magnetic field measured at 5K; (d) temperature dependence of J_c^{wk} (dashed line) and J_c^{str} (solid line) fitted from the $J_c^{7T}(T)$ plot (scatter + line) using Equation 2-13 and Equation 2-14 for a typical TFA-YBCO film.

3. Nucleation, Microstructure and Superconducting Properties of YBCO Films Grown from Flash Heating Process

Motivation

Obtaining high quality biaxially textured YBCO coated conductors (CCs) with high performance by metal-organic decomposition (MOD) using trifluoroacetate (TFA) has attracted tremendous interest for both achieving a cost-effective production of superconducting tapes and promoting its large scale power applications [19, 53, 152, 153]. The continuous reel-to-reel production of long-length CC tapes is now a well-established technique owing to its advantages of no limitation of length, continuous production and low equipment investment [19, 27, 154]. It is essential then to develop a fabrication route in laboratory scale adapt to the industrial production of long tapes, and study the relevant processing parameters and their cross-linking.

In the previous study in Suman group at ICMAB, a series of intermediate processing steps have been optimized, including TFA solution preparation and deposition [23], metal-organic pyrolysis at low thermal temperature [29, 30], intermediate phase evolution into the final YBCO film at high thermal temperature [28, 32, 37, 46, 53] and the transformation process of the structure from the tetragonal to the orthorhombic phase via oxygenation [12]. Especially, the high temperature phase transition processes, which consist of intermediate phase evolution, nucleation and the following growth process, are complex thermodynamic, kinetic and crystal-chemical processes and their interplay into the final YBCO films. Moreover, the influence of processing parameters such as temperature, gas flow, water partial pressure, total pressure oxygen pressure on the final YBCO microstructure and superconducting properties have been reported in previous publication [37, 38, 46, 53, 155]. However, transferring the optimized processing parameters to the long-length or large-scale CCs fabrication systems such as continuous reel-to-reel and batch type processing is not a straightforward task. There are still some crucial parameters, in particularly the ones related to the reel-to-reel CCs production which remain controversial and poorly understood in some aspects.

In the continuous reel-to-reel CCs production system, the CCs undergo a different thermal history compared with lab-scale experimental conditions. Firstly, the transportation process of CCs tapes undergoes a flash heating process to the YBCO nucleation and growth temperature [27]. Similar heating process are recently reported by P.

Cayado et al. [156] who were able to successfully avoid multiple nucleation events though a fast heating to the c-axis oriented grains preferred supersaturation conditions. Furthermore, the water introduction time is also an essential factor which should be taken into consideration owing to the fast compaction feature of YBCO during the growth process [70]. Additionally, achieving low-temperature growth of YBCO thin films with promising microstructural quality and superconducting performance is also a pivotal factor for realizing a cost-effective production of YBCO CCs. With the aim to achieve optimal YBCO CCs processing conditions related to the flash heating growth process, in this chapter, we focus our concentration on the investigation of the influence of water vapor introduction time and growth temperature on the microstructure and superconducting performance of YBCO thin films. Besides, a detailed study on the YBCO intermediate transition phenomena (intermediate phase evolution, growth kinetics and microstructure evolution) that occur during the flash heating process is also carried out in the present work.

In the first section, a detailed discussion of the intermediate phase evolution, growth kinetic and microstructure evolution during the flash heating growth process is presented. To do this, a series of quench studies have been carried out at different thermal conditions (i.e. gas humidity, growth temperature and annealing time). The intermediate phase evolution of YBCO films at different thermal stages, both qualitatively and quantitatively, have been carried out by using X-ray diffraction. Then, a detailed analysis of the scanning electron microscope (SEM) and focused-ion-beam (FIB) images discloses the microstructural characteristic (e.g. inner or open porosity, intermediate phase segregation) of the quenched films. This work is of great importance because our present knowledge of intermediate transformation process can be extended to a wider range of growth conditions and thus provides us guidance for the optimization of YBCO growth conditions and explain the phenomena appearing during the flash heating growth process.

In the second section, we investigate the influence of a very important processing parameter which is usually not much treated as the main factor for determining the film microstructure but should be finely controlled in the CCs industrial productions: the water supply time. For the purpose of obtaining the optimal water open time, we conduct a series of YBCO growth experiences at a fixed growth temperature (810 °C) and the normal water pressure ($P(H_2O)$ = 23 mbar) but with a series of water supply times. The structural characteristics, such as phase composition, texture quality, surface morphology and microstructure of fully converted YBCO thin films grown from different gas procedures are examined by X-ray diffraction, SEM and TEM, respectively. We also present an explanation for these structural phenomena, on the basis of our present understanding of the microstructure evolution, nucleation and growth mechanisms of YBCO thin film. Then, the superconducting properties in self-field and in-field are evaluated via SQUID measurement conducted at 5K and 77K.

In the third section, a full series of experimental studies of YBCO film growth are carried out in a wide temperature window (730 ºC to 840 ºC) based on the optimal processing conditions and the flash heating growth process, in order to realize the low-temperature growth for CCs. This work is of tremendous importance for achieving a cost-effective fabrication of YBCO coated conductors from the energy consumption point of view. Additionally, the film grown from the flash heating process present high density of stacking faults homogeneously distributed in the YBCO matrix, which are proposed to be effective for improving the vortex pinning properties.

Finally, we summarize the main conclusions of the investigations about the flash heating growth process presented in all the sections of this chapter.

3.1 Phase and morphology evolution in YBCO thin films grown under flash heating process

As it has been detailed illustrated in the Introduction (section 1.2.1.3), the formation of epitaxial YBCO thin films from TFA precursor experience intricate intermediate phase evolution (such as amorphous BYF, CuO, Y_2O_3, Ba-oxyfluoride, $Y_2Cu_2O_5$, $BaCuO_2$, etc.), c-axis oriented YBCO grains nucleation and growth of YBCO nuclei towards film surface during the conventional thermal annealing (CTA) process. These converting processes are strongly influenced by intricate thermodynamic and kinetic effects and ultimately of significant importance for determining the final microstructure and superconducting properties of YBCO films. Several processing parameters such as atmosphere, gas flow, growth temperature have been optimized in the previous works [29, 30, 32, 37, 38, 46, 53]. Although a deep understanding of the involved mechanisms and intermediate transformations related to the conventional heating (25 ºC/min) has been achieved in the previous work in Suman group, knowledge translation is not a straightforward work. In other words, growth parameters related to the intricate thermodynamic parameters and kinetic driving forces based on the flash heating growth process is remain poorly understood. Therefore, a new understanding of the formation trajectory and microstructure evolution of YBCO films based on the flash heating (~1200 ºC/min) process is of the essence of reel-reel continuous CCs production.

In order to figure out the chemical and microstructural evolution of TFA-YBCO films based on the flash heating process, we have conducted a series of quench experiments in different gas atmospheres with different annealing times at given temperatures. Starting from the standard solution, deposition and pyrolysis routes, the as-deposited YBCO solid precursor films are annealed at conditions (I)-(III) and then cooled down to room temperature in atmospheric environment; see the detailed thermal profiles in Figure 3-1. The flash heating process has been illustrated in details in section 2.1.2.4, while the

quenching process is carried out after annealing at selected temperatures for various annealing times. The gas flow in this study is 0.6 l/min N_2 + 0.12 ml/min O_2 with a total pressure of ~1 bar. Besides, for condition (II) and (III), humid gas flow with water partial pressure of ~23 mba, is introduced during the preheating stage at 110 °C. The quenched samples are named in the form of "(N)-t", where (N) and t denote the annealing condition and the annealing time at the maximum temperature, respectively.

The phase compositions and their texture are characterized with GADDS. The corresponding θ-2θ XRD patterns are obtained via integrating the area of the GADDS frames, in which a clearly marked phase composition and quantitative analysis of the selected phases can be achieved. Moreover, the mean size of CuO (-111), OF (111) and Y225 (211) nanoparticles was estimated according to the Debye-Scherrer formula by analyzing the corresponding Bragg peak in integrated XRD plots. Finally, microstructural features such as surface morphology and inner porosity evolution are studied by SEM in a planar view and in transversal cuts made by FIB, respectively.

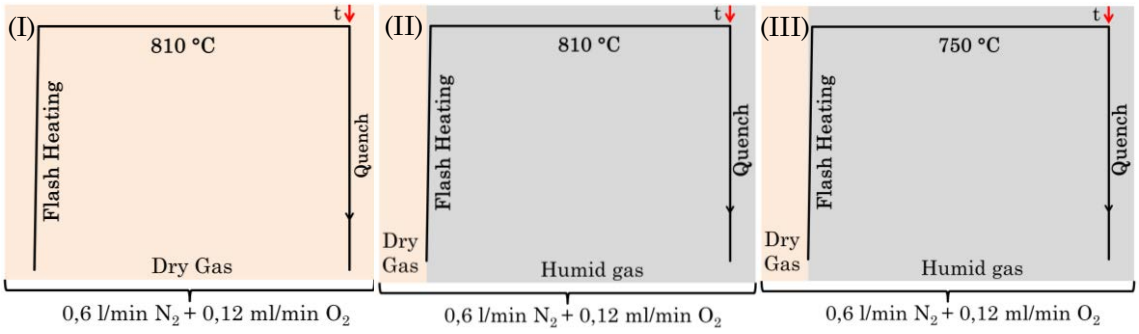

Figure 3-1: Schematic diagrams of quench study conducted at (I) 810 °C, dry gas; (II) 810 °C, humid gas; (III) 750 °C, humid gas. The as-pyrolyzed films are flash heated to the growth temperature, and then quickly pushed out from the tube and cool down to room temperature after annealing for certain times. The water vapor is introduced into the gas flow at 110 °C for condition (II) and (III).

3.1.1 Intermediate phase evolution and growth kinetics

Two dimensional XRD frames of YBCO thin films quenched from condition (I)-(III) after different annealing times are presented in Figure 3-2, Figure 3-3 and Figure 3-4, respectively. The corresponding integrated XRD patterns are shown in Figure 3-5 (a)-(c). Hence, a clear transformation of the chemical path of the TFA route to YBCO films during the flash heating growth process can be followed.

After flash heated to the corresponding growth temperatures, all the quenched YBCO films (i.e. (I)-0min, (II)-0min and (III)-0min) consist of $Ba_{1-x}Y_xF_{2+x}$ (BYF) and CuO phases; see Figure 3-2 (a), Figure 3-3 (a) and Figure 3-4 (a). The XRD patterns (Figure 3-5 (a)-(c)) only reveal sharp BYF peaks, as compared with the as-pyrolyzed film, indicating crystallization of BYF occurs during heating process. The results suggest, therefore, that no

intermediate phase transformation occurs during the heating process of our novel growth route, in contrast to what other authors have previously revealed for MOD YBCO thin films grown based on relative moderate heating rate processes (i.e. conventional heating process) [32, 157-159]. In this scenario, all the intermediate phase transformations are evidenced to occur at higher temperature, where supersaturation ($|\Delta\mu|$) for YBCO nucleation is reduced, thus promoting c-axis oriented YBCO grains nucleation [38, 46, 51].

Upon annealing for longer times, relevant changes are observed. Overall, the formation process of YBCO follows the chemical route which has been detailed illustrated in the section 1.2.1.3, whereas dominated by kinetic effects in our present conditions. The first trace of this change is the liberation of Y from BYF solid solutions with the formation of barium oxyfluoride (OF), where a shift of BYF Bragg peaks to smaller angle positions can be observed, for instance, BYF (111) peak moves from ~25.5˚ to ~25˚ [28, 32]. As shown in Figure 3-5 (a), a complete conversion of BYF to OF can be obtained after annealing for 3 min at condition (I). By contrast, this time is shortened to 1 min when films have been annealed in humid gas atmosphere (condition (II) and (III)), independently of the annealing temperature. This phenomenon is in accordance with the previous results which disclosed that the participation of water vapour in the intermediate phase evolution process facilitate the release of Y from the BYF solid solution [157].

Unfortunately, however, the present data do not enable us to evidence the point when Y_2O_3 appears, attributing either to the coincidence of the most intense Y_2O_3 (i.e. Y_2O_3 (222)) and BYF (002) peaks at $2\theta \approx 29^\circ$ or, to the appearance of Y_2O_3 phase in an amorphous state [32]. It has been proposed in the literature [28, 35, 160] that formation of Y225 phase from the reaction CuO + Y_2O_3 is probably a competing reaction towards the formation of YBCO [22].

For films grown under conditions (II) and (III), first traces of YBCO nucleation are seen after annealing during 3 min and 5 min, respectively, where the strongest YBCO peak appears at $2\theta \approx 38.5^\circ$ as a shoulder of CuO (111) peak. In the meantime, Y225 phase appears at 2θ positions of 31.4˚, 33.3˚ and 43.2˚ corresponding to (211) (204) and (006) reflections of this phase, respectively. Upon annealing, a gradual weakened XRD diffraction of OF and CuO peaks can be observed, together with the increase of YBCO and Y225 peaks. Finally, a fully converted film can be achieved for film (II)-11 min and (III)-17 min, respectively, even though some secondary phases (Y225, Y_2O_3 or $BaCuO_2$) remained at an impurity level. For films quenched from condition (I), however, neither randomly oriented Y225 phase nor YBCO nucleation trace can be observed in the present annealing time range, thus leaving a peak with high intensity corresponding to Y_2O_3 (400) phase in the XRD plot of (I)-5min.

On the other hand, we should notice that the randomly oriented Y225 phase disappears with the formation of the YBCO phase, i.e. it is only a transient phase. This observation agrees with the previous reports based on conventional heating rates (≤ 25 °C/min) [22, 32], which stated that YBCO also forms as a consequence of Y225 + $Ba(O, F)_2$ + CuO reaction. Nevertheless, the Y225 (006) peak (2θ = 43.6°) is unchanged during the annealing process. We propose that the origin of this phenomenon is the fast nucleation and growth of YBCO grains, due to which the interfacial secondary phases are buried and the atomic diffusion becomes sluggish. Taking into account the overall behavior of the Y225 phase in our quench study, our present observations support the previous assessment [28, 32] that the formation of Y225 phase performs as a competing path in the YBCO formation process. Moreover, a high kinetic induced rapid formation of YBCO thin films affects the chemical reaction and the atomic diffusion for further conversion of these secondary phases, thus being left as impurities trapped in the YBCO matrix. In this scenario, it is preferable to avoid its formation. On the other hand, however, further analysis of secondary phase induced YBCO structural imperfections will be presented hereinafter.

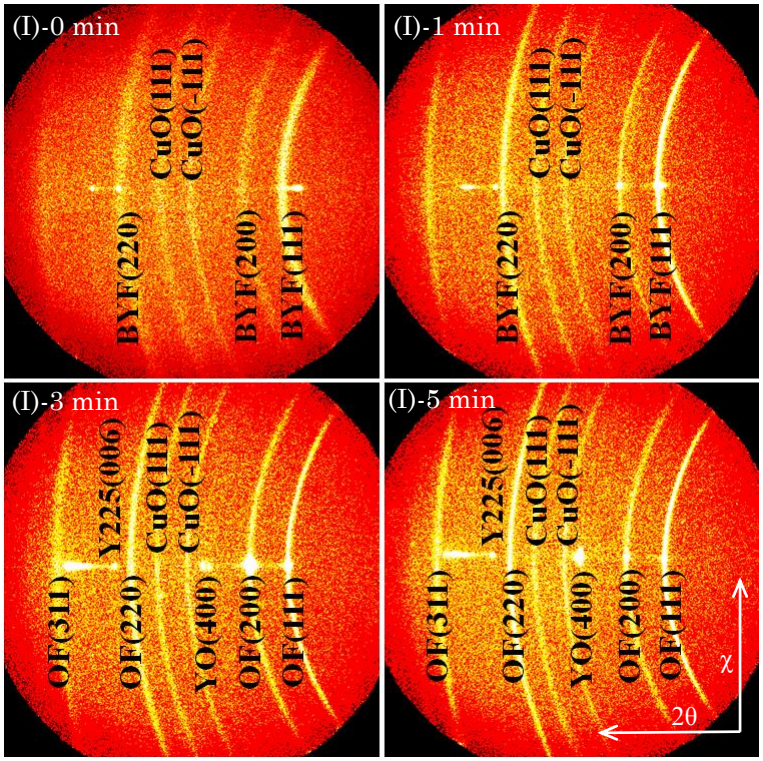

Figure 3-2: GADDS frames of pristine YBCO thin films quenched from 810 °C after annealing for 0, 1, 3 and 5 min, respectively. The processing conditions are illustrated in Figure 3-1 (I).

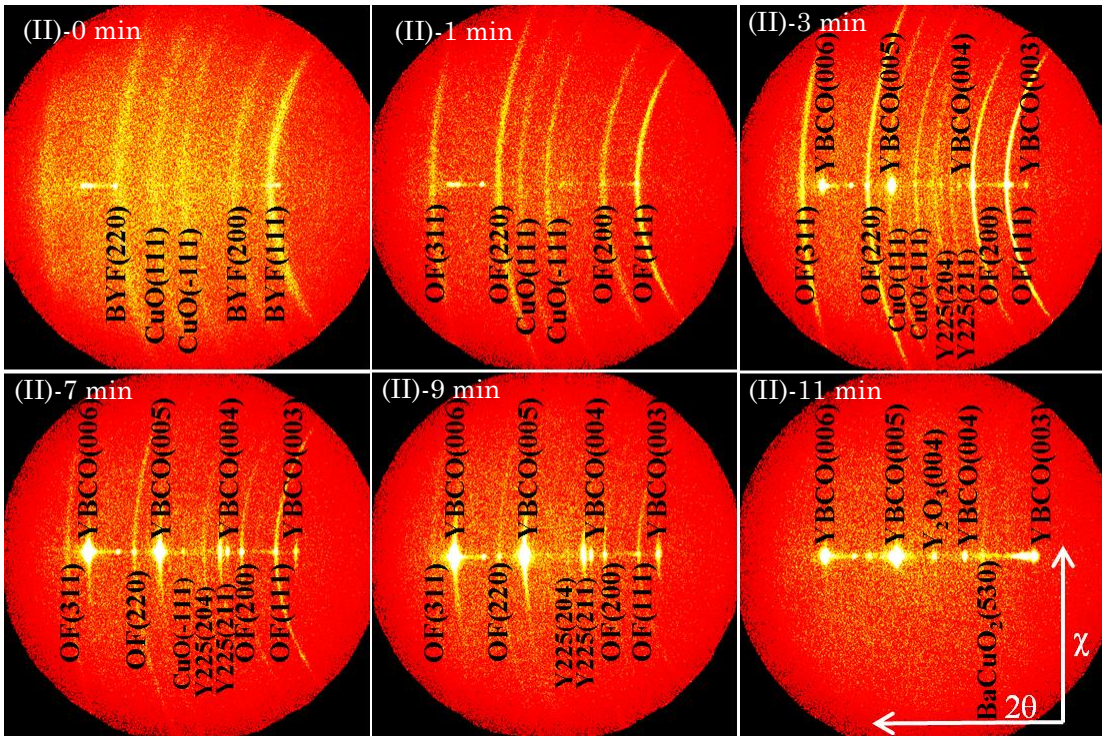

Figure 3-3: GADDS frames of pristine YBCO thin films quenched from 810 °C after annealing for 0, 1, 3, 7, 9 and 11 min, respectively. The thermal profile is schematically shown in Figure 3-1 (II).

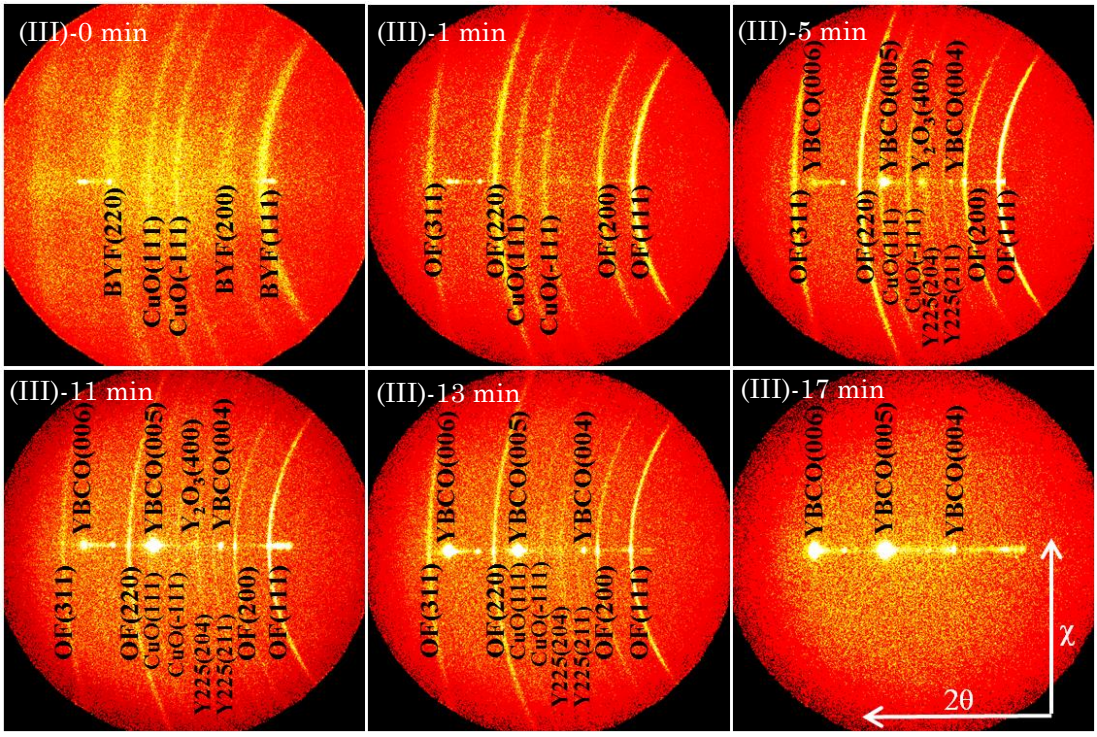

Figure 3-4: GADDS frames of pristine YBCO thin films quenched from 750 °C after annealing for 0, 1, 5, 11, 13 and 17 min, respectively. The thermal process is demonstrated in Figure 3-1 (III).

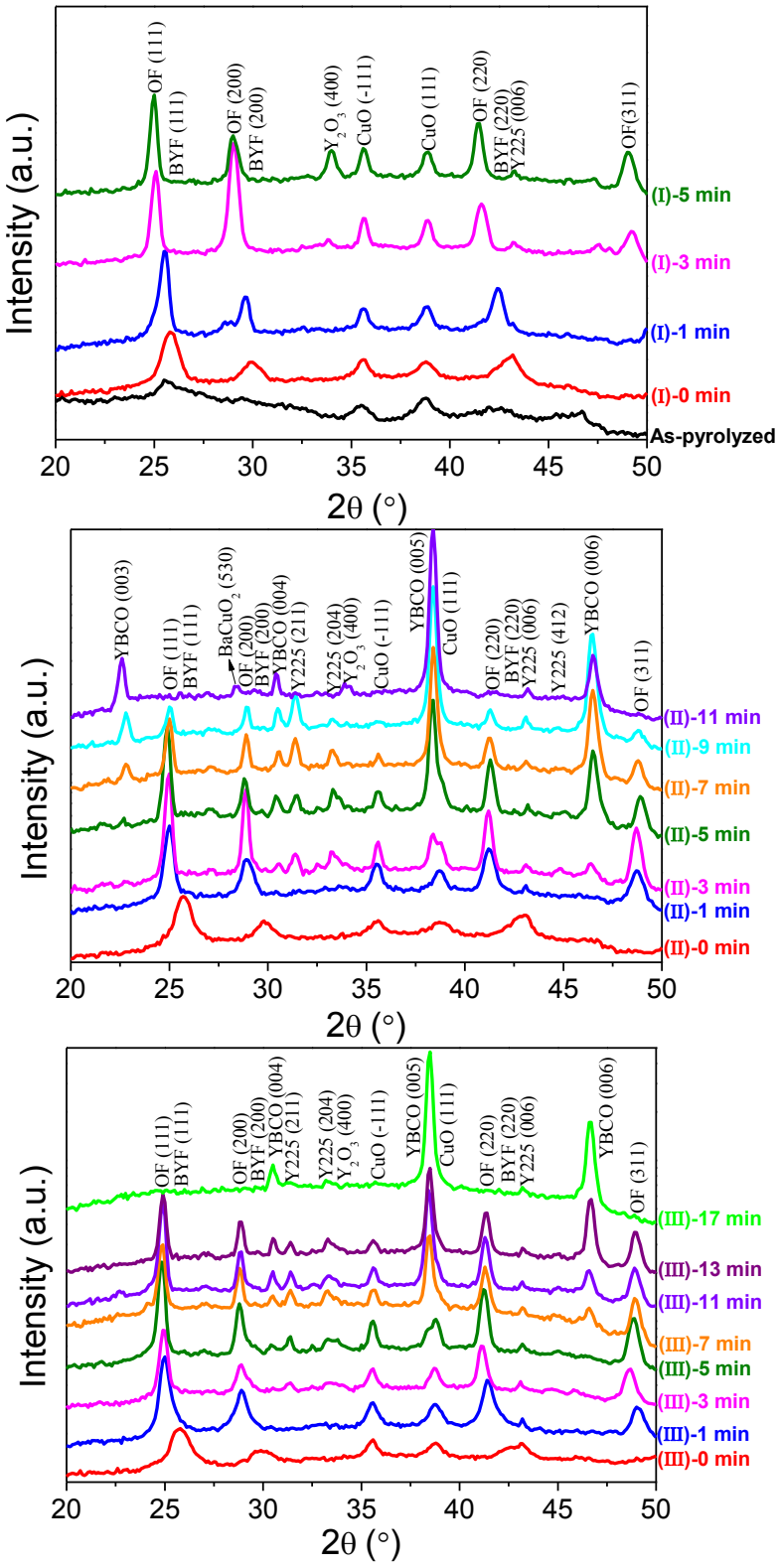

Figure 3-5: Integrated XRD patterns of pristine YBCO thin films quenched from conditions (I)-(III), where the intermediate phase evolution during the flash heating growth process can be followed.

In order to quantitatively draw the phase evolution trend and follow the formation kinetics of YBCO with annealing time under growth conditions (I)-(III), we have integrated the area under the XRD peaks (Figure 3-5 (a)-(c)) of selected phases such as YBCO (005), CuO (-111), OF (111) and $Y_2Cu_2O_5$ (211). The evolution trends of the selected phases for films quenched from different growth conditions are shown in Figure 3-6 (a)-(d), in which the annealing time dependences of the integrated areas of the selected XRD peaks are presented after normalizing to the maximum value for each one obtained in the studied thermal process.

In Figure 3-6 (a), we display the evolution of the YBCO (005) intensity with annealing time, for films grown from condition (I)-(III). We define the incubation time (t_{inc}) as that consumed at the growth temperature until a stable linear growth rate of YBCO is achieved. During this period, stable YBCO islands are formed at energetically favourable sites on the interface of substrate, and then grow along the in-plane orientation until coalesce, followed by the out-of-plane growth where a linear increase of the YBCO intensity is obtained. Meanwhile, the growth time (t_G) represent the total time consumed during the linear growth until a full conversion of YBCO phase is achieved. For films grown under condition (I), no conversion of precursors towards YBCO can be observed, demonstrating that moisture is essential to the formation of YBCO phase which is in accordance with previous reports [34, 37]. In contrast, with the introduction of moisture in the gas flow, we note that YBCO nuclei start to be detected after annealing for ~1.7 min and ~3.4 min for films thermally treated under conditions (II) and (III), respectively. These times are significantly decreased compared with the conventional heating routes detected by in-situ electrical resistance measurements [38, 56, 161] and X-Ray diffraction [38]. Moreover, the growth rate of each can be estimated to be 0.47 nm/s and 0.32 nm/s, respectively. Here, we note that the FH process promote a significant increase of growth rate (by a factor of ~2) at 750 ºC while the growth rate keeps similar value when the growth conducted at 810 ºC, as compared with films grown after conventional heating rate processes by Sánchez-Valdés C F et al [56] and Qu Timing et al [161], deduced in both cases from in-situ resistance measurements. We will analyze the origin of this phenomenon later on.

On the other hand, a quantitative behavior of other intermediate phases, such as CuO (-111), OF (111) and Y225 (211), are plotted and presented in Figures 3-6 (b)-(d). As shown in Figure 3-6 (b), the intensity of the CuO (-111) peak decreases constantly and vanishes at the time where a full conversion of YBCO phase is reached. This result indicates that CuO participates in the conversion reactions towards both Y225 and YBCO phases during the thermal process, following the reaction routes proposed in the previous reports [22, 32].

In addition, the formation process of YBCO during the annealing process is also accompanied by a phase evolution of OF and Y225, as shown in Figure 3-6 (c) and (d). In Figure 3-6 (c), we can observe a sharp increase of the intensity of OF (111) peak reaching

the maximum after annealing during ~3-5 min. Ba oxyfluoride is prone to form a well-ordered and large coherent lattice during the high temperature thermal treatment [162], although polycrystalline features of the OF phase are observable in the GADDS frame (see Figure 3-3 and Figure 3-4). This phase is one of the precursors for the formation of YBCO phase, attributing, on one hand, to the low barrier of YBCO nucleation sites provided by the (111)-oriented OF domains [28, 163], on the other hand, to the important role it played in the YBCO formation reactions [38]. These observations verify the primary YBCO formation reaction in the FH growth process follows the same reaction route: $Ba(O_xF_y)_2 + \frac{3}{2}CuO + \frac{1}{4}Y_2O_3 + yH_2O\ (s) \rightarrow \frac{1}{2}YBa_2Cu_3O_{6.5} + 2yHF\ (s)$ [37].

It is also noteworthy that OF formation is very sluggish in a dry atmosphere. This phenomenon can be explained by the hydrolysis process which leads to the formation of the Y_2O_3 following the reactions:

$$YF_3 + H_2O \rightarrow Y(O, F) + HF \quad (1a)$$

$$Y(O, F) + H_2O \rightarrow Y_2O_3 + HF \quad (1b)$$

This process allows the formation of Y_2O_3, thus enhancing the kinetics of Y liberation from the solid solution [157, 162]. However, the transformation of BYF to OF in the dry atmosphere indicates that there is still some water vapour in the dry gas. Meanwhile, the $Y_2O_3 + CuO \rightarrow Y_2Cu_2O_5$ reaction takes place after annealing during ~1 min in humid gas atmosphere, indicating that $Y_2Cu_2O_5$ and YBCO formation follow similar kinetic effects, in agreement with the observations obtained made in the conventional heating process [32]. However, in contrast to annealing in humid atmosphere, no crystalline $Y_2Cu_2O_5$ (211) is observed when annealing is conducted in dry atmosphere during the studied annealing time; see Figure 3-6 (d), because of the delay in the liberation of Y ions from the BYF phases. We should also note that no YBCO is formed when annealing is kept under a dry atmosphere because Ba^{2+} ions are not liberated from the OF precursor. Finally, the OF (111) and $Y_2Cu_2O_5$ (211) intensities vanish at the same time that the YBCO phase is fully converted. This phenomenon demonstrates that the intermediate reaction $Y_2Cu_2O_5 + 4BaO + 4CuO \rightarrow 2YBa_2Cu_3O_{7-x}$, which has been proposed in the previous report [22, 38], also occurs during the FH growth process as a competing reaction path towards YBCO formation.

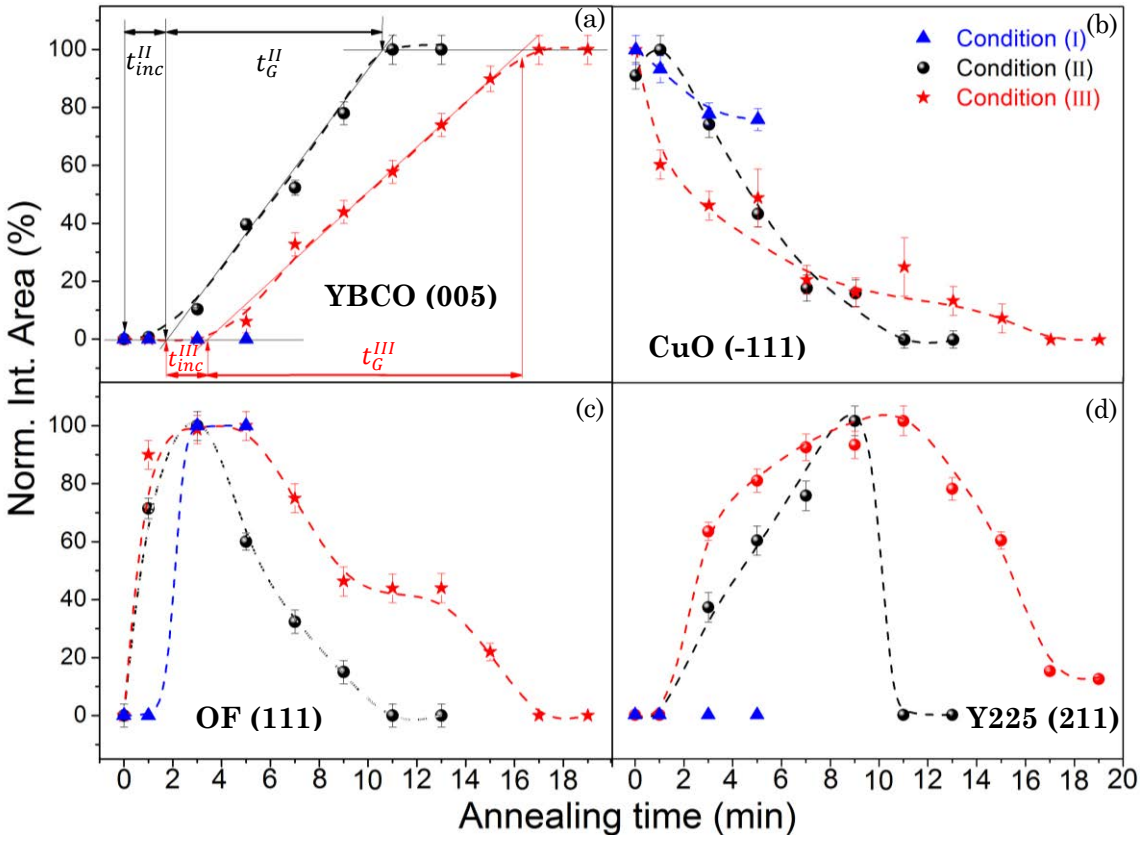

Figure 3-6: Normalized integrated area dependences with annealing time of XRD peaks of (a) YBCO (005), (b) CuO (-111), (c) OF (111) and (d) Y225 (211), respectively, while quench studies are conducted at condition (I) (blue ▲), condition (II) (black ●) and condition (III) (red ★) after annealing for selected times.

Another very important interphase behavior that affects the nucleation/growth process and the eventual microstructure of YBCO films is the coarsening of the precursor phase nanoparticles (mainly CuO, Y225 and OF). It has been early reported that processing parameters such as gas humidity, heating rate, growth temperature and annealing time induce size changes of CuO nanoparticles during either pyrolysis [36, 145, 164] or the following growth [28, 145, 165] process. In previous works [36, 145, 164, 165], it was suggested that inhomogeneous segregation of CuO associated to the coarsening effect leads to non-uniform YBCO crystallization and large pores may remain which ultimately affect negatively the superconducting properties of YBCO thin films. In this respect, it is clear that a fine control of CuO nanoparticle size, as well as keeping a homogeneous distribution during the thermal processing procedure is of significant importance for determining the final film quality and homogeneity of the YBCO films.

Figure 3-7 (a) displays the CuO nanoparticle size evolution with annealing time of films annealed at the following thermal processing conditions: 810 ºC in dry gas atmosphere, 810 ºC in humid gas atmosphere and 750 ºC in humid gas atmosphere. The grain size of CuO

nanoparticles is estimated from the integral breadth of XRD reflections by Debye-Scherrer formula (Equation 2-8) using (-111) Bragg peak of CuO, taking into account the similar diffraction angle between YBCO (005) peak and CuO (111) peak. The mean size of (-111)-oriented CuO nanoparticles is estimated to be ~8 nm for films after pyrolysis. It is worth noting that CuO nanoparticle size monotonically increases during the following thermal annealing process until reaching maximum values of 20±1 nm, 33±1 nm and 29±1 nm for films annealed at 810 ºC (dry gas), 810 ºC (humid gas) and 750 ºC (humid gas) after annealing for 3, 5 and 13 min, respectively. Their values are considerably smaller than those obtained in YBCO thin films heated at low heating rates (1-25 ºC/min), where CuO nanoparticles with size of ~50-100 nm are observed by TEM [145, 165]. We also note that a remarkable decline of nanoparticle size is detected after a certain maximum. This is due to the significant consumption of CuO phase during the annealing process and resulting in an increased YBCO and Y225 peak intensity; see Figure 3-5 (b) and (c). For films annealed at 810 ºC and humid gas atmosphere, CuO nanoparticle size displays a more drastic coarsening as compared to films annealed at 810 ºC and dry gas atmosphere. It is clear on any case that for films annealed at the same humid atmosphere, a lower growth temperature leads to a smoother coarsening effect of CuO nanoparticles. We attribute this phenomenon to the thermally activated behavior of atomic diffusion which enhances kinetic effects thus leading to a drastic size evolution of CuO at 810 ºC and humid gas atmosphere.

Moreover, the particle size evolution of two important reactants, i.e. OF and Y225, was also followed, as shown in Figure 3-7 (b)-(c). The mean nanoparticle size of both phases shows similar evolution trend as compared to the integrated area previously presented in Figure 3-6 (c) and (d). For the OF phase, its dependence with the annealing time shows a sharp initial coarsening which then saturates to a mean size of 22±2 nm after annealed for ~3 min until a complete consumption. This suggests that the particle consumption and coarsening occurs simultaneously during the YBCO formation process. However, as to the Y225 phase, its mean nanoparticle size keeps a persistent coarsening up to ~35 nm for films annealed at 750 ºC in humid gas, contrasting to the one annealed at 810 ºC in humid gas. The continuous coarsening with time of the Y225 nanoparticles suggests a sluggished consumption of this phase, thus, confirming the low reaction kinetics displayed by the intermediate reaction $Y_2Cu_2O_5 + 4BaO + 4CuO \rightarrow 2YBa_2Cu_3O_{7-x}$.

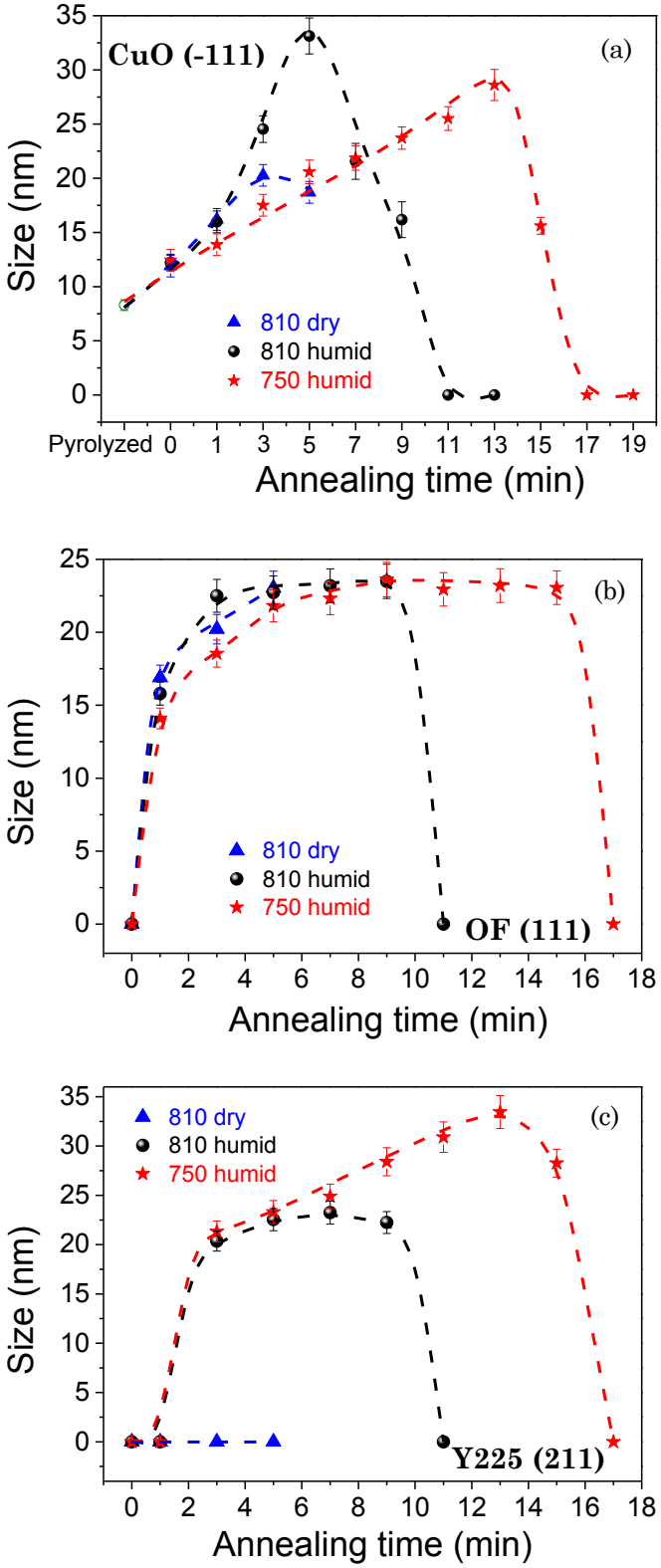

Figure 3-7: Nanoparticles size evolution of (a) CuO (b) OF and (c) Y225 in YBCO thin films quenched from 810 °C in dry gas atmosphere (blue triangle), 810 °C in humid gas atmosphere (black sphere) and 750 °C in humid gas atmosphere (red star), where the nanoparticles size evolution in the flash heating process can be followed. The nanoparticle size have been calculated from Scherrer formula using CuO (-111), OF (111) and Y225 (211) Bragg peaks.

As a concise representation of the intermediate phase transformation paths and growth kinetics, we have set up a schematic kinetic phase diagram defining different areas of phase coexistence for 250 nm YBCO films grown under the FH processes, as indicated in Figure 3-8. As a general trend, we can state that the YBCO precursor films experienced the same phase transformations previously observed with the commonly used conventional heating rates [22, 32]. It is seen that the kinetics for the intermediate phase transformations towards YBCO phase are slightly degraded as the temperatures decrease. This diagram reconfirms that the FH process can indeed provide high growth kinetics, but the windows of intermediate phase transformation are significantly compressed compared with the CTA growth process [32], and hence special care should be taken during the nucleation and growth processes for achieving high quality YBCO films.

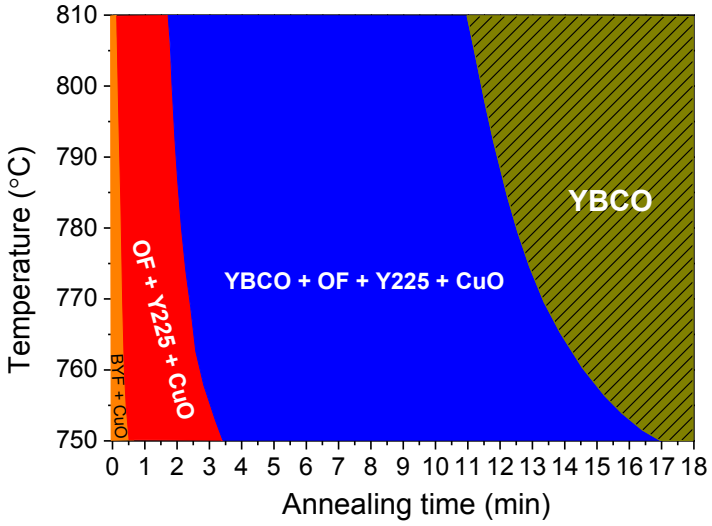

Figure 3-8: Phase diagram of 250 nm YBCO thin films heated in a humid atmosphere using the FH process to given temperatures, and quenched after annealing for different times.

3.1.2 Morphological evolution during the growth process

It has been recently revealed in the study by A. Llordes et al. [29] that solid precursor films pyrolyzed in O_2 atmosphere present strong vertical porosity, as high as 30%, which is attributed to a fast gas escape and thermal runaway associated with the thermodynamic and kinetic effects during the metal-organic decomposition process. During the following high temperature growth process, densification of films can be realized via a tight control of several growth parameters such as the water partial pressure [39], oxygen partial pressure [166, 167], growth temperature [32], annealing time [168], F/Ba ratio [169], etc. After a series of subtle optimization of growth conditions, the residual porosity in the fully converted films has been shown in our previous reports [22, 53] to be highly reduced to a negligible level based on our CTA process. Previous works [70, 166, 169] have detailed the extensive proposition of the correlation between pore healing and the liquid-assisted growth

YBCO model, however, it is actually difficult to obtain a direct evidence of melt formation in films due to the small volume of the films, to the transient nature of the melt in the case that it really forms and to the presence of additional reactions in the film. On one hand, a certain degree of porosity is beneficial to the gas diffusion process, after the presence of the crystallized films. For instance, H_2O and HF gas transportation is needed during the growth process [37] while oxygen ion exchange is needed during the oxygenation process, [12] on the other hand, the existence of residual porosity in the ex-situ grown YBCO films has been shown to exhibit a critical current blocking effect [29] and induce magnetic granularity [170]. Moreover, phase segregation such as CuO, Y_2O_3 and Y225 coarsening during the thermal process, will also become detrimental to the epitaxial growth and compromise the homogeneity of the YBCO films [39, 70, 171], especially for films grown in a fast growth rate taking into account the relevance of atomic diffusion factor during the YBCO formation process. In this scenario, it is very likely that a comprehensive understanding of the morphological microstructure evolution under different growth condition based on the flash heating process is of significant importance for reaching optimal growth conditions based on the requirements of reel-to-reel manufacturing process in industry. However, the morphological and microstructural evolution in the bulk and at the surface during conversion to YBCO films using the flash heating growth process is still unknown. Therefore, a systematic morphological analysis of the conversion to YBCO thin films during the flash heating growth process has been carried out via SEM and FIB imaging.

Figure 3-9 displays SEM micrographs of YBCO thin films quenched from condition (I)-(III) after annealing for different time, where the surface morphological evolution at different annealing conditions can be easily followed. As it can be seen in Figure 3-9 (a), the film shows a very rough surface with a high density of pores or pinholes, while some signs of a crystalline surface are also exhibited as compared to the as-pyrolyzed film [29]. For the film (I)-5 min, the film displays a dense surface morphology, coincident with the film shrinkage preciously observed via FIB measurement (see Figure 3-10). In contrast, the films quenched from humid gas atmosphere present a much smoother surface morphology and a reduced residual open porosity; see Figure 3-9 (c)-(f). Figure 3-9 (a) and (c) compare SEM images quenched from 810 ºC with and without moisture in the gas atmosphere, where a faster densification of precursor film annealed in humid gas atmosphere can be observed, in agreement with the report of J.S. Matsuda et al [39] who stated that a fast growth of YBCO induced by high water partial pressure show benefits to control the pore size. A comparison of the surface morphology of films quenched from different temperatures, i.e. 810 ºC (condition (II)) and 750 ºC (condition (III)), both annealed during 5 min, is exhibited in Figure 3-9 (d) and (e). The SEM micrographs reveal that a denser surface can be obtained when the film is annealed at a higher temperature. Furthermore, further

increase of the annealing time promotes a progressive reduction of the residual porosity, see Figure 3-9 (e) and (f). This observation follows the previous research work conducted by K Zalamova and her coworkers [32, 34], who concluded that the surface porosity of YBCO thin films is gradually decreased as growth temperature and annealing time increase. The detailed features of the fully converted YBCO films grown from our flash heating process at both 810 ºC and 750 ºC will be presented in the following two sections in this chapter. On the other hand, we can observe that the density of Cu-rich particles (as confirmed by EDS analysis) progressively increases as annealing time increase; see Figure 3-9 (d) and (f). As revealed by XRD analysis, the quenched films consist of YBCO, Y_2O_3, $Y_2Cu_2O_5$, CuO and OF. Here, we attribute this scenario to the pushing effect of the epitaxial surface during the annealing process, thus intermediate Cu-rich phases outcrop to the surface. A similar phenomenon has been extensively illustrated in the previous works [39, 166].

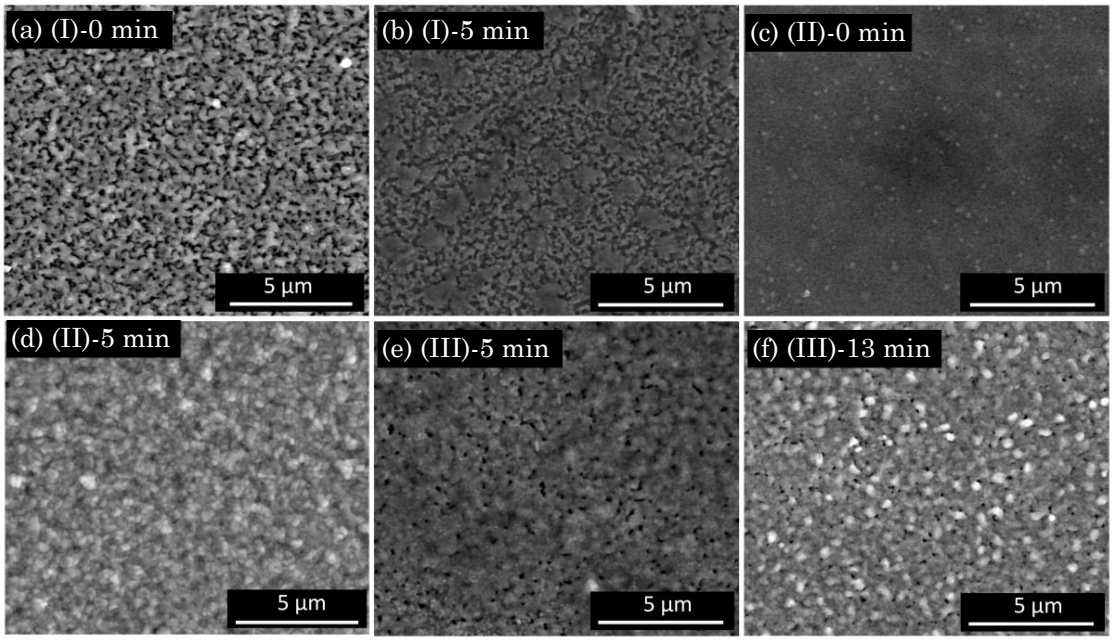

Figure 3-9: SEM images of pristine YBCO thin films quenched from condition (a) (I)-0 min, (b) (I)-5 min, (c) (II)-0 min, (d) (II)-5 min, (e) (III)-5 min and (f) (III)-13 min.

Cross-sectional FIB analysis has also been conducted to study the inner porosity evolution of the as-pyrolyzed film and the films quenched from different thermal processing step, as shown in Figure 3-10. The FIB cross-sectional image of the conventional as-pyrolyzed YBCO film evidences the formation of unconventional vertical open porosity which can be attributed to the poor mechanical properties of the films during this stage [152] and a fast gas escape toward the film surface associated with the high kinetics of the decomposition process [29]. A similar phenomenon was observed, with an optimized porosity of ~30% after the same pyrolysis process [29]. Notice that the density of these pores is significantly decreased during the flash heating process to the growth temperature; see Figure 3-10 (b)-(d). For film (I)-0 min, there are still some pores remaining, which are

mostly distributed at the film-substrate interface; see Figure 3-10 (b). It is remarkable to note that the inner pores in the films (I)-5 min and (II)-0 min are almost completely absent; see Figure 3-10 (c) and (d). The film thicknesses are estimated to be 320 nm, 270 nm and 263 nm for films (I)-0 min, (I)-5 min and (II)-0 min, respectively, which therefore exhibit a strong shrinkage from the as-pyrolyzed YBCO precursor film (450 nm). These observations are of great importance to illustrate that the densification process starts during the thermal heating process, before YBCO nucleation and growth. It is concluded, therefore, that the application of the FH process is beneficial to minimize the film porosity prior to the YBCO nuclei appear, ensuring a continuous atomic diffusion at the YBCO nucleation and growth stages. On the other hand, the vertical open pores are necessary to the water diffusion to the heterogeneous nucleation sites of YBCO to some extent. Taking this two conflicting requirements into account, it is clear that some further optimizations should be achieved to obtain highly dense epitaxial YBCO coated conductors. Therefore, further works towards the achievement of high microstructural and superconducting properties will be illustrated in the next two sections.

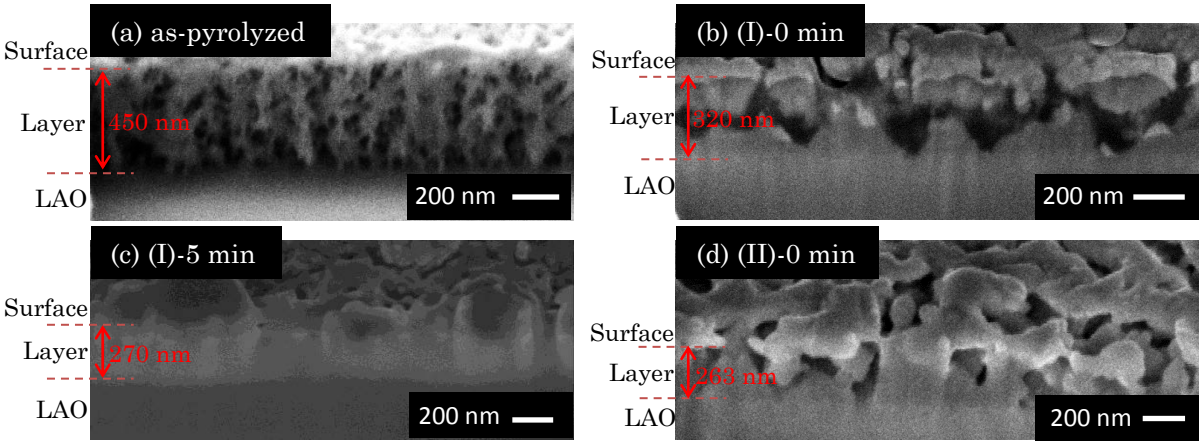

Figure 3-10: FIB images of (a) as-pyrolyzed YBCO and pristine YBCO films quenched from (b) (I)-0 min; (c) (I)-5 min and (d) (II)-0 min.

Up to now, we have presented a thorough investigation of the conversion process of TFA-YBCO films based on a novel FH growth process via a series of quenching studies, in which the influence of processing parameters, such as gas atmosphere, annealing temperature and annealing time have been compared.

First, we have demonstrated that there is no intermediate phase evolution during the heating process of our studied conditions (I)-(III), i.e. the crystalline phases existing after the pyrolysis are the same that those existing at high temperature after the FH process. In the following isothermal annealing processes, diverse intermediate transformations and kinetic behaviors have been observed. On one hand, the participation of water vapor in the gas flow promotes the intermediate phase evolution process of YBCO films, while no

evidence of any nucleation of YBCO grains has been observed during annealing under a dry gas atmosphere. On the other hand, a higher annealing temperature provides an enhanced growth kinetic, thus leading to a faster conversion to YBCO films. It would be certainly worth mentioning that a remarkably reduced incubation time is achieved using the novel FH process, even though no clear improvement of growth rate can be achieved during this process. Additionally, owing to the fast converting feature of the FH growth process, a limited coarsening effect of CuO nanoparticles occurs during our present thermal process. This is probably the reason why the YBCO nucleation rate is enhanced and so the incubation time shortened.

Second, considering the overall microstructural evolution of YBCO thin films during the FH growth process, we are able to conclude that the densification process of YBCO precursor films starts before the YBCO nucleation and growth process. Importantly, film densification shows a strong gas atmosphere, annealing temperature and annealing time dependence. The clarification of this process is significant to achieve an in-depth understanding of the origin of the diversity of microstructure and performance of YBCO thin films grown following the corresponding growth processes.

We should stress that classifying all these issues is a very important advancement because it provides us some guidance to define the optimal growth condition in the continuous low cost reel-to-reel CCs production in future work.

3.2 Influence of the water introduction temperature

An efficient transportation of H_2O gas to the growth interface of YBCO and the corresponding transport of HF towards the surface are of significant importance for controlling the nucleation and growth process of YBCO thin films. The role of water vapor during the annealing process has been initially demonstrated via a thermodynamic analysis of the fluorine removal reaction [172]. Extensive research works have indicated that water vapor shows impact on the transformation of YBCO phase in several respects such as intermediate phase transition [157, 173], microstructure transition [39, 168], YBCO nucleation [46, 53] and growth process [37], which have a complex interplay into the final YBCO film microstructure and superconducting performances. Ron Feenstra et al. [168] have suggested to perform fast heating ramps (300 °C/min) to high-temperature (T ~ 775 °C) intermediate annealing steps under dry conditions, in order to control the film porosity and then provide water supply for YBCO nucleation and growth. Additionally, as we have mentioned in the previous section, the phase transformation kinetics and microstructure evolution during our flash heating process also show evident water dependence. Consequently, a longitudinal water vapor feeding has an extraordinary impact on the long-length tape production.

On the basis of the optimal H_2O partial pressure for ensuring the epitaxial growth of TFA-YBCO, obtained in the previous reports [37, 46, 53], we decided, to concentrate our effort in exploring an optimized H_2O gas introduction point, which is one of the most important processing parameters for achieving continuous reel-to-reel production methodology of YBCO-coated conductors.

In this study, we present an investigation of the influence of moisture introduction time on the microstructure and the superconducting properties of YBCO films grown from our novel flash heating process. To achieve this, the as-pyrolyzed YBCO films have been flash heated to 810 °C in a tubular furnace and the humidity has been well controlled during different thermal stages. Here, the YBCO thin films are named in the form of "T-t", where T and t denote the water opening temperature and the dwell time, respectively, as shown in Figure 3-11. In addition, the detailed operational process and gas compositions at different thermal processing stages have been illustrated in the section 2.1.2.4.

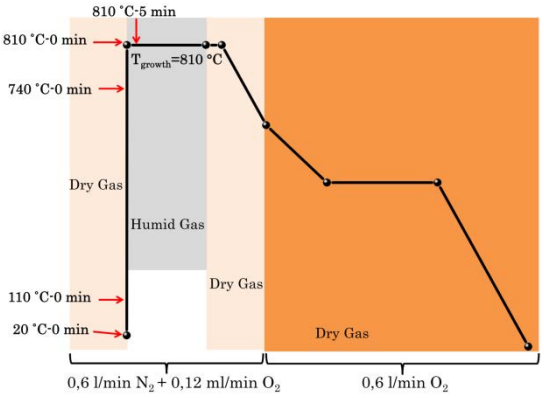

ID	Heating process	T_{growth} (°C)	H_2O at T (°C)	H_2O at t (min)
20 °C-0 min	FH	810	20	0
110 °C-0 min	FH	810	110	0
740 °C-0 min	FH	810	740	0
810 °C-0 min	FH	810	810	0
810 °C-5 min	FH	810	810	5

Figure 3-11: Schematic thermal profile of films grown at 810 °C with a series of water vapor introduction points of 20 °C-0 min, 110 °C-0 min, 740 °C-0 min, 810 °C-0 min and 810 °C-5 min. The detailed operational process and gas compositions at different thermal processing stages have been illustrated in the section 2.1.2.4.

3.2.1 Morphology and microstructure investigation

XRD θ-2θ scans have been carried out systematically on all the pristine YBCO films, as shown in Figure 3-12. In Figure 3-12 (a) and (b), we present GADDS frames of film 110 °C-0 min and 810 °C-5 min, respectively. These x-ray diffraction frames display typical epitaxially grown YBCO (single spots, Figure 3-12 (a)) and polycrystalline features of the YBCO (diffraction rings, Figure 3-12 (b)), which can be easily used to identify the phase composition and texture of YBCO thin films. The corresponding θ-2θ integrated XRD spectra of YBCO thin films grown from our flash heating process with different water introduction times are shown in Figure 3-12 (c). Qualitatively, all the precursors are completely converted into YBCO. However, diverse grain orientation scenarios can be observed in samples grown from different H_2O introduction points which indicate modified nucleation events. YBCO thin films grown from the process when H_2O was introduced at

110-810 °C without dwell show only (00l) peaks, indicating an epitaxial nature of these films. It is noteworthy, however, that there is an extra peak appearing at 2θ = 32.8° for films 20 °C-0 min and 810 °C-5 min, indexed as corresponding to the (103) Bragg peak of YBCO and indicates that some randomly oriented grains have been found. However, further high resolution XRD (HRXRD) studies on two epitaxial films (i.e. film 110 °C-0 min and 810 °C-0 min) indicate that some residual intermediate phases, such as OF, Y_2O_3 and Y225, still remain, as shown in Figure 3-12 (d).

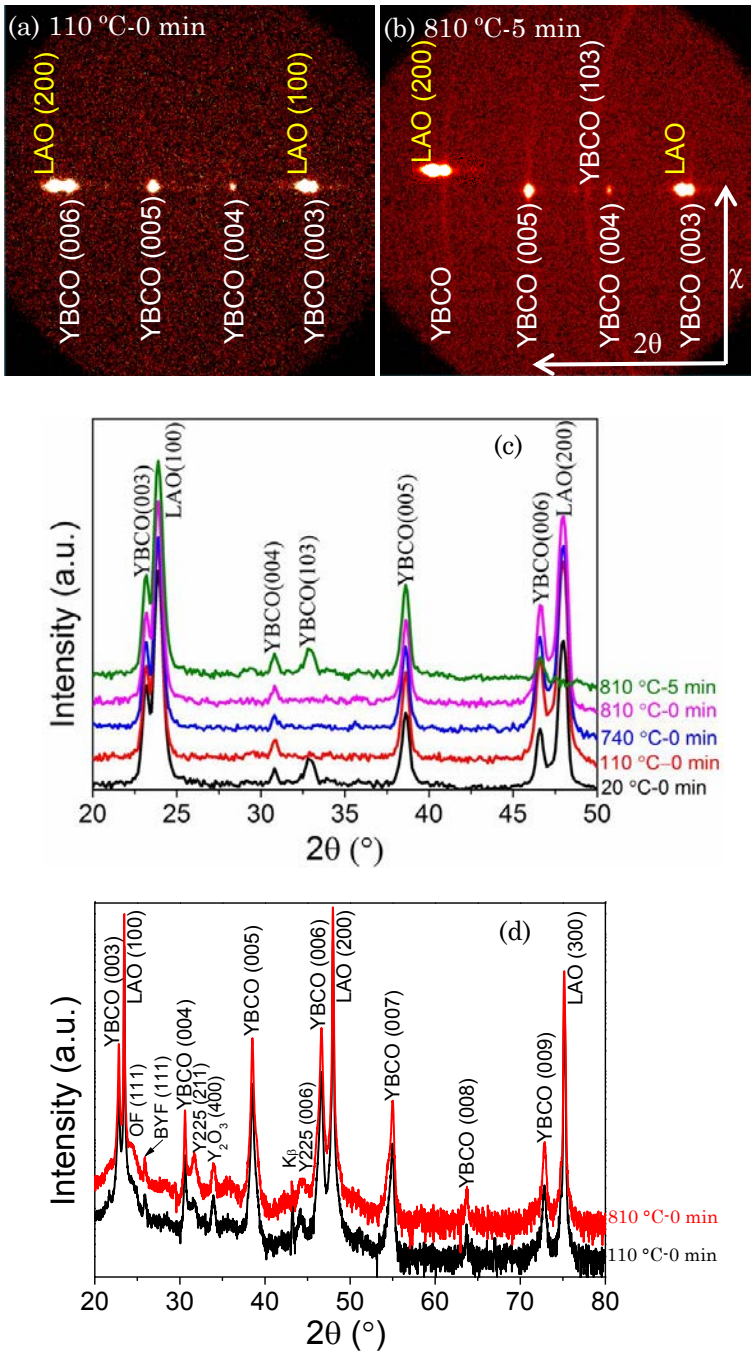

Figure 3-12: (a) and (b) Two dimensional XRD frames of pristine YBCO thin films at (a) 110 °C-0 min and (b) 810 °C-5 min; (c) Integrated X-Ray diffraction patterns from GADDS frames of film 20 °C-0 min, 110 °C-0 min, 740 °C-0 min, 810 °C-0 min and 810 °C-5 min; (d) High resolution XRD (HRXRD) patterns of the films 110 °C-0 min and 810 °C-0 min.

On the other hand, the crystalline perfection of the epitaxial YBCO thin films (i.e. films 110 ºC-0 min, 720 ºC-0 min and 810 ºC-0 min) has been investigated by estimating the FWHM of the Bragg peaks using XRD ω-scans and ϕ-scans for (005) and (103) YBCO peaks, respectively. Figure 3-13 (a) presents the rocking curve of the YBCO (005) for all the epitaxial YBCO thin films. The estimated Δω values show a gradual increase from ~0.6º for film 110 ºC-0 min to 0.8º for film 810 ºC-0 min. Figure 3-13 (b) displays the XRD φ-scan of the YBCO (103) peak performed in film 110 ºC-0 min, where a Δϕ value of ~1.3º has been obtained. It is clear that the film 110 ºC-0 min presents the best out-of-plane and in-plane texture quality, which is comparable with YBCO films grown from the CTA process (Δω = ~0.5º and Δϕ = ~1.2º). Moreover, the c-parameter for all the epitaxial FH films are estimated to be 11.692 ± 0.003 Å, which is very similar to the CTA films (11.689 ± 0.002 Å).

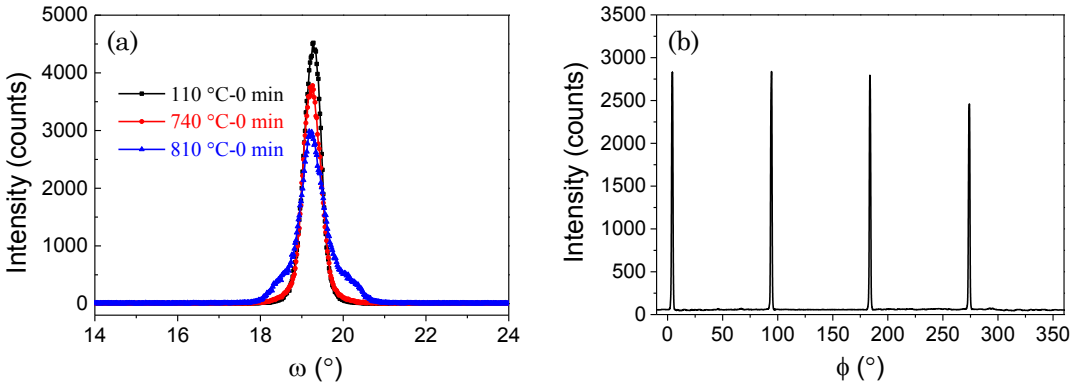

Figure 3-13: (a) Rocking curves of the (005) YBCO diffraction peak for films 110 ºC -0 min, 740 ºC-0 min and 810 ºC-0 min, respectively; b) XRD ϕ-scan of the YBCO (103) for film 110 ºC-0 min.

Surface morphological features of the fully converted YBCO thin films have been studied by SEM. Figure 3-14 presents SEM images of all the YBCO thin films grown from our flash heating process with diverse water introduction conditions compared with a CTA YBCO thin film, from where diverse morphological landscapes can be observed. SEM micrographs of the YBCO film 20 ºC-0 min and 810 ºC-5 min indicate that randomly oriented YBCO grains, i.e. (103) oriented YBCO grain (see Figure 3-14 (a) and (e)), formed during the growth process. In contrast, highly c-oriented and homogeneous YBCO thin films can be obtained when H_2O is introduced at 110-810 ºC without dwell time; see Figures 3-14 (b)-(d). Note that the porosity of YBCO films presents an increasing trend with the delay of H_2O opening point, especially, the film grown at 810 ºC (5 min) shows an extremely high residual porosity. Noteworthy, the film 110 ºC-0 min (Figure 3-14 (b)) exhibits a highly dense and homogeneous surface morphology with c-oriented YBCO grains, i.e. at a similar level than the CTA YBCO thin films (Figure 3-14 (f)).

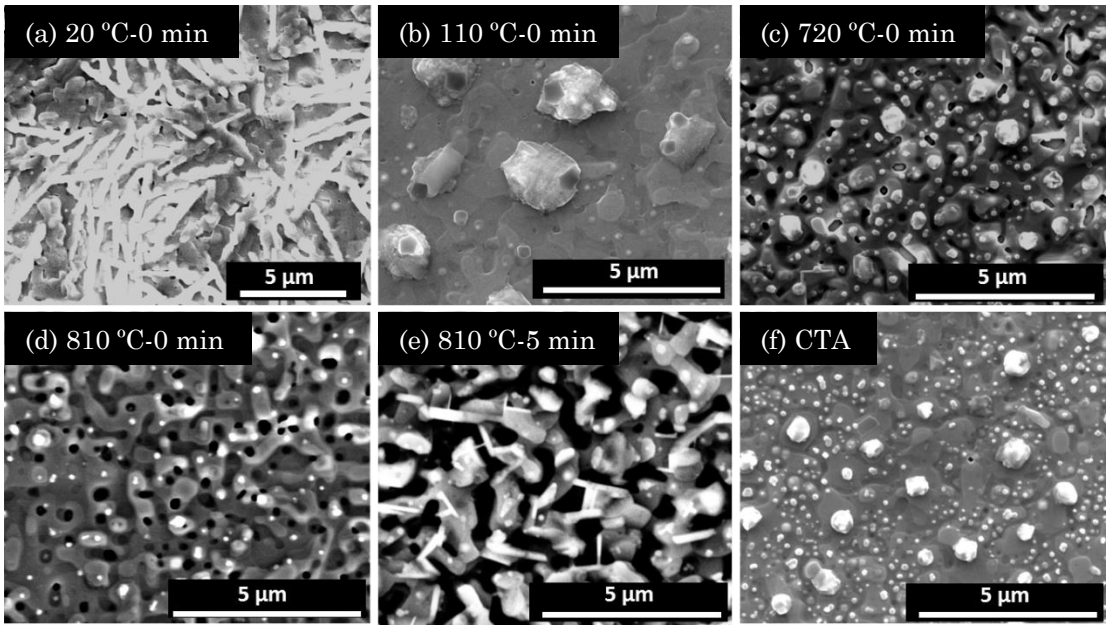

Figure 3-14: (a)-(e) SEM micrographs of YBCO thin films grown from our flash heating process with water introduction at (a) 20 ºC-0 min, (b) 110 ºC-0 min, (c) 720 ºC-0 min, (d) 810 ºC-0 min and (e) 810 ºC-5 min compared with (f) CTA YBCO.

Classical nucleation theory establishes that the nucleation process of epitaxial YBCO films occurs when the energy of first nuclei overcome their energy barriers described in Equation 1-4. A detailed analysis (see section 1.2.2.1) of the relationship between this energy barrier and $|\Delta\mu|$ predicted that the orientation of YBCO nuclei strongly depends on the $|\Delta\mu|$, i.e. c-axis grains are prone to nucleate under low $|\Delta\mu|$ while a/b-axis and randomly oriented nuclei appear at high $|\Delta\mu|$. The nucleation events of YBCO thin films can be safely explained by this analysis when precursor film has a good permeability. However, the influence of gas diffusion issues on the nucleation energy should be taken into account when the gas impedance appears. In this scenario, Solovyov et al [43, 174] extended the schema established based on the classical nucleation theory to a collective effect in the nucleation events taking into account the influence of the gas impedance. In low film permeability systems (i.e. thick or dense films), it is predicted that there exists high surface energy sites which are influenced by the already existing stable nuclei. These sites provide areas with high energy barriers thus retarding nucleation events. The supersaturation degrees (or driving force) of these sites could then be correlated with several processing parameters:

$$s = \frac{\Delta\mu}{kT} \propto \frac{dr}{P\,(H_2O)^{1/2}\,D_s} \qquad \text{Equation 3-1}$$

where d is the film thickness, r the growth rate and D_s the HF diffusion permeability through the film precursor. From Equation 3-1, it is clearly seen that s is directly influenced by the gas (H_2O and HF) transfer though the YBCO precursor layer. As it has been shown in the previous FIB studies, the precursor layer is gradually densified during

the annealing processes; see Figure 3-10 (b)-(d). The densification of these precursor layers could decrease the film permeability (D_s) and/or $P(H_2O)$. This effect could increase the $|\Delta\mu|$, leading to the formation of a-axis or randomly oriented grains and, consequently, damage the growth uniformity of the epitaxy. Therefore, an earlier introduction of H_2O vapour is required in order to ensure high permeability for gas diffusion though the film during the nucleation and growth process of YBCO films.

In order to further visualize the complexity of YBCO thin films grown from the flash heating process, it seems very appealing to further investigate the microstructure by means of transmission electron microscope (TEM). Figure 3-15 and Figure 3-16 cross-sectional STEM images of pristine YBCO thin films 810 ºC -0 min and 110 ºC-0 min, respectively.

From the TEM images of the film 810 ºC-0 min (Figure 3-15), it is clearly seen that a large amount of unreacted secondary phases existing after growth in the form of interfacial layer (Figure 3-15 (a)) and nubby precipitate (Figure 3-15 (b)) as well as lamellar precipitate parallel to a-b plane of YBCO (Figure 3-15 (c)). Although there are still some secondary precipitates distributing in the bulk of the film 110 ºC-0 min, a fully converted YBCO has been achieved at the YBCO/LAO interface; see Figure 3-16 (a). Figure 3-16 (b) present a typical cross-section Y, Ba and Cu EDX maps corresponding to the secondary phase area in the green box, evidencing a Y-enriched area of the dark particle thus corresponding to the Y_2O_3 intermediate phase. This is in good agreement with previous HRXRD patterns (Figure 3-12 (d)) in which residual intermediate phases are indeed detected. The formation of precipitates such as Y_2O_3 and $Y_2Cu_2O_5$ within YBCO matrix has been mentioned to be associated with the densification process of YBCO films [70, 175]. In the scenario that YBCO underwent a fast formation process based on the FH growth process, atomic diffusion of some secondary phases is limited by the diffusion time. Thus, these secondary phases are suspending within solid precursor film, until the YBCO growth front reach and trap them in their high temperature form after annealing at high temperature for a few minutes. Moreover, high density of long stacking faults (dark horizontal stripes) generated in the YBCO matrix; see Figure 3-15 (a) and Figure 3-16 (a).

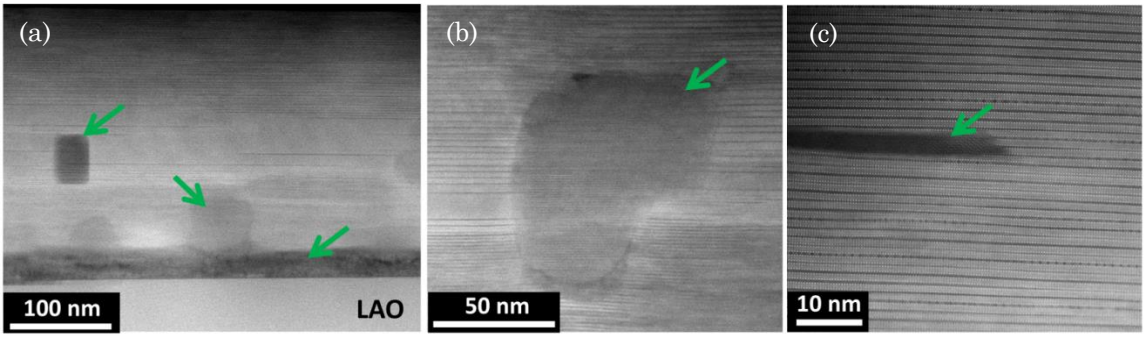

Figure 3-15: Cross section TEM images of the film 810 ºC-0 min, where different type of unreacted secondary phases can be observed.

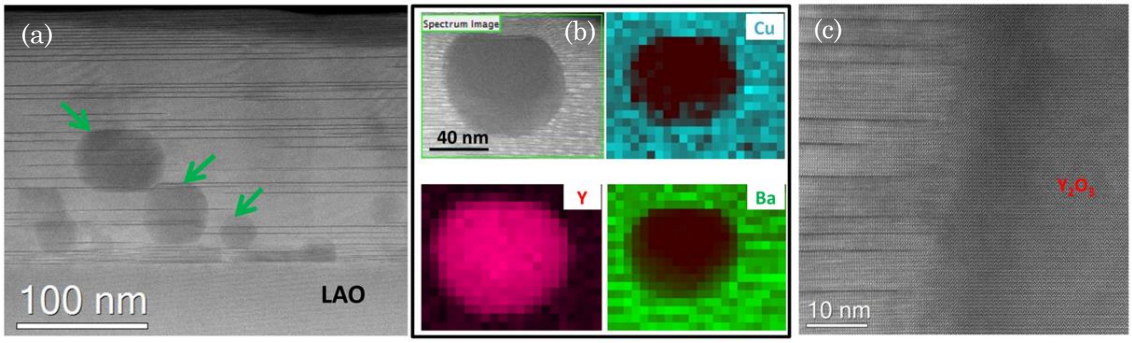

Figure 3-16: (a) Low-magnification TEM image of the film 110 °C-0 min; (b) typical cross sectional STEM EDAX Cu, Y and Ba elemental maps of one secondary phase identified as Y_2O_3; (c) high-magnification STEM image evidencing that an oriented nanoparticles is surrounded by stacking faults.

3.2.2 The study of superconducting properties

Now we will tune our interest to the assessment of superconducting properties of the YBCO thin films grown from our flash heating process with different water introduction times. In this section, the superconducting properties at, both self-field and in-field, has been determined inductively by SQUID measurement. All the performance parameters are determined following the detailed illustration in section 2.2.3.1.

Figure 3-17 (a) displays several superconducting properties, including the onset superconducting transition temperature (T_c^{onset}), transition width (ΔT_c) and self-field critical current (J_c^{sf}) measured at 5K and 77K. The T_c^{onset} and ΔT_c values of the epitaxially grown YBCO thin films are ~88.5±0.5 K and ~7.5±3.0 K, respectively. Besides, both J_c^{sf}(5K) and J_c^{sf}(77K) show similar evolution trend with water introduction time, as observed from the J_c evolution plots shown in Figure 3-17 (a). Note that YBCO thin film 110 °C-0 min presents the highest J_c^{sf}(5K) and J_c^{sf}(77K) values, 28.9 MA/cm² and 3.2 MA/cm², respectively. A significant degradation of J_cs arise for films 20 °C-0 min and 810 °C-5 min, which is accounted for the current blocking effect due to the formation of large angle grain boundaries generated between c-axis and non-c-axis oriented YBCO grains [176]. Moreover, a small reduction of J_c occurs in the epitaxial YBCO thin films following the increase of water opening temperature, i.e. films 110-810 °C-0 min. This result indicates a distinct scenario compared to the previously reported result by K. Nakaoka et al. [177] who observed that superconductivity only was achieved when H_2O vapor was introduced at temperature above 200 °C, whereas their work is based on YBCO growth from a slow heating process (2 °C/min). This phenomenon is in agreement with the evolution of film porosity and unreacted secondary phases where the current blocking effect stems from [69], but also the decrease of the texture quality shares the responsibility.

Finally, it is generally known that the assessment of J_c behavior at magnetic field is essential for promoting high magnetic field applications. Figure 3-17 (b) presents the magnetic field dependence of J_c(H//c) obtained at 5K and 77K of the YBCO thin films 110 ºC-0 min and 810 ºC-0 min compared with CTA YBCO thin film. As it can be clearly seen, the magnetic field dependence of YBCO thin films grown from flash heating process is smoothed as compared with CTA YBCO thin film. Furthermore, the enhancement of the pinning efficiency is quantitatively assessed by the crossover magnetic field μ_0H^* (J_c decrease at 90 % level), i.e. the transition magnetic field of two pinning regimes (single and collective pinning), as detailed in section 1.3.1. The film 110 ºC-0 min presents a value of μ_0H^* = 101.2 mT, which is much higher compared with CTA YBCO (μ_0H^* = 37.8 mT). This improvement of pinning efficiency relates to the enhanced nanoscale strained areas generated within YBCO matrix associated with the partial dislocations distributed surrounding the boundary of stacking faults [54, 113, 116].

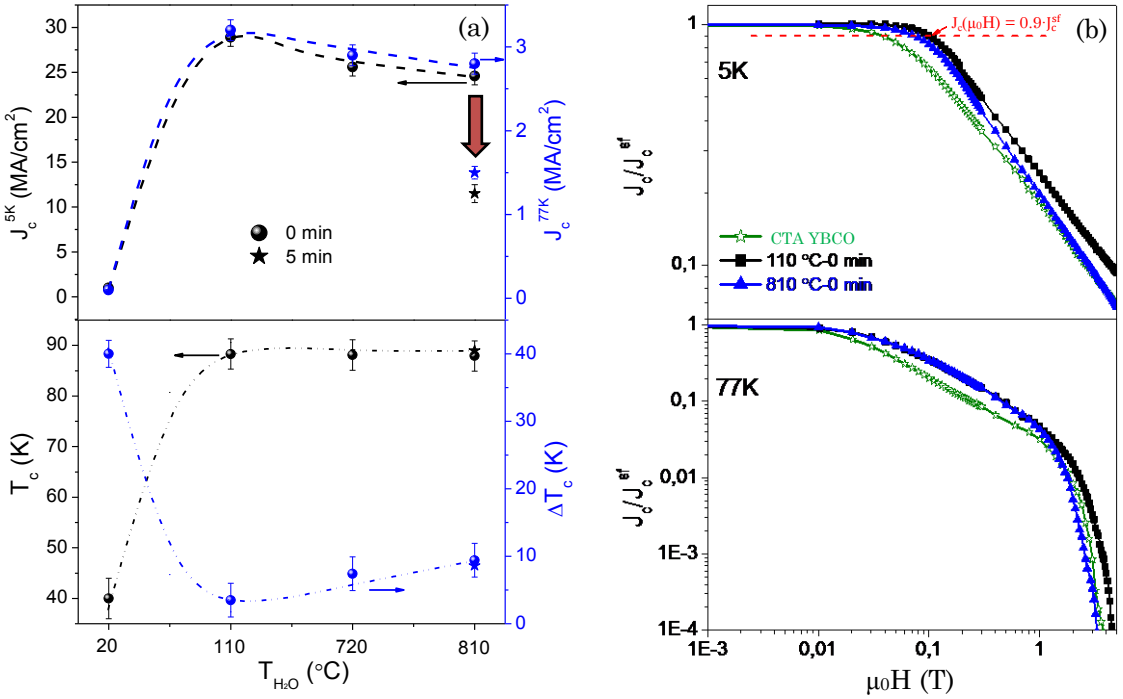

Figure 3-17: (a) Superconducting properties of YBCO thin films grown from the flash heating process with different water introduction time measured at self-field; (b) magnetic field dependence of the normalized J_c obtained at 5K and 77K of films 110 ºC-0 min and 810 ºC-0 min compared with a CTA YBCO thin film.

To conclude the present chapter, we have investigated the dependence of microstructure and superconducting properties on the water introduction time based on the FH process. It has been found that the densification of YBCO precursor films during thermal process causes a collective effect in the nucleation events and thus, the microstructure and superconducting properties of YBCO thin films achieve the best effects when water vapor is introduced into the gas flow at 110 ˚C, from which a dense, homogeneous and epitaxial YBCO thin film has been obtained. Specially, we also achieve improved vortex pinning

performance, owing to the appearance of high density of stacking faults within YBCO thin films. However, several issues still need to be further analyzed, such as the large residual precipitates and the stacking faults dimensions. Therefore, further analysis of these issues is required.

3.3 Influence of the growth temperature

After achieving a detailed summary in section 1.2 and conclusion in section 3.1, it becomes clear then that the microstructure of YBCO thin films grown from the flash heating growth process should be strongly dependent on the growth temperature. Here, we focus our attention on investigating the influence of growth temperature on the microstructural and physical performances of YBCO thin films. The main objectives are achieving a low-temperature growth of YBCO thin films, to control the residual phase impurities, and to improve the compatibility of YBCO superconducting films with CeO_2 cap layer on metallic substrates. All these requirements are essential for long length CCs production for power applications.

In this section, the microstructural characteristics of the fully converted pristine YBCO films grown within a wide temperature window of 730-840 °C (Figure 3-18) will be presented. Additionally, the thermal processing related defect landscape will be observed by TEM analysis and the corresponding relationship with superconducting properties will be built.

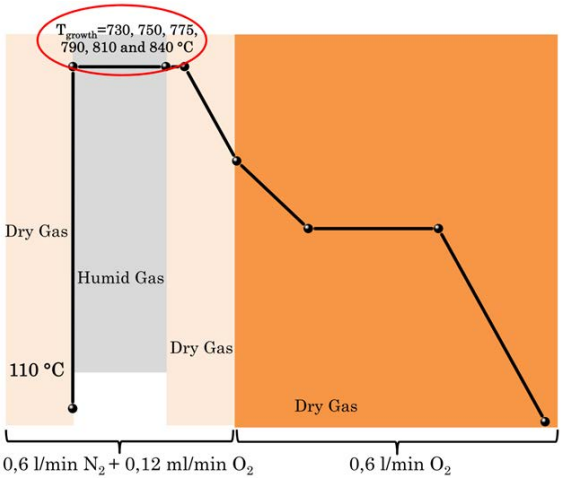

T_{growth} (°C)	Heating process	H_2O at T (°C)-	Dewell time (min)
730	FH	110	(150+30)
750	FH	110	(150+30)
775	FH	110	(150+30)
790	FH	110	(150+30)
810	FH	110	(150+30)
840	FH	110	(150+30)

Figure 3-18: Schematic thermal profile of YBCO thin films grown at temperatures ranging from 730 °C to 840 °C based on the flash heating process with water introduction at 110 °C.

3.3.1 Microstructure analysis

The two dimensional XRD frames of pristine YBCO thin films grown at 730 °C, 750 °C, 810 °C and 840 °C based on the flash heating growth process are presented in Figure 3-19

(a)-(d), respectively. Simultaneously, Figure 3-20 displays the corresponding integrated 1D-XRD diffraction patterns.

It is clearly seen that some randomly oriented YBCO grains (i.e. YBCO (103)) appear when the growth process is carried out at 730 ºC; see the diffraction ring in Figure 3-19 (a) and the extra peak located at 2θ = 32.8˚ in Figure 3-20. At higher growth temperatures (750-840 ºC), instead, all the YBCO thin films present c-axis oriented grains (Figure 3-20) epitaxially grown on LAO (see Figure 3-19 (b)-(d)). However, it is notably that some Y_2O_3 remains as a final phase when the growth process is conducted at 840 ºC; see Figure 3-19 (d) and Figure 3-20.

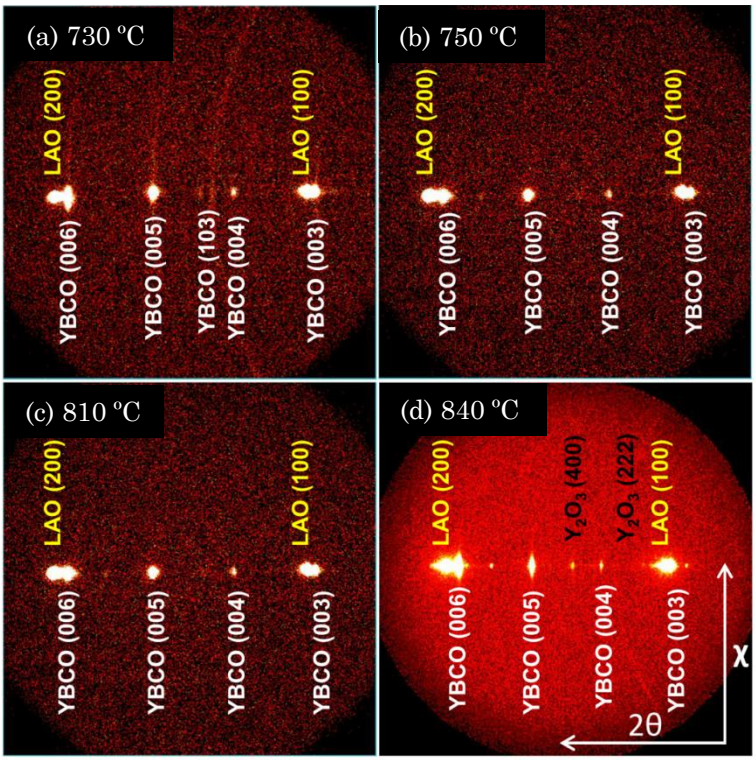

Figure 3-19: Two dimensional XRD frames of pristine YBCO thin films grown at (a) 730 ºC, (b) 750 ºC, (c) 810 ºC and (d) 840 ºC based on the flash heating growth process.

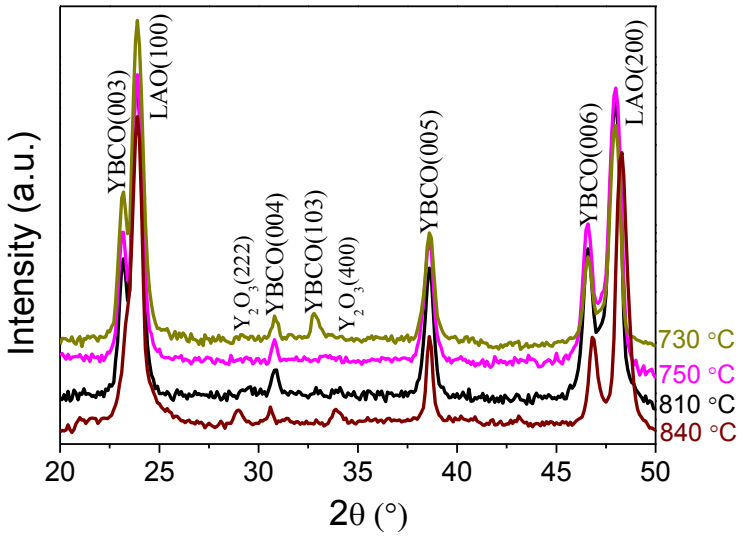

Figure 3-20: X-Ray diffraction patterns of YBCO thin films integrated from GADDS frames in Figure 3-19 (a)-(d).

Figure 3-21 (a)-(f) present SEM micrographs of YBCO thin films grown at different temperatures ranging from 730 ºC to 840 ºC based on the flash heating growth process. It is noteworthy that randomly oriented grains appear when the growth process is carried out at 730 ºC, in accordance with the result detected by XRD measurement. It is also straightforward to note that films with a negligible porosity is obtained when growth is performed within the window T_{growth} = 750-810 ºC, although a tendency towards a progressively reduced porosity is observed when the growth temperature is increased. This follows the trend previously observed on our CTA process [38, 53].

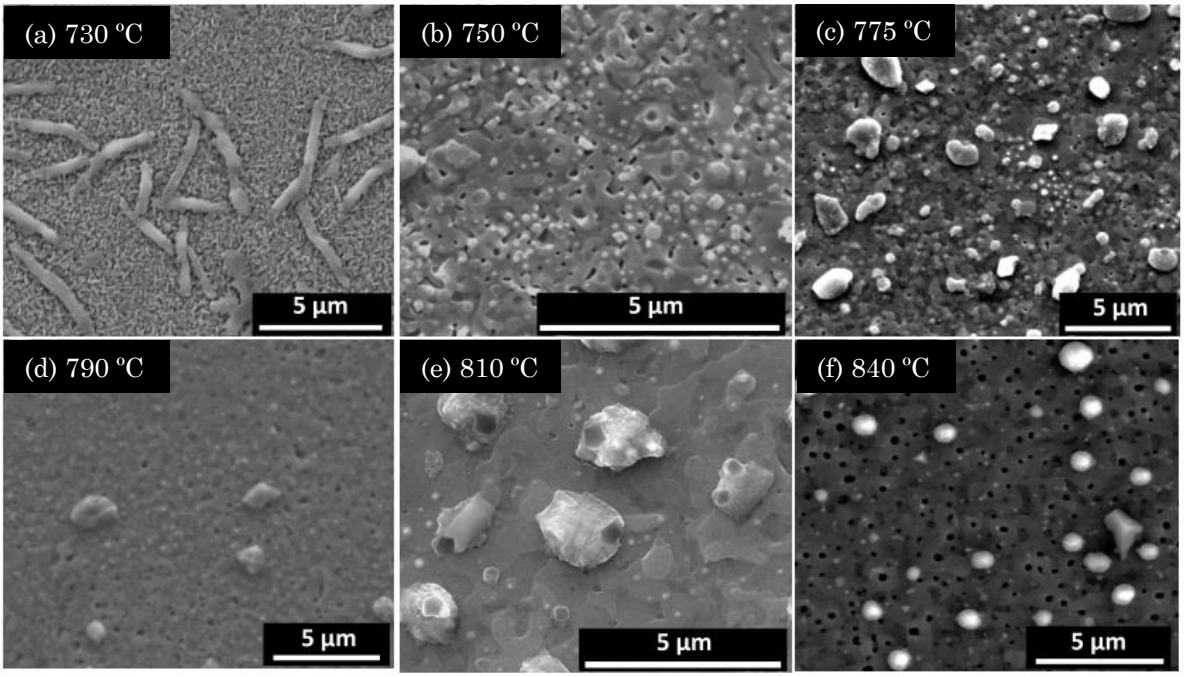

Figure 3-21: SEM images of pristine YBCO thin films grown at (a) 730 ºC, (b) 750 ºC, (c) 775ºC, (d) 790 ºC, (e) 810 ºC, and (f) 840 ºC based on the flash heating growth process.

So far we conclude therefore that the nucleation of c-axis oriented YBCO grains can be ensured in a wide temperature window of 750-840 ºC, while the optimal growth temperatures are 750-810 ºC on the condition of our present growth condition. This result clearly illustrates that the flash heating growth process ensures optimal nucleation and growth of YBCO thin films in a lower and wider temperature window compared with the previous works based on the slow heating process [53]. The FH process, therefore, have some similarity to the experimental results obtained on YBCO films prepared with Ag additives on LAO substrates and growth though the CTA process [38].

Furthermore, several parameters for evaluating the lattice and texture quality of the fully converted YBCO thin films such as the FWHM of the ω-scan and ϕ-scan, c-parameter and nanostrain. The values of c-parameter of YBCO thin films grown under the FH process are estimated to be ~11.691±0.010 Å. Texture analysis of the YBCO film grown at 750 ◦C present x-ray ω-scan YBCO (005) $\Delta\omega = 0.62^{\circ}$ and ϕ-scan YBCO (103) $\Delta\phi = 1.29^{\circ}$, reveling good out-of-plane and in-plane texture, respectively. Nevertheless, a slight decrease of both in-plane and out-of-plane texture qualities can be observed when the samples are grown at 775 ºC and 790 ºC. It is also important to mention that the nanostrain displays a significant increase when the flash heating process is applied in the growth of pristine YBCO thin films, i.e. ε increases from 0.11% (CTA YBCO) up to 0.25% (FH YBCO), i.e. similar values to those obtained in nanocomposite films [54, 65, 118].

Figure 3-22 (a) and (b) show low-magnification cross-sectional TEM images of pristine YBCO thin films grown from the flash heating process at 750 ºC and CTA process, respectively. As previously mentioned, the presence of Y248 intergrowths is evidenced by the appearance of dark stripes distributing parallel to the (001) YBCO plane in our present imaging mode, while the regular Y123 matrix appears as a homogeneous contrast in the TEM images. Note that the film grown from the flash heating process presents a high density of long stacking faults (≥ 200 nm of lateral extension) homogeneously distributed in the bulk of the whole film; see Figure 3-22 (a). In contrast, the stacking faults are scarcely observed in the bulk of the CTA YBCO film; see Figure 3-22 (b). Importantly, both films are free of secondary impurities, compared with the film grown at 810 ºC based on the flash heating growth process (Figure 3-16 (a)). It is also noteworthy that film grown at 750 ºC (Figure 3-22 (a)) presents a higher density and more homogeneously distributed stacking faults compared with the film grown at 810 ºC (Figure 3-16 (a)).

Figure 3-22 (c) shows a high-resolution TEM image of a pristine YBCO thin film grown from the flash heating process at 750 ºC, in which an extra Cu−O chain layer inserted between two Ba−O layers surrounded by partial dislocations can be clearly seen. It has been pointed out in previous reports [54, 113] that the presence of partial dislocations bends the YBCO (00l) plane thus generating locally nano-scale distorted regions. The generation of the strained nanoareas has been proposed to share the main responsibility for

pinning vortex centers [54]. As we have already illustrated in detail in subsection 1.3.1, the density of partial dislocations present a negative correlation with the extension of stacking faults. Therefore, for the purpose of increasing the density of the valid pinning centers, a finely control of the size of stacking faults becomes the priority on the condition that a homogeneous distribution of stacking faults can be obtained.

In order to interpret the genesis of high density of stacking faults during the flash heating growth process, we should first get a review of the general mechanisms of stacking faults generation which has been illustrated in subsection 1.3.1. Since the same oxygenation process was used in both growth processes, we focus our concentration on the formation mechanisms during the growth process. It is generally known that the formation of c-axis oriented Y123 films from YBCO precursor phases undergo a series of crystallographic events, including overcoming the Gibbs free energy barrier to form YBCO nuclei, a series of chemical reactions for YBCO growth, coalescence of individual grains and the final merging of grain boundaries to release energy. We notice that the kinetic effects influence the nucleation rate of YBCO considerably (Equation 1-12), thus flash heating process increases nucleation rate. Hence, we suggest that high density of cluster of stacking faults and dislocations generate at the contact between grains in order to relive the energy at this regions [116]. Besides, the atomic diffusion effects could not be treated as the dominant factor, owing to the fact that both films are free of secondary precipitates.

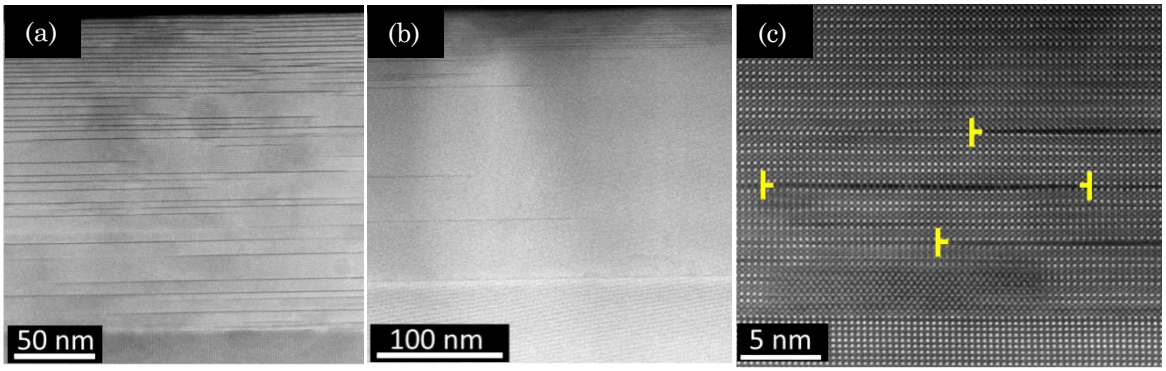

Figure 3-22: Low-magnification cross-sectional TEM images of pristine YBCO thin films grown from (a) flash heating process at 750 °C; (b) CTA process; (d) a high-magnification TEM image of the film displayed in (a) showing the presence of stacking faults in the Y123 matrix. The yellow symbols point to the position of partial locations around the stacking faults.

3.3.2 Superconducting properties

The experimental investigations of superconducting properties of the YBCO thin films, at both self-field and in-field, have been conducted via SQUID measurement, intending to achieve a final assessment of their relevance with growth temperature.

Figure 3-23 (a) displays the growth temperature (730-840 °C) dependence of superconducting properties including T_c, ΔT_c, J_c (5K) and J_c (77K) which are measured at

self-field. Once again, the films grown at 750-810 ºC display optimal self-field physical properties, following the trend of the microstructural features evolution. Nevertheless, physical properties drop significantly when the growth process is carried out at 730 ºC and 840 ºC, which are accounted for the high-angle grain boundaries between (103)-oriented and (00l)-oriented YBCO grains [22] and high density of secondary precipitates, respectively. It is noteworthy that faintly constant superconducting properties are obtained in the optimal growth temperature window (750-810 ºC), although a precipitate-free film has been only obtained when the growth is conducted at 750 ºC. We tend to assign this phenomenon to the synergistic influence of the structural features observed in the microstructural studies, e.g. residual porosity, precipitates, as well as texture quality of the final films.

Figure 3-23 (b) displays the magnetic field dependence of the normalized critical current density ($J_c(H)$) measured at both 5K and 77K. An overall smoother J_c (H) dependence is observed in films grown from the flash heating process at different temperatures compared with the CTA YBCO thin film, indicating an enhanced pinning efficiency due to the nanostrain arising from the highly distorted YBCO matrix. Although all the films grown from the flash heating process display similar nanostrain values, the μ_0H^* displayed in the film grown from the flash heating process at 750 ºC shows the highest value, i.e. μ_0H^* increases from 37.8 mT (CTA YBCO) and 101.2 mT (FH (810 ºC)) to 116.2 mT (FH (750 ºC)). We suggest that the density and the length of stacking faults share the main responsibility for the observed improvement of pinning efficiency, in accordance with the proposition previously reported [55, 87].

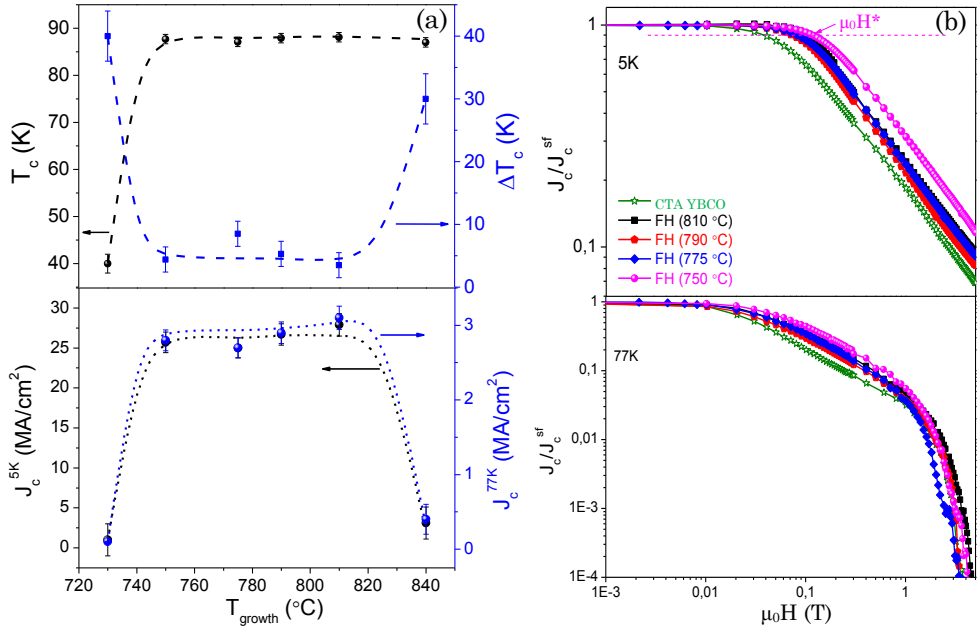

Figure 3-23: (a) Superconducting properties of YBCO thin films grown at different temperature measured in self-field; (b) magnetic field dependence of the normalized J_c obtained at 5K and 77K of films grown from 750 ºC, 775 ºC and 810 ºC based on the flash heating process compared with a CTA YBCO thin film.

Finally, we also evaluated the compatibility of the optimized FH growth process with the nucleation and growth of YBCO thin films (~150 nm) on the ^{CSD}CZO/^{ABAD}YSZ/SS metallic substrates from Bruker HTS which have been previously shown to be a suitable CC architecture for thin YBCO films [26, 138]. For achieving a successful growth of ^{CSD}YBCO/^{CSD}CZO/^{ABAD}YSZ/SS CCs, the chemical reactivity issue which takes place between BaF_2 precursor and CZO cap layer with the formation of $BaCeO_3$ (BCO) layers needs to be properly handled [178, 179]. The main objective is to achieve a fast c-axis YBCO nuclei formation on top of CZO cap layers and thus, avoid the nucleation of YBCO on the BCO interlayer which then strongly degrades the YBCO film texture due to the large lattice mismatch among both oxides.

Figure 3-24 (a) shows a GADDS XRD pattern of a 150 nm YBCO CC grown under the FH (750 ºC) process. It is seen that the CC exhibits good c-axis epitaxy as (00l) peaks only appear as spots and no ring intensity or ab- peaks are observed. The CZO cap layer has been completely transformed to epitaxial BCO with two orientations perpendicular to that substrate ((200) and (110)). The film epitaxy is significantly enhanced compared to the 200 nm YBCO CC grown under the CTA (770 ºC) process (see Figure 3-24 (b)). SEM observation (Figure 3-24 (c)) demonstrates that the FH (750 ºC) YBCO CC presents dense and homogeneous surface morphology with only c-axis oriented grains, which are remarkably improved compared with the morphology in Figure 3-24 (d). Moreover, the FH (750 ºC) YBCO CC presents good superconducting properties: T_c = 88.5 K and J_c(77K) = 0.6 MA/cm^2. The results indicate, therefore, that our optimized FH growth process exhibits high potential for fabricating YBCO CCs on top of the ^{CSD}CZO/^{ABAD}YSZ/SS metallic tapes.

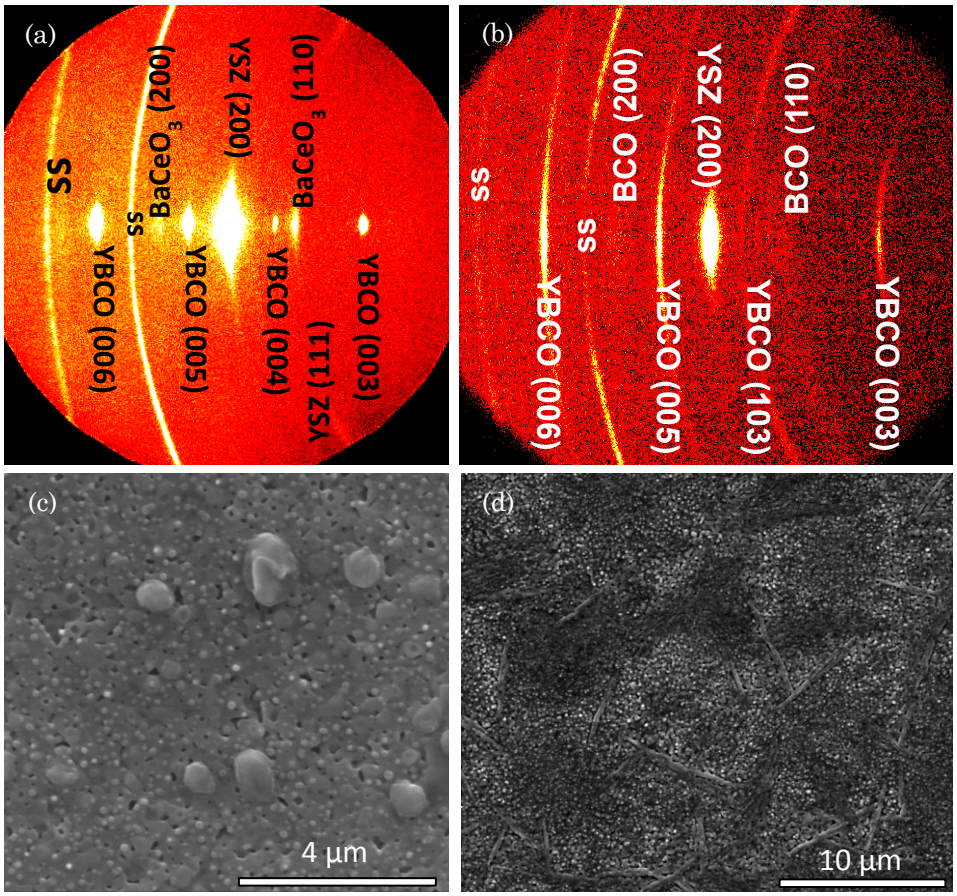

Figure 3-24 (a)-(b): 2D-XRD θ-2θ patterns and (c)-(d): SEM images of a 150 nm thick YBCO coated conductor grown under the FH (750 °C) growth process ((a) and (c)) and a 200 nm thick YBCO coated conductor grown under the CTA (770 °C) growth process ((b) and (d)).

In this section, we have achieved high quality YBCO films grown under the FH process at 750 °C. Optimal microstructural and superconducting performances of YBCO films have been identified for films grown at a wide temperature window of 750-810 °C. Microstructure studies by means of XRD and SEM demonstrate that epitaxial YBCO thin film with negligible porosity, high texture quality and homogeneous surface morphology can be obtained when the growth is carried out at 750 °C. Further analysis conducted by TEM observation shows that the film are free of secondary precipitate and a high density of stacking faults are homogeneously distributed within YBCO matrix. In addition, the vortex pinning properties of the film have been strongly enhanced due to the generation of nanostrain in the YBCO lattice. More importantly, the optimized FH 750 °C has been shown to be suitable for YBCO growth on CeO_2 capped metallic tapes avoiding $BaCeO_3$ polycrystalline formation and being compatible with the continuous reel-to-reel industrial production. This work will be further extended in Chapter 5 in connection with the preparation of nanocomposite thin films.

3.4 Conclusions

In this Chapter, the flash heating growth process has been demonstrated to be valid for the growth of CSD-based YBCO superconducting thin films at a low temperature (i.e. 750 ºC) with controllable microstructural and superconducting performances. We have presented detailed studies of the YBCO converting process during this novel growth process, as well as the influence of two processing parameters: water vapor introduction time and growth temperature.

In the first section, we have studied the YBCO converting process at two different growth temperatures (750 ºC and 810 ºC) under dry or humid gas atmosphere. The results indicate that intermediate phase transitions are significantly delayed when the FH processes are applied, nevertheless, densification of the precursor films starts during this stage in any case. The water vapor and annealing temperature have been shown to be crucial parameters for the intermediate phase transformation (BYF to OF), the microstructure evolution and the YBCO nucleation and growth during the FH growth process. The FH process ensures a limited intermediate nanoparticle coarsening effects and thus, leads to a fast formation of c-axis YBCO films.

In the second section, we have reported a series of studies of the microstructure and superconducting properties of YBCO thin films grown at 810 ºC with different water vapor introduction times. Epitaxial growth of YBCO can be ensured when the water vapor is introduced at 110-810 ºC during the heating process, while residual porosity presents an increasing trend when the water vapor introduction is deferred within this temperature range. Through a microstructural analysis by TEM, we observe that the interfacial unreacted secondary phase disappears when we introduce water vapor at low temperature (110 ºC), although some secondary precipitates remain within the YBCO matrix. Specially, we have achieved an improved vortex pinning performance, owing to the increased nanostrain arising from partial locations. Consequently, it is concluded that the optimal water introduction time is at 110 ºC during the heating process, however, there are also some issues, such as residual precipitate and inhomogeneous distribution of long stacking, faults, that need to be further improved.

In the third section, we have investigated the influence of growth temperature (730 ºC-840 ºC) on the microstructure and superconducting properties of YBCO thin film grown from the flash heating process with water vapor introduction at 110 ºC. Epitaxial YBCO thin films with negligible porosity, a high texture quality and a homogeneous surface morphology can be obtained when the growth is carried out within the temperature window of 750-810 ºC. The microstructural analysis via TEM imaging reveals that the film grown at 750 ºC displays a precipitate-free YBCO matrix, where a high density of quite short

stacking faults is homogeneously distributed. Thus, a strongly enhanced vortex pinning properties of this film has been achieved.

As a consequence, through comprehensively considering the overall analyses in this chapter, we can achieve as a final conclusion the FH process is very appealing due to several reasons. It leads to a shortened converting time, it allows to perform a low temperature growth and it leads to an improved vortex pinning.

We have widely discussed the possible origin of the observed difference in nucleation and growth of YBCO which we tentatively attribute to a reduced precursors nanoparticle coarsening during the heating process. The enhanced compositional homogeneity at the nanoscale should deeply modify the atomic diffusion kinetic required to nucleate YBCO crystals and so we suggest that the nucleation rate of YBCO is enhanced though this new process. All these advantages achieved in the FH growth process lead to a successful deposition of YBCO thin film on top of CeO_2 capped metallic tapes.

4. Preparation and Characterization of YBCO Pristine and Nanocomposite Ultrathin Films

Motivation

YBCO ultrathin films are highly attractive for the material's use in technical applications such as single-photon detectors [180], bolometers [181], fast terahertz detectors [182, 183], etc. The use of a pristine YBCO ultrathin layer on the substrate has been demonstrated to be effective for either enhancing flux pinning of YBCO films via generation of nanoscale defects decorated substrates [184, 185], or promoting epitaxial growth of YBCO nanocomposite films [118, 125]. Besides, an in-depth understanding of the microstructure of YBCO thin films down to several unit cells is of vital importance if one wants to explore in depth the structure-properties correlations of YBCO superconducting films from a fundamental point of view [186]. To the best of our knowledge, there was no systematic reported work on the CSD-based YBCO ultrathin films grown directly on LAO substrate at the beginning of this thesis. Therefore, we are interested in setting further knowledge on the CSD-based ultrathin films. The aim of this work is:

Firstly, to develop valid processing conditions which are well compatible with the Volmer-Weber growth mode [28] of CSD-based YBCO films when the film thickness decreases below 50 nm. Several detrimental macroscopic film defects (e.g. film dewetting, large scale secondary precipitates, grain misalignment, etc.) should be avoided in order to obtain high quality YBCO ultrathin films.

Secondly, to depict the microstructural characteristics of YBCO ultrathin films and investigate their influence on the final superconducting properties. The tendency of T_c decay with the decrease of film thickness has been significantly reported in earlier studies, which have been linked either to epitaxial mismatch strain induced reorganization of interatomic distances [79, 187], or to the strain induced oxygen vacancies [188, 189]. However, a clear consensus for the origin of this phenomenon is still in debate. Moreover, in order to estimate the functional (seed layer) or technological (single-photon detectors) application prospect, it is also important to further investigate the surface morphological characteristics (topography and roughness) and superconducting properties of CSD-based YBCO ultrathin films.

Thirdly, to study the film thickness dependence of nucleation and growth process of spontaneously segregated nanoparticles in the solution-based YBCO-BYTO system. The main purpose is to investigate the nanoparticle behaviors (size, shape and distribution) in

ultrathin YBCO films, and their influence on both the microstructural defects and the superconducting performances.

In this chapter, we will investigate the growth and characterization of TFA-YBCO ultrathin films, which display superconductivity down to 25 nm. YBCO-8 mol% BYTO ss-nanocomposite films, with thicknesses down to 25 nm, have also been successfully fabricated and characterized. To achieve these, we deposited diluted TFA solutions with metal concentration of 0.03, 0.06, 0.15 and 0.3 M on substrates (LAO or STO), leading to ultrathin YBCO films with thickness of 5, 10, 25 and 50 nm, respectively. Hereafter, we define YBCO thin films with thickness ≤ 50 nm as ultrathin films. Also, the growth processes are defined in the form of, for instance, FH T °C (t_1 + t_2), denoting the films were flash heated (FH) to the growth temperature (T °C) and then annealed in humid and dry gas atmosphere for t_1 and t_2 min, respectively, as schematically shown in Figure 4-1.

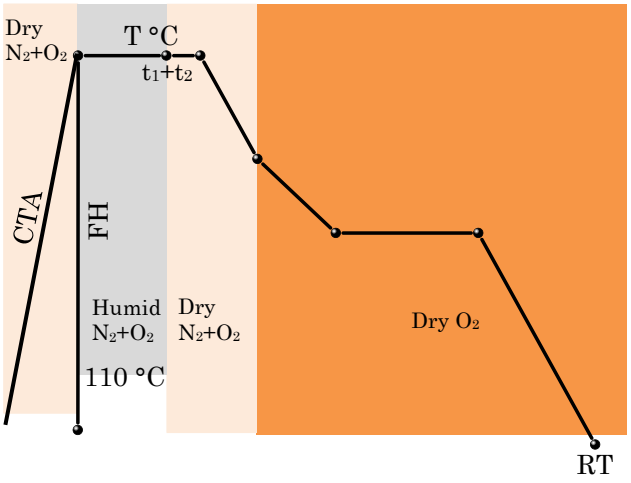

Figure 4-1: Schematic thermal profile applied for the formation of YBCO ultrathin films. More details about the operation and gas composition have been illustrated in subsection 2.1.2.4.

4.1 Optimization of growth conditions for pristine YBCO ultrathin films

Achieving an efficient and viable fabrication of YBCO ultrathin films is the prerequisite for promoting their applications in both scientific and technological field. In the past decades, many efforts have been devoted to this subject using a various manufacturing routes, such as pulsed laser deposition (PLD) [183, 190], magnetron sputtering [180, 186], activated reactive evaporation [191, 192], etc. In the case of the CSD approach, which is an ex-situ growth technique where the formation of epitaxial YBCO layer is approximately under thermodynamic equilibrium conditions, however, the optimized processing conditions towards high quality ultrathin films are still poorly known. In the previous work of our group, a series of processing parameters for the growth of 100-350 nm TFA-YBCO thin

films were properly optimized, as illustrated in Chapter 3 and refs [38, 46, 53, 71]. However, transferring these conditions to the fabrication of ultrathin films is not a straightforward work, taking into account the stress relaxation, nucleation and growth events at the initial stage of TFA-YBCO formation. It is therefore important to develop a further understanding of the influence of these essential processing parameters on the final properties of TFA-YBCO ultrathin films.

In this section, we study the influence of four important processing parameters: heating process, growth temperature, annealing time and mismatch strain induced by substrate, on the microstructure and superconducting properties of TFA-YBCO ultrathin films. Our aim is to probe an optimal processing condition for a successful fabrication of YBCO ultrathin films, which is essential then in the fundamental studies that will take place in this chapter.

4.1.1 The influence of heating rate: conventional vs flash heating

In the previous chapter, it has been suggested several advantages when applied FH, such as fast phase transition, promising defect landscape and enhanced pinning properties. In this scenario, we decided, therefore, to study the influence of heating processes on the microstructure and superconducting properties of YBCO ultrathin films. In this work, TFA solutions with metal concentration of 0.06 M and 0.3 M were deposited on LAO substrate and grown from the CTA 810 ºC (20+10) and FH 810 ºC (20+10) process, respectively.

Figure 4-2 shows Z-contrast images of 10 nm films grown from (a) CTA 810 ºC (20+10) and (b) FH 810 ºC (20+10). The film grown from the CTA process is discontinuous, identifying the dewetting effect [71], forming YBCO islands (Figure 4-2 (a)). The film grown from the FH process appears as a continuous YBCO layer (see Figure 4-2 (b)). The results confirm that using FH, we can obtain continuous YBCO films with thickness down to 10 nm. As we have discussed in Chapter 3, the FH process provides high driving force for YBCO formation, leads to an increased effective nucleation sites and, consequently, to an enhanced heterogeneous nucleation rate and to a more efficient grain coalescence and zipping process [38]. In addition, thermal processing time is remarkably reduced when the FH process is applied.

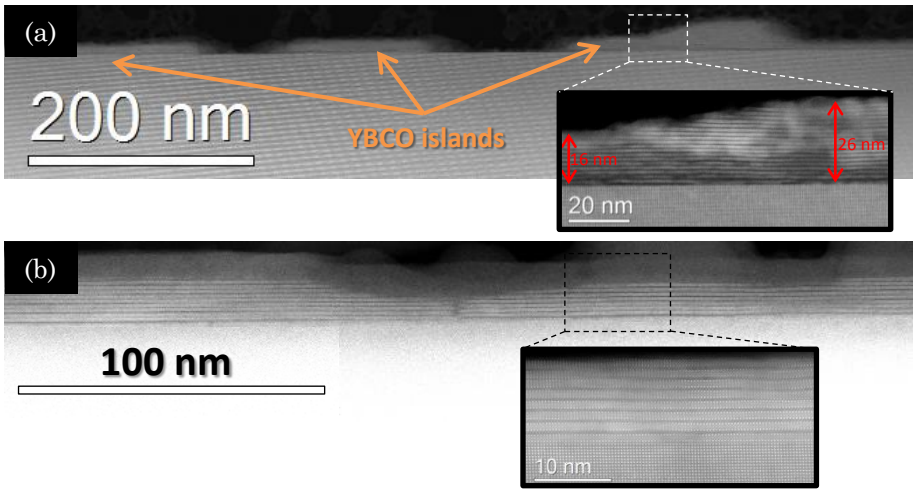

Figure 4-2: Cross section Z-contrast STEM images of 10 nm YBCO ultrathin films grown from (a) CTA 810 °C (20+10) and (b) FH 810 °C (20+10).

By increasing film thickness to 50 nm, the YBCO films are continuous with some thickness fluctuation, small amount of precipitates and homogeneous surface (see Figure 4-3), being consistent with the fact that the interfacial elastic energy of the heterostructure is gradually decreased with the increase of film thickness [71]. Z-contrast images of films grown from both processes are displayed in Figure 4-4 (a)-(d). Once again, the observation confirms that both films are continuous; see Figure 4-4 (a) and (c). The mean value of the film thickness for both films is estimated to be 50 nm. It is remarkably to note that high density of stacking faults is identified to be homogeneously distributed throughout the whole YBCO thickness for both films. Importantly, using FH, the film presents higher amount of short stacking faults with extension ranging from 10 to 20 nm homogeneously dispersed (see Figure 4-4 (b)), compared with the film grown from the CTA process (see Figure 4-4 (d)). The shortened stacking faults extension has been proposed to play vital importance for tuning nanostrain landscape within YBCO films, being thus very promising for enhancing the vortex pinning properties of YBCO thin films [55], as will be further discussed in Chapter 5.

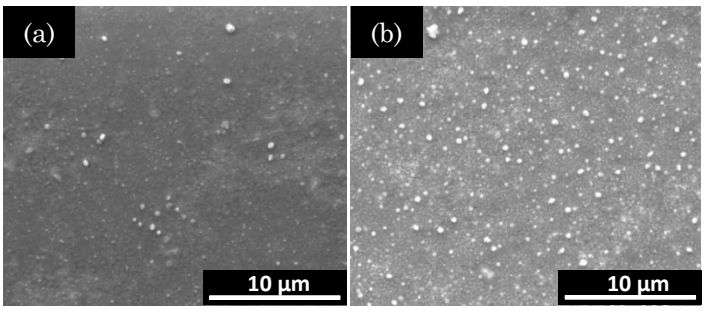

Figure 4-3: SEM micrographs of 50 nm YBCO films grown from (a) CTA 810 °C (20+10) and (b) FH 810 °C (20+10) process, respectively.

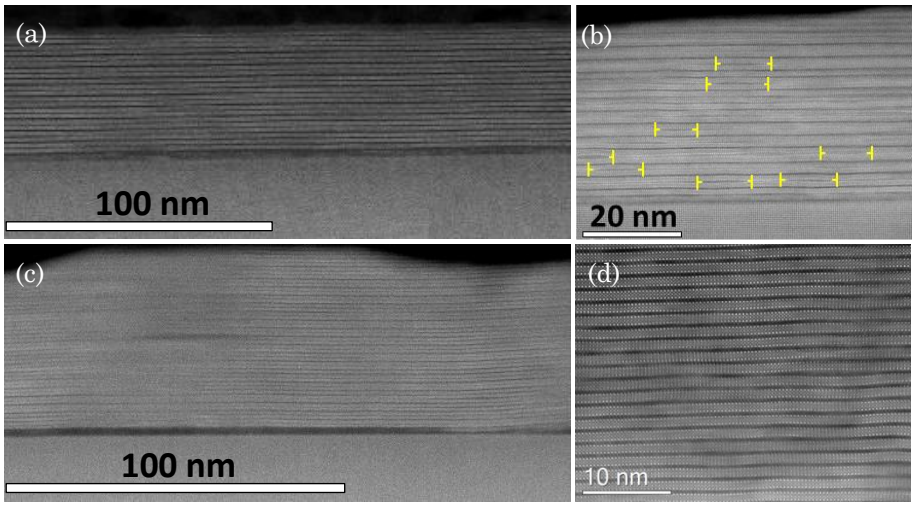

Figure 4-4: ADF Z-contrast images of 50 nm YBCO ultrathin films grown from the (a)-(b) FH 810 °C (20+10) and (c)-(d) CTA 810 °C (20+10) process.

Additionally, both films present high texture quality ($\Delta\omega = 0.6 \pm 0.1^{o}$ and $\Delta\phi = 1.0 \pm 0.1^{o}$). Meanwhile the strain values along the c-axis direction obtained for the 50 nm YBCO films grown from the FH and CTA process are estimated to be 0.25 ± 0.02 % and 0.23 ± 0.01 %, respectively. These values are higher than thicker (250 nm) pristine films obtained by solution deposition approach [54, 65]. The study of its influence on the vortex pinning properties will be discussed below.

The superconducting properties of the 50 nm YBCO films grown from the CTA and FH processes were routinely analyzed by SQUID measurements. The J_c^{sf} (J_c at self-field) values for both films were estimated to be $J_c^{sf}(5K)$ = 28.2 ± 1.5 MA/cm² and $J_c^{sf}(77K)$ = 2.5 ± 0.3 MA/cm², which are in the similar level as 250 nm pristine YBCO thin films grown from both FH and CTA processes (Chapter 3). Both films present onset T_c values of 87.1 ± 0.5 K, which are lower than the CTA thicker (~250 nm) pristine films (T_c = 90.5 ± 0.5 K). We attribute the degradation of T_c to the highly distorted YBCO lattice associates with the insertion of high density of stacking faults, taking into account that the films with high texture and morphology quality.

In Figure 4-5, we present the plots of normalized critical current density J_c/J_c^{sf} as function of magnetic field (H//c) measured at 5 K. When comparing the crossover magnetic field, H* which was determined at 90% of J_c^{sf} decrease (see subsection 1.3), between the film grown from the FH process and that grown by CTA, we could see that there exists a slightly move of $\mu_0 H^*$, giving a smoother $J_c(H)$ dependence. This could be ascribed to the presence of high amount of short stacking faults, as identified from the analysis from the Z-contrast images (Figure 4-4 (b)). The result, therefore, indicates that the extension of the stacking faults influence the nanostrain landscape (amount and distribution), and ultimately determine the vortex pinning efficiency of YBCO thin films, in agreement with the precious observation achieved in YBCO nanocomposite system [55].

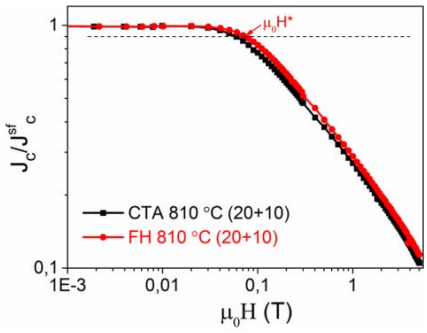

Figure 4-5: Magnetic field dependence of the normalized $J_c(H)/J_c^{sf}$ at 5K for the pristine 50 nm YBCO ultrathin films grown from the CTA 810 °C (20+10) (black square) and FH 810 °C (20+10) (red circle), data were obtained via SQUID measurement with H//c.

In conclusion, FH process allows the growth of continuous TFA-YBCO ultrathin films in a large thickness window (10-50 nm). Additionally, the presence of short stacking faults induced by the FH process leads to an enhancement of vortex pinning efficiency. Therefore, the FH process will be widely used for the growth of YBCO ultrathin films in the following work.

4.1.2 The influence of annealing time

In order to disclose the possibility of obtaining continuous YBCO ultrathin films by tuning growth kinetics, the growth of 50 nm YBCO films was carried out using FH 810 °C process annealed for (20+10) min, (20+30) min and (60+30) min. The films were firstly investigated by means of SEM observation, as shown in Figure 4-6. As it can be clearly seen in the micrographs, the film grown from the FH 810 °C (20+10) process has a dense, homogeneous surface with negligible amount of precipitates, as shown in Figure 4-6 (a). Further increase of annealing time to (20+30) and (60+30) min induces severe film dewetting (Figure 4-6 (b) and (c)), indicating that the fully converted ultrathin films obtained from the FH 810 °C (20+10) process in a metastable state where a new equilibrium state can be reached via a slow atom diffusion, similar phenomenon occurs for the films with larger thickness (≥ 150 nm) in the previous work based on the MOD approach [71].

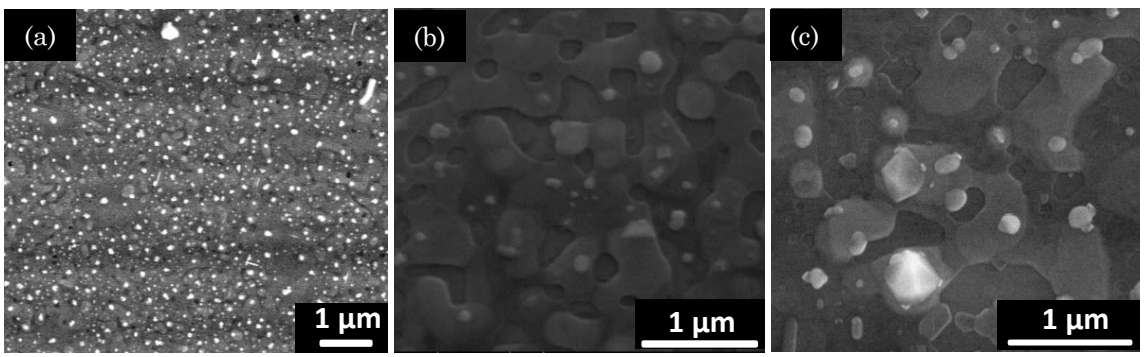

Figure 4-6: SEM micrographs of 50 nm YBCO ultrathin films grown following the same conditions (FH 810 °C) except for the annealing time, i.e. (a) (20+10) min, (b) (20+30) min and (c) (60+30) min.

Then, microstructure was further characterized by STEM analysis. Figure 4-7 displays low resolution cross-sectional STEM images of 50 nm YBCO ultrathin films grown from the (a) FH 810 ºC (20+10) and (b) FH 810 ºC (60+30), respectively. Figure 4-7 (a) confirms that the YBCO ultrathin film grown from short annealing time is continuous. From Figure 4-7 (b), it is identified that the FH 810 ºC (60+30) film displays severely dewetted regions cross the whole layer, where the substrate surface is partially exposed due to due to the absence of any coverage outside the islands.

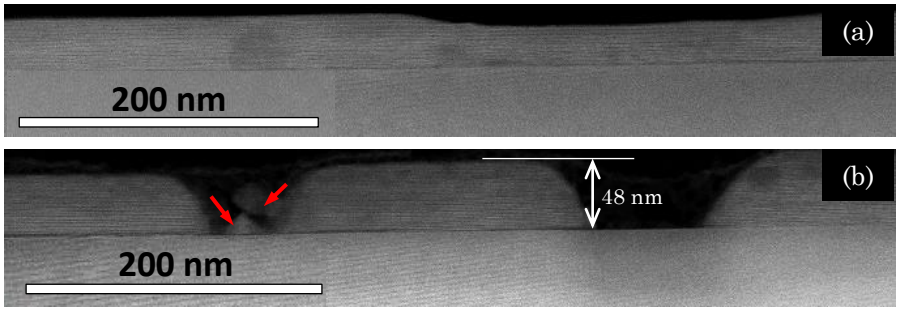

Figure 4-7: Cross sectional STEM image of 50 nm YBCO ultrathin films grown from the (a) FH 810 ºC (20+10) and (b) FH 810 ºC (60+30) process.

In order to experimentally investigate the influence of annealing time on the superconducting properties of the ultrathin films, SQUID measurements were performed. In Figure 4-8 (a), the granularity effect, which is characterized by the shift to positive fields of the maximum magnetization in magnetic hysteresis loops [170, 193], is identified in the films with dewetted regions. The existing dewetted areas promote the formation of constrictions making the sample behaves as a granular material and the current percolation is reduced [170], leading to significant degradation of current-carrying capability (see Figure 4-8 (b)).

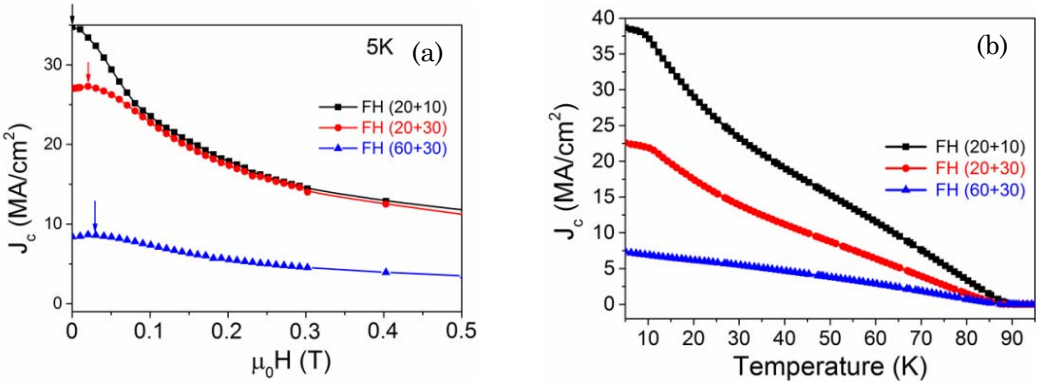

Figure 4-8: (a) J_c at 5 K evolution with magnetic field and (b) temperature dependence of J_c^{sf} for the 50 nm YBCO//LAO films grown from the FH 810 ºC (20+10) (black square), FH 810 ºC (20+30) (red circle) and FH 810 ºC (60+30) (blue triangle) processes.

Consequently, a shortened annealing time is needed for obtaining high quality heteroepitaxial YBCO ultrathin films.

4.1.3 The influence of growth temperature

In this subsection, we present our investigations of the influence of growth temperatures on the microstructure and superconducting properties of YBCO ultrathin films, where three growth processes were applied, i.e. FH 750 °C (20+10), FH 810 °C (20+10) and FH 830 °C (20+10).

HRXRD θ-2θ scans were carried out for the TFA-YBCO ultrathin films grown from FH 810 °C (20+10) and FH 830 °C (20+10), respectively, as shown in Figure 4-9. It is observed in all the XRD patterns that besides the LAO (l00) Bragg reflections, it is also appear the (00l) oriented YBCO reflections, indicating c-axis preferred orientation of the YBCO. However, intermediate phases such as $Y_2Cu_2O_5$ (Y225) have also been detected for the film grown at 830 °C. The presence of more intense secondary phase Bragg peaks for the film grown at 830 °C should be accounted for the fast growth of YBCO phase, which may trap some secondary phases due to the limited atom diffusion [171]. This phenomenon is in agreement with the observations which have been presented in Chapter 3 for 250 nm YBCO//LAO films following similar growth supersaturation conditions.

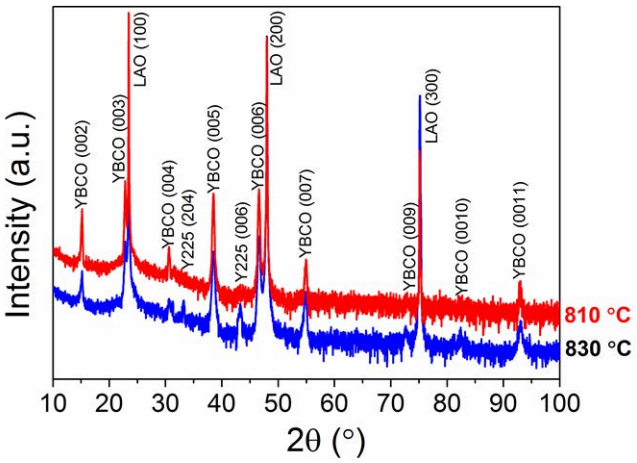

Figure 4-9: HRXRD θ-2θ scans of 50 nm YBCO//LAO films grown from FH 810 °C (20+10) (red) and FH 830 °C (20+10) (blue), respectively.

Additionally, surface morphological investigation via SEM observation indicates that the film grown by the FH 750 °C (20+10) process (Figure 4-10 (a)) displays high density of large pores and small amount of randomly oriented grains. While the film grown from FH 810 °C (20+10) process presents a homogeneous surface with a small amount of precipitates and a negligible concentration of pores, as shown in Figures 4-10 (b). In contrast, the surface of the film grown from the FH 830 °C (20+10) process appear to be severely inhomogeneous with some anomalous bright regions appearing in the SEM image, as shown in Figure 4-10 (c).

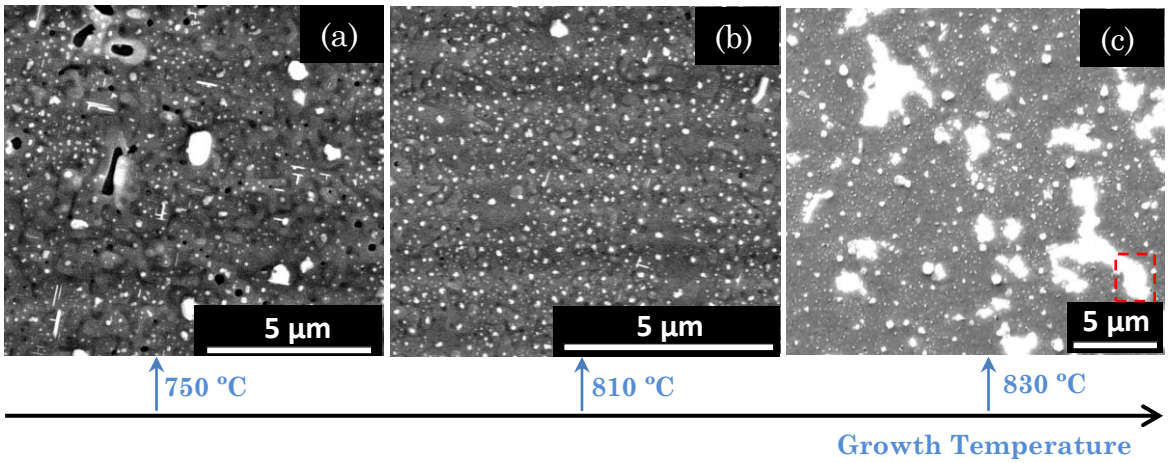

Figure 4-10 SEM micrographs of 50 nm TFA-YBCO films grown following the growth process of (a) FH 750 °C (20+10); (b) FH 810 °C (20+10) and (c) FH 830 °C (20+10).

A higher amplification SEM micrograph focusing on one bright area (from Figure 4-10 (c)) is presented in Figure 4-11 (a). As can be clearly seen, this bright region presents a pronounced dewetting character, where an anomalous pit appears within the layer with apparent lateral faces being in a wandering manner. It is worth noting that some cylindrical-like grains distribute within this region. On the other hand, EDX analysis was also employed in order to disclose the chemical composition of the bright regions. We analyzed the point from the marked area in Figure 4-11 (a) and the corresponding EDX spectrum is shown in Figure 4-11 (b). The EDX analysis demonstrates the presence of La, Al and O, which are in good accordance with the components of the single crystal substrate: $LaAlO_3$. In contrast, the peaks of YBCO components (i.e. Y, Ba and Cu) are negligible, indicating a full exposure of LAO. Therefore, it is reasonable to conclude that a full migration of the YBCO film occurs in these regions.

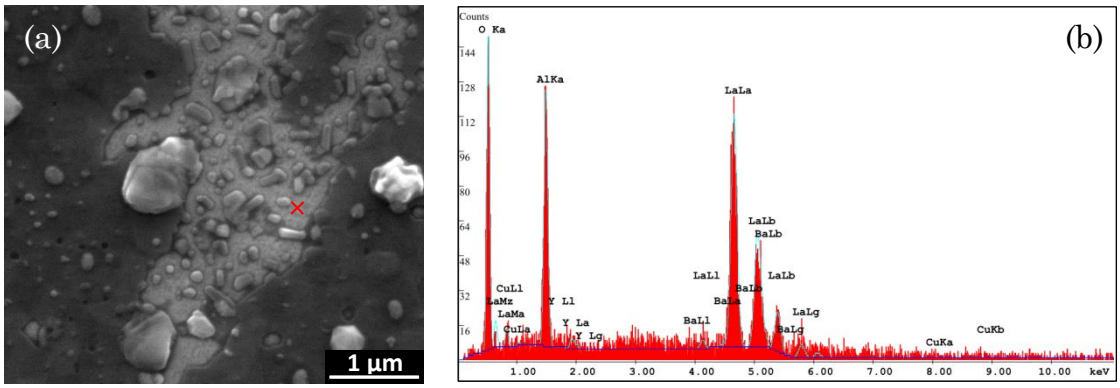

Figure 4-11 (a) a higher resolution SEM micrograph focusing on the squared region in Figure 4-10 (c); (b) EDX spectra of the point marked in Figure 4-11 (a).

The superconducting properties of the 50 nm YBCO ultrathin films grown at different temperatures were measured inductively by SQUID measurement. Figure 4-12 displays J_c vs magnetic field plots measured at 5K. For the film grown at 750 °C, we can observe the

appearance of a peak in the plot at positive fields (~0.1 T), indicating the residual porosity induced granularity effects [170] appears in this film leads to a J_c^{sf}(5K) = ~6.1 MA/cm², which is a significant degradation compared with the dense film (J_c^{sf}(5K) = ~35.2 MA/cm²) grown at 810 ºC without any influence of this detrimental effect. Unfortunately, the severely dewetting effect and the appearance of secondary phases within YBCO film grown at 830 ºC result in the absence of superconducting properties for the film.

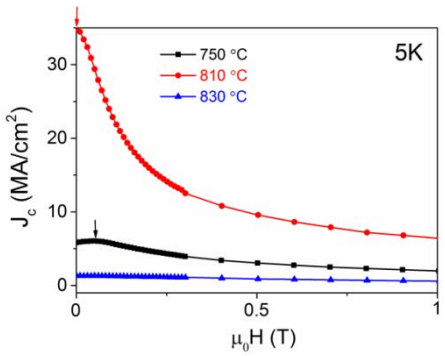

Figure 4-12 Magnetic field dependence of the critical current density measured at 5K of the 50 nm TFA-YBCO film grown at temperatures of 750 ºC, 810 ºC and 830 ºC.

Therefore, we can conclude that the optimal growth temperature is 810 ºC to achieve continuous YBCO ultrathin films with a high homogeneity and good superconducting properties.

4.1.4 The influence of mismatch strain from substrate

The pristine YBCO ultrathin films (≤ 50 nm) were successfully grown on top of LAO single crystals using the optimized growth condition: FH 810 ºC (20+10). In this subsection, we turn our interest to explore the influence of mismatch strain from substrate on the nucleation, microstructure and superconducting properties of YBCO ultrathin films grown from this optimized thermal process. The in-plane lattice mismatch rates of YBCO with the substrates (LAO and STO) are summarized in Table 4-1.

Table 4-1: A summary of lattice parameters of substrates: LAO and STO and the corresponding mismatch strain to YBCO, ε, is also given by ε (%) = 100 x (a_0Substrate – a_0YBCO)/a_0YBCO.

Material	Crystal structure	a_0, b_0 and c_0, Lattice Parameter (Å)	Mismatch to YBCO (%)	
			a	b
YBCO	perovskite	a_0 = 3,823 b_0 = 3,886	-	-
$LaAlO_3$	Pseudo cubic	3,792	-0,81	-2,42
$SrTiO_3$	Cubic	3,905	2,14	0,49

High resolution XRD scan was performed to have a more accurate study of the phase composition of the 50nm YBCO//LAO and 50nm YBCO//STO films grown from the FH 810

ºC (20+10) process, as shown in Figure 4-13. The 50 nm YBCO//LAO film presents only c-axis oriented grains. For the YBCO//STO film, random oriented YBCO grains, i.e. YBCO (103) are also identified. This phenomenon is probably due to the modified Gibbs free energy barrier for YBCO nucleation associated with the different strain energy presented in both substrates [45, 194]. The result indicates that the energy barrier is different for different strained systems at a given supersaturation, and thus, different optimized growth conditions is needed to achieve desired YBCO nucleation.

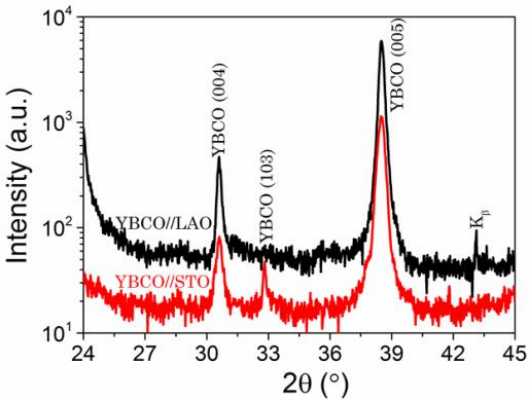

Figure 4-13: 1D θ-2θ XRD diffraction pattern of the 50nm YBCO//LAO and 50nm YBCO//STO films grown from the FH 810 ºC (20+10) process.

Figures 4-14 (a) and (b) display SEM micrographs of 50 nm YBCO films grown from the FH 810 ºC (20+10) process on LAO and STO single crystals, respectively, where the influence of mismatch strain on the film surface morphology can be clearly observed. The film grown on LAO displays a homogeneous surface with negligible porosity; see Figure 4-14 (a). The 50 nm YBCO//STO film presents a high amount of holes. This result demonstrates that film grown on STO single crystal presents a higher tendency to dewet than with LAO substrate, in agreement with the previous prediction [71] that the tensile strain generated associated with the YBCO/STO lattice misfit shows higher tendency for the formation of dewetting regions compared with the compact strain. It is also remarkable that we observed a small fraction of randomly oriented grains distributed on the film surface, consistently with the result previously detected from the XRD technique.

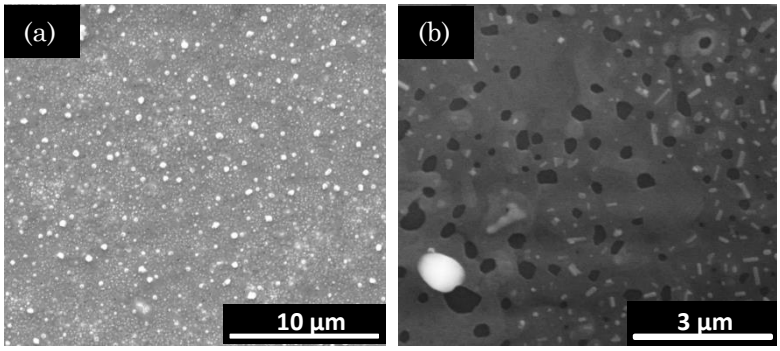

Figure 4-14: SEM planar morphology of (a) 50 nm YBCO//LAO and (b) 50 nm YBCO//STO film grown from the optimized FH 810 ºC (20+10) process.

Moreover, the plots of Zero Field Cooled (ZFC) magnetization dependence with temperature of the films are presented in Figure 4-15. It is clear seen that the 50 nm YBCO film grown on STO shows degraded T_c compared with the one on LAO, and it is consistent with the previous observation [187] which has attributed the T_c difference to the substrate-induced strain effects. Moreover, for the film grown on STO, we observe a broadened transition width (ΔT_c) compared with the one on LAO. This broadening can be attributed to dewetting regions induced low current percolation.

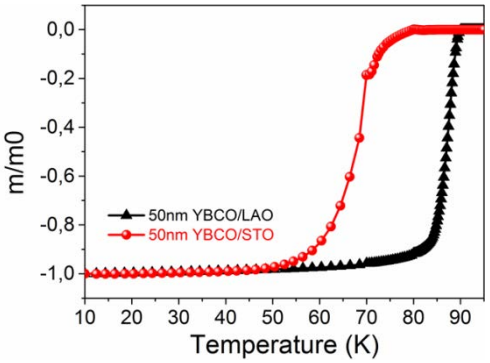

Figure 4-15: Temperature dependence of Zero Field Cooled (ZFC) magnetization of 50 nm YBCO films grown on top of LAO (black triangle) and STO (red ball) substrates from the FH 810 °C (20+10) process.

In this case, we can conclude therefore that LAO substrate is less prone to form dewetted regions in YBCO ultrathin films, making it more compatible to the optimized growth conditions for a valid preparation of high quality YBCO ultrathin films.

4.2 Thickness dependence of the microstructure and superconducting properties of pristine YBCO ultrathin films

In order to evaluate the thickness dependence of the microstructure and superconducting properties of YBCO thin films, we prepared a series of films with thicknesses ranging from 5 nm to 250 nm processed following the FH annealing process. For comparison, some results from the CTA annealing process are also presented in this section. It is worth mentioning that the annealing times for the growth of 100-250 nm films is (150+30) min and those with thicknesses of 5-50 nm are (20+10) min.

4.2.1 Microstructure of ultrathin YBCO films

The texture and phase composition of YBCO ultrathin films was firstly analyzed by X-ray diffraction techniques. Firstly, it is worth mentioning that the 50 nm YBCO films are epitaxially grown on the substrate. Unfortunately, however, the 2D-GADDS patterns give

anomalously weak signals and they become featureless when thickness is reduced down to 25nm.

We conducted high resolution 1D θ-2θ x-ray scan (see subsection 2.2.2.1) in order to identify the phase composition and grain orientation of films with thicknesses ranging from 5 nm to 250 nm, as shown in Figure 4-16 (a). It is observed that YBCO thin films only show (00l) Bragg reflections, demonstrating that c-axis oriented YBCO grains can be obtained throughout the investigated film thickness. The result suggests, therefore, that c-oriented YBCO thin film can be obtained in an extended thickness window down to 5 nm for CSD-based YBCO thin films, in a similar thickness limitation compared with the vacuum-based deposition methodologies [180, 187, 195]. However, we note that the (005) YBCO peaks are shifted to smaller angles when the film thickness decreases below 25 nm, which denotes an increase in the c-axis lattice parameter [187].

Texture analyses were carried out by the rocking curve measurement (ω-scan) measured on the (005) YBCO reflection and the ϕ-scan of the (104) YBCO reflection, respectively. The FWHM values of the rocking curves (Δω) decrease from ~1.2º to ~0.5º when film thickness increases from 5 nm to 250 nm (Figure 4-16 (b)), point us to the conclusion that the out-of-plane grain alignment of YBCO films present strong thickness dependence. This tendency, similar to what other authors have been previously reported for YBCO films deposited by sputtering method [196]. Moreover, the 25-50 nm YBCO ultrathin films show good in-plane texture confirmed by the FWHM (Δϕ) of (104) YBCO reflections: Δϕ = 1.0 ± 0.1º, similar level as has been illustrated in the study of 250 nm YBCO films in Chapter 3.

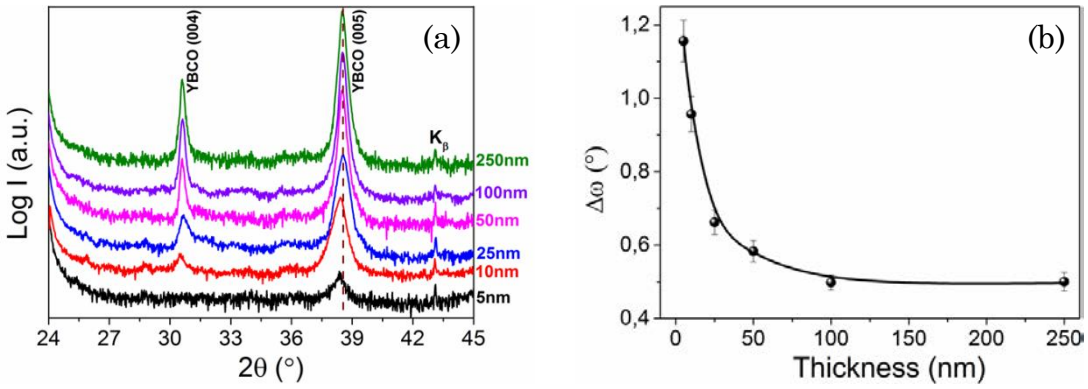

Figure 4-16: (a) 1D XRD θ-2θ patterns of YBCO films with different thicknesses ranging from 5 nm to 250 nm; (b) the Δω values evolution with film thicknesses. All the films were grown from the FH thermal process with different annealing times of (150+30) min and (20+10) min for films with thicknesses of 100-250 nm and 5-50 nm, respectively.

Cross-sectional STEM investigations performed on a 10 nm YBCO ultrathin film disclosed an intricate microstructure of the films characterized by a highly distorted YBCO matrix; see Figure 4-17. Figure 4-17 (a)-(b) show Z-contrast images of the film grown from the FH 810 ºC (20+10) process. It is clearly seen that a high density of Y124 intergrowths, as well as several Y125 intergrowths (indicated by arrows), intercalate within the YBCO

matrix, leading to a highly distorted lattice and strongly bended (00l) YBCO planes. In Figure 4-17 (c), it is shown a Z-contrast image of a 10 nm YBCO film grown from the CTA 810 ºC (20+10) process. We should remind, however, that the formation of the 10 nm YBCO film from the CTA 810 ºC (20+10) process was characterized by dewetting effects, as has been illustrated in subsection 4.1.1. It is observed in the STEM image (4-17 (c)) that the film is full of Y248 intergrowths. Y248 intergrowths are usually nucleated at incoherent interfaces and highly mismatched epitaxial interfaces to release the interfacial energy [54, 113]. Therefore, it is reasonable to consider that the mismatch YBCO//LAO interfacial stress acts as the main driving force for the generation of this microstructural landscape, taking into account that the CTA 250 nm YBCO films (see Figure 3-22 (b)) are nearly free of secondary defects.

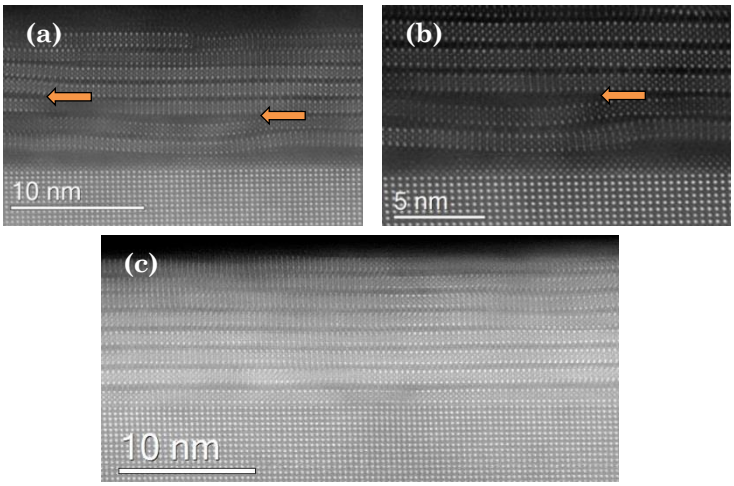

Figure 4-17 Z-contrast images of 10 nm YBCO films grown from the (a)-(b) FH 810 ºC (20+10) and (c) CTA 810 ºC (20+10) process.

To follow the Y123 phase evolution with film thickness, after full phase conversion, we can also calculate the integrated area of X-ray diffraction patterns of (005) YBCO Bragg peaks from Figure 4-16 (a), as shown in Figure 4-18 (a). It is clearly seen from the plot that the integrated intensity values display a non-linear relationship with the film thicknesses. Nevertheless, from the XRD (Figure 4-16 (a)), all the films are free of secondary phases after growth. It is particularly striking to note that the CTA 250 nm pristine YBCO film presents higher integrated area compared with the FH 250 nm pristine YBCO film, in agreement with the observed defects scenario from the STEM analysis that carried out in Chapter 3, section 3.2. This phenomenon should be related with the intergrowth induced lattice distortion, which influences the X-ray diffraction, leading to the degradation of integrated intensity. The results reflect, indirectly, the existence of stacking faults, although no clear evidence can be found in XRD plot contrasting to the previous report [197]. Figure 4-18 (b) displays the ratio of Y123 phase (r_{Y123}) evolution with film thicknesses. Note that the values of r_{Y123} increase linearly with the increase of film thickness. Especially, films with thickness ≤ 25 nm display very low r_{Y123} values (< 20%),

evidencing the highly distorted lattice for these films, which are in consistence with the previous STEM observation. In this scenario, it is very clear that the lattice distortion induced by the lattice mismatch in the form of Y248 intergrowth becomes severe when decrease the film thickness.

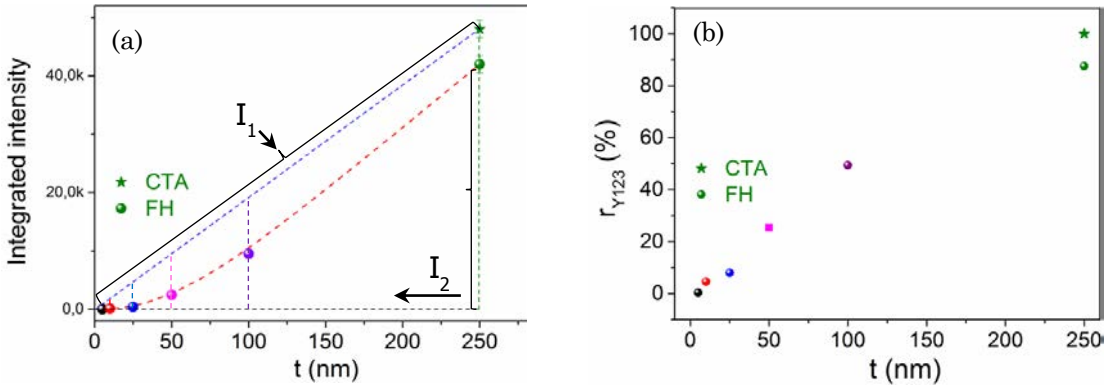

Figure 4-18 (a) Thickness dependence of the integrated area of (005) YBCO Bragg peak in the XRD patterns in Figure 4-16 (a); (b) normalized integrated area of the (005) YBCO peak dependence with film thickness.

$r_{Y123}(\%) = 100 * I_1/I_2$; where we assume that the CTA 250 nm YBCO films are 100% of Y123 phase.

At the same time, the quantification of the averaged strain in c-axis direction for the whole film volume was achieved by performing HRXRD θ-2θ scan and determined via Williamson-Hall approach, in order to supplement the TEM analysis which solely provides local structural information. In Figure 4-19 (a) it is summarized the strain values for pristine YBCO films with thicknesses ranging from 10 nm to 250 nm grown from either FH or CTA processes. As a general trend, the strain values increase with the decrease of film thickness for films grown from the same heating process. While a crossover values appears (~0.25%) when the film thickness decrease down to 50 nm. It is also worth noting that the increment of strain becomes more drastic when the film thickness decreases below 25 nm, this may be attributed to the severely distorted YBCO lattice in c-axis direction as observed though TEM analysis. Therefore, the release of mismatch interfacial energy which is accumulated at the YBCO//LAO interface induces highly strained YBCO matrix at the initial stage of YBCO growth.

To calculate the c-axis lattice parameter, HRXRD θ-2θ scans with longer collecting time were carried out and determined by using the method introduced in subsection 2.2.2.1. Figure 4-19 (b) displays the evolution of c-axis lattice parameters of the YBCO films (10 - 250 nm) compared with the referenced bulk values. The c-axis lattice parameter shows an increasing trend with the decrease of film thicknesses, ranging from 11.69 Å to 11.87 Å, while the trend becomes noticeable when film thickness below 50 nm. The c-axis lattice expansion has usually been observed in the in-situ grown YBCO ultrathin films, attributing either to the lattice misfit induced lattice distortion [79, 187, 198] or to the oxygen content [190, 199]. Nevertheless, a different structural defects landscape has emerged in the ex-situ

solution-based YBCO ultrathin films characterized by the insertion of high density of Y248 intergrowths which displays higher c-axis lattice parameter: c = 27.22 Å. Thus, the results indicate that the presence of a high density of Y248 intergrowth inserted within Y123 matrix influences the lattice parameter in c-axis direction. Additionally, the in-plane (a-, b-axis) parameters were also estimated by performing XRD direct in-plane measurements (subsection 2.2.2.1). Both 25 nm and 50 nm films present constant in-plane parameters of a = 3.83 ± 0.01 Å and b = 3.86 ± 0.01 Å, demonstrating the in-plane parameters were barely modified when the misfit stress can be released with the formation of secondary defects (i.e. Y248 intergrowth).

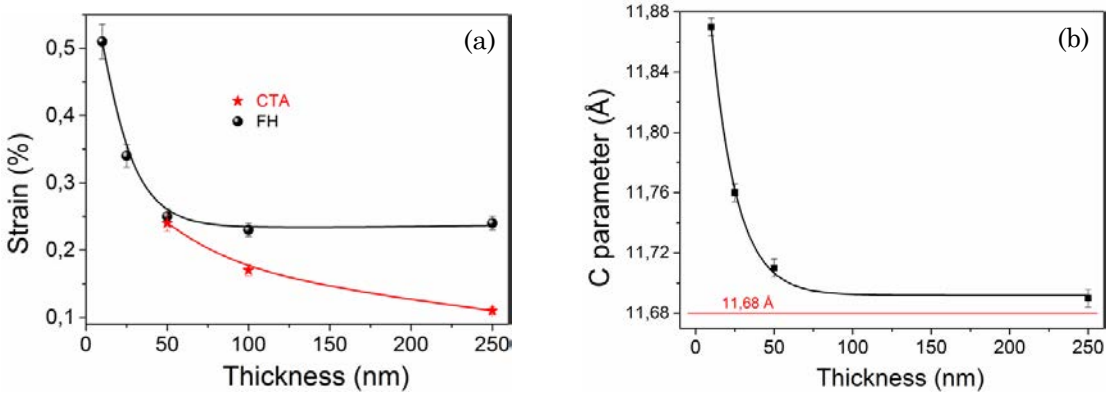

Figure 4-19: (a) Thickness dependence of strain values in c-axis direction for YBCO films grown from CTA and FH processes; (b) the evolution of c-axis lattice parameter with film thickness of the films grown from the FH process.

4.2.2 Morphological characterization

The surface morphology of CSD-based YBCO films are always observed to be rough, although these films displayed promising superconducting properties. Generally, the surface roughness comes from any sources related to the generation of surface inhomogeneity, such as residual pores or pinholes, out-of-plane c-axis growth, surface outgrowths or secondary precipitate, as well as other sources [200]. The early stage of YBCO growth should play an important role for the formation of the film surface morphology.

To quantitatively study the formation of the surface morphology at the initial growth stage, an AFM analysis was carried out on both as-pyrolyzed and fully converted YBCO ultrathin films, as shown in Figure 4-20. It is remarkable to note that outgrowths have already formed even at the initial stage of growth, compared with the as-pyrolyzed YBCO ultrathin film (see Figure 4-20 (a)). The as-deposited YBCO ultrathin film displays a homogeneous surface by covered close-packed and well-aligned grains with unit cell height. The image obtained on the 5 nm film displays outgrowths with height of ~15-25 nm and size of ~40-60 nm, indicating the growth event is still at the early stage. Note that the

height and size of these outgrowths are gradually increased when the film thickness increase up to 50 nm; see Figure 4-20 (c) and (d). From the topographical images, it is also visible that some pinholes start to appear for YBCO films with thickness ≥10 nm. Overall, the height of these outgrowths is well above film thicknesses. This is further confirmed by the line-scan profile taken from the corresponding image in a randomly selected line AB. Interestingly, many terraced islands shows growth steps of 1-2 nm high and ~20 nm long are visible in the 5 nm film; see the line-scan profile in Figure 4-20 (b). Similar phenomenon was observed on ultrathin YBCO films deposited on a YBaCuNbO buffer layer in the previous report [199], in which the nucleation and growth of films have been suggested to be governed by a step-flow mode. It should be mentioned, however, that CSD-based YBCO nucleation and growth follows the Volmer-Weber growth mode and so continuous films arise as a result of individual grain merging after the appearance of YBCO nuclei [38]. Therefore, the appearance of these terraced islands, maybe attribute to the limited atomic diffusion at in-plane direction during the merging process of YBCO nuclei.

Furthermore, the root-mean-square roughness (R_{rms}) was also calculated from AFM measurements over 2 × 2 μm^2 areas. Figure 4-21 presents R_{rms} values as function of fully converted film thickness compared with as-deposited film and as-treated LAO. Evidently, an increase in film thickness is accompanied by an increase in the roughness, from 4.1 nm to 34.3 nm when the film thickness increased from 5 nm to 250 nm, which are significantly roughened compared to the as-treated LAO (R_{rms} = ~0.33 nm) and as-deposited YBCO film (R_{rms} = ~1.55 nm). Although no obvious relationship can be observed between film roughness and superconductivity [22], epitaxially grown YBCO ultrathin films with ultralow roughness is vital in superconducting nanowire single photon detectors [180] and also as buffer layer in functional oxide heterostructures such as HTS coated conductors [132]. Our present analysis of YBCO film morphology point out that several surface defects such as residual porosity or pinholes, surface outgrowths and terraced islands are the main sources of film roughness, which have been observed at the early stage of YBCO growth. In the particular case of the CSD-based YBCO nucleation and growth mode it becomes indispensable further optimized the processing condition for reaching reliable manufacturing methodologies of YBCO ultrathin films, in order to reach epitaxial YBCO films with high flatness and ultimately reach the applications in the microwave scattering and for the stacking of multi layers. For this purpose, more experimental work is still needed. At this stage, our observation verifies that the surface morphological characteristics of the as-deposited YBCO ultrathin film present high potential to act as interfacial seed layer to promote the epitaxial growth of YBCO nanocomposites using preformed nanoparticles, which has been frequently reported in the resent years [118, 125, 132].

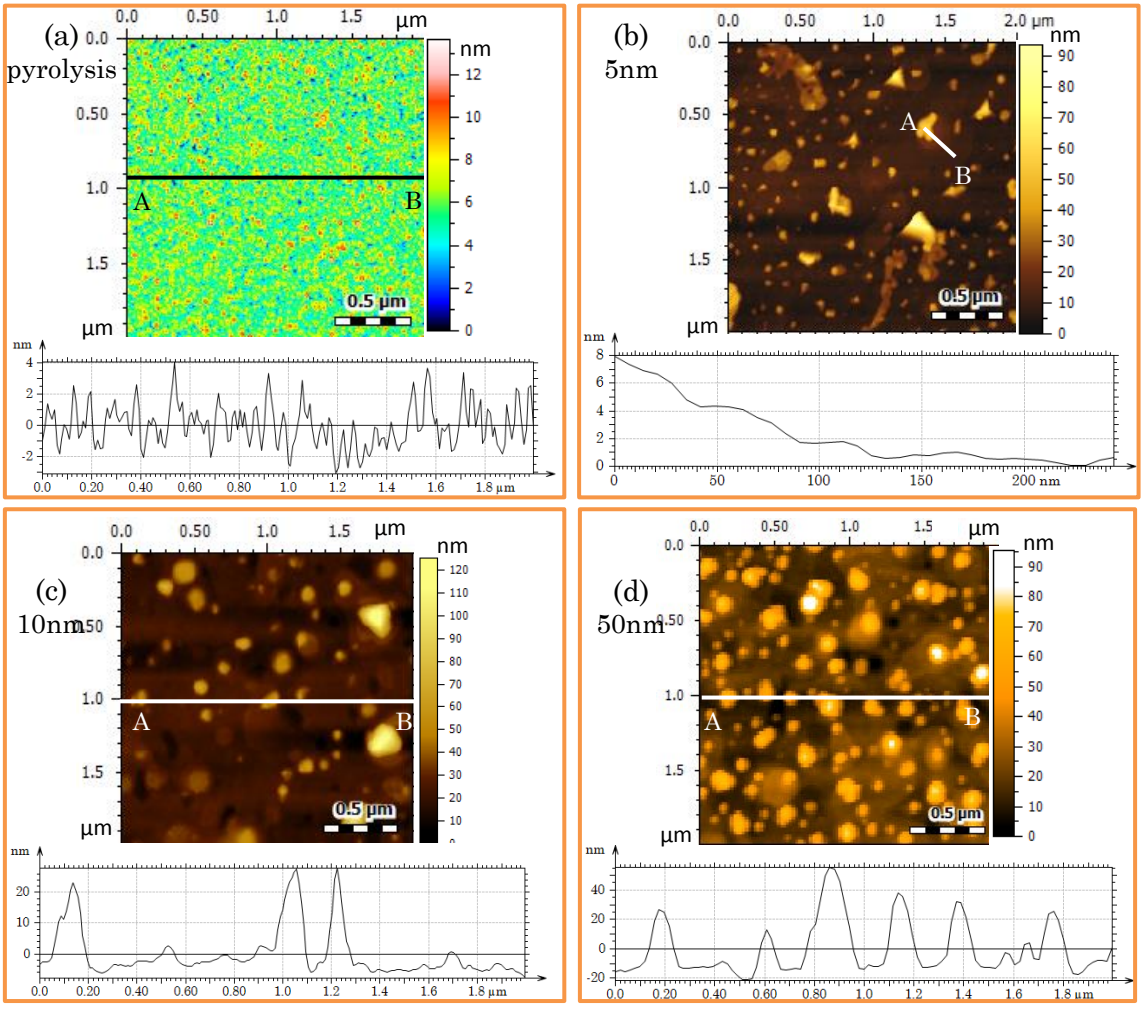

Figure 4-20: AFM analysis of (a) as-pyrolyzed YBCO (10nm) film and fully converted YBCO films with thickness of (b) 5 nm, (c) 10 nm and (d) 50 nm, while the line-scan profile along the AB line is shown below the corresponding topographical image.

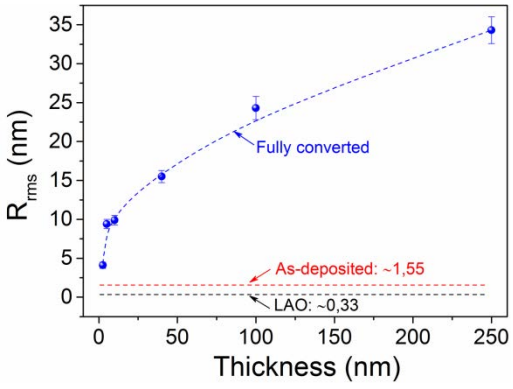

Figure 4-21: Root-mean-square roughness (R_{rms}) evolution with film thickness for fully converted YBCO ultrathin films with thicknesses ranging from 5 to 250 nm compared with an as-treated LAO and as-pyrolyzed YBCO film. The values of R_{rms} were evaluated from a 2 × 2 µm² area scan from these films.

4.2.3 Superconducting properties of ultrathin YBCO films

The dependence of T_c and ΔT_c on the YBCO films thickness is shown in Figure 4-22 (a). It is noteworthy that T_c is nearly constant at 86.5 ± 1.5 K for films with thicknesses ≥ 25 nm, evidencing that the lattice mismatch induced YBCO lattice distortion do not influence on T_c at this thickness range. However, T_c values drop sharply for films below 25 nm. It has been previously reported that T_c was decreased in a strained YBCO films due either to the in-plane mismatch with the substrate [187, 201] or the strain induced oxygen deficiency/disorder [188, 189]. Note that further decrease or increase of the oxygenation time presents no improvement of T_c. Reasonably, it is believed that the T_c deterioration is dominated by the lattice distortion induced by the high density of Y248 intergrowth which were generated as a mechanism to release the mismatch stress. In addition, the ΔT_c gradually widened with the decrease of film thicknesses, consistent with the out-of-plane texture quality.

Figure 4-22 (b) displays $J_c^{sf}(5K)$ and $J_c^{sf}(77K)$ values evolution as a function of film thickness. We observe that J_c^{sf} values, both at 5 K and 77 K, keep constant values, i.e. $J_c^{sf}(5K)$ = 30.0 ± 2.0 MA/cm² and $J_c^{sf}(77K)$ = 3.2 ± 0.2 MA/cm², for films with thicknesses ranging from 50 nm to 250 nm. While a strong tendency of J_c^{sf} degradation is clearly observed when the film thicknesses decrease below 25 nm. The degradation of J_c^{sf} is accounted for the presence of a highly distorted interfacial layer which would probably quench the Cooper pair formation [54] and acts as a non-superconducting layer.

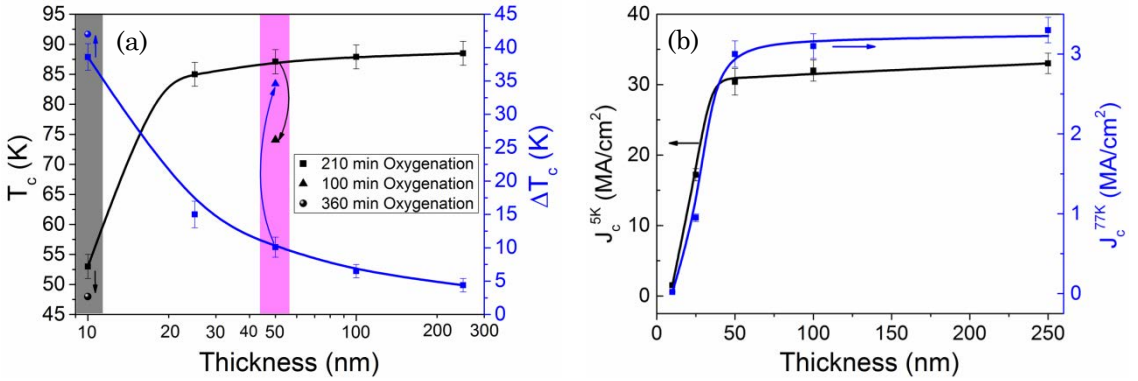

Figure 4-22: (a) Dependence of the T_c and ΔT_c with film thickness. (b) Thickness dependence of $J_c^{sf}(5K)$ and $J_c^{sf}(77K)$ values. Dots account for the mean value of each while error bars account for the statistical distribution.

4.3 YBCO nanocomposite ultrathin films

In this section, we explore how the decrease in thickness can influence the microstructure and the vortex pinning landscape in YBCO-BYTO ss-nanocomposite films. The BYTO nanoparticle concentration used in this study is 8 mol%, which is the optimized one in the previous studies [55, 65].

4.3.1 Structure characterization of ultrathin YBCO nanocomposite films

Figure 4-23 (a)-(d) shows X-ray diffraction patterns of YBCO-8 mol% BYTO ss-nanocomposite films with thicknesses of 25 nm, 50 nm and 250 nm. Integrated XRD θ-2θ patterns of fully grown films demonstrate (00l) YBCO oriented films; see Figure 4-23 (a). Note that the presence of BYTO is identified in the 250 nm nanocomposite film. All the films are epitaxially grown on top of LAO substrates, as shown in Figure 4-23 (b)-(d). It is noteworthy that the BYTO phase can be clearly identified for the film with thickness of 250 nm, indicating that BYTO nanoinclusions are formed under the FH processing condition. Two diffraction rings locating at 2θ = 30.1° and 2θ = 42.0° are identified, corresponding to BYTO (220) and BYTO (400) reflections, respectively, indicating that the random and epitaxial BYTO particles coexist within epitaxial YBCO matrix, in agreement with the previous investigations on the YBCO-BYTO nanocomposite films grown from the CTA process [55, 65]. Moreover, the BYTO (220) peak is very strong, leading to a high random fraction of 96%. However, the BYTO peaks become obscure when the film thickness decreased below 50 nm, due to the small amount of BYTO phase.

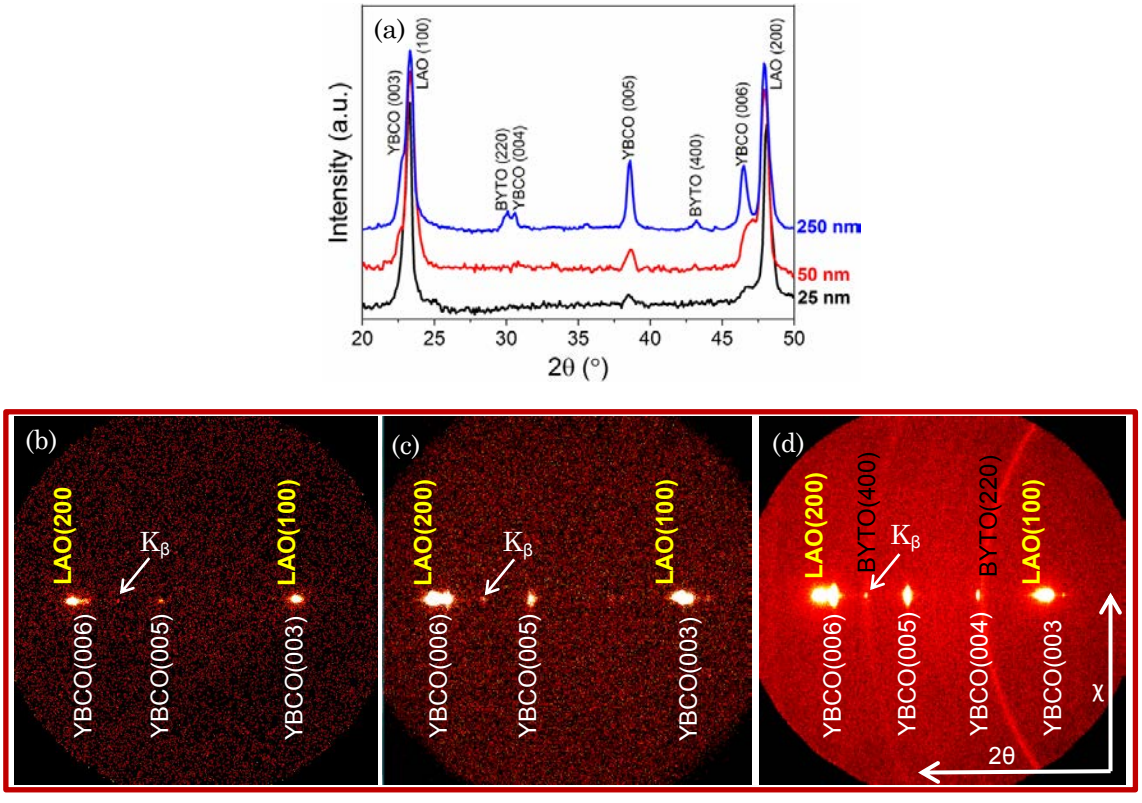

Figure 4-23: (a) Integrated X-ray diffraction θ-2θ scans of YBCO-8 mol% BYTO ss-nanocomposite films with thicknesses of 25 nm, 50 nm and 250 nm; 2D XRD patterns of fully grown (b) 25 nm, (c) 50 nm and (d) 250 nm YBCO-8 mol% BYTO ss-nanocomposite films.

Z-contrast images of the 250 nm YBCO-8 mol% BYTO nanocomposite films are shown in Figure 4-24. The low resolution STEM image reveals that BYTO nanoparticles are mostly distributed within the bulk of the film, although some nanoparticles are prone to aggregate leading to large nanoparticles with diameter sizes up to 80 nm; see Figure 4-24 (a). It is remarkable that almost all the nanoparticles are randomly distributed within the YBCO matrix, in accordance with the high random fraction (96%) estimated though XRD technique, which suggests that no nanoparticle has nucleated at the interface. The result demonstrates that the strong tendency to epitaxial nucleation of nanoparticles previously detected in ss-nanocomposite films [65, 77] can be basically avoided. Higher resolution Z-contrast images which are focused on a randomly oriented individual nanoparticle (Figure 4-24 (b)) and the coalescence of two nanoparticles (Figure 4-24 (c)), giving detailed observation of nanoparticles and the microstructural characteristics around them. It is important to note that the size of the individual particle is ~10-15 nm, however, nanoparticle aggregation results in cuboid-shaped particles with increased nanoparticle size. In this scenario, a high density of stacking faults is also formed.

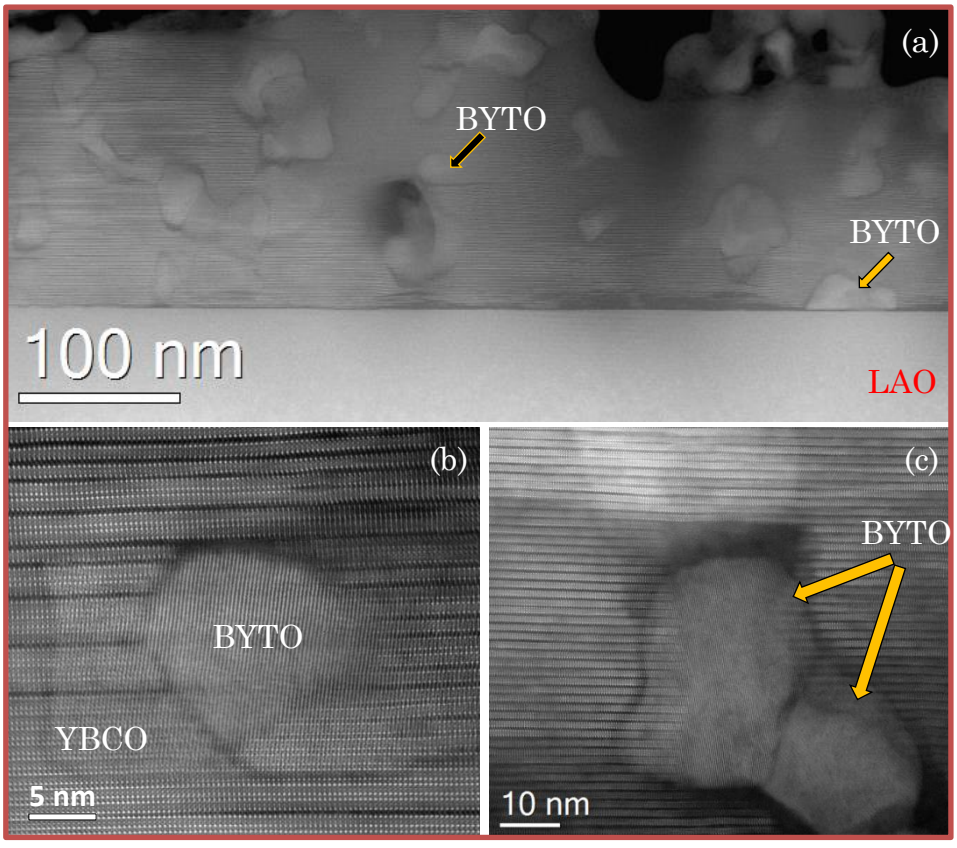

Figure 4-24: STEM images of the 250 nm YBCO-8 mol% BYTO nanocomposite film. (a) Low resolution STEM images with a general view of the films; (b)-(c) High resolution STEM images showing (b) random oriented and (c) agglomerated BYTO nanoparticles.

When decreasing the film thickness from 250 nm to 50 nm, the features of BYTO nanoparticles in YBCO ultrathin films is also analyzed by STEM, as shown in Figure 4-25 (a)-(d). Concerning the nanoparticle distributions, the low resolution STEM image, Figure

4-25 (a), reveals an anomalous landscape, from where large epitaxial nanoparticles are observed locating at the interface and the randomly oriented nanoparticles are scarcely seen, in contrast to the microstructure recently characterized for the CTA YBCO-BYTO ss-nanocomposites [65]. As it can be observed from higher resolution STEM images, any of the randomly oriented (Figure 4-25 (b)) and epitaxially grown (Figure 4-25 (c)) nanoparticles, coexist in the ultrathin nanocomposite film. Also, nanoparticle coalescence is observed and in this case it is much more dramatic since it covers the whole film thickness; see Figure 4-25 (d). Once again, all these nanoparticles are surrounding by stacking faults, resulting in a high density of long stacking faults inserted within the YBCO matrix.

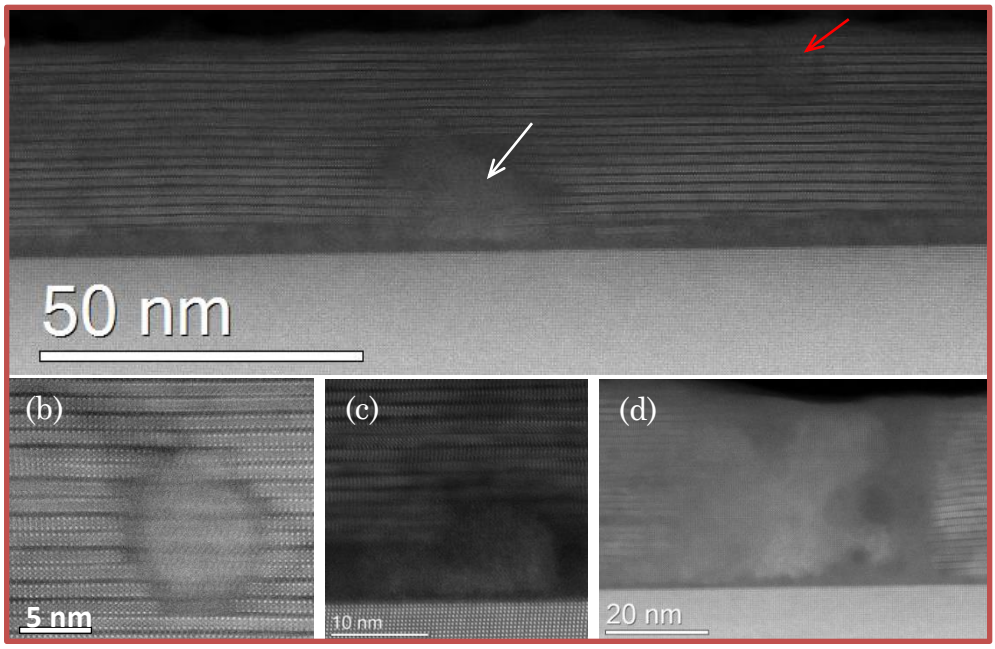

Figure 4-25: (a)-(d) STEM images of the 50 nm YBCO-8 mol% BYTO nanocomposite film. (a) Low resolution STEM image with a general view of the films; (b)-(d) high resolution STEM images showing (b) randomly oriented, (c) epitaxially grown and (d) agglomerated BYTO nanoparticles.

In this scenario, we believe that the diverse nanoparticles distribution landscape have their own thermodynamic and kinetics origins. At the present stage, it is still not possible to detect the BYTO behavior during the flash heating process using the XRD measurement, attributing to the approximate peak positions for BYF and BYTO phases, even though we know that kinetics and the thermodynamic barrier for BYTO nucleation is lower than epitaxial YBCO growth on LAO from quenching studies in the previous report [55]. As it has been illustrated in subsection 1.2.2.1, the homogeneous nucleation of a secondary phase within a YBCO film requires a larger driving force than the heterogeneous nucleation. From the growth kinetic investigations displayed in Chapter 3, it is proved that the FH process provides a large driving force for nucleation and enables the phase transformation with high kinetics. In this case, the ΔG^* difference between homogeneous and heterogeneous nucleation becomes negligible and, thus homogeneous nucleation of

nanoparticles within the volume of YBCO film becomes dominant. Therefore, a high nanoparticle random fraction (96%) can be obtained when YBCO ss-nanocomposite films are grown from our novel FH growth process. However, for YBCO nanocomposite ultrathin films, the nucleation sites provided within the volume of the film become inefficient because the thickness of the film is too close to that of the nanoparticle, leading to a fast nucleation and growth of epitaxial BYTO nanoparticles across the whole film. It is worth reminding that the YBCO phase from the precursors underwent a fast transformation process during the FH growth process, as it has been demonstrated in Chapter 3. In this case, atomic diffusion mostly occurs in YBCO tetragonal matrix (a= 3.9 Å, b = 3.9 Å c = 11.9 Å) which are significantly reduced compared with OF solid solution (a = 7.4 nm, b = 10.5 nm, c = 4.3 nm) [35] and especially the amorphous BYF phase. According to Euqation 1-14, 1-15 and 1-16, the activation energy for atomic diffusion is reduced when the diffusion event occurs in the dense YBCO microstructures. In this scenario, atomic diffusion of the BYTO nanoparticle composition occurs at low D condition while a decreased annealing time are achieved when FH growth process is used. In this case, the nanoparticles are confined within YBCO matrix during the high temperature annealing process, leading to a restrained nanoparticle coarsening. Accordingly, a tight control of nucleation and growth events of BYTO nanoparticles are proposed to be achieved by modifying supersaturation conditions via properly tuning $P(H_2O)$ or growth temperature [38, 55]. However, a proper optimization of other growth parameters is still needed to avoid the nanoparticle coalescence issue.

The YBCO c lattice parameter is barely modified for the YBCO nanocomposite films grown from the Ta added TFA precursors, as compared to the pristine YBCO films, with the same thickness. The results further confirm that there is no Ta substitution in YBCO matrix, as proposed in the earlier report [65]. Moreover, the out-of-plane strain displayed in the YBCO-8 mol% BYTO ss-nanocomposite are 0.29%, 0.33% and 0.42% for films with thickness of 250 nm, 50 nm and 25 nm, respectively.

4.3.2 Superconducting properties of ultrathin YBCO nanocomposite films

First of all, we would like to discuss the T_c and ΔT_c for YBCO-BYTO ss-nanocomposite films with thicknesses of 25 nm, 50 nm and 250 nm. Figure 4-26 (a) presents the normalized low field m(T) curves of the nanocomposite films, as compared with the pristine YBCO films with the same films thicknesses. The fact that the addition of Ta in the precursor solution do not degrade the onset T_c is consistent with the the constant c lattice parameters and further confirms the previous analysis of the issue of the substitution of Ta atom within the YBCO lattice [65, 202]. Nevertheless, the nanocomposite films show broadened transition widths ΔT_c, while the trend becomes more evident with the decrease

of film thickness, an indication of the negative influence of the nanoparticles on the film homogeneity for YBCO ultrathin films. Combined with the previous TEM analysis, we conclude, therefore, that in YBCO nanocomposite ultrathin films, the nanoparticles play a current blocking role.

In Figure 4-26 (b), we present the $J_c^{sf}(T)$ for YBCO-8 mol% BYTO nanocomposite films, as compared with pristine films with the same thickness. As observed from the graph, a significant J_c^{sf} degradation occurs for all the ss-nanocomposite ultrathin films, while J_c keeps constant value for both 250 nm pristine and nanocomposite films. The degradation of J_c^{sf} for YBCO-BYTO nanocomposite ultrathin films is attributed to the current blocking effect due to the presence of large nanoparticles within YBCO matrix, which become already significant in comparison to the film cross section. Taking into account the thickness of the ultrathin films and the size of BYTO nanoparticles we conclude that they are detrimental defects and account for the diminution of the percolative current paths. In this scenario, we would like to conclude that the J_c^{sf} of YBCO nanocomposite films, is affected by both the secondary phase dimension and the size effect already mentioned when the film thickness decrease below a ultrathin level (i.e. ≤50 nm). Very likely, a further optimization of the nanoparticle size and distribution could be made to achieve nanocomposite ultrathin films with improved properties where the current blocking effect of the insulating secondary particles could be minimized.

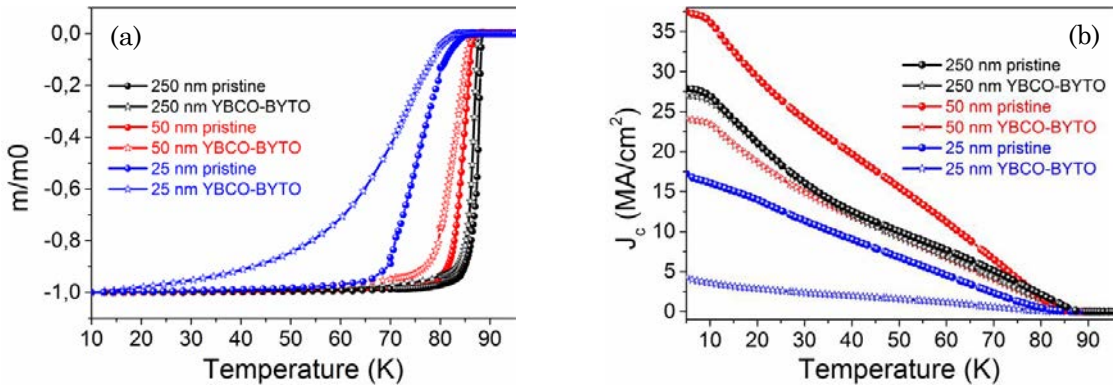

Figure 4-26: Temperature dependence of (a) normalized low field magnetization and (b) J_c^{sf} for YBCO-8 mol% BYTO ss-nanocomposite films (star) with thickness of 25 nm (blue), 50 nm (red) and 250 (black) compared with pristine YBCO films (ball) with the same thickness.

In order to further evaluate the vortex pinning properties, in Figure 4-27 (a) it is shown the normalized $J_c(H//c)$ measured at 5 K for YBCO-BYTO nanocomposite films compared with pristine films with the same thickness. As it is observed, the $J_c(H)$ dependence is smoothed in YBCO-BYTO systems (stars), as compared with the pristine YBCO films (spheres), similarly to previous reports [55, 65]. Note that for the nanocomposites $\mu_0 H^*$ is extended to higher fields in all the film thickness evaluated, as compared to the pristine YBCO with the same thickness, indicating that the insertion of BYTO nanoparticles within the YBCO matrix indeed promotes the generation of effective pinning centers and thus

enhance the vortex pinning efficiency. A further comparison indicates that μ_0H^* is higher for the 250 nm nanocomposites film than for the ultrathin nanocomposite films, i.e. μ_0H^*~220 mT vs μ_0H^*~130 mT at 5 K for the 250 nm and 25-50 nm film, respectively. The shift in μ_0H^* indicates that the APCs induced in thicker nanocomposite films are able to preserve the single vortex pinning regime up to higher fields [87], as compared with ultrathin nanocomposite films. However, in the 25 nm YBCO-8 mol% BYTO nanocomposite film, a sharp decrease at high fields of $J_c(H)$ occurs, indicating a weak vortex pinning efficiency at high magnetic fields.

The magnetic field dependences of the pinning forces ($F_p = J_c(H) \times \mu_0H$) for pristine and YBCO-BYTO ss-nanocomposite films with different thickness and measured at 5 K are presented in Figure 4-27 (b). This evaluation is based on SQUID measurements of $J_c(H)$ with the magnetic field parallel to c-axis direction. It is important to mention, first of all, that the F_p obtained by SQUID displays lower values as compared to those obtained via transport measurements, due to flux creep effects [203]. It is noteworthy that a remarkable enhancement of F_p is obtained for the 250 nm YBCO-BYTO nanocomposite, as compared to the 250 nm pristine YBCO film. In the 50 nm ultrathin films, very similar F_p values are seen among the overall measuring magnetic fields, in spite of the fact that the 50 nm pristine YBCO ultrathin film presents much higher $J_c^{sf}(5K)$ (~37.5 MA/cm^2), as compared to the 50 nm nanocomposite film (~24.2 MA/cm^2). This result confirms the efficiency of pinning centers for the 50 nm nanocomposite film, which compensate the current blocking effect. Finally, for the 25 nm YBCO-BYTO nanocomposite film the values of F_p are already well below those obtained from the 25 nm pristine YBCO film. These results imply that the enhancement of vortex pinning efficiency for the YBCO-BYTO ss-nanocomposite can not compensate the decrease of J_c^{sf} associated to the percolation effect.

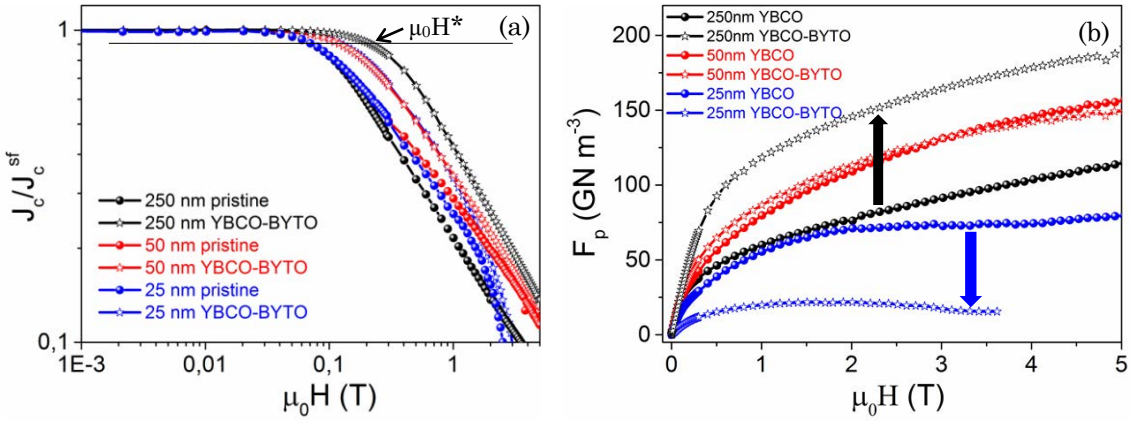

Figure 4-27: (a) Normalized $J_c(H)$ and (b) Pinning forces dependence with magnetic field measured at 5K for YBCO-8 mol% BYTO nanocompsite films (star) with thickness of 25 nm (blue), 50 nm (red) and 250 (black) compared with the corresponding pristine YBCO films (ball) with the same thickness.

4.4 Summary and conclusions

In this chapter, we have presented a comprehensive investigation on the growth, microstructure, morphology and superconducting properties of CSD-based YBCO ultrathin films, in order to reach a clear understanding of the fundamental issues involved in the initial growth stage of pristine and nanocomposite YBCO ultrathin films. Three main conslusions can be extracted from this study, as follows:

First, we have investigated the influence of three processing parameters, i.e. heating rate, growth temperature and annealing time, on the fabrication of TFA-YBCO ultrathin films grown on $LaAlO_3$ single crystals. We have determined the optimized growth conditions, i.e. FH 810 ºC (20+10), which are valid to aviod macroscale defects, such as the dewetting effect, the formation of secondary precipitates and of mis-oriented YBCO grains. The mismatch between the substrate and the films induced remarkable stress effects influencing the nuclation and surface morphology of YBCO ultrathin films.

The optimized growth conditions have been successfully applied in the fabrication of pristine YBCO ultrathin films with thicknesses ranging from 5 nm to 50 nm. The release of YBCO//LAO mismatch interfacial energy has been shown to promote the generation of Y248 intergrowths, leading to a highly strained YBCO matrix and thus, to a degradation of out-of-plane texture quality and c-axis expansion at the initial stage of YBCO growth. Nevertheless, the in-plane lattice appears to be barely influenced. The out-of-plane lattice distortion becomes severe when the film thickness decreases below 25 nm, leading to layers where superconductivity is absent. Additionally, the surface outgrowths or precipitates appear at the early stage of YBCO growth (5 nm) while the size and concentration are enhanced with the increase of film thickness, leading to an enhanced film roughness.

High quality YBCO-BYTO ss-nanocomposite ultrathin films with thickness down to 25 nm have also been sucessfully fabricated using the optimized growth process. YBCO biaxial texture was maintained in the nanocomposite films. BYTO nanoparticles are prone to be randomly distributed within the YBCO matrix, owing to the FH process inducing a high driving force towards homogeneous nucleation of BYTO nanoparticles. The high growth kinetics arising from the FH process is proposed to be effective in retarding atomic diffusion and thus, in avoiding nanoparticles coarsenning. However, the current percolation effects become more relevant when the nanoparticle size increases and the film thickness decreases, due to the current blocking effect from insulating secondary particles. We also observed that all the ss-nanocomposite films (25-250 nm) show improved vortex pinning efficiency, however, below a certain thickness range (25-50 nm) it can not compensate the effect of the thickness on J_c^{sf} and thus leads to a degradation of the pinning forces.

5. YBCO Nanocomposites with Preformed Perovskite Nanoparticles

Motivation

The outstanding ability of YBCO nanocomposite thin films to carry high critical currents at high magnetic fields offers an unprecedented opportunity to be used in electric power applications [6, 75, 96, 184, 204, 205]. However, a reliable manufacturing methodology for reducing the cost/performance ratio is required to speed up market penetration [6, 19, 206, 207]. As it has been illustrated in the Section 1.3, the preparation of CSD nanocomposites based on the colloidal solution approach shows high potential to achieve a tight control of the nanoparticle size and shape and thus, display high potential to create attractive microstructural landscapes that are appealing for enhancing vortex pinning efficiency. Research studies in the last few years identified that for this methodology, one of the most important properties that the preformed nanoparticles have to process is chemical stability during YBCO growth [118, 125]. In this line, preformed perovskite nanoparticles with unreactive character, such as $BaMO_3$ (M = Zr, Hf), are the most promising ones.

Achieving a fine control of the size, density and distribution of nanoparticles is needed to optimize the balance between supercurrent percolation and vortex pinning efficiency [55]. Moreover, very recently it has been reported [54, 55] that the characteristics of the Y248 intergrowths (density, distribution and size) influence the landscape of pinning centers (i.e. nanostrain) and they can be a relevant parameter to tune and further increase the vortex pinning. The preformed nanoparticle colloidal solution route shows a high potential to prepare nanocomposites with a tight control of the pinning landscape, however, several issues related to the formation process, such as nanoparticle coarsening and segregation, have to be overcome.

In the previous chapters, we observed that the optimized FH growth process enables a fast nucleation and growth of YBCO even at temperatures as low as 750 ºC and ultimately, leads to high quality TFA-YBCO films with an attractive structural landscape. Therefore, the synergistic use of the preformed nanoparticle colloidal route and the novel FH growth process should be an appealing approach for achieving further enhancement of the structural and superconducting properties of YBCO nanocomposite films.

The main focus of this work is to carry out a thorough study of the influence of large quantities of $BaMO_3$ nanoparticles on the pn-nanocomposite structure and pinning performance. The use of the fast conversion process (i.e. FH) is here presented as a

powerful strategy to achieve a synergetic effect between small nanoparticle and partial dislocations for enhanced pinning performances in applied magnetic fields.

5.1 Properties of the $BaMO_3$ (M=Zr, Hf) colloidal solutions

The preparation of stable nanoparticle colloidal solutions is a key point to achieve high quality solution-based pn-nanocomposite approach. Besides the advantages of $BaMO_3$ (M = Zr, Hf) we mentioned in the Introduction (subsection 1.3.3), it is especially important to control several nanoparticle behaviors: (i) mono-dispersed nanoparticles without aggregation, (ii) high stability in polar and acidic environments (e.g. TFA-YBCO solution), (iii) controllable nanoparticle size and shape, etc.

In this thesis, the $BaMO_3$ (M = Zr, Hf) nanoparticles were synthesized via solvothermal-assisted method with two different sizes: 5 and 10 nm of initial mean diameter. The reaction started from $Ba(OH)_2$ and $Zr(OBu)_4$ or $Hf(OBu)_4$ as molecular precursors in $C_6H_{14}O_4$(TEG)/C_2H_6O(EtOH) and $NH_3 \cdot H_2O$. The precursors were treated at 180 °C for 1-20 h in a sealed reactor, resulting in well-dispersed $BaZrO_3$ and $BaHfO_3$ nanoparticles. The basic experimental process of the synthesis of the $BaMO_3$ (M = Zr, Hf) nanoparticles has been demonstrated in subsection 2.1.1.2 and more details can be found in ref. [136].

The crystallinity and microstructure of the as-synthesized nanoparticles are checked by XRD diffraction patterns, as shown in Figure 5-1 (a) and (b). $BaZrO_3$ (BZO) and $BaHfO_3$ (BHO) nanoparticles display good crystallinity, and nanoparticles have both a cubic crystal structure with lattice parameters of a = 4.193 Å (JCPDS-ICDD 06-0399) and a = 4.171 Å (00-022-0084), respectively, see Figure 5-1 (a) and (b).

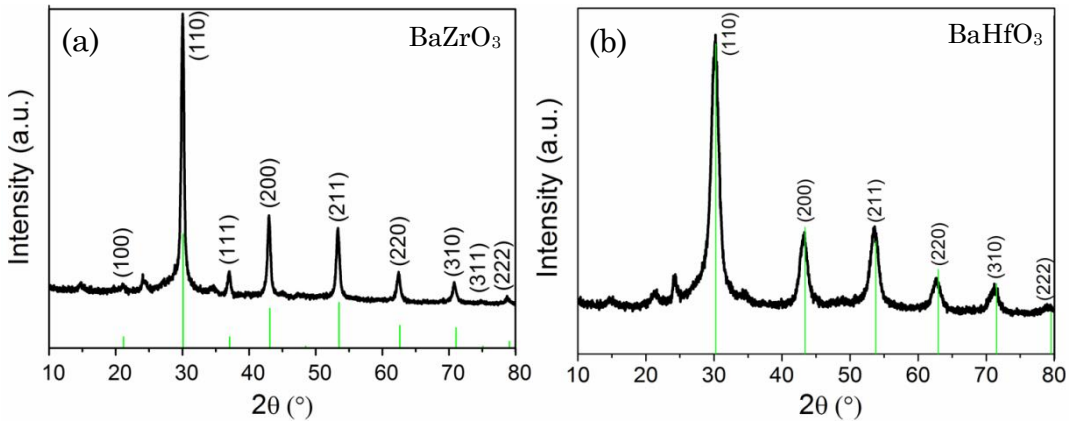

Figure 5-1: XRD powder patterns of solvothermal activated nanoparticles (a) BZO and (b) BHO.

Dynamic light scattering (DLS) measurement is routinely conducted to check size distribution of the nanoparticles in both colloidal and TFA precursor solutions, as shown in Figure 5-2 (a) and (b). These measurements provide important information about the

nanoparticle size distributions which enable us to achieve a good estimation about the degree of nanoparticle agglomeration.

We have used three batches of nanoparticles, which have been defined as BZO (10nm), BHO (10nm) and BHO (5nm) in this work, according to their compositions and mean nanoparticle sizes (see Figure 5-2 (a)). Nanoparticles synthesis and size control are beyond the scope of this thesis, and more details can be found in the reference [136]. It is clearly seen from Figure 5-2 (a) that the as-obtained nanoparticles are free of nanoparticle agglomeration.

At this stage, it is important for us to assess nanoparticles characteristics (size distribution, stability) once incorporated into the TFA-based YBCO precursor to form YBCO-BMO pn-nanocomposite solutions. Figure 5-2 (b) presents DLS spectra of a TFA-20 mol% BZO (10nm) hybrid solution for 1 day, 15 days, 30 days and ≥ 1 year after mixing, and they are compared with BZO (10nm) nanoparticles in a colloidal solution. The results indicate that these nanoparticles can be effectively introduced in the methanol-based TFA-YBCO precursor solution up to 20 mol% and the suspensions are stable for more than 1 year, even though a negligible amount of aggregated nanoparticles appear. These results point to the fact that hybrid solutions are stable enough for its usage for at least 1 month.

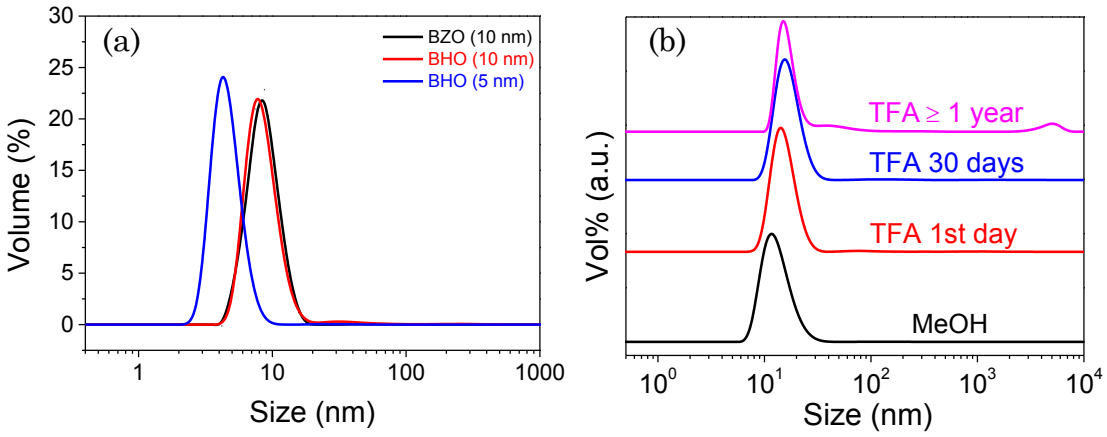

Figure 5-2: (a) DLS spectra of the BZO (10nm), BHO (10nm) and BHO (5nm) nanoparticles in colloidal solutions and (b) DLS spectra of a TFA-20 mol% BZO (10nm) hybrid solution after mixed for 1 day, 15 days, 30 days and ≥ 1 year compared with BZO (10nm) nanoparticles in a colloidal solution.

TEM analyses reveal the formation of $BaMO_3$ (M = Zr, Hf) colloidal solutions of monodispersed nanoparticles without agglomerations, in good agreement with the previous DLS studies. The BZO nanoparticles present a square-like shape (Inset Figure 5-3 (a)) whereas the BHO nanoparticles are spherical (Inset Figure 5-3 (b) and (c)).

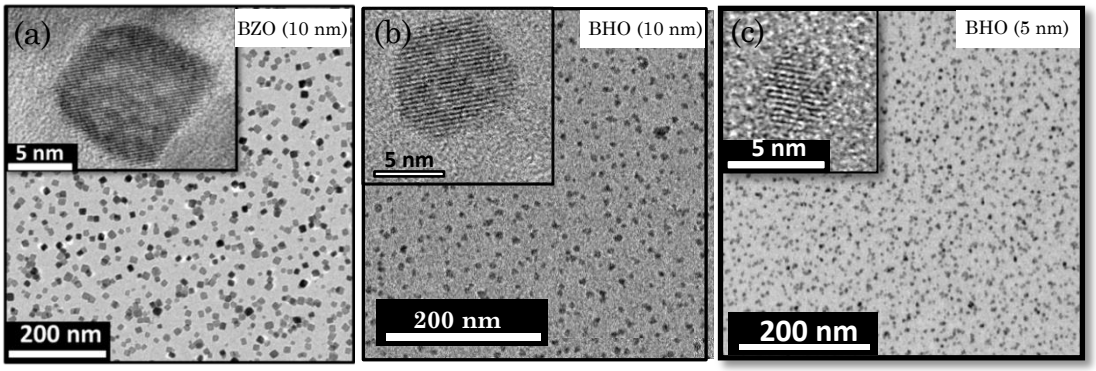

Figure 5-3: TEM images of the (a) BZO (10 nm), (b) BHO (10 nm) and (c) BHO (5 nm) nanoparticles in colloidal solutions, respectively. Inset: high resolution TEM image of the corresponding individual nanoparticle.

Statistical representations of the size distribution have been made on the basis of a significantly large population of particles observed by TEM technique, as shown in Figure 5-4. Figures 5-4 (a) and (b) display statistical size distribution histograms obtained by analyzing TEM images for BZO (10 nm) and BHO (5 nm), respectively. It is clearly seen that the mean nanoparticle diameters are 9.1 nm and 5.2 nm with a standard deviation of 1.5 nm and 0.9 nm, giving a size dispersion of ~16.5% and ~17.3% for BZO (10 nm) and BHO (5 nm), respectively. These TEM images show that the nanoparticles size distribution is small enough at the present stage to analyze its efficiency as vortex pinning centers.

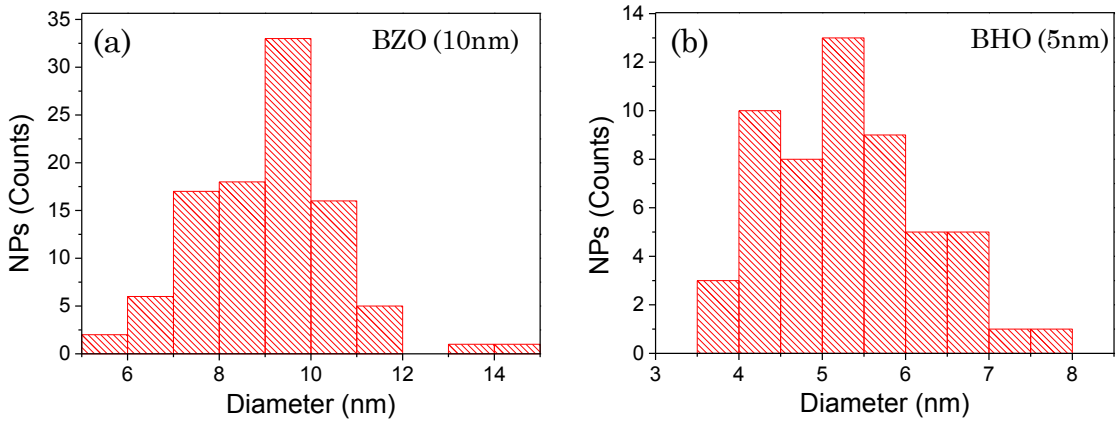

Figure 5-4: Histograms show statistical size distribution of (a) BZO (10 nm) and (b) BHO (5 nm) in the corresponding colloidal solutions. Data obtained from the TEM analysis.

In summary, we are able to synthesize mono-dispersed $BaMO_3$ (M = Zr, Hf) nanoparticles with cubic structure and the nanoparticle size and shape are controllable. The nanoparticles keep stable in MeOH colloidal solutions at high concentration (~200 mM) for more than 1 year. Importantly, the physicochemical features of these nanoparticles can be successfully preserved when incorporated into TFA-YBCO precursor solutions, being stable for ~1 year, and so they are ready for the CSD preparation of YBCO pn-nanocomposite films.

The YBCO-BMO (M = Zr, Hf) precursor solutions were prepared by introducing stoichiometric amounts of the BMO colloidal nanoparticles to a TFA-YBCO precursor solution to prepare a wide range of BMO compositions, from 0 to 25 mol%. The YBCO-nanoparticles precursor solution was deposited on a 5-50 nm YBCO seed layer prepared on a 5 × 5 mm^2 (100) LAO single-crystal substrates. The pyrolysis of the YBCO-nanocomposite/YBCO seed layer//LAO system was carried out using the pyrolysis process which has been detailed in subsection 2.1.2.3. All these suspensions lead to homogeneous and crack-free pyrolyzed films (see Figure 5-5 (a)), mandatory to fabricate high quality YBCO-$BaMO_3$ pn-nanocomposite films. Subsequently, the pyrolyzed layers were crystallized using the CTA (820 °C) or FH (750 °C) growth process (Figure 5-5 (b)); more details have been reported in subsection 2.1.2.4.

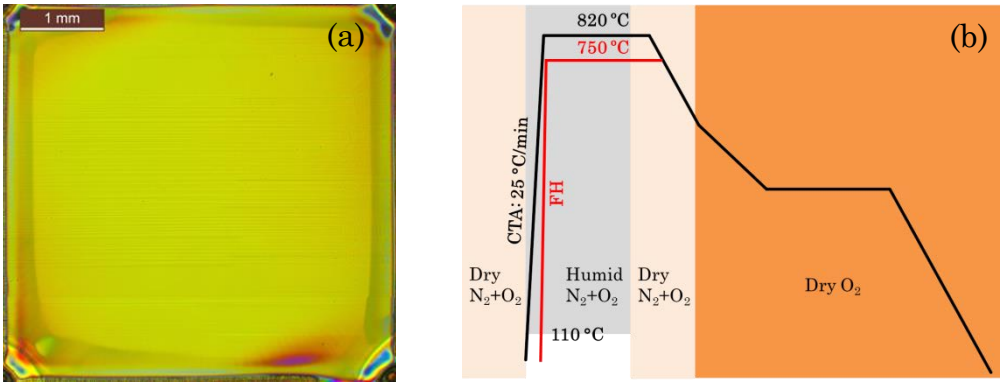

Figure 5-5: (a) Typical optical microscope image of as-pyrolyzed YBCO pn-nanocomposite films showing a homogeneous surface morphology; (b) heating profiles used in this work to convert the YBCO pn-nanocomposite thin films: CTA (820 °C) and FH (750 °C) growth process.

In this work, typical film thicknesses of the (YBCO (0.75M) pn-nanocomposite)//(50nm YBCO)//LAO nanocomposite systems were estimated to be 150 ± 10 nm. To achieve thicker YBCO nanocomposite films (up to 350 nm), a multi-deposition process separated by intermediate pyrolysis steps was performed, as schematically shown in Figure 5-6.

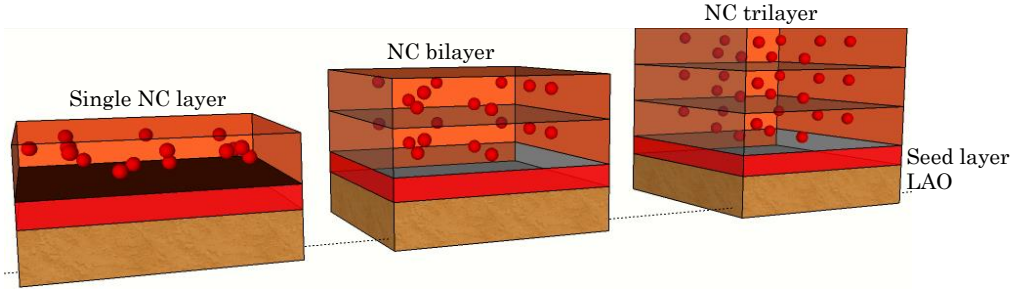

Figure 5-6: Sketches showing the heterostructure of the pn-nanocomposite films studied in this work. Note that all the multi-deposition processes were separated by intermediate pyrolysis steps.

5.2 YBCO Nanocomposites with preformed nanoparticles

5.2.1 Influence of $BaZrO_3$ nanoparticle concentration

As a first step, we study the influence of preformed BZO nanoparticle load in the YBCO nanocomposite structure and physical properties. This study was carried out using BZO nanoparticles with initial mean diameter of 10 nm and prepared following the CTA growth process (Figure 5-5 (b)).

In previous works, it was shown that the heterogeneous c-axis oriented nucleation of YBCO films with ZrO_2 nanoparticles on single crystalline substrates may be perturbed when pn-nanocomposite films are grown because the nanoparticles nucleated at the film//substrate interface [118, 125]. In the case of YBCO-BZO pn-nanocomposite grown on bare LAO substrate, we have found that the critical nanoparticle load for an epitaxial growth is 12 mol%, beyond which randomly oriented YBCO grains appear; see Figure 5-7 (a) and (b). This is mainly due to the fact that an excessive concentration of secondary phases may be accumulated at the interface and then, due to the large lattice mismatch of YBCO with the BZO nanoparticles, other crystalline orientations may also nucleate, thus perturbing the texture quality of the films. This difficulty could be overcome by using pristine YBCO seed layers at the substrate interface. A single layer of pyrolyzed YBCO ultrathin films was shown to be effective to overcome this difficulty [118, 125]. On top of this layer the nanocomposite films develop a robust homoepitaxial growth and preserve a high quality film texture. We attribute this effect to an enhanced effectiveness of the homoepitaxial growth of YBCO-$BaMO_3$ (M = Zr, Hf) nanocomposites which may keep a high quality even when the percentage of available YBCO interface (seed layer) is reduced at high concentration of preformed $BaMO_3$ (M = Zr, Hf) nanoparticles [118, 125]. We have found that using an interfacial seed layer in between the substrate and pn-nanocomposite film, the YBCO films keep the c-axis nucleation up to 20-25 mol% (Figures 5-7 (c)-(d)). This compositional range goes well beyond that previously achieved based on the spontaneously segregated approach where strong texture degradation appeared beyond about 10-12 mol% [54, 65]. This molar concentration corresponding to ~7.7 vol% of nanoparticles and thus it approaches the optimal volume of secondary phases in PLD or MOCVD nanocomposite films having a nanorod structure [208-210]. The introduction of the pristine YBCO seed layer appears, therefore, very attractive to reach high concentrations of $BaMO_3$ (M = Zr, Hf) nanoparticles in the pn-nanocomposite films.

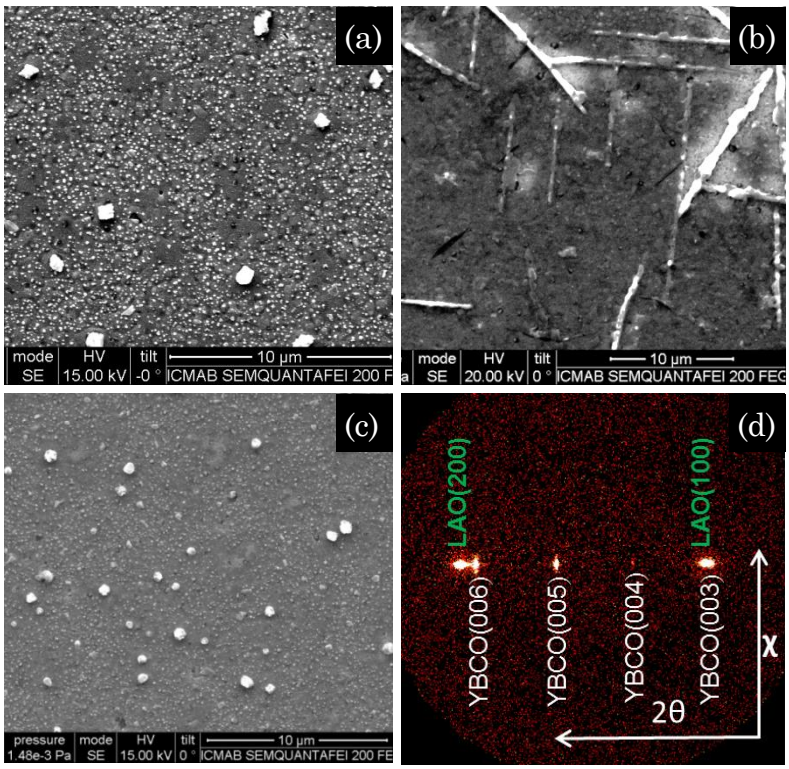

Figure 5-7 (a)-(b): SEM images of (a) YBCO-6 mol% BZO (10nm) and (b) YBCO-12 mol% BZO (10 nm) pn-nanocomposites deposited on bare LAO single crystals; (c)-(d): (c) SEM image and (d) 2D θ-2θ XRD diffraction pattern of YBCO-25 mol% BZO (10 nm) pn-nanocomposite on 50 nm pristine YBCO//LAO single crystal and processed following the CTA process.

To design a cost-effective process, it is important to identify the minimum seed layer thickness required to ensure (00l) pn-nanocomposite texture. Full width at half maximum (FWHM) of (005) YBCO rocking curve (Δω) and self-field J_c (J_c^{sf}) at 77K were the chosen parameters to identify the YBCO pn-nanocomposite quality for different seed layer thicknesses. From Figure 5-8 it can be clearly identified that 25 nm is the threshold seed layer thickness with Δω (005) below 0.3º and J_c^{sf} at 77 K of > 4 MA/cm². Therefore, from here on, seed layers with thicknesses of 25-50 nm have been used.

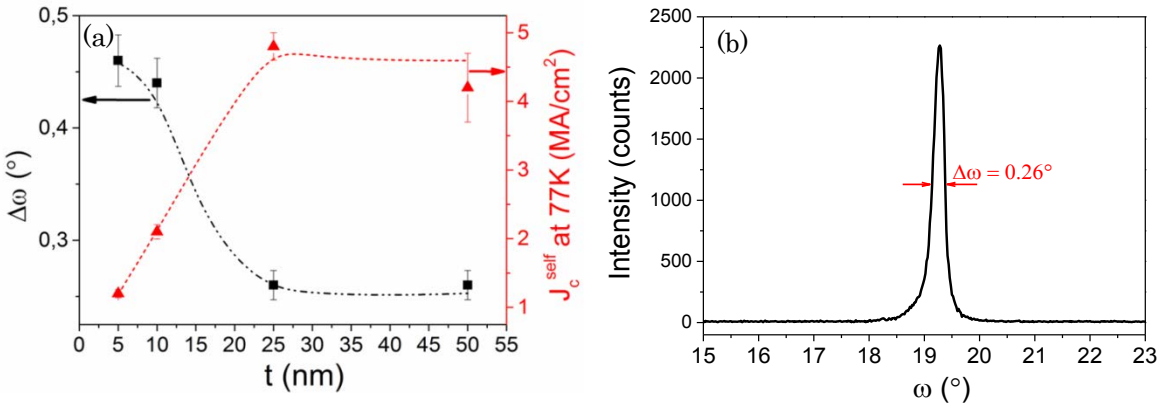

Figure 5-8 (a) FWHM of XRD ω-scan (005) YBCO (black square) and J_c^{sf} (77K) (red triangle) dependence with the YBCO seed layer thickness (t) for YBCO-20 mol% BZO (10nm) pn-nanocomposite films (b) Δω (005) YBCO of a YBCO-20 mol% BZO pn-nanocomposite film grown on 50 nm YBCO seed//LAO substrate.

Another critical parameter related to the improvement of superconducting performances of YBCO nanocomposite films is the nanoparticle concentration. To disclose the optimal nanoparticle concentration for further enhancing the YBCO vortex pinning, YBCO precursor solutions with increasing BZO nanoparticle loads starting from 6 to 25 mol% were systematically deposited on YBCO seed//LAO. Figure 5-9 (a) shows the HRXRD θ-2θ scan for 20 mol% BZO pn-nanocomposite where only (00l) YBCO and (00l) LAO Bragg reflections are identified, indicating c-axis oriented growth. Biaxial texture was further confirmed from in-plane (Δϕ (103) YBCO = 0.9º) (Figure 5-9 (b)) and out-of-plane (Δω (005) YBCO = 0.3º) texture analysis. As it has been illustrated previously that epitaxial pn-nanocomposite films with BZO concentrations as high as 25 mol% can be obtained, however, texture degradation is devised (Δω (005) YBCO = 0.7º) for this nanoparticle load.

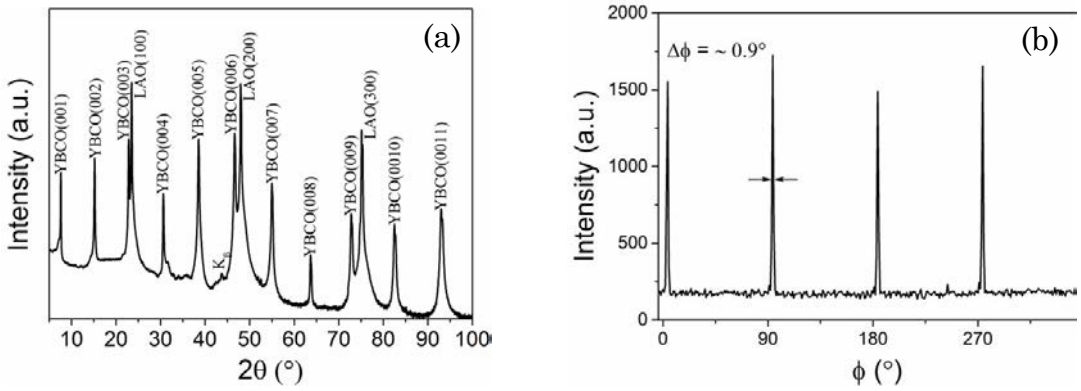

Figure 5-9: (a) HRXRD θ-2θ scan and (b) ϕ-scan of the (103) YBCO reflection of YBCO-20 mol% BZO (10 nm) pn-nanocomposite film grown on 50 nm YBCO seed//LAO substrate by the CTA growth process.

The first common feature of all the films was that the superconducting transition temperatures could be kept as high as those of pristine films. Figure 5-10 (a) displays one example of a low field ZFC magnetization measurement where the onset temperature is around 90 K and the transition width stay in the range of 4-6 K in films with a high quality texture. The onset T_c values were found to be constant up to the maximum BZO content of 25 mol% (Figure 5-10 (b)) strengthening the assumption that the nanoparticles do not react with the YBCO, however, the transition widths were found to degrade at this nanoparticle content. Figure 5-10 (c)-(d) compares the J_c^{sf} dependence on the BZO nanoparticle concentration in YBCO-BZO pn-nanocomposite and ss-nanocomposite films. For the YBCO-BZO ss-nanocomposites, a maximum J_c^{sf}(5K) of 50 MA/cm² was identified at 10 mol% and then rapidly decreased down to 10 MA/cm² by increasing the nanoparticle load [54]. By contrast, the YBCO-BZO pn-nanocomposites show a fairly constant J_c^{sf} (5K) = ~40 MA/cm² up to 20 mol%, being the highest nanoparticle loading reported in epitaxial YBCO pn-nanocomposite with high critical current [118, 125]. Then, at 25 mol% load the J_c^{sf} starts to decrease being in agreement with the texture degradation identified in the out-of-plane texture analysis above. Moreover, we also observed that the J_c^{sf} (77K) evolution, for both

types of nanocomposite follows a similar trend as compared with the J_c^{sf} (5K) evolution. It is clearly appreciated that the colloidal solution approach allows to preserve high superconducting performances at higher nanoparticle concentrations. At the present stage 20 mol% has been found to be the maximum concentration of nanoparticles which keep a high texture quality and a high percolating critical current density J_c^{sf}. Nevertheless, this result has been reached for BZO nanoparticles with a diameter of 10 nm and it could be certainly modified by using small nanoparticle size. The effect of preformed BZO nanoparticles on the YBCO nanostructure (i.e. nanostrain ε, structural defect scenario) and the pinning performance will be evaluated in the next section.

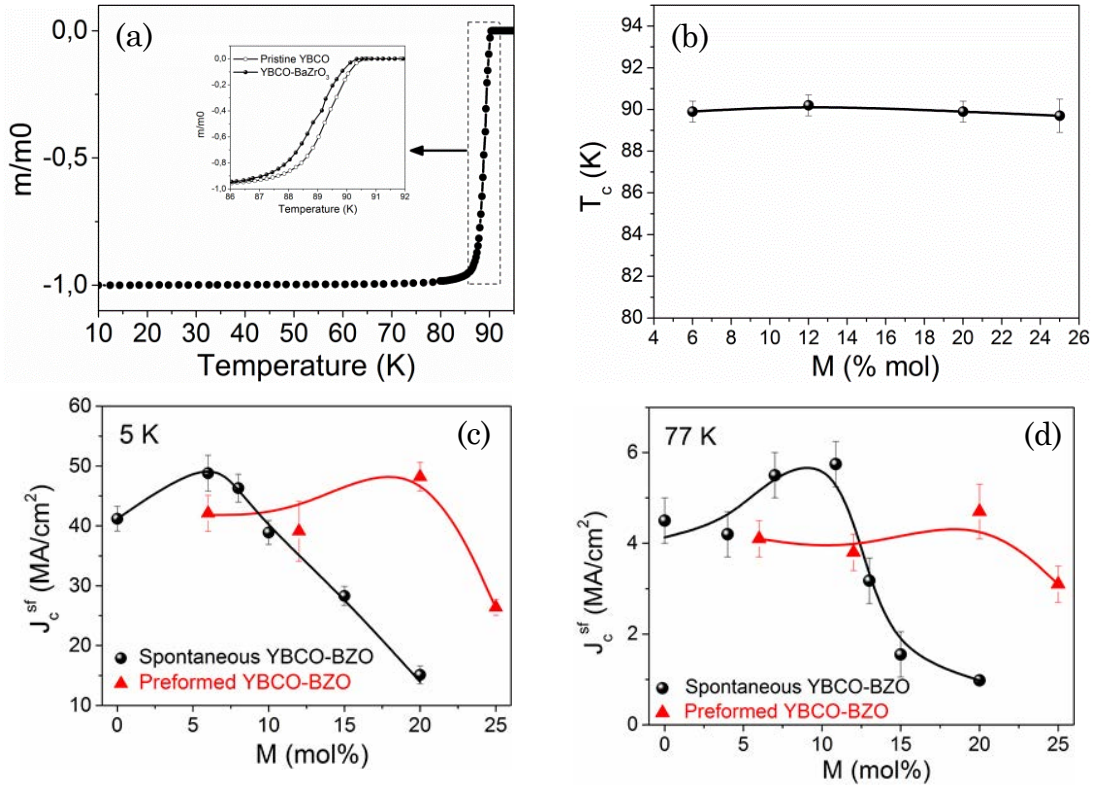

Figure 5-10: (a) Typical low magnetic field magnetization measurement of a YBCO nanocomposite film showing a sharp transition and a high T_c value. Inset: detail of the transition in a pristine and a TFA-YBCO-BZO pn-nanocomposite film; (b) Dependence of T_c determined inductively on the BZO content in TFA-YBCO-BZO pn-nanocomposite films; (c)-(d): J_c^{sf} dependence with nanoparticles molar concentration (M) measured at (c) 5K and (d) 77K of YBCO-BZO (10 nm) pn-nanocomposite films (red triangle) compared with YBCO-BZO ss-nanocomposite films (black sphere). Error bars are determined from the fit uncertainty in the corresponding data analysis.

5.2.2 The Influence of Nanoparticle Composition and Size

On the basis of the above investigations, we focused our work on 20 mol% nanoparticles using a 25-50 nm YBCO seed layer and comparing first, two different compositions BZO and BHO, and then two different nanoparticle sizes: 10 and 5 nm of initial mean diameter. Starting by nanoparticle composition, epitaxial YBCO pn-nanocomposites with 20 mol%

BZO and BHO nanoparticles of 10 nm were prepared following the CTA growth process. Figures 5-11 (a)-(b) shows 2D GADDS X-ray diffraction pattern and the corresponding integrated spectrum of the YBCO-20 mol% BHO pn-nanocomposite film. Notice that a high quality epitaxial YBCO nanocomposite film is achieved thus confirming high compatibility of the selected nanoparticle composition and YBCO. Texture analyses of the YBCO pn-nanocomposite films show good in-plane ($\Delta\phi \approx 0.8^{o}$) and out-of-plane ($\Delta\omega$ = ~0.2-0.4^{o}) texture quality.

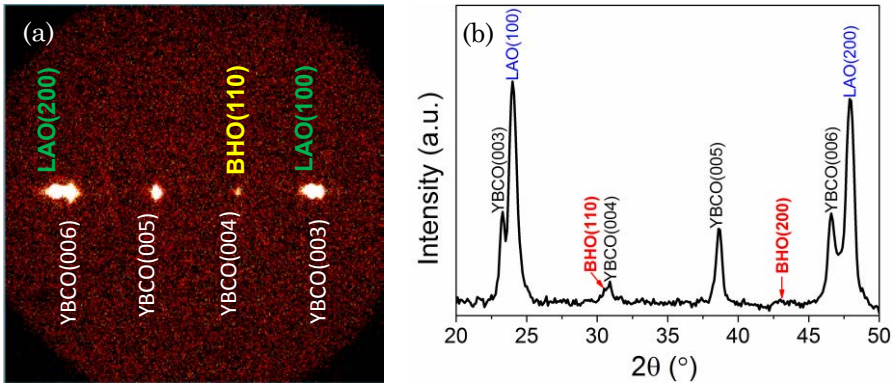

Figure 5-11: (a) Representative 2D θ-2θ XRD pattern of YBCO-20 mol% BHO pn-nanocomposite grown on 25-50 nm pristine YBCO buffered LAO substrate from the CTA growth process; (b) integrated spectrum of (a).

In order to explore the nanoparticle distribution within the YBCO matrix and stacking faults scenario, Z-contrast images were acquired. Figure 5-12 (a) and (c) show the cross-sectional images of YBCO-BZO and YBCO-BHO pn-nanocomposites, respectively. In both cases, 50 nm pristine YBCO seed layer with high density of long stacking faults are clearly identified. For YBCO-BZO, nanoparticles are homogeneously distributed within the nanocomposite layer although stacking faults are mainly located in the upper part of the nanocomposite film. By contrast, in YBCO-BHO, nanoparticles and long stacking faults are identified throughout the nanocomposite thickness. Isolated BZO and BHO nanoparticles embedded in the YBCO matrix are shown in Figure 5-12 (b) and (d), respectively. BZO are square-like and BHO are spherical with nanoparticle size of 15-20 nm. Therefore, the nanoparticles preserve the initial shape from the colloidal solutions (Figure 5-3 (a) and (b)) and undergo a limited nanoparticle size increase, from 10 nm to 20 nm. Therefore, the use of unreactive $BaMO_3$ nanoparticles allows to better control the nanoparticle distribution and coarsening than previously reported spontaneously segregated nanocomposites or even pn-nanocomposites with reactive ZrO_2, $MFeO_4$ (M = Co, Mn) and CeO_2 nanoparticles [118, 125, 128, 129].

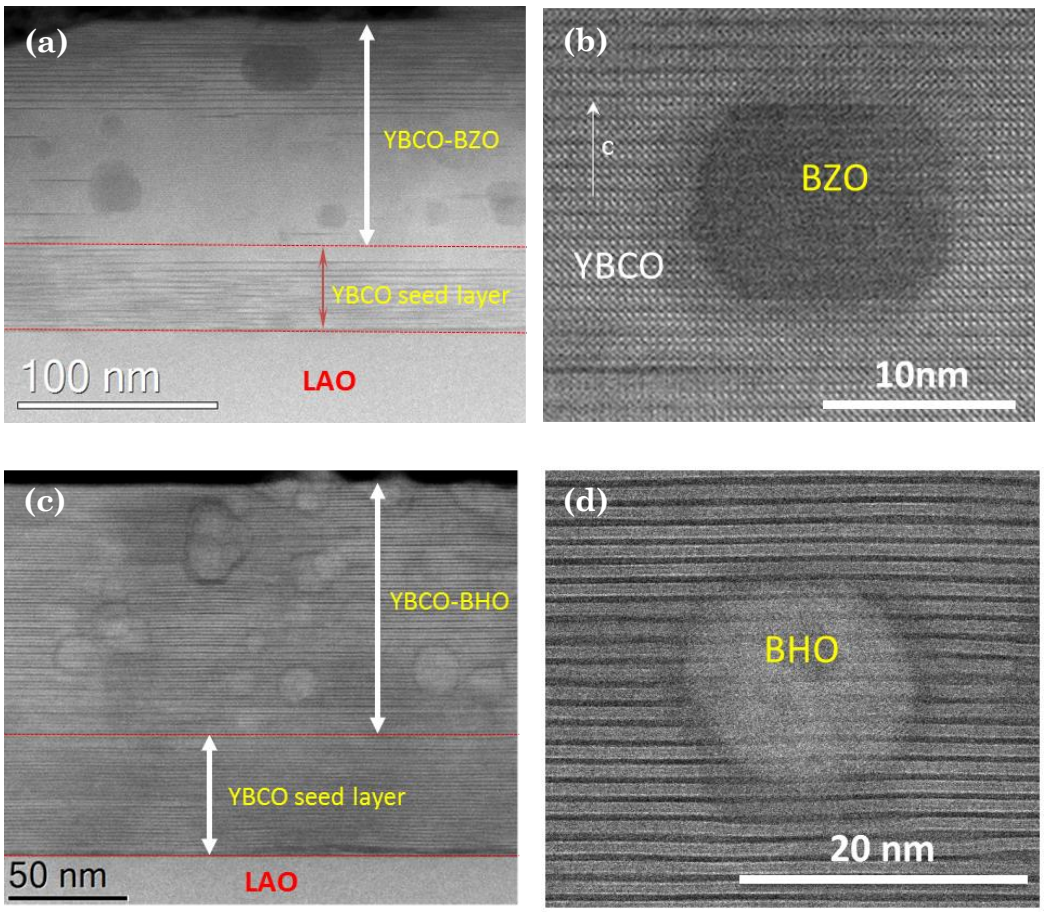

Figure 5-12: ADF Z-contrast images of YBCO-20 mol% $BaMO_3$ (M = Zr and Hf, 10nm) pn-nanocomposite films deposited on 50 nm YBCO seed//LAO. (a)-(b): YBCO-BZO composition and (c)-(d): YBCO-BHO composition.

In this scenario, the nanostrain obtained for the YBCO-20 mol% BZO (10 nm) and YBCO-20 mol% BHO (10 nm) pn-nanocomposite is ε = 0.18% and ε = 0.20%, respectively, in well agreement with the Y248 intergrowth scenario identified from STEM. Also, there is a significant increase from pristine YBCO (ε = 0.11%) and these values are similar to those obtained in optimal spontaneously segregated YBCO nanocomposites [54].

High critical currents J_c^{sf} (77K) of 4.3 MA/cm² and T_c = 90K are routinely obtained for these YBCO-20 mol% BZO (10 nm) and YBCO-20 mol% BHO (10 nm) pn-nanocomposites. In order to evaluate the influence of nanoparticle composition on the pinning landscape, the magnetic field dependence of normalized critical current density $J_c(H//c)/J_c^{sf}$ has been investigated at two typical temperatures (5 and 77K) and compared with a pristine YBCO film, see Figure 5-13. The crossover magnetic field, $\mu_0 H^*$ (determined at 90% of J_c^{sf}), identifies the transition between single vortex pinning (regime in which the vortices are pinned individually) to collective vortex pinning (vortex-vortex interactions start to be relevant and J_c decreses with the magnetic field) [87]. Here $\mu_0 H^*$ is shifted to higher fields for the nanocomposite samples ($\mu_0 H^*_{YBCO-BHO\ (10\ nm)}$ = 71 mT; $\mu_0 H^*_{YBCO-BZO\ (10\ nm)}$ = 62 mT),

compared to the pristine YBCO film ($\mu_0 H^*_{YBCO}$ = 38 mT), giving a smoother dependence. This is the typical $J_c(H)$ performance previously identified in CSD nanocomposites [54, 118, 131]. When comparing the two pn-nanocomposite compositions, YBCO-BHO shows slightly higher $\mu_0 H^*$ which could be ascribed to the higher values of nanostrain reported above. Another interesting feature that can be extracted from Figure 5-13 is the fact that there is no apparent change in the irreversibility line at 77K when comparing the two nanocomposites. Overall, both nanocomposites compositions are effective to improve the pinning landscape.

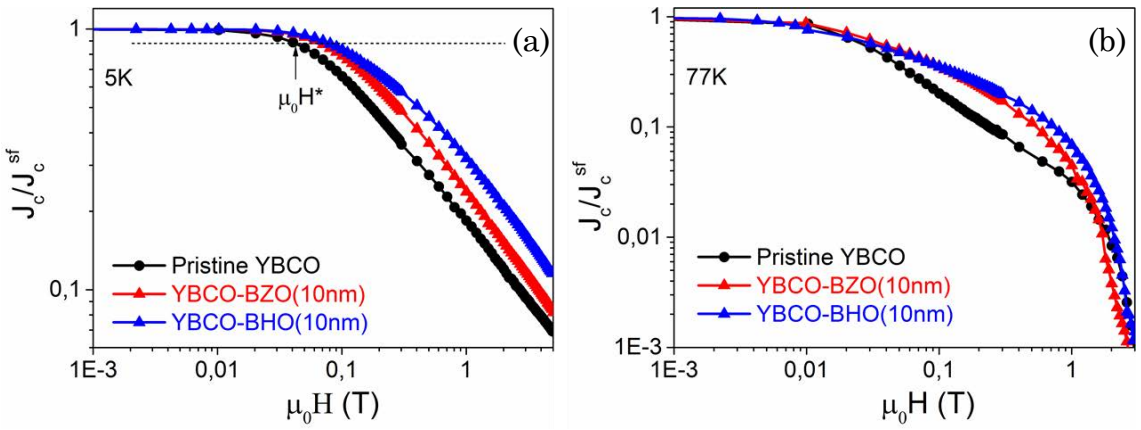

Figure 5-13 Magnetic field dependence of the critical current density at (a) 5 K and (b) 77 K normalized to its self-field value for pn-nanocomposite films with 20 mol% BZO (10 nm) (red triangle) and 20 mol% BHO (10 nm) (blue triangle) compared with a pristine YBCO film (black circle). The horizontal dashed line in Figure 5-13 (a) marks the criterion to determine the $\mu_0 H^*$ value ($J_c(\mu_0 H^*) = 0{,}9 \cdot J_c^{sf}$).

In order to study the influence of the initial nanoparticle size (5 nm vs 10 nm) on the final microstructure and pinning performance of the YBCO pn-nanocomposite, YBCO-20 mol% BHO composition is selected and processed following the CTA growth process. ADF Z-contrast images of the YBCO-20 mol% BHO (5 nm) pn-nanocomposite are shown in Figure 5-14. Homogeneously distributed BHO nanoparticles are identified throughout the nanocomposite thickness along with high density of Y248 intergrowths with 40-50 nm of lateral extension. Closer look at the embedded nanoparticles shows that the mean particle diameter increased up to a maximum of 10 nm; see Figure 5-14 (b). This nanoparticle size has also been confirmed by XRD using the Debye-Scherrer formula. Hence, starting from smaller nanoparticles, the final diameter is also increased by a factor of two although they remain as discrete nanoparticles. Texture analysis reveals a biaxially textured superconducting matrix with $\Delta\phi$ (103) YBCO = 0.9º and $\Delta\omega$ (005) YBCO = 0.5º. The nanostrain of these YBCO-20 mol% BHO (5 nm) pn-nanocomposites is ε = ~0.21%, similar to the analogous YBCO-BHO (10 nm) pn-nancomposite films.

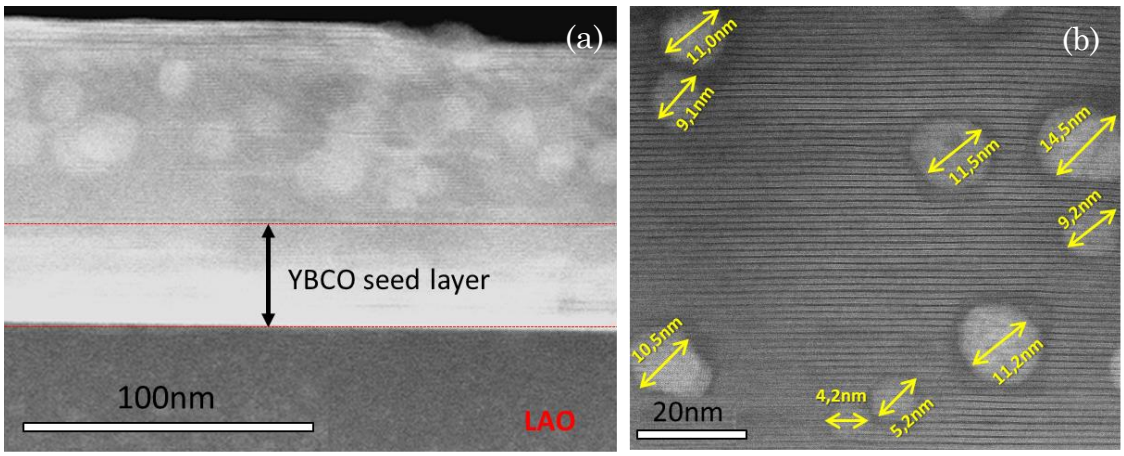

Figure 5-14 Cross-sectional Z-contrast images of the YBCO-20 mol% BHO (5nm) pn-nanocomposite. (a) Low resolution image of YBCO nancomposite with embedded BHO nanoparticles; (b) High resolution image of mono-dispersed BHO nanoparticles with limited coarsening and surrounded by high density of stacking faults.

Figure 5-15 compares the J_c(H//c) dependence for YBCO pn-nanocomposite with 10 nm and 5 nm initial mean diameter at (a) 5K and (b) 77K. Noteworthy, the YBCO-BHO (5 nm) pn-nanocomposites show an overall J_c enhancement for the whole range of magnetic field here studied. Remarkable critical current densities of $J_c^{sf}(5K) = 48$ MA/cm² and $J_c^{sf}(77K) = 4.5$ MA/cm² are obtained. Furthermore, a softer magnetic field decay appears for the YBCO-BHO (5 nm) pn-nanocomposite with $H^*_{YBCO-BHO\ (5\ nm)} = 100$ mT, indicating that smaller nanoparticles help increasing the pinning efficiency at applied magnetic fields.

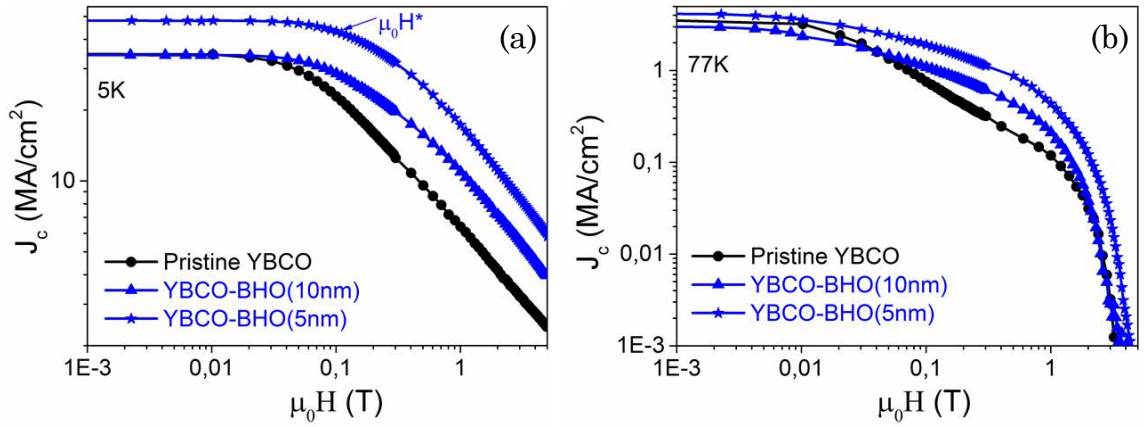

Figure 5-15 Critical current density versus magnetic field at (a) 5K and (b) 77K in YBCO-20 mol% BHO pn-nanocomposite films with initial nanoparticle size of 10 nm (blue triangle) and 5 nm (blue star) compared with a pristine YBCO film (black circle).

When looking at the μ_0H^* dependence with nanostrain for the YBCO pn-nanocomposite films grown under the CTA process, Figure 5-16, it is easily identified that the incorporation of nanoparticles in the YBCO leads to a large increase in the nanostrain and consequently larger μ_0H^*, pointing that the increased nanostrain has been effectively

translated to the enhancement of $\mu_0 H^*$. Therefore, non-reactivity and small nanoparticle size are both key parameters to modulate the nanostrain generated in the YBCO matrix.

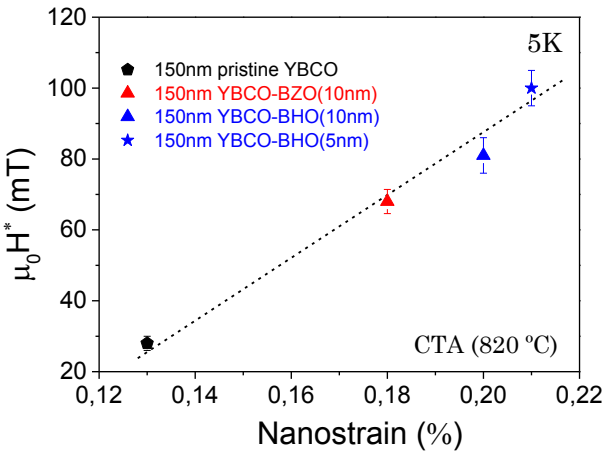

Figure 5-16 Dependence of the $\mu_0 H^*$ at 5K on the nanostrain for pristine YBCO and YBCO-BMO pn-nanocomposites comparing composition (BHO vs BZO) and size (5 nm vs 10 nm) of the nanoparticles. All the films were grown under the CTA process with the same final thickness of 150 nm.

5.2.3 Nanoparticle coarsening and Y248 intergrowth control

In order to further tune the formation of Y248 intergrowths and better control the nanoparticle size of the preformed nanoparticles during the YBCO growth, the FH growth process (see Figure 5-5 (b)) which has been systematically optimized in Chapter 3 were applied for the growth of YBCO-BMO pn-nanocomposite films. It has been previously observed that the FH growth process provides high kinetics for YBCO nucleation and growth and thus, leads to a fast formation of YBCO films. This thermal profile enables an epitaxial growth of pristine YBCO thin films at low growth temperature and within a wide range of temperatures (750 ºC - 810 ºC), leading to samples with a reduced porosity (Figure 3-21), a high density of stacking faults (Figure 3-22), and an enhanced pinning efficiency, as detailed in Section 3.3. The FH process in pristine YBCO leads to $T_c \approx 88$ K and $J_c^{sf}(77\ K) =$ 2-3 MA cm^{-2}. This slight reduction of J_c^{sf} is attributed to the presence of some secondary phases, such as $Y_2Cu_2O_5$ (Y225), which compete for the YBCO formation, see Figure 5-17.

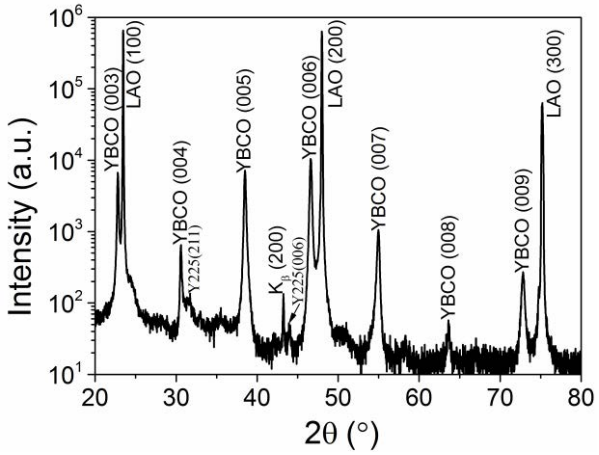

Figure 5-17 XRD θ-2θ scan of YBCO + 20 mol% BHO (5 nm) pn-nanocomposite grown from the FH (750 °C) process. $Y_2Cu_2O_5$ (Y225) secondary phase is identified due to a different kinetic process.

The effect of the FH thermal process on the YBCO pn-nanocomposite structure and pinning properties has been investigated for the YBCO-BHO composition. High quality epitaxial YBCO-BHO pn-nanocomposite films Δϕ (103) YBCO = 1.1° and Δω (005) YBCO = 0.5° are routinely obtained under the optimized FH growth process (i.e. FH (750 °C)).

Figure 5-18 shows ADF Z-contrast images of YBCO-20 mol% BHO (5 nm) film grown under the FH (750°C) process. From the general overview image, in Figure 5-18 (a), the film shows the typical microstructure identified in the previous samples: pn-nanocomposite film full of stacking faults where the nanoparticles are homogeneously distributed within the superconducting matrix. Deeper insight (Figure 5-18 (b)) reveals that the nanoparticle mean diameter after the YBCO growth (~7 nm) almost coincides with the diameter of the BHO nanoparticles in the colloidal solution (Figure 5-18 (c)), also confirmed by the Debye-Scherrer formula. In this scenario, it is important to mention that the initial nanoparticle size can be preserved after growth. The result indicates, therefore, that the coarsening is minimized by the application of the FH growth process.

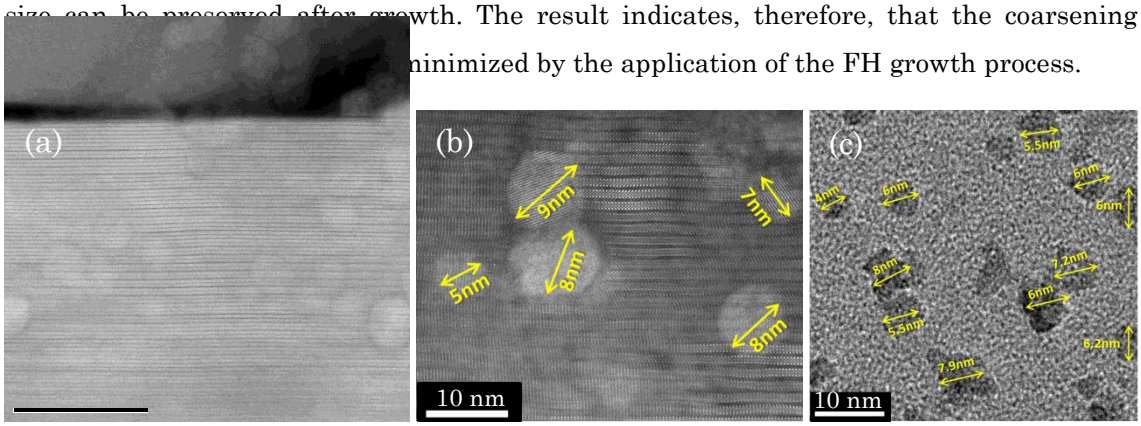

Figure 5-18: (a)-(b) ADF Z-contrast images of YBCO-20 mol% BHO (5 nm) pn-nanocomposite processed following with flash heating at 750 °C, (a) Low-resolution image showing a general view of the YBCO pn-nanocomposite layer and the seed layer, (b) High-resolution image of BHO nanoparticles with minimal coarsening within the YBCO matrix; (c) a bright field TEM image of preformed BHO (5 nm) nanoparticles in colloidal solution, where the nanoparticles size have been marked by yellow arrows.

Along with this important finding, it is observed that the Y248 intergrowths surrounding the nanoparticles show a much shorter lateral extension, Figure 5-19 (a), than what has been previously obtained in the pn-nanocomposites processed under CTA growth processes [54, 55, 118, 125]. From the STEM images of pn-nanocomposites processed under CTA and FH growth processes, and pristine FH (Figure 3-22 (a)) it has been calculated the length and number of intergrowth generated in the YBCO matrix. Figure 5-19 (b) displays histograms showing length distribution of stacking faults of YBCO-BHO (5 nm) pn-nanocomposite films grown from the FH (750 ºC) process and the CTA growth process compared with a pristine YBCO film grown from the FH (750 ºC) process. It is clearly seen from the histograms that the FH (750 ºC) growth process leads to a higher amount of intergrowths, as compared to the CTA growth process, and FH nanocomposites display the highest amount of short stacking faults.

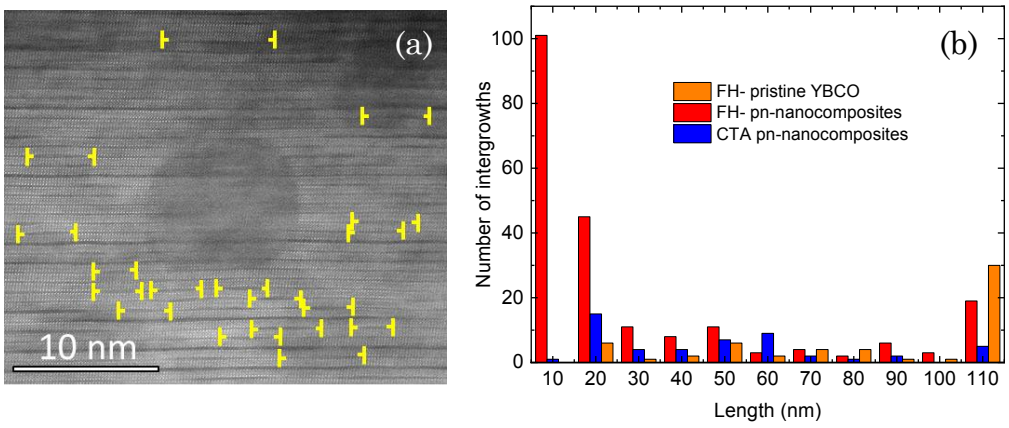

Figure 5-19: (a) High-resolution image of an isolated BHO surrounded by short stacking faults (indicated by yellow arrows) for the YBCO-BHO (5 nm) pn-nanocomposite grown under the FH (750 ºC) growth process; (b) Histogram showing the length and number of intergrowths for pristine and pn-nanocomposite films grown under the FH (750 ºC) or CTA process, data extracted from STEM images.

Strain analysis combined with different STEM imaging modes confirmed that the lattice deformation of the YBCO matrix is localized around the partial dislocations that surrounds the intergrowths and this local deformation may be extended up to a volume of several nanometers (see Figure 5-20) [113]. The dislocation volume can be calculated as [211]

$$V_i = \pi(R_i + \delta/2)^2\delta - \pi(R_i - \delta/2)^2\delta = 2\pi R_i\delta^2$$

where V_i is the volume of each dislocation, R_i the radius of the stacking fault and δ is the size of the strained region caused by the dislocation ($\approx$ 0.8 nm). Then, to compute the volume density of dislocations, ρ_i, we take into consideration the volume of the n dislocations found in a well-defined volume image (Δx, Δy, Δz)

$$\rho_{dis} = \frac{\sum_i^n V_i}{\Delta_x\Delta_y\Delta_z}$$

From this equation and combined with the stacking fault length distribution statistics (Figure 5-19 (b)), it has been estimated that the ρ_{dis} displayed in FH YBCO-BHO pn-nanocomposite (~2.3%) is remarkably higher than in the CTA YBCO-BHO pn-nanocomposite (~0.7%) and the FH pristine YBCO (~0.3%). Therefore, FH process offers several advantages over the CTA: faster growth, preservation of small nanoparticle size and generation of shorter stacking faults and higher density of partial dislocations being thus very promising to improve the vortex pinning of the nanocomposites.

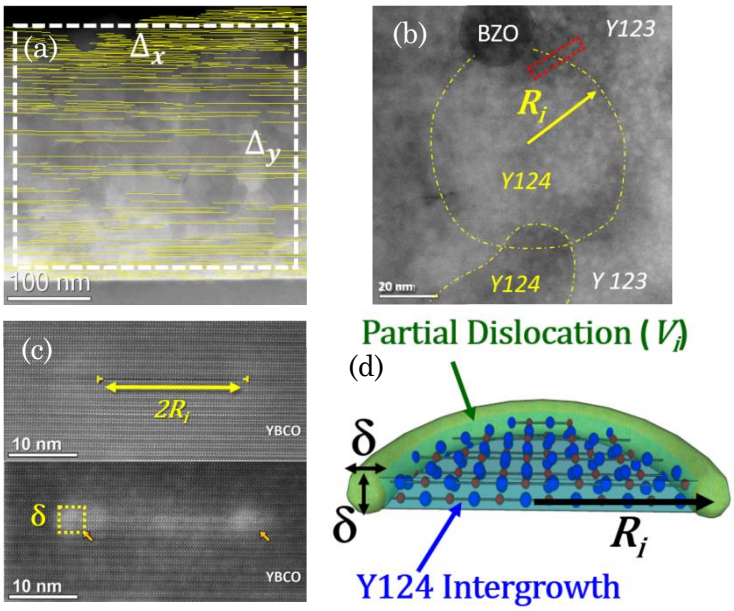

Figure 5-20: STEM observation of stacking faults in YBCO nanocomposite films and schematic descriptions of the defect. (a) Cross-sectional low magnification Z-contrast images of solution deposited YBCO nanocomposite where stacking faults are marked with yellow stripes and the observed YBCO area $\Delta_x\Delta_y$ is delimited. (b) Plan view low magnification Z-contrast image of a solution deposited YBCO nanocomposite. The boundaries of intergrowths are highlighted in yellow. (c) Z-contrast (above) and Low-Angle Annular Dark Field (below) images of an isolated 25 nm-long stacking fault. The yellow symbols in the images point to partial dislocations while the arrows to their surrounding strain fields, with size δ = 0.8nm. (d) Schematic view of the partial dislocation surrounding the stacking fault [211].

Figure 5-21 presents the $J_c(H)$ dependence of pristine YBCO, YBCO-20 mol% BHO (10 nm) and YBCO-20 mol% BHO (5nm) pn-nanocomposite films grown by the FH (750 ºC) process and measured at (a) 5 K and (b) 77 K. Once again the nanocomposite samples present a much smoother $J_c(H)$ dependence compared to the pristine YBCO being the 5 nm nanoparticle nanocomposite much better than the 10 nm. Indeed, the $\mu_0 H^*_{FH-YBCO-BHO(5\,nm)}$ is 195 mT, similar to the best performances reported up to date in solution deposited films [66]. At this stage, when looking at the $\mu_0 H^*$ dependence with nanostrain, Figure 5-22 right side (FH (750 ºC)), it is observed that the nanostrain of the FH films, are all shifted to higher nanostrain consistent with the fact that FH samples show higher ρ_{dis} than samples processed under CTA conditions. Even though, the FH pristine films have longer stacking faults than the nanocomposite CTA films (see Figure 5-19 (b)), thus contributing to a larger

nanostrain, but this does not transform in a corresponding increase on $\mu_0 H^*$ because the volume of partial dislocations remains unchanged. It is remarkable that the nanostrain of 150 nm films, independently of being nanocomposite or pristine film is $\varepsilon \approx 0.25$ %, nonetheless, the $\mu_0 H^*$ is significantly higher for the nanocomposite. Therefore, besides the ρ_{dis}, there is a new added contribution to the $\mu_0 H^*$ of nanocomposites.

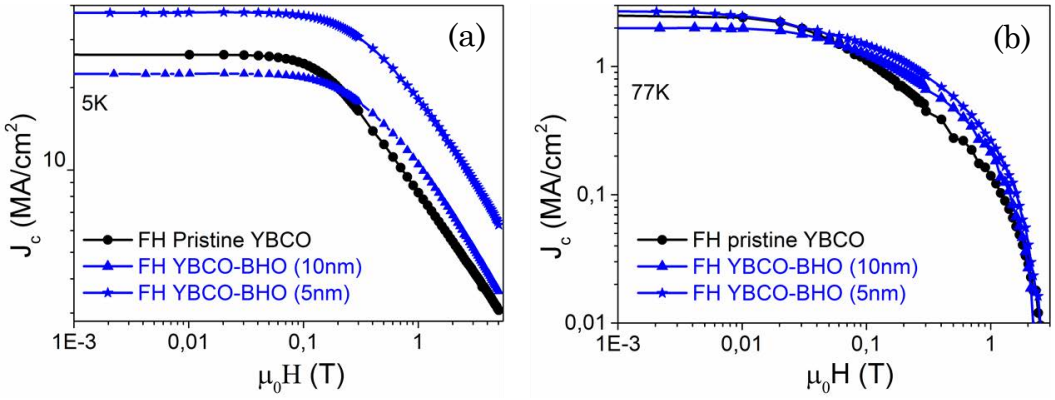

Figure 5-21: Magnetic field dependence of the critical current density $J_c(H)$ measured at (a) 5K and (b) 77K of YBCO-20 mol% BHO pn-nanocompostite films with initial nanoparticles size of 10 nm (blue triangle) and 5 nm (blue star) compared with pristine YBCO thin films (black circle). All the samples are grown using FH.

Importantly, the density of nanoparticles, n_{np}, for the FH pn-nanocomposite films with an initial nanoparticle size of 5 nm increased by more than a factor two ($n_{np} \approx 40.1 \times 10^{22}$ m^{-3}) compared to CTA nanocomposites ($n_{np} \approx 16.2 \times 10^{22}$ m^{-3}) because the nanoparticle size were 7 and 10 nm, respectively. This nanoparticle size is similar to the maximum one achieved so far through the multi-deposition approach recently reported [66]. Therefore, it is very likely that when the mean diameter of the nanoparticle size can be preserved down to 5-7 nm in CSD-nanocomposite films, the nanoparticles themselves could also act as artificial pinning centers because their mean diameter is close to the coherence length (ξ) which could be consistent with the increased in $\mu_0 H^*$ identified above (see Figure 5-22).

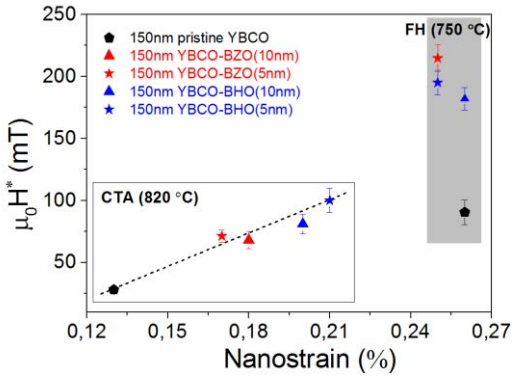

Figure 5-22 Dependence of the $\mu_0 H^*$ at 5K on the nanostrain for pristine YBCO and YBCO-BMO pn-nanocomposites comparing composition (BHO vs BZO) and size (5 nm vs 10 nm) of the nanoparticles. The films were grown under the CTA (white shadow region) or FH (750 °C) (grey shadow region) growth process with the same thickness of 150 nm.

From the temperature dependence of J_c it is possible to classify the strength of the active artificial pinning centers according to their thermal activation process [22, 87]. We can differentiate two contributions: strong pinning, J_c^{str}, which shows a smooth decay with temperature (i.e. nanostrain, planar defects, twin boundaries, nanoparticles or nanorods with diameter size in the range of the coherent length, ξ) and weak pinning, J_c^{wk}, which is characterized by a fast J_c decay with temperature (i.e. point defects such as oxygen vacancies and atomic substitutions). Here we compare pristine YBCO, pn-nanocomposite with BZO (10 nm), BZO (5 nm) and BHO (5 nm). Figure 5-23 (a) shows the contribution of J_c^{str} at 0 K ($J_c^{str}(0)$), obtained by fitting the weak and strong $J_c(T)$ dependences as detailed in subsection 2.2.3.1 using Equation 2-14. The pn-nanocomposite films show higher $J_c^{str}(0)$ than pristine and those that are flash heated with small nanoparticle size (5 nm) presents the highest $J_c^{str}(0)$ values.

In this scenario the nanoparticles themselves would be synergetically associated to the partial dislocations to enhance vortex pinning in these nanocomposites (Figure 5-23 (b)). Importantly, up to date, this scenario had been only clearly reported for vacuum deposited films where such small diameter of nanoparticles or nanorods could be achieved [66, 96, 98, 208, 212-214].

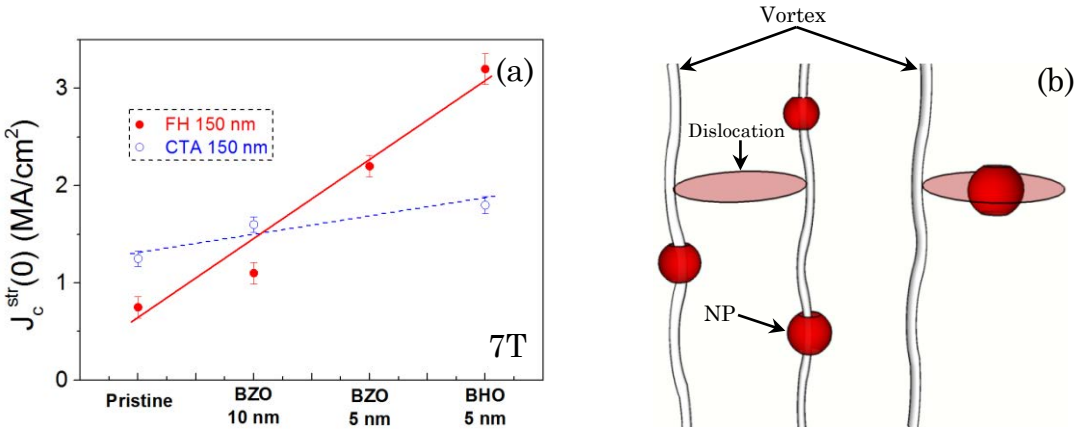

Figure 5-23 (a) Strong pinning contribution J_c^{str} at 0K measured at 7T for pristine and pn-nanocomposites prepared from CTA and FH thermal process. (b) A sketch showing synergetic vortex pinning effects between the dislocations and the small nanoparticles.

5.2.4 Multi-deposition: a feasible route to increase thickness

Based on the success of the results illustrated in the previous sections, the effort has been then focused on increasing pn-nanocomposite thickness using YBCO-20 mol% BHO (5 nm) composition by multi-deposition processes, as detailed in section 5.1 and Figure 5-6.

Typical 2D XRD θ-2θ patterns of 350 nm nanocomposite film are displayed in Figure 5-24. The YBCO film is epitaxial and the BHO phase can be identified at 2θ = 30.2º as a strong ring and at 2θ = 43.4º as a faint spot corresponding to BHO (110) and BHO (200) Bragg reflections, respectively, as shown in Figure 5-24 (a)-(b). In 350 nm film, we are

above the minimum detectable amount of BHO to differentiate the ring. The percentage of randomly oriented nanoparticles, key feature to ensure high nanostrain in CSD nanocomposites [54], is estimated to be 94% in YBCO-BHO nanocomposite following the methodology detailed in subsection 2.2.2.1. This result is similar to the results obtained in optimal spontaneously segregated YBCO nanocomposites [55, 65]. The in-plane and out-of-plane texture quality slightly degrades with thicknesses (150 nm, 250 nm, 350 nm) with FWHM ϕ-scan (103) values of 0.72º, 1.01º and 1.45º and FWHM of ω-scan = 0.52º, 0.63º and 0.73º, respectively, an issue that will influence the percolating critical current, as it will be detailed below.

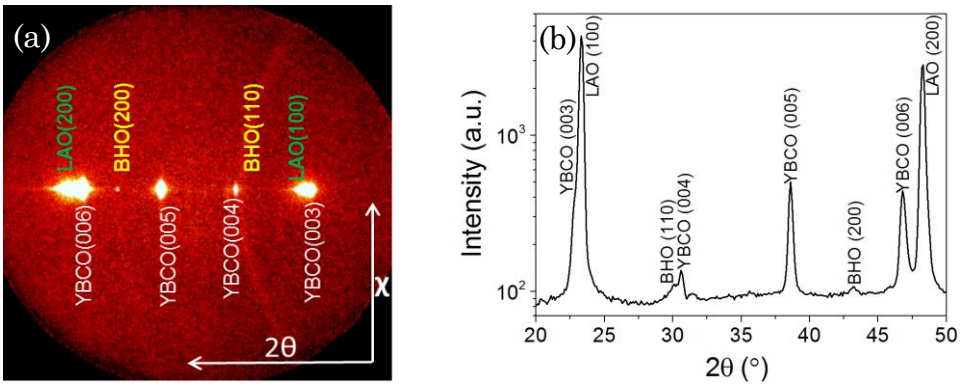

Figure 5-24: (a) 2D θ-2θ XRD pattern for 350 nm YBCO-20 mol% BHO (5nm) pn-nanocomposite layer deposited on a 50 nm YBCO buffered LAO substrate grown from the FH (750 °C) process. (b) Integrated XRD spectrum from (a).

From the ADF Z-contrast images of the 350 nm films, Figure 5-25, it can be extracted that the nanoparticles preserve the original diameter size and are homogeneously distributed within the YBCO matrix. No layer boundaries, neither the appearance of CuO segregation between the layers have been identified in this multideposited samples [70]. Therefore, by increasing the film thickness a factor of 2 the YBCO structural defect scenario and embedded nanoparticle characteristics are essentially preserved.

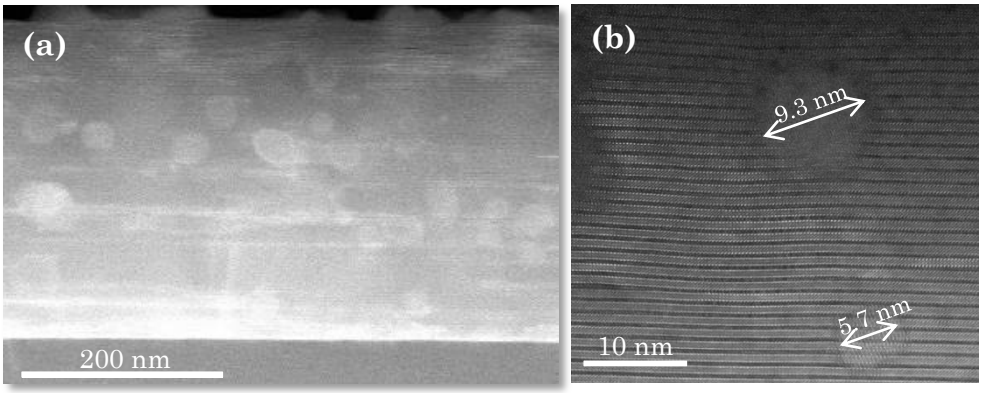

Figure 5-25: ADF Z-contrast images of the 350 nm YBCO-20 mol% BHO (5nm) pn-nanocomposite film grown from the FH (750 °C) process. (a) Low resolution image of the overview of the pn-nanocomposite film and (b) high resolution image of the BHO nanoparticle embedded inside in the highly bended YBCO matrix.

In Figure 5-26, it is summarized an overall μ_0H^* evolution with nanostrain for pristine YBCO and nanocomposite films with different thicknesses (150 nm, 250 nm and 350 nm) and grown under two types of growth conditions (i.e. CTA and FH (750 ºC)). The nanostrain has also been calculated for the multilayered systems identifying a clear increase from 0.25% to 0.33%, being the latter the highest obtained in preformed nanocomposites [118, 125]. The μ_0H^* in these nanocomposites is continuously increased with film thickness, from 195 mT (150 nm) to 216 mT (250 nm) and ultimately to 270 mT (350 nm), indicating a continuous increase of vortex pinning efficiency at higher magnetic fields. This would suggest that the single vortex pinning regime ($\mu_0H < \mu_0H^*$) is extended towards higher fields probably because there is some increase of the density of short stacking faults and so of the partial dislocation total density while the final nanoparticle size is preserved, although further microstructural and physical properties analysis would be necessary to sort out the relative weight of each contribution.

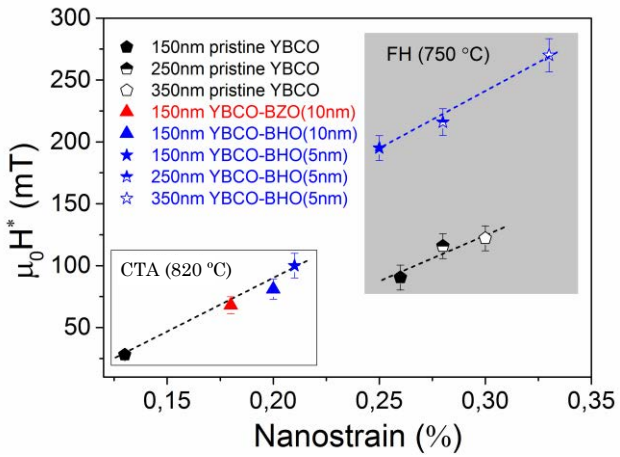

Figure 5-26 Dependence of the μ_0H^* at 5K on the nanostrain for pristine YBCO and YBCO-BMO pn-nanocomposites comparing composition (BHO vs BZO) and size (5 nm vs 10 nm) of the nanoparticles. The films were grown under the CTA (white shadow region) or FH (750 ºC) (grey shadow region) with different thicknesses of 150 nm, 250 nm and 350 nm.

Another very relevant parameter to assess the success in keeping high superconducting performance when increasing the film thickness is the dependence of $I_c = J_c^{sf} \times t$ with thickness t. Figure 5-27 displays the $I_{c\text{-}w}(t)$ dependence measured at 77 K for the different films described in this chapter, together with two slopes corresponding to different J_c^{sf} values. It is seen that our nanocomposite films grown under the FH (750 ºC) growth condition keep high J_c^{sf} values (~2-3 MA/cm^2) within the whole explored thickness range. Nevertheless, for the YBCO-BHO (5 nm) pn-nanocomposite films, a tendency to a slight decrease of the J_c^{sf} at large film thickness (J_c^{sf} = ~2.2 MA/cm^2) has been observed. One possible reason leads to the J_c^{sf} degradation could be associated with the granularity effect, which is characterized by the existence of two different critical current densities: one inside the grains (J_c^G) and the other one associated with the grain boundary network (J_c^{GB}) [140, 156,

215]. It has been reported in the literature that the increase of film thickness usually causes a decrease of grain density and thus, leads to an increase of the internucleus spacing. The consequence is that poor intergranular connectivity among grains occurs and granularity effect starts to appear [43, 216]. The existence of granularity can be experimentally identified by checking the position of maximum J_c value at magnetic field [140, 215]. The overall $J_c(H)$ behaviors displayed in Figure 5-28 confirms that no granularity effect occurs for all the films. Therefore, the degradation of J_c^{sf} can be very likely associated to the degradation of texture quality. The overall $I_{c\text{-}w}$ behavior confirms that the increase of film thickness via multi-deposition enables a further improvement of current-carrying capacity of YBCO pn-nanocomposite films. The highest $I_{c\text{-}w}$ value achieved in our present work using multi-deposition method is $I_{c\text{-}w}$ = ~70 A/cm-w at 77 K for a film 350 nm thick. However, further enhancement of current-carrying capacity should be expected if the J_c^{sf} is maintained for the whole film thicknesses.

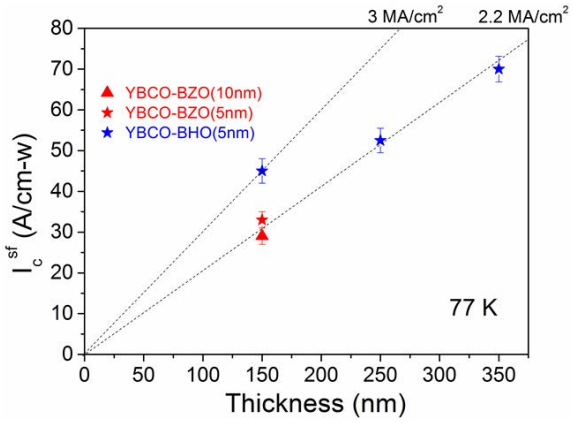

Figure 5-27 Critical current per cm in width ($I_{c\text{-}w}$) evolution with films thickness of YBCO-BMO (M = Zr and Hf) grown under the FH (750 °C) growth process measured at 77K.

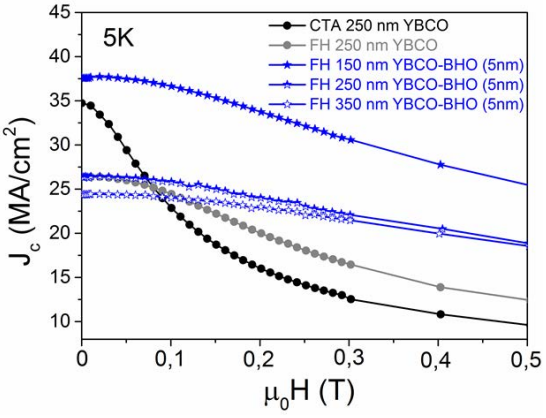

Figure 5-28 J_c at 5 K evolution with magnetic field for pristine YBCO and YBCO-BHO (5 nm) pn-nanocomposite films.

The success in improving the superconducting performances when the nanocomposite film thickness is increased can be better monitored by displaying the corresponding $I_{c\text{-}w}(\mu_0 H)$ curves. Figure 5-29 (a) shows the magnetic field dependence of the total critical current ($I_{c\text{-}w}$)

for a 150 nm pristine YBCO and a 350 nm YBCO-BHO pn-nanocomposite films, measured at 5 and 77K. The pn-nanocomposite film shows a smoothed magnetic field dependence when compared to the pristine YBCO films. Figure 5-29 (b) shows the $J_c(T)$ dependence measured under a constant field of 7 T for a 250 nm pristine YBCO film and a 350 YBCO-BHO pn-nanocomposite films together with the J_c^{wk} and J_c^{str} plots fitted according to the Equation 2-13 and the Equation 2-14 as detailed in subsection 2.2.3.1. It is observed that the pn-nanocomposite curve is well above the pristine YBCO and the major contribution comes from strong pinning (blue solid line), although the weak contribution is also slightly increased in the pn-nanocomposite (blue dashed line). This general behavior appears to be characteristic of solution derived nanocomposite films and here it is associated to the increase of the nanostrain generated by a much higher stacking fault concentration in nanocomposite films [54, 87], as well to the increase of the density of small nanoparticles which also contribute to strong pinning as discussed before.

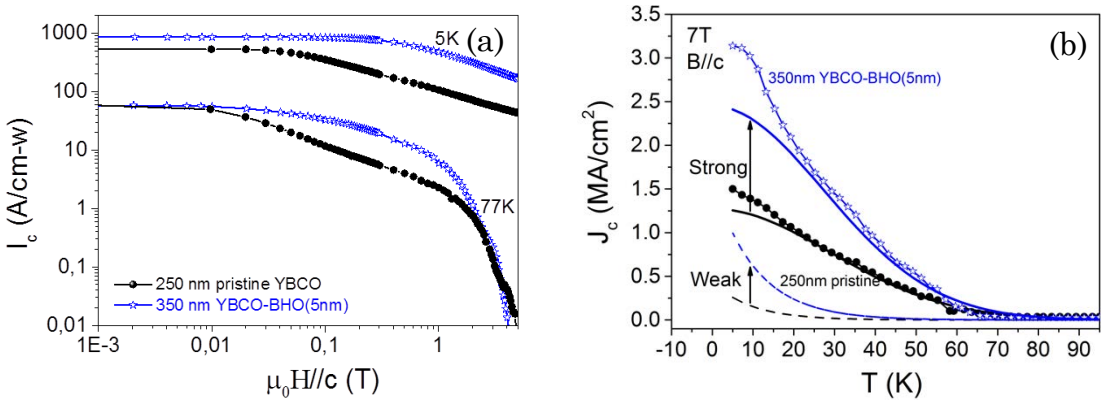

Figure 5-29: (a) Magnetic field dependence of the total critical current, $I_{c\text{-}w}(H)$, for a 250 nm pristine YBCO (black line) and a 350nm YBCO-20 mol% BHO (5nm) pn-nanocomposite (blue line) measured at 5K and 77K (SQUID); (b) Temperature dependence of the critical current density $J_c(T)$ measured at 7T for the pristine YBCO and 350 nm YBCO-20 mol% BHO (5nm) pn-nanocomposite. The curves have been fitted with two contributions (strong and weak pinning). The 250 nm pristine YBCO film is processed by the CTA process and the 350 nm pn-nanocomposite following the FH (750 °C) process.

5.3 Conclusions

To sum up, we have demonstrated the versatility and validity of the solution deposited YBCO nanocomposites with preformed nanoparticles to tune the microstructure of the YBCO films and further tailor the pinning performance in applied magnetic field. A progressive optimization of the microstructural and superconducting performances of the YBCO films has been achieved through tight control of processing parameters.

The introduction of a 25-50 nm pristine YBCO seed layer is beneficial to the epitaxial growth of YBCO-$BaMO_3$ (M = Zr, Hf) pn-nanocomposites, while an optimal texture quality and superconducting properties was found for a 20 mol% nanoparticle addition when the initial nanoparticle size was 10 nm (BZO) and the growth process was CTA. This is already

a noteworthy progress as compared to the solution derived superconducting nanocomposites in previously reported which had the optimal concentration at 7 mol%. Some critical characteristics of Y248 intergrowths, such as their length, distribution and density, which plays a crucial role in enhancing vortex-pinning performance, have been finely tuned through a tight control of $BaMO_3$ (M = Zr, Hf) nanoparticle composition and size. Strongly improved YBCO superconducting properties have been achieved by incorporating 20 mol% BHO (5nm) nanoparticles within YBCO matrix. The FH (750 °C) process has been proved to be a very efficient approach to grow YBCO-$BaMO_3$ (M = Zr, Hf) pn-nanocomposite films with tightly trapped, homogeneously distributed and finely size preserved nanoparticles. These features lead to a further optimized stacking fault landscape (i.e. high density and small dimension). The optimized structural defect landscape ensures a synergetic effect between small nanoparticle and partial dislocations which enhance the pinning performances under applied magnetic fields. Finally, a further enhancement of vortex pinning efficiency and total critical current carrying capability has been reached via the design of a multi-deposited structure.

In conclusion, our innovative approaches lead to an optimization of the YBCO structural defect scenario via a tight control of nanoparticle characteristics (concentration, composition and size) as well as the film thickness which hold the best prospect for an effective and economical application of the second generation superconductors in high magnetic field applications. However, at this stage, all the nanoparticle concentrations applied in this chapter are the optimized concentration of BZO (10 nm) based on the CTA growth process. Further optimization of nanoparticle concentrations is needed when a decreased nanoparticle size and the FH growth process are incorporated.

6. General Conclusions and Outlook

In this work, we have presented a systematic study of $YBa_2Cu_3O_{7-\delta}$ and nanocomposite thin films deposited by the Chemical Solution Deposition approach, in particular by the Trifluoroacetate precursor route, which allows a cost-effective, versatile and scalable fabrication of long tapes for large scale applications.

As a first step it has been investigated the kinetics of a new processing step: flash heating. A thorough study of intermediate phase evolution it has been observed that a limited precursor nanoparticle coarsening during the heating process, provide an accelerated kinetics for nucleation and growth. The evolution of film permeability during the heating process has been found to be a key parameter influencing the gaseous (H_2O and HF) diffusion rate and so the growth process. We have shown that we can control the influence of this parameter by an early introduction of water vapour during the heating process. Epitaxial YBCO films can be obtained in a wider growth temperature window starting at lower temperature (750-810 ºC) making this process compatible with the deposition of $YBa_2Cu_3O_{7-\delta}$ coated conductors on CeO_2-caped metallic tape substrates because the formation of polycrystalline interlayer can be avoided. In addition, we have also found that the Flash Heating growth process promotes the formation of a high concentration of stacking faults and thus nanostrain, a key parameter to improve the vortex pinning properties.

The exploration of the optimized conditions for the growth of Chemical Solution Deposited $YBa_2Cu_3O_{7-\delta}$ ultrathin films (5-50 nm) has been crucial to obtain high quality films for further investigations. The lattice mismatch between $YBa_2Cu_3O_{7-\delta}$ and substrates lead to incoherent or semi-coherent interfaces which is the one influencing the microstructural evolution of the ultrathin films. The relief of the interfacial energy induces a high density of stacking faults, leading to a highly distorted $YBa_2Cu_3O_{7-\delta}$ matrix. Such microstructural disorder becomes extremely serious when the film thickness decreases below 25 nm, significantly degrading the superconductivity. Unlike the nano-sized strained areas ensued from partial dislocations associated to intergrowths as pinning centers, the insertion of an ultrahigh density of long interfacial stacking faults induce an absence of superconductivity. In addition, we have demonstrated that the nucleation and growth behaviors of spontaneously segregated nanocomposites (in the case of $YBa_2Cu_3O_{7-\delta}$-Ba_2YTaO_6) and their influence on the superconducting properties present also a strong thickness dependence. The accelerated growth kinetics ensued from the Flash Heating process promotes the random distribution of spontaneously segregated nanoparticles as well as avoiding nanoparticle coarsening, however, this appealing nanoparticle behavior vanished for ultrathin films. Moreover, the current percolation effects become more

relevant when the nanoparticle size increases and the film thickness decreases, due to the current blocking effect from insulating secondary particles. We also observed that all the spontaneously segregated $YBa_2Cu_3O_{7-\delta}$-Ba_2YTaO_6 nanocomposite films (25-250 nm) showing improved vortex pinning efficiency, however, at a certain thickness range (25-50 nm) it can not compensate the effect of thickness in self-field critical current density and thus leads to a degradation of pinning forces.

The preparation of $YBa_2Cu_3O_{7-\delta}$ nanocomposites from non-reactive preformed oxide colloidal solutions has appeared as a very successful technique to achieve a tight control of the nanoparticle characteristics (size, shape and distribution) and the optimized nanostructural landscape on the superconducting films. The use of non-reactive preformed $BaMO_3$ (M = Zr, Hf) perovskites led to high quality nanocomposite films at high nanoparticle concentrations (20-25 mol%), a significant progress, as compared to previously reported solution derived superconducting spontaneously segregated nanocomposites. The composition and size of nanoparticles have demonstrated to be crucial factors for tailoring vortex pinning performance in applied magnetic field. In particular, the use of the Flash Heating growth process in the growth of nanocomposite films allows both the preservation of nanoparticle size and the generation of a high density of short stacking faults, which play a synergistic effect to increase the artificial pinning centers and enhance the strong pinning contribution. Multi-deposition process is proven effective to further enhance the vortex pinning efficiency and current-carrying capacity of nanocomposite films.

Our present work enriches the knowledge of the Chemical Solution Deposited $YBa_2Cu_3O_{7-\delta}$ and nanocomposite thin films. The achievements in this work will help to promote this material to be efficient in power applications at high magnetic fields and low-costs.

However, there are still certain issues that remain unsolved and should be addressed in future investigations. For instance, the study of $YBa_2Cu_3O_{7-\delta}$ coated conductors growth on CeO_2-capped metallic substrates under the Flash Heating conditions is still in its initial stage, where the reproducibility and performance requires to be further improved. The incorporation of our optimized Flash Heating growth process in the reel-to-reel industrial production of coated conductors is still unknown and further works are also required. In addition, the maximum $BaHfO_3$ nanoparticle load and their incorporation in CeO_2-caped metallic tape substrates are also worth to be further investigated to disclose the optimal performance which can be achieved with our novel Flash Heating growth process. Last but not the least, a careful sorting out of the vortex pinning mechanisms associated with small nanoparticles or dislocation induced nanostrain is still pending and needs to be deployed in our future works via advanced measurements (transport and high resolution transmission electron microscopy).

References

[1] Wu M K, Ashburn J R, Torng C J, Hor P H, Meng R L, Gao L, Huang Z J, Wang Y Q and Chu C W 1987 Superconductivity at 93 K in a new mixed-phase Y-Ba-Cu-O compound system at ambient pressure *Physical Review Letters* **58** 908

[2] Ray P J 2015 Figure 2.4 in Master's thesis, "Structural investigation of $La_{(2-x)}Sr_{(x)}CuO_{(4+y)}$ - Following staging as a function of temperature" *Niels Bohr Institute, Faculty of Science, University of Copenhagen.*

[3] Llordés A 2010 Thesis: Superconducting nanocomposite films grown by chemical solution deposition: synthesis, microstructure and properties *ICMAB, Universitat Autónoma de Barcelona*

[4] Chaddah P 2003 Critical current densities in superconducting materials *Sadhana* **28** 273-82

[5] Waldram J R 1996 Superconductivity of metals and cuprates *Institut of Physics Publishing*

[6] Larbalestier D, Gurevich A, Feldmann D M and Polyanskii A 2001 High-T_c superconducting materials for electric power applications *Nature* **414** 368-77

[7] Jorgensen J D, Beno M A, Hinks D G, Soderholm L, Volin K J, Hitterman R L, Grace J D, Schuller I K, Segre C U, Zhang K and Kleefisch M S 1987 Oxygen ordering and the orthorhombic-to-tetragonal phase transition in $YBa_2Cu_3O_{7-x}$ *Physical Review B* **36** 3608

[8] Guzmán R 2013 Thesis: In-depth investigation of the origin, evolution and interaction of structural defects in YBCO nanocomposite thin films *ICMAB-CSIC, Univesitat Autónoma de Barcelona*

[9] Breit V, Schweiss P, Hauff R, Wühl H, Claus H, Rietschel H, Erb A and Müller-Vogt G 1995 Evidence for chain superconductivity in near-stoichiometric $YBa_2Cu_3O_x$ single crystals *Physical Review B* **52** 15727-30

[10] Mori Z, Doi T and Hakuraku Y 2010 Optimal annealing conditions for $Y_1Ba_2Cu_3O_{7-\delta}$ thin films *Journal of Applied Physics* **107** 023903

[11] Chikumoto N, Machi T, Tokunaga Y, Izumi T and Tajima S 2005 Optimization of oxygenation process in YBCO tapes fabricated by TFA-MOD method *Physica C: Superconductivity and its applications* **426-431** 1118-21

[12] Cayado P, Sanchez-Valdes C F, Stangl A, Coll M, Roura P, Palau A, Puig T and Obradors X 2017 Untangling surface oxygen exchange effects in $YBa_2Cu_3O_{6+x}$ thin films by electrical conductivity relaxation *Physical chemistry chemical physics* **19** 14129-40

[13] Ma Y and Xiao L 2004 Second generation YBCO coated conductors: A review *Chinese Science Bulletin* **49** 2435-9

[14] Blaugher R D, Schwall R E, Sokolowski R S, Suenaga M and Willis J O 1997 Power applications of superconductivity in Japan and Germany *World Technology Evaluation Center Panel Report*

[15] Goyal A, Paranthaman M P and Schoop U 2004 The RABiTS approach: Using rolling-assisted biaxially textured substrates for high-performance YBCO superconductors *MRS bulletin* **29** 552-61

[16] Goyal A, Norton D P, Budai J D, Paranthaman M, Specht E D, Kroeger D M, Christen D K, He Q, Saffian B, List F A, Lee D F, Martin P M, Klabunde C E, Hartfield E and Sikka V K 1996 High critical current density superconducting tapes by epitaxial deposition of $YBa_2Cu_3O_x$ thick films on biaxially textured metals *Applied Physics Letters* **69** 1795-7

[17] Iijima Y, Tanabe N, Kohno O and Ikeno Y 1992 In-plane aligned $YBa_2Cu_3O_{7-x}$ thin films deposited on polycrystalline metallic substrates *Applied Physics Letters* **60** 769-71

[18] Vlad R 2011 Thesis: Growth and characterization of chemical solution based nanostructured coated conductors with CeO_2 cap layers *ICMAB, Universitat Autonoma de Barcelona*

[19] Obradors X and Puig T 2014 Coated conductors for power applications: materials challenges *Superconductor Science and Technology* **27** 044003

[20] Coll M 2006 Thesis: Chemical Solution Deposition of Oxide Buffer and Superconducting Layers for $YBa_2Cu_3O_7$ Coated Conductors *ICMAB-CSIC, Universitat Autónoma de Barcelona*

[21] Iijima Y and Matsumoto K 2000 High-temperature-superconductor coated conductors: technical progress in Japan *Superconductor Science and Technology* **13** 68

[22] Obradors X, Puig T, Ricart S, Coll M, Gazquez J, Palau A and Granados X 2012 Growth, nanostructure and vortex pinning in superconducting $YBa_2Cu_3O_7$ thin films based on trifluoroacetate solutions *Superconductor Science and Technology* **25** 123001

[23] Roma N, Morlens S, Ricart S, Zalamova K, Moreto J M, Pomar A, Puig T and Obradors X 2006 Acid anhydrides: a simple route to highly pure organometallic solutions for superconducting films *Superconductor Science and Technology* **19** 521

[24] Araki T, Kurosaki H, Yamada Y, Hirabayashi I, Shibata J and Hirayama T 2001 Coating processes for $YBa_2Cu_3O_{7-x}$ superconductor by metalorganic deposition method using trifluoroacetates *Superconductor Science and Technology* **14** 783

[25] Falter M, Häßler W, Schlobach B and Holzapfel B 2002 Chemical solution deposition of $YBa_2Cu_3O_{7-x}$ films by dip coating *Physica C: Superconductivity* **372** 46-9

[26] Van Driessche I, Feys J, Hopkins S C, Lommens P, Granados X, Glowacki B A, Ricart S, Holzapfel B, Vilardell M, Kirchner A and Bäcker M 2012 Chemical solution deposition using ink-jet printing for YBCO coated conductors *Superconductor Science and Technology* **25** 065017

[27] Vilardell M 2014 Thesis: Inkjet printing: a flexible manufacturing of functional ceramic coatings by Chemical Solution Deposition *ICMAB, Universitat Autónoma de Barcelona*

[28] Gazquez J, Sandiumenge F, Coll M, Pomar A, Mestres N, Puig T, Obradors X, Kihn Y, Casanove M J and Ballesteros C 2006 Precursor Evolution and Nucleation Mechanism of $YBa_2Cu_3O_x$ Films by TFA Metal-Organic Decomposition *Chemistry of Materials* **18** 6211-9

[29] Llordes A, Zalamova K, Ricart S, Palau A, Pomar A, Puig T, Hardy A, Van Bael M K and Obradors X 2010 Evolution of Metal-Trifluoroacetate Precursors in the Thermal Decomposition toward High-Performance $YBa_2Cu_3O_7$ Superconducting Films *Chemistry of Materials* **22** 1686-94

[30] Zalamova K, Romà N, Pomar A, Morlens S, Puig T, Gázquez J, Carrillo A E, Sandiumenge F, Ricart S, Mestres N and Obradors X 2006 Smooth stress relief of trifluoroacetate metal-organic solutions for $YBa_2Cu_3O_7$ film growth *Chemistry of Materials* **18** 5897-906

[31] Dawley J T, Clem P G, Boyle T J, Ottley L M, Overmyer D L and Siegal M P 2004 Rapid processing method for solution deposited $YBa_2Cu_3O_{7-\delta}$ thin films *Physica C: Superconductivity* **402** 143-51

[32] Zalamova K, Pomar A, Palau A, Puig T and Obradors X 2009 Intermediate phase evolution in YBCO thin films grown by the TFA process *Superconductor Science and Technology* **23** 014012

[33] Gàzquez J 2006 Thesis: TEM investigation of growth mechanisms and microstructure of model YBCO coated conductor architectures deposited by metalorganic decomposition *ICMAB-CSIC, Univesitat Autónoma de Barcelona*

[34] Zalamova K 2009 Thesis: Fast growth rate of superconducting coated conductors based on metal-organic chemical solutions *ICMAB, Universitat Autónoma de Barcelona*

[35] Wong-Ng W, Levin I, Feenstra R, Cook L P and Vaudin M 2004 Phase evolution of $Ba_2YCu_3O_{6+x}$ films during the BaF_2 process *Superconductor Science and Technology* **17** S548

[36] Araki T, Hirabayashi I, Shibata J and Ikuhara Y 2002 High critical current density scheme of $YBa_2Cu_3O_{7-x}$ films by the metalorganic deposition using trifluoroacetates *Superconductor Science and Technology* **15** 913

[37] Chen H, Zalamova K, Pomar A, Granados X, Puig T and Obradors X 2010 Growth rate control and solid-gas modeling of TFA-$YBa_2Cu_3O_7$ thin film processing *Superconductor Science and Technology* **23** 034005

[38] Obradors X, Martínez-Julián F, Zalamova K, Vlad V R, Pomar A, Palau A, Llordés A, Chen H, Coll M, Ricart S, Mestres N, Granados X, Puig T and Rikel M 2012 Nucleation and mesostrain influence on percolating critical currents of solution derived $YBa_2Cu_3O_7$ superconducting thin films *Physica C: Superconductivity and its applications* **482** 58-67

[39] Matsuda J S, Tokunaga Y, Teranishi R, Fuji H, Kaneko A, Asada S, Honjo T, Yajima A, Iijima Y and Saitoh T 2004 Effects of heat-treatment conditions on microstructure of multi-coating Y123 films deposited by advanced TFA-MOD method *Physica C: Superconductivity* **412** 890-5

[40] Volmer M and Weber A 1926 Germ-formation in oversaturated figures *Zeitschrift Fur Physikalische Chemie-Stochiometrie Und Verwandtschaftslehre* **119(3/4)** 277

[41] Frank F C and Vandermerwe J H 1949 One-Dimensional Dislocations. 1. Static Theory. *Proceedings of the Royal Society of London Series a-Mathematical and Physical Sciences* **198(1053)** 205

[42] Krastanow L and Stranski I N 1938 Short notifications and notes. On the crystallisation of alkali halogenide crystals on fluorite *Zeitschrift Fur Kristallographie* **99(1)** 444

[43] Solovyov V F, Wiesmann H J and Suenaga M 2004 Nucleation of $YBa_2Cu_3O_{7-x}$ on buffered metallic substrates in thick precursor films made by the BaF_2 process *Superconductor Science and Technology* **18** 239

[44] Schwartz R W, Schneller T and Waser R 2004 Chemical solution deposition of electronic oxide films *Comptes Rendus Chimie* **7** 433-61

[45] Queraltó A 2015 Thesis: Growth of functional oxide heterostructures from chemical solutions using advanced processing methodologies *ICMAB, Universitat Autónoma de Barcelona*

[46] Chen H, Zalamova K, Pomar A, Granados X, Puig T and Obradors X 2011 Nucleation and growth rate influence on microstructure and critical currents of TFA-$YBa_2Cu_3O_7$ under low-pressure conditions *Journal of Materials Research* **25** 2371-9

[47] Shchukin V A and Bimberg D 1999 Spontaneous ordering of nanostructures on crystal surfaces *Reviews of Modern Physics* **71** 1125-71

[48] Gibert M, Abellán P, Martínez L, Román E, Crespi A, Sandiumenge F, Puig T and Obradors X 2011 Orientation and shape selection of self-assembled epitaxial $Ce_{1-x}Gd_xO_{2-y}$ nanostructures grown by chemical solution deposition *CrystEngComm* **13** 6719-27

[49] Granozio F M, Salluzzo M, di Uccio U S, Maggio-Aprile I and Fischer Ø 2000 Competition between a-axis and c-axis growth in superconducting $RBa_2Cu_3O_{7-x}$ thin films *Physical Review B* **61** 756

[50] Granozio F M and di Uccio U S 1997 Simple model for the nucleation of (001) and (100) oriented grains in YBCO films *Journal of Crystal Growth* **174** 409-16

[51] Ichino Y, Sudoh K, Miyachi K, Yoshida Y and Takai Y 2003 Orientation mechanism of $REBa_2Cu_3O_y$ (RE= Nd, Sm, Gd, Y, Yb) thin films prepared by pulsed laser deposition *IEEE transactions on applied superconductivity* **13** 2735-8

[52] Solovyov V F, Wiesmann H J and Suenaga M 2003 A new method of HF control for synthesizing YBCO using the BaF_2 ex situ process *Superconductor Science and Technology* **16** L37

[53] Puig T, González J C, Pomar A, Mestres N, Castaño O, Coll M, Gázquez J, Sandiumenge F, Piñol S and Obradors X 2005 The influence of growth conditions on the microstructure and critical currents of TFA-MOD $YBa_2Cu_3O_7$ films *Superconductor Science and Technology* **18** 1141-50

[54] Llordés A, Palau A, Gázquez J, Coll M, Vlad R, Pomar A, Arbiol J, Guzman R, Ye S, Rouco V, Sandiumenge F, Ricart S, Puig T, Varela M, Chateigner D, Vanacken J, Gutiérrez J, Moshchalkov V, Deutscher G, Magen C and Obradors X 2012 Nanoscale strain-induced pair suppression as a vortex-pinning mechanism in high-temperature superconductors *Nature Materials* **11** 329-36

[55] Coll M, Guzman R, Garcés P, Gazquez J, Rouco V, Palau A, Ye S, Magen C, Suo H, Castro H, Puig T and Obradors X 2014 Size-controlled spontaneously segregated Ba_2YTaO_6 nanoparticles in $YBa_2Cu_3O_7$ nanocomposites obtained by chemical solution deposition *Superconductor Science and Technology* **27** 044008

[56] Sánchez-Valdés C F, Puig T and Obradors X 2015 In situ study through electrical resistance of growth rate of trifluoroacetate-based solution-derived $YBa_2Cu_3O_7$ films *Superconductor Science and Technology* **28** 024006

[57] Ostwald W 1897 Studies on the Formation and Change of Solid Matter *Z. Phys. Chem.* **22** 289-302

[58] Beysens D, Knobler C M and Schaffar H 1990 Scaling in the growth of aggregates on a surface *Physical Review B* **41** 9814

[59] Bardotti L, Bartelt M C, Jenks C J, Stoldt C R, Wen J M, Zhang C M, Thiel P A and Evans J W 1998 Formation and equilibration of submonolayer island distributions in Ag/Ag (100) homoepitaxy *Langmuir* **14** 1487-92

[60] Mehrer H 2007 Diffusion in solids: fundamentals, methods, materials, diffusion-controlled processes *Springer Science & Business Media* **155**

[61] Rupp J L M, Infortuna A and Gauckler L J 2006 Microstrain and self-limited grain growth in nanocrystalline ceria ceramics *Acta Materialia* **54** 1721-30

[62] Löffler J F and Johnson W L 2000 Model for decomposition and nanocrystallization of deeply undercooled $Zr_{41.2}Ti_{13.8}Cu_{12.5}Ni_{10}Be_{22.5}$ *Applied Physics Letters* **76** 3394-6

[63] Mihalache V and Pasuk I 2011 Grain growth, microstructure and surface modification of textured CeO_2 thin films on Ni substrate *Acta Materialia* **59** 4875-85

[64] Miura M, Maiorov B, Willis J O, Kato T, Sato M, Izumi T, Shiohara Y and Civale L 2013 The effects of density and size of $BaMO_3$ (M=Zr, Nb, Sn) nanoparticles on the vortex glassy and liquid phase in (Y, Gd)$Ba_2Cu_3O_y$ coated conductors *Superconductor Science and Technology* **26** 035008

[65] Coll M, Ye S, Rouco V, Palau A, Guzman R, Gazquez J, Arbiol J, Suo H, Puig T and Obradors X 2012 Solution-derived $YBa_2Cu_3O_7$ nanocomposite films with a Ba_2YTaO_6 secondary phase for improved superconducting properties *Superconductor Science and Technology* **26** 015001

[66] Miura M, Maiorov B, Sato M, Kanai M, Kato T, Kato T, Izumi T, Awaji S, Mele P, Kiuchi M and Matsushita T 2017 Tuning nanoparticle size for enhanced functionality in perovskite thin films deposited by metal organic deposition *NPG Asia Materials* **9** e447

[67] Li P, Abraimov D, Xu A and Larbalestier D 2011 Observation of important current-limiting defects in a recent high pinning force MOCVD IBAD-MgO coated conductor *Superconductor Science and Technology* **25** 025002

[68] Durrell J H and Rutter N A 2008 Importance of low-angle grain boundaries in $YBa_2Cu_3O_{7-\delta}$ coated conductors *Superconductor Science and Technology* **22** 013001

[69] Bartolomé E, Gömory F, Granados X, Puig T and Obradors X 2007 Universal correlation between critical current density and normal-state resistivity in porous $YBa_2Cu_3O_{7-x}$ thin films *Superconductor Science and Technology* **20** 895

[70] Holesinger T G, Civale L, Maiorov B, Feldmann D M, Coulter J Y, Miller D J, Maroni V A, Chen Z, Larbalestier D C, Feenstra R, Li X P, Huang M B, Kodenkandath T, Zhang W, Rupich M W and Malozemoff A P 2008 Progress in Nanoengineered Microstructures for Tunable High-Current, High-Temperature Superconducting Wires *Advanced Materials* **20** 391-407

[71] Coll M, Gazquez J, Pomar A, Puig T, Sandiumenge F and Obradors X 2006 Stress-induced spontaneous dewetting of heteroepitaxial $YBa_2Cu_3O_7$ thin films *Physical Review B* **73** 075420

[72] Cayado P 2016 Thesis: Multifunctional nanostructured superconductors by chemical routes: towards high current conductors *ICMAB-CSIC, Univesitat Autónoma de Barcelona*

[73] Blamire M G, MacManus-Driscoll J L, Mathur N D and Barber Z H 2009 The materials science of functional oxide thin films *Advanced Materials* **21** 3827-39

[74] Zhang W, Ramesh R, MacManus-Driscoll J L and Wang H 2015 Multifunctional, self-assembled oxide nanocomposite thin films and devices *MRS Bulletin* **40** 736-45

[75] Foltyn S R, Civale L, MacManus-Driscoll J L, Jia Q X, Maiorov B, Wang H and Maley M 2007 Materials science challenges for high-temperature superconducting wire *Nature Materials* **6** 631-42

[76] Rouco V, Bartolomé E, Palau A, Coll M, Obradors X and Puig T 2012 Nanostrain induced pinning in $YBa_2Cu_3O_{7-x}$ nanocomposites even close to the irreversibility line *Superconductor Science and Technology* **25** 122001

[77] Gutierrez J, Llordes A, Gazquez J, Gibert M, Roma N, Ricart S, Pomar A, Sandiumenge F, Mestres N, Puig T and Obradors X 2007 Strong isotropic flux pinning in solution-derived $YBa_2Cu_3O_{7-x}$ nanocomposite superconductor films *Nature Materials* **6** 367-73

[78] Kim J H, Dou S X, Hossain M S A, Xu X, Wang J L, Shi D Q, Nakane T and Kumakura H 2007 Systematic study of a MgB_2+$C_4H_6O_5$ superconductor prepared by the chemical solution route *Superconductor Science and Technology* **20** 715

[79] Varela M, Sefrioui Z, Arias D, Navacerrada M A, Lucía M, de La Torre M A L, León C, Loos G D, Sánchez-Quesada F and Santamaría J 1999 Intracell changes in epitaxially strained $YBa_2Cu_3O_{7-x}$ ultrathin layers in $YBa_2Cu_3O_{7-x}$/$PrBa_2Cu_3O_7$ superlattices *Physical review letters* **83** 3936

[80] Colino J, Sacedon J L and Vicent J L 1991 Study of the oxygen depletion in the film-substrate interface of superconducting $YBa_2Cu_3O_{7-x}$ films *Applied physics letters* **59** 3327-9

[81] Lee D, Yoon A, Jang S Y, Yoon J G, Chung J S, Kim M, Scott J F and Noh T W 2011 Giant flexoelectric effect in ferroelectric epitaxial thin films *Physical Review Letters* **107** 057602

[82] Lee D and Noh T W 2012 Giant flexoelectric effect through interfacial strain relaxation *Phil. Trans. R. Soc. A* **370** 4944-57

[83] Shaked H, Jorgensen J D, Hunter B A, Hitterman R L, Paulikas A P and Veal B W 1995 Local ordering and charge transfer during room-temperature annealing of quenched tetragonal $YBa_2Cu_3O_{6.25}$ *Physical Review B* **51** 547

[84] Wimbush S C, Li M, Vickers M E, Maiorov B, Feldmann D M, Jia Q and MacManus-Driscoll J L 2009 Interfacial Strain-Induced Oxygen Disorder as the Cause of Enhanced Critical Current Density in Superconducting Thin Films *Advanced Functional Materials* **19** 835-41

[85] Gutierrez J 2008 Tesis: Vortex pinning and critical currents in $YBa_2Cu_3O_{7-x}$ MOD-TFA thin films and Coated Conductors *ICMAB, Universitat Autonoma de Barcelona*

[86] Klaassen F C, Doornbos G, Huijbregtse J M, Van der Geest R C F, Dam B and Griessen R 2001 Vortex pinning by natural linear defects in thin films of $YBa_2Cu_3O_{7-\delta}$ *Physical Review B* **64** 184523

[87] Palau A, Vallès F, Rouco V, Coll M, Li Z, Pop C, Mundet B, Gàzquez J, Guzman R, Gutierrez J, Obradors X and Puig T 2018 Disentangling vortex pinning landscape in chemical solution deposition superconducting $YBa_2Cu_3O_{7-x}$ films and nanocomposites *Superconductor Science and Technology* **31** 034004

[88] Dam B, Huijbregtse J M, Klaassen F C, Van der Geest R C F, Doornbos G, Rector J H, Testa A M, Freisem S, Martinez J C, Stäuble-Pümpin B and Griessen R 1999 Origin of high critical currents in $YBa_2Cu_3O_{7-\delta}$ superconducting thin films *Nature* **399** 439

[89] Palau A, Puig T, Gutierrez J, Obradors X and de La Cruz F 2006 Pinning regimes of grain boundary vortices in $YBa_2Cu_3O_{7-x}$ coated conductors *Physical Review B* **73** 132508

[90] Matsumoto K and Mele P 2009 Artificial pinning center technology to enhance vortex pinning in YBCO coated conductors *Superconductor Science and Technology* **23** 014001

[91] Plain J, Puig T, Sandiumenge F, Obradors X and Rabier J 2002 Microstructural influence on critical currents and irreversibility line in melt-textured $YBa_2Cu_3O_{7-x}$ reannealed at high oxygen pressure *Physical Review B* **65** 104526

[92] Blatter G, Feigel'man M V, Geshkenbein V B, Larkin A I and Vinokur V M 1994 Vortices in high-temperature superconductors *Reviews of Modern Physics* **66** 1125

[93] Nelson D R and Vinokur V M 1993 Boson localization and correlated pinning of superconducting vortex arrays *Physical Review B* **48** 13060

[94] Puig T, Gutiérrez J, Pomar A, Llordés A, Gazquez J, Ricart S, Sandiumenge F and Obradors X 2008 Vortex pinning in chemical solution nanostructured YBCO films *Superconductor Science and Technology* **21** 034008

[95] Gutiérrez J, Puig T and Obradors X 2007 Anisotropy and strength of vortex pinning centers in $YBa_2Cu_3O_{7-x}$ coated conductors *Applied Physics Letters* **90** 162514

[96] MacManus-Driscoll J L, Foltyn S R, Jia Q X, Wang H, Serquis A, Civale L, Maiorov B, Hawley M E, Maley M P and Peterson D E 2004 Strongly enhanced current densities in superconducting coated conductors of $YBa_2Cu_3O_{7-x}$+$BaZrO_3$ *Nature Materials* **3** 439-43

[97] Varanasi C V, Barnes P N, Burke J, Brunke L, Maartense I, Haugan T J, Stinzianni E A, Dunn K A and Haldar P 2006 Flux pinning enhancement in $YBa_2Cu_3O_{7-x}$ films with $BaSnO_3$ nanoparticles *Superconductor Science and Technology* **19** L37

[98] Maiorov B, Baily S A, Zhou H, Ugurlu O, Kennison J A, Dowden P C, Holesinger T G, Foltyn S R and Civale L 2009 Synergetic combination of different types of defect to optimize pinning landscape using $BaZrO_3$-doped $YBa_2Cu_3O_7$ *Nature Materials* **8** 398-404

[99] Sparing M, Reich E, Hänisch J, Gottschall T, Hühne R, Fähler S, Rellinghaus B, Schultz L and Holzapfel B 2017 Controlling particle properties in nanocomposites by combining PLD with an inert gas condensation system *Superconductor Science and Technology* **30** 104007

[100] Ye S, Suo H, Wu Z, Liu M, Xu Y, Ma L and Zhou M 2011 Preparation of solution-based YBCO films with $BaSnO_3$ particles *Physica C: Superconductivity* **471** 265-9

[101] Sieger M, Pahlke P, Lao M, Eisterer M, Meledin A, Van Tendeloo G, Ottolinger R, Hänisch J, Holzapfel B, Usoskin A, Kursumovic A, MacManus-Driscoll J L, Stafford B H, Bauer M, Nielsch K, Schultz L and Hühne R 2017 Tailoring Microstructure and Superconducting Properties in Thick $BaHfO_3$ and $Ba_2Y(Nb/Ta)O_6$ Doped YBCO Films on Technical Templates *IEEE Transactions on Applied Superconductivity* **27** 1-7

[102] Wee S H, Zuev Y L, Cantoni C and Goyal A 2013 Engineering nanocolumnar defect configurations for optimized vortex pinning in high temperature superconducting nanocomposite wires *Scientific Reports* **3** 2310

[103] Horide T, Otsubo K, Kita R, Matsukida N, Ishimaru M, Awaji S and Matsumoto K 2017 Strong c-axis correlated pinning and hybrid pinning in $YBa_2Cu_3O_{7-\delta}$ films containing $BaHfO_3$ nanorods and stacking faults *Superconductor Science and Technology* **30** 074009

[104] Birlik I, Erbe M, Freudenberg T, Celik E, Schultz L and Holzapfel B 2010 Flux pinning improvement of YBCO superconducting films with $BaZrO_3$ nanoparticles prepared by chemical solution deposition method *Journal of Physics: Conference Series* **234** 012004

[105] Miura M, Yoshizumi M, Izumi T and Shiohara Y 2009 Formation mechanism of $BaZrO_3$ nanoparticles in $Y_{1-x}Sm_xBa_2Cu_3O_y$-coated conductors derived from trifluoroacetate metal-organic deposition *Superconductor Science and Technology* **23** 014013

[106] Ding F Z, Gu H W, Zhang T, Wang H Y, Qu F, Qiu Q Q, Dai S T and Peng X Y 2013 Strong flux pinning enhancement in $YBa_2Cu_3O_{7-x}$ films by embedded $BaZrO_3$ and $BaTiO_3$ nanoparticles *Chinese Physics B* **22** 077401

[107] Ding F Z, Gu H W, Zhang T, Wang H Y, Qu F, Dai S T, Peng X Y and Cao J L 2012 Enhanced flux pinning in MOD-YBCO films with co-doping of $BaZrO_3$ and Y_2O_3 nanoparticles *Journal of Alloys and Compounds* **513** 277-81

[108] Jin L H, Zhang S N, Yu Z M, Li C S, Feng J Q, Sulpice A, Wang Y and Zhang P X 2015 Influences of $BaZrO_3$ particles on the microstructure and flux pinning of YBCO film prepared by using modified TFA-MOD approach *Materials Chemistry and Physics* **149** 188-92

[109] Petrisor T, Mos R B, Nasui M, Gabor M S, Augieri A, Celentano G, De Felicis D, Bemporad E, Ciontea L and Petrisor T 2014 The Vortex Path Model Analysis of the Field Angle Dependence of the Critical Current Density in Nanocomposite $YBa_2Cu_3O_{7-x}$–$BaZrO_3$ Films Obtained by Low Fluorine Chemical Solution Deposition *Journal of Superconductivity and Novel Magnetism* **27** 2493-500

[110] Engel S, Thersleff T, Hühne R, Schultz L, Holzapfel B, Engel S, Thersleff T, Schultz L, Holzapfel B and Schultz L 2007 Enhanced flux pinning in $YBa_2Cu_3O_7$ layers by the formation of nanosized $BaHfO_3$ precipitates using the chemical deposition method *Applied Physics Letters* **90** 102505

[111] Erbe M, Hänisch J, Hühne R, Freudenberg T, Kirchner A, Molina-Luna L, Damm C, Van Tendeloo G, Kaskel S, Schultz L and Holzapfel B 2015 $BaHfO_3$ artificial pinning centres in TFA-MOD-derived YBCO and GdBCO thin films *Superconductor Science and Technology* **28** 114002

[112] Molina-Luna L, Duerrschnabel M, Turner S, Erbe M, Martinez G T, Van Aert S, Holzapfel B and Van Tendeloo G 2015 Atomic and electronic structures of $BaHfO_3$-doped TFA-MOD-derived $YBa_2Cu_3O_{7-\delta}$ thin films *Superconductor Science and Technology* **28** 115009

[113] Guzman R, Gazquez J, Mundet B, Coll M, Obradors X and Puig T 2017 Probing localized strain in solution-derived $YBa_2Cu_3O_{7-\delta}$ nanocomposite thin films *Physical Review Materials* **1** 024801

[114] Rouco V, Palau A, Guzman R, Gazquez J, Coll M, Obradors X and Puig T 2014 Role of twin boundaries on vortex pinning of CSD YBCO nanocomposites *Superconductor Science and Technology* **27** 125009

[115] Deutscher G and de Gennes P G 2009 A spatial interpretation of emerging superconductivity in lightly doped cuprates *PG De Gennes' Impact on Science-Volume I* **18** 49-53

[116] Gazquez J, Coll M, Roma N, Sandiumenge F, Puig T and Obradors X 2012 Structural defects in trifluoroacetate derived $YBa_2Cu_3O_7$ thin films *Superconductor Science and Technology* **25** 065009

[117] Gazquez J, Guzman R, Mishra R, Bartolomé E, Salafranca J, Magén C, Varela M, Coll M, Palau A, Valvidares S M, Gargiani P, Pellegrin E, Herrero-Martin J, Pennycook S J, Pantelides S T, Puig T and Obradors X 2016 Emerging Diluted Ferromagnetism in High-T_c Superconductors Driven by Point Defect Clusters *Advanced Science* **3** 8

[118] Cayado P, De Keukeleere K, Garzón A, Perez-Mirabet L, Meledin A, De Roo J, Vallés F, Mundet B, Rijckaert H, Pollefeyt G, Coll M, Ricart S, Palau A, Gázquez J, Ros J, Van Tendeloo G, Van Driessche I, Puig T and Obradors X 2015 Epitaxial $YBa_2Cu_3O_{7-x}$ nanocomposite thin films from colloidal solutions *Superconductor Science and Technology* **28** 124007

[119] Solano E, Perez-Mirabet L, Martinez-Julian F, Guzmán R, Arbiol J, Puig T, Obradors X, Yañez R, Pomar A and Ricart S 2012 Facile and efficient one-pot solvothermal and microwave-assisted synthesis of stable colloidal solutions of MFe_2O_4 spinel magnetic nanoparticles *Journal of Nanoparticle Research* **14** 1034

[120] Solano E, Yáñez R, Ricart S and Ros J 2015 New approach towards the polyol route to fabricate MFe_2O_4 magnetic nanoparticles: The use of MCl_2 and $Fe(acac)_3$ as chemical precursors *Journal of Magnetism and Magnetic Materials* **382** 380-5

[121] Pérez-Mirabet L, Solano E, Martínez-Julián F, Guzmán R, Arbiol J, Puig T, Obradors X, Pomar A, Yáñez R and Ros J 2013 One-pot synthesis of stable colloidal solutions of MFe_2O_4 nanoparticles using oleylamine as solvent and stabilizer *Materials Research Bulletin* **48** 966-72

[122] De Keukeleere K, De Roo J, Lommens P, Martins J C, Van Der Voort P and Van Driessche I 2015 Fast and tunable synthesis of ZrO_2 nanocrystals: mechanistic insights into precursor dependence *Inorganic chemistry* **54** 3469-76

[123] Garzón M A 2016 Thesis: Synthesis of Metal Oxide Nanoparticles for Superconducting Nanocomposites and Other Applications *ICMAB, Universitat Autónoma de Barcelona*

[124] Baghbanzadeh M, Carbone L, Cozzoli P D and Kappe C O 2011 Microwave-assisted synthesis of colloidal inorganic nanocrystals *Angewandte Chemie International Edition* **50** 11312-59

[125] De Keukeleere K, Cayado P, Meledin A, Vallès F, De Roo J, Rijckaert H, Pollefeyt G, Bruneel E, Palau A, Coll M, Ricart S, Van Tendeloo G, Puig T, Obradors X and Van Driessche I 2016 Superconducting $YBa_2Cu_3O_{7-\delta}$ Nanocomposites Using Preformed ZrO_2 Nanocrystals: Growth Mechanisms and Vortex Pinning Properties *Advanced Electronic Materials* **2** 1600161

[126] Martinez-Julian F, Ricart S, Pomar A, Coll M, Abellán P, Sandiumenge F, Casanove M J, Obradors X, Puig T, Pastoriza-Santos I and Liz-Marzán L M 2011 Chemical Solution Approaches to $YBa_2Cu_3O_7$-Au Nanocomposite Superconducting Thin Films *Journal of nanoscience and nanotechnology* **11** 3245-55

[127] Bretos I, Schneller T, Falter M, Bäcker M, Hollmann E, Wördenweber R, Molina-Luna L, Van Tendeloo G and Eibl O 2015 Solution-derived $YBa_2Cu_3O_{7-\delta}$ (YBCO) superconducting films with $BaZrO_3$ (BZO) nanodots based on reverse micelle stabilized nanoparticles *Journal of Materials Chemistry C* **3** 3971-9

[128] Bartolomé E, Cayado P, Solano E, Mocuta C, Ricart S, Mundet B, Coll M, Gázquez J, Meledin A, van Tendeloo G, Valvidares S M, Herrero-Martín J, Gargiani P, Pellegrin E, Magén C, Puig T and Obradors X 2017 Hybrid $YBa_2Cu_3O_7$ Superconducting-Ferromagnetic Nanocomposite Thin Films Prepared from Colloidal Chemical Solutions *Advanced Electronic Materials* **3** 1700037

[129] Meledin A, Turner S, Cayado P, Mundet B, Solano E, Ricart S, Ros J, Puig T, Obradors X and Van Tendeloo G 2016 Unique nanostructural features in Fe, Mn-doped YBCO thin films *Superconductor Science and Technology* **29** 125009

[130] Solano E, Geenen F, Puig T, Obradors X, Mocuta C and Detavernier C 2017 Axiotaxy in oxide heterostructures: Preferential orientation of $BaCeO_3$ nanoparticles embedded in superconducting $YBa_2Cu_3O_{7-\delta}$ thin films *Thin Solid Films* **638** 105-13

[131] Rijckaert H, Pollefeyt G, Sieger M, Hanisch J, Bennewitz J, De Keukeleere K, De Roo J, Huhne R, Backer M, Paturi P, Huhtinen H, Hemgesberg M and Van Driessche I 2017 Optimizing Nanocomposites through Nanocrystal Surface Chemistry: Superconducting $YBa_2Cu_3O_7$ Thin Films via Low-Fluorine Metal Organic Deposition and Preformed Metal Oxide Nanocrystals *Chemistry of Materials* **29** 6104-13

[132] Obradors X, Puig T, Li Z, Pop C, Mundet B, Chamorro N, Vallés F, Coll M, Ricart S, Vallejo B, Pino F, Palau A, Gazquez J, Ros J and Usoskin A 2018 Epitaxial $YBa_2Cu_3O_{7-x}$ nanocomposite films and coated conductors from $BaMO_3$ (M= Zr, Hf) colloidal solutions *Superconductor Science and Technology* **31** 044001

[133] Vassen R, Cao X, Tietz F, Basu D and Stöver D 2000 Zirconates as new materials for thermal barrier coatings *Journal of the American Ceramic Society* **83** 2023-8

[134] Maekawa T, Kurosaki K and Yamanaka S 2006 Thermal and mechanical properties of perovskite-type barium hafnate *Journal of Alloys and Compounds* **407** 44-8

[135] Zhang J L and Evetts J E 1994 $BaZrO_3$ and $BaHfO_3$: preparation, properties and compatibility with $YBa_2Cu_3O_{7-x}$ *Journal of Materials Science* **29** 778-85

[136] Chamorro N 2018 In preparation

[137] Huijbregtse J M, Rector J H and Dam B 2001 Effect of the two (100) $SrTiO_3$ substrate terminations on the nucleation and growth of $YBa_2Cu_3O_{7-\delta}$ thin films *Physica C: Superconductivity* **351** 183-99

[138] Usoskin A, Betz U, Hofacker F, Dietrich R and Schlenga K 2017 Long HTS Tapes With High In-Field Performance Manufactured via Multibeam PLD With "Dynamic" Drum Concept *IEEE Transactions on Applied Superconductivity* **27** 1-5

[139] Coll M, Gazquez J, Huhne R, Holzapfel B, Morilla Y, Garcia-Lopez J, Pomar A, Sandiumenge F, Puig T and Obradors X 2009 All chemical $YBa_2Cu_3O_7$ superconducting multilayers: critical role of CeO_2 cap layer flatness *Journal of Materials Research* **24** 1446-55

[140] Bartolomé E, Vlad V R, Calleja A, Aklalouch M, Guzmán R, Arbiol J, Granados X, Palau A, Obradors X and Puig T 2013 Magnetic and structural characterization of inkjet-printed $^{TFA}YBa_2Cu_3O_{7-x}/^{MOD}CZO/^{ABAD}YSZ/SS$ coated conductors *Superconductor Science and Technology* **26** 125004

[141] Obradors X, Puig T, Pomar A, Sandiumenge F, Pinol S, Mestres N, Castano O, Coll M, Cavallaro A, Palau A, Gázquez J, González J C, Gutiérrez J, Romà N, Ricart S, Moretó J M, Rossell M D and Van Tendeloo G 2004 Chemical solution deposition: a path towards low cost coated conductors *Superconductor Science and Technology* **17** 1055

[142] Nelson J B and Riley D P 1945 An experimental investigation of extrapolation methods in the derivation of accurate unit-cell dimensions of crystals *Proceedings of the Physical Society* **57** 160

[143] Nelson J B and Riley D P 1945 The thermal expansion of graphite from 15 °C to 800 °C: Part I. Experimental *Proceedings of the Physical Society* **57** 477

[144] He B B 2009 Two-dimensional X-Ray diffraction *Wiley*

[145] Matsuda J, Nakaoka K, Izumi T, Yamada Y and Shiohara Y 2008 Microstructure evolution of YBCO films deposited by advanced TFA-MOD process *Physica C: Superconductivity and its applications* **468** 1017-23

[146] Moram M A and Vickers M E 2009 X-ray diffraction of III-nitrides *Reports on Progress in Physics* **72** 036502

[147] Vickers M E, Kappers M J, Datta R, McAleese C, Smeeton T M, Rayment F D G and Humphreys C J 2005 In-plane imperfections in GaN studied by x-ray diffraction *Journal of Physics D: Applied Physics* **38** A99

[148] Lafford T A, Tanner B K and Parbrook P J 2003 Direct measurement of twist mosaic in GaN epitaxial films as a function of growth temperature *Journal of Physics D: Applied Physics* **36** A245

[149] Heying B, Wu X H, Keller S, Li Y, Kapolnek D, Keller B P, Den B S P and Speck J S 1996 Role of threading dislocation structure on the x-ray diffraction peak widths in epitaxial GaN films *Applied Physics Letters* **68** 643-5

[150] Palau A 2005 Thesis: Critical current and dissipation of grain boundary networks in coated conductors *ICMAB-CSIC, Univesitat Autónoma de Barcelona*

[151] Bean C P 1962 Magnetization of hard superconductors *Physical Review Letters* **8** 250

[152] Obradors X, Puig T, Pomar A, Sandiumenge F, Mestres N, Coll M, Cavallaro A, Romà N, Gázquez J, González J C, Castaño O, Gutierrez J, Palau A, Zalamova K, Morlens S, Hassini A, Gibert M, Ricart S, Moretó J M, Piñol S, Isfort D and Bock J 2006 Progress towards all-chemical superconducting $YBa_2Cu_3O_7$-coated conductors *Superconductor Science and Technology* **19** S13-S26

[153] Lin J X, Liu X M, Cui C W, Bai C Y, Lu Y M, Fan F, Guo Y Q, Liu Z Y and Cai C B 2017 A review of thickness-induced evolutions of microstructure and superconducting performance of $REBa_2Cu_3O_{7-\delta}$ coated conductor *Advances in Manufacturing* **5** 165-76

[154] Izumi T, Yoshizumi M, Miura M, Sutoh Y, Nakanishi T, Nakai A, Ichikawa Y, Yamada Y, Goto T, Yajima A, Aoki Y, Hasegawa T and Shiohara Y 2008 Research and development of reel-to-reel TFA–MOD process for coated conductors *Physica C: Superconductivity* **468** 1527-30

[155] Araki T and Hirabayashi I 2003 Review of a chemical approach to $YBa_2Cu_3O_{7-x}$-coated superconductors-metalorganic deposition using trifluoroacetates *Superconductor Science and Technology* **16** R71

[156] Cayado P, Mundet B, Eloussifi H, Vallés F, Coll M, Ricart S, Gázquez J, Palau A, Roura P, Farjas J, Puig T and Obradors X 2017 Epitaxial superconducting $GdBa_2Cu_3O_{7-\delta}/Gd_2O_3$ nanocomposite thin films from advanced low-fluorine solutions *Superconductor Science and Technology* **30** 125010

[157] Dou W, Liu Z, Peng C, Bai C, Lu Y, Guo Y and Cai C 2016 Phase Transition During Heat Treatment of Precursor Before $YBa_2Cu_3O_{7-\delta}$ Nucleation in TFA–MOD Method *Journal of Superconductivity and Novel Magnetism* **29** 1997-2001

[158] Wu W, Feng F, Zhao Y, Tang X, Grivel J C, Han Z, Hong Z and Jin Z 2016 Intermediate Phase Study on YBCO Films Coated by Precursor Solutions With F/Ba Atomic Ratio of 2 *IEEE Transactions on Applied Superconductivity* **26** 1-5

[159] Vandaele K, Mosiadz M, Hopkins S C, Patel A, Van Driessche I and Glowacki B A 2012 The influence of heat treatment parameters on pyrolysed TFA-derived YBCO films deposited by inkjet printing *Materials Research Bulletin* **47** 2032-9

[160] Yoshizumi M, Seleznev I and Cima M J 2004 Reactions of oxyfluoride precursors for the preparation of barium yttrium cuprate films *Physica C: Superconductivity* **403** 191-9

[161] Qu T, Zhu Y, Feng F, Lin G, Deng S, Lu H, Zhang X, Fu Q, Xiao S, Zeng P and Han Z 2016 Thermodynamics and Kinetics Analysis of MOD-YBCO Heat Treatment Process Using in situ Resistance Measurement Method *IEEE Transactions on Applied Superconductivity* **26** 1-5

[162] Armenio A A, Augieri A, Ciontea L, Contini G, Davoli I, Giovannantonio M D, Galluzzi V, Mancini A, Rufoloni A and Petrisor T 2011 Structural and chemical evolution of propionate based metal-organic precursors for superconducting$YBa_2Cu_3O_{7-\delta}$ epitaxial film growth *Superconductor Science and Technology* **24** 115008

[163] Wu L, Zhu Y, Solovyov V F, Wiesmann H J, Moodenbaugh A R, Sabatini R L and Suenaga M 2001 Nucleation and growth of $YBa_2Cu_3O_x$ on $SrTiO_3$ and CeO_2 by a BaF_2 postdeposition reaction process *Journal of Materials Research* **16** 2869-84

[164] Matsuda J, Nakaoka K, Teranishi R, Kitoh Y, Aoki Y, Fuji H, Yamada Y, Izumi T and Shiohara Y 2006 Microstructure and crystallization mechanism of $YBa_2Cu_3O_{7-y}$ films formed by advanced TFA-MOD process *Physica C: Superconductivity and its applications* **445** 563-9

[165] Matsuda J, Nakaoka K, Sutoh Y, Nakanishi T, Yoshizumi M, Yamada Y, Izumi T and Shiohara Y 2007 Microstructural analysis on growth and crystallization mechanism of YBCO

films deposited by advanced TFA-MOD process *Physica C: Superconductivity and its applications* **463** 712-6

[166] Wesolowski D E, Patta Y R and Cima M J 2009 Conversion behavior comparison of TFA–MOD and non-fluorine solution-deposited YBCO films *Physica C: Superconductivity* **469** 766-73

[167] Zhao Y, Qureishy T, Mikheenko P and Grivel J C 2016 Characterization of $YBa_2Cu_3O_{7-\delta}$ Films With Various Porous Structures Grown by Metalorganic Decomposition Route *IEEE Transactions on Applied Superconductivity* **26** 1-4

[168] Feenstra R, List F A, Li X, Rupich M W, Miller D J, Maroni V A, Zhang Y, Thompson J R and Christen D K 2009 A modular ex situ conversion process for thick MOD-Fluoride RBCO precursors *IEEE Transactions on Applied Superconductivity* **19** 3131-5

[169] Wesolowski D E, Yoshizumi M and Cima M J 2006 Trajectory-property relationships in MOD-derived YBCO films *Physica C: Superconductivity and its applications* **450** 76-82

[170] Pomar A, Gutiérrez J, Palau A, Puig T and Obradors X 2006 Porosity induced magnetic granularity in epitaxial $YBa_2Cu_3O_7$ thin films *Physical Review B* **73** 214522

[171] Yoshida J, Tada K, Tanaka T, Mori N, Yamada K, Teranishi R, Mukaida M, Kiss T, Inoue M, Shiohara Y, Izumi T, Nakaoka K and Matsuda J 2008 Effect of calcination conditions on microstructures and J_c of YBCO films fabricated by TFA-MOD method *Physica C: Superconductivity* **468** 1550-3

[172] Chan S W, Bagley B G, Greene L H, Giroud M, Feldmann W L, Jenkin K R and Wilkins B J 1988 Effect of the post-deposition processing ambient on the preparation of superconducting $YBa_2Cu_3O_{7-x}$ coevaporated thin films using a BaF_2 source *Applied Physics Letters* **53** 1443-5

[173] Lei L, Zhao G, Zhao J and Xu H 2010 Water-Vapor-Controlled Reaction for Fabrication of YBCO Films by Fluorine-Free Sol-Gel Process *IEEE Transactions on Applied Superconductivity* **20** 2286-93

[174] Solovyov V F, Wiesmann H J and Suenaga M 2005 Nucleation of $YBa_2Cu_3O_7$ from precursor films using the barium fluoride process *IEEE transactions on applied superconductivity* **15** 2739-42

[175] Holesinger T G, Maiorov B, Coulter J Y, Civale L, Li X, Zhang W, Huang Y, Kodenkandath T and Rupich M W 2007 Key Microstructural Features of MOD $YBa_2Cu_3O_{7-x}$ Films on Textured Nickel Substrates *IEEE Transactions on Applied Superconductivity* **17** 3259-62

[176] Hilgenkamp H and Mannhart J 2002 Grain boundaries in high-T_c superconductors *Reviews of Modern Physics* **74** 485

[177] Nakaoka K, Matsuda J, Yoshizumi M, Goto T, Yamada Y, Izumi T and Shiohara Y 2007 Optimization of process parameters for calcination in TFA-MOD method *IEEE Transactions on Applied Superconductivity* **17** 3313-6

[178] Wesolowski D E and Cima M J 2007 Large-area quantification of $BaCeO_3$ formation during processing of metalorganic-deposition-derived YBCO films *Journal of Materials Research* **22** 1077-81

[179] Sutoh Y, Nakaoka K, Matsuda J, Kitoh Y, Nakanishi T, Nakai A, Yoshizumi M, Miyata S, Yamada Y, Izumi T, Shiohara Y and Saitoh T 2007 Effective thickness of CeO_2 buffer layer for YBCO coated conductor by advanced TFA-MOD process *Physica C: Superconductivity and its applications* **463-465** 571-3

[180] Lyatti M, Savenko A and Poppe U 2016 Ultra-thin $YBa_2Cu_3O_{7-x}$ films with high critical current density *Superconductor Science and Technology* **29** 065017

[181] Hammar A, Cherednichenko S, Bevilacqua S, Drakinskiy V and Stake J 2011 Terahertz Direct Detection in $YBa_2Cu_3O_7$ Microbolometers *IEEE Transactions on Terahertz Science and Technology* **1** 390-4

[182] Probst P, Scheuring A, Hofherr M, Rall D, Wünsch S, Il'in K, Siegel M, Semenov A, Pohl A, Hübers H W, Judin V, Müller A S, Hoehl A, Müller R and Ulm G 2011 $YBa_2Cu_3O_{7-\delta}$ quasioptical detectors for fast time-domain analysis of terahertz synchrotron radiation *Applied Physics Letters* **98** 043504

[183] Probst P, Semenov A, Ries M, Hoehl A, Rieger P, Scheuring A, Judin V, Wünsch S, Il'in K, Smale N, Mathis Y L, Müller R, Ulm G, Wüstefeld G, Hübers H W, Hänisch J, Holzapfel B,

Siegel M and Müller A S 2012 Nonthermal response of $YBa_2Cu_3O_{7-\delta}$ thin films to picosecond THz pulses *Physical Review B* **85** 174511

[184] Haugan T, Barnes P N, Wheeler R, Meisenkothen F and Sumption M 2004 Addition of nanoparticle dispersions to enhance flux pinning of the $YBa_2Cu_3O_{7-x}$ superconductor *Nature* **430** 867-70

[185] Yue J S, Chen Y Q, Bian W B, Yin X R, Tang X N and Li Z 2016 Enhanced Flux Pinning of YBCO Films by a Simple Self-Decoration Method *IEEE Transactions on Applied Superconductivity* **26** 1-5

[186] Schlepütz C M, Björck M, Koller E, Pauli S A, Martoccia D, Fischer Ø and Willmott P R 2010 Structure of ultrathin heteroepitaxial superconducting $YBa_2Cu_3O_{7-x}$ films *Physical Review B* **81** 174520

[187] Zhai H Y and Chu W K 2000 Effect of interfacial strain on critical temperature of $YBa_2Cu_3O_{7-\delta}$ thin films *Applied Physics Letters* **76** 3469-71

[188] Kawashima K, Christiani G, Logvenov G and Habermeier H U 2015 Superconductivity in $YBa_2Cu_3O_{7-\delta}/La_{1-x}Ca_xMnO_3$ Bilayers (x= 0.3, 0.45, 0.55 and 0.8) *Journal of Superconductivity and Novel Magnetism* **28** 1993-2002

[189] Habermeier H U, Zhang P X, Haage T and Li J Q 1997 T_c reduction and related phases at early stages of $YBaCuO_{7-\delta}$ film growth on $LaSrAlO_4$ *Physica C: Superconductivity* **282** 661-2

[190] Arpaia R, Golubev D, Baghdadi R, Ciancio R, Dražić G, Orgiani P, Montemurro D, Bauch T and Lombardi F 2017 Transport properties of ultrathin $YBa_2Cu_3O_{7-\delta}$ nanowires: A route to single-photon detection *Physical Review B* **96** 064525

[191] Kamigaki K, Terauchi H, Terashima T, Bando Y, Iijima K, Yamamoto K, Hirata K, Hayashi K, Nakagawa I and Tomii Y 1991 Anomalous misfit strain relaxation in ultrathin $YBa_2Cu_3O_{7-\delta}$ epitaxial films *Journal of Applied Physics* **69** 3653-62

[192] Matsuda Y, Komiyama S, Onogi T, Terashima T, Shimura K and Bando Y 1993 Thickness dependence of the Kosterlitz-Thouless transition in ultrathin $YBa_2Cu_3O_{7-\delta}$ films *Physical Review B* **48** 10498

[193] Palau A, Puig T, Obradors X, Pardo E, Navau C, Sanchez A, Usoskin A, Freyhardt H C, Fernandez L, Holzapfel B and Feenstra R 2004 Simultaneous inductive determination of grain and intergrain critical current densities of $YBa_2Cu_3O_{7-x}$ coated conductors *Applied Physics Letters* **84** 230-2

[194] Queraltó A, de la Mata M, Arbiol J, Hühne R, Obradors X and Puig T 2017 Unveiling the nucleation and coarsening mechanisms of solution-derived self-assembled epitaxial $Ce_{0.9}Gd_{0.1}O_{2-y}$ nanostructures *Crystal Growth & Design* **17** 504-16

[195] Gao J, Tang W H and Chui T C 2000 Enhanced initial epitaxy of $YBa_2Cu_3O_y$ ultrathin films grown on YSZ substrates by using a new buffer layer of Nd_2CuO_4 *Physica C: Superconductivity* **330** 33-8

[196] Xiong J, Qin W, Cui X, Tao B, Tang J and Li Y 2007 Thickness-induced residual stresses in textured YBCO thin films determined by crystalline group method *Physica C: Superconductivity and its applications* **455** 52-7

[197] Zhang C, Zhang H and Wei J Y T 2017 Phase transformation in ultrathin Y-Ba-Cu-O films by high-pressure oxygen annealing *International Journal of Modern Physics B* **31** 1745010

[198] Savvides N and Katsaros A 1994 Growth and evolution of microstructure of epitaxial $YBa_2Cu_3O_{7-x}$ ultrathin and thin films on MgO *Physica C: Superconductivity* **226** 23-36

[199] Grekhov I, Delimova L, Liniichuk I, Lyublinsky A, Veselovsky I, Titkov A, Dunaevsky M and Sakharov V 1999 Growth mode study of ultrathin HTSC YBCO films on YBaCuNbO buffer *Physica C: Superconductivity* **324** 39-46

[200] Gao J, Wong W H and Xhie J 1995 Formation of outgrowths at the initial growing stage of $YBa_2Cu_3O_x$ ultrathin films on ZrO_2 substrates *Applied Physics Letters* **67** 2232-4

[201] Suh J D and Sung G Y 1995 Thickness dependence of resistance-temperature characteristics of c-axis and a-axis oriented $YBa_2Cu_3O_{7-x}$ ulrathin films *Physica C: Superconductivity* **252** 54-60

[202] Babu T G N and Koshy J 1997 Ba_2GdTaO_6, a ceramic substrate for $YBa_2Cu_3O_{7-\delta}$ films *Materials Letters* **33** 7-11

[203] Tinkham M 1996 Introduction to superconductivity: Second Edition *Dover Publications*

[204] Obradors X, Puig T, Palau A, Pomar A, Sandiumenge F, Mele P, Matsumoto K, Scholes G D and Wiederrecht G P 2011 Nanostructured superconductors with efficient vortex pinning *Comprehensive Nanoscience and Technology. Academic Press, Amsterdam* 303-49

[205] Kang S, Goyal A, Li J, Gapud A A, Martin P M, Heatherly L, Thompson J R, Christen D K, List F A and Paranthaman M 2006 High-performance high-T_c superconducting wires *Science* **311** 1911-4

[206] Chen M, Donzel L, Lakner M and Paul W 2004 High temperature superconductors for power applications *Journal of the European Ceramic Society* **24** 1815-22

[207] Marchionini B G, Yamada Y, Martini L and Ohsaki H 2017 High-Temperature Superconductivity: A Roadmap for Electric Power Sector Applications, 2015–2030 *IEEE Transactions on Applied Superconductivity* **27** 1-7

[208] Selvamanickam V, Chen Y, Shi T, Liu Y, Khatri N D, Liu J, Yao Y, Xiong X, Lei C and Soloveichik S 2013 Enhanced critical currents in (Gd, Y)$Ba_2Cu_3O_x$ superconducting tapes with high levels of Zr addition *Superconductor Science and Technology* **26** 035006

[209] Xu A, Zhang Y, Gharahcheshmeh M H, Yao Y, Galstyan E, Abraimov D, Kametani F, Polyanskii A, Jaroszynski J and Griffin V 2017 Je (4.2 K, 31.2 T) beyond 1 kA/mm^2 of a ~3.2 μm thick, 20 mol% Zr-added MOCVD REBCO coated conductor *Scientific Reports* **7** 6853

[210] Yoshida Y, Miura S, Tsuchiya Y, Ichino Y, Awaji S, Matsumoto K and Ichinose A 2017 Approaches in controllable generation of artificial pinning center in $REBa_2Cu_3O_y$-coated conductor for high-flux pinning *Superconductor Science and Technology* **30** 104002

[211] Vallès F Thesis *Universitat Autónoma de Barcelona* to be publish

[212] Cantoni C, Gao Y, Wee S H, Specht E D, Gazquez J, Meng J, Pennycook S J and Goyal A 2011 Strain-driven oxygen deficiency in self-assembled, nanostructured, composite oxide films *Acs Nano* **5** 4783-9

[213] Koshelev A E and Kolton A B 2011 Theory and simulations on strong pinning of vortex lines by nanoparticles *Physical Review B* **84** 104528

[214] Willa R, Koshelev A E, Sadovskyy I A and Glatz A 2017 Strong-pinning regimes by spherical inclusions in anisotropic type-II superconductors *Superconductor Science and Technology* **31** 014001

[215] Palau A, Puig T, Obradors X and Jooss C 2007 Simultaneous determination of grain and grain-boundary critical currents in$YBa_2Cu_3O_7$-coated conductors by magnetic measurements *Physical Review B* **75**

[216] Solovyov V, Dimitrov I K and Li Q 2012 Growth of thick $YBa_2Cu_3O_7$ layers via a barium fluoride process *Superconductor Science and Technology* **26** 013001